THE UNIVERSITY OF HULL

Modelling the Fracture of Advanced Carbon and Related Materials

being a Thesis submitted for the Degree of
Doctor of Philosophy, Department of Engineering
in the University of Hull

by

Gary David Kipling, BEng (University of Hull)

November 2012

Abstract

This thesis outlines the development of a novel computational model which is used to simulate the mechanical response of nuclear graphites on a microstructural scale. Application of finite element analysis (FEA) to the simulated microstructure models allows for the determination of material properties and demonstrates the effect of porosity on these outputs. Further, a methodology for crack propagation through the model enables the simulation of load-displacement curves and fracture parameters.

A comprehensive microstructural characterisation programme was undertaken to ascertain pore data for use in computational models. Composite images were generated through optical microscopy in order to sample large areas (10 x 10 mm) of the graphite surface. Results for this work demonstrated the inherent variability of graphite and successfully quantified the pore size distribution.

Extensive mechanical testing was undertaken to determine the failure distribution of graphite and two additional brittle materials (glass and ligament material). Biaxial and three-point flexural experiments were employed in order to test a large number of samples. Data from these test programmes was determined to be consistent with a normal distribution and did not provide conclusive evidence for disparate flaw populations. Additional experimental tests were performed to provide data that could be used in the determination of suitable modelling input parameters.

Development and solution of the microstructure model allowed accurate representation of pore distributions in an FEA environment which in turn enabled computationally derived mechanical properties to be determined. These properties were comparable to values expected of graphite. Additionally, some simulated fracture parameters compared favourably with experimental results. However, not all properties were representative due to the significant geometric contrast between computational models and experimental samples.

Dedication

This thesis is dedicated to my Dad, Mum and Nana. Without their love, support and devotion, all my achievements would not have been possible.

Acknowledgments

The author would like to express his sincere gratitude to EDF Energy Ltd. for their financial support. Specific thanks go to Mr. Alan Steer and Dr. Jim Reed for their valuable guidance throughout my PhD.

Thanks to my supervisor, Dr. Gareth Neighbour for his advice, guidance and knowledge.

Thanks also to the University of Hull department of engineering, specifically, Prof. Michael Fagan, Dr. Jim Gilbert and Mr. Nathan Brown for their assistance in preparing my thesis. Additional thanks to all the engineering technical and support staff, in particular Mr. Garry Robinson for his dedication and advice.

Finally, I would like to thank my friends and colleagues for all their support and encouragement.

Table of Contents

Chapter 1 – Introduction

The United Kingdom (U.K.) currently operates sixteen nuclear reactors which supply a significant amount of electricity to the country (approximately 17.2% in 2011)[1]. Graphite plays a crucial role in the operation of some reactors in the form of an active core. The state of a core is monitored throughout the life of the reactor using specialist equipment and inspections have revealed cracks in some components. Currently, the quantity and location of these cracks is not considered to be critical enough to compromise the operation of the reactors. However, safety cases must be satisfied to demonstrate the continued safe operation, taking into account worst case scenarios. Experimental testing and modelling work is undertaken to determine mechanical properties of the materials and simulate scenarios involving varying quantities of cracked components. Although this work is fundamental in the satisfaction of safety cases, the primary focus is on an engineering scale (*i.e.* whole brick components). The assumption is often that the materials in question are homogeneous; however, this is certainly not the case when considering nuclear graphite. The microstructure is highly heterogeneous and is comprised of different constituents as well as porosity. The role of these microstructural constituents and porosity on the failure mechanisms of the graphite is not straightforward and is difficult to predict. It is for this reason, that a microstructural model, taking into consideration porosity distributions is desirable. The application of a representative microstructure into a finite element environment would enable stress distributions through the material to be observed and also enable crack propagation to be predicted.

This thesis presents a novel approach to simulate the failure of nuclear graphite on a microstructural scale and aims to deliver an improved fracture model for advanced carbon materials. These models are based upon a simulated microstructure including a representative flaw population. The model will be used to predict mechanical properties and identify how this changes with variations in material microstructure. Better characterisation of fracture in graphite may allow for more accurate predictions regarding the initiation and behaviour of cracks. Results from the work may help in

[1] Number of reactors and percentage contribution of nuclear power sourced from IAEA database (accessed 18th July 2012). http://www.iaea.org/PRIS/CountryStatistics/CountryDetails.aspx?current=GB

demonstrating the safety and tolerability of nuclear graphite cores thus potentially contributing to life extension of the U.K.'s nuclear power stations. An extensive microstructural characterisation programme has been undertaken to provide accurate data regarding pore sizes and distributions over a large scale sample (see Chapter 6). In addition, microstructural data will aid in the development of representative models. The primary aims and objectives of this thesis are outlined below:

- Development of a methodology to create computational models that incorporate representative microstructural variations.
- Utilisation of these methods to output representative data, thus enabling mechanical characterisation of the models.
- Characterisation of the material microstructure to determine input parameters for the microstructural models.
- Mechanical test programmes to determine the strength distribution of advanced carbon materials. Data from these tests will assist in the definition of input parameters and support the validity of the computational results.

This thesis is primarily related to nuclear applications of graphite and therefore this chapter will briefly outline the history of nuclear energy and the key role of graphite in the industry including synthetic manufacture and its properties. Additionally, a broad background of graphite will be briefly described along with applications to other industries. Chapters Two and Three will review relevant literature with particular emphasis on the microstructural features of graphite and how these affect the mechanical performance. Chapter Four will review existing graphite fracture models with an emphasis on computational approaches. Chapter Five explains the considerations that are taken into account when developing an experimental test programme detailing the selection of materials and experimental geometries. Additionally, Chapter Five presents and analyses the experimental results. Chapter Six presents extensive microstructural characterisation work and explains the methods utilised to ascertain this data. Chapters Seven and Eight explain the development of representative microstructure models and present the computational results respectively. Finally, Chapter Nine discusses and concludes the work undertaken in this thesis in addition to suggesting potential future directions which could be carried out by similar studies.

1.1. Introduction to the History of Graphite and its Applications

Polygranular graphite is used on a global scale and has a large number of different uses and applications ranging from the modest pencil 'lead' to playing a key role in the steel production industry. Due to the extreme variation in graphite applications, manufacturing processes are often tailored to specific material properties (*e.g.* density, particle sizes *etc*.) in order to facilitate the desired function. One such function is the use of graphite as a neutron moderator in the nuclear energy industry, which is discussed further in Section 1.3.

Graphite is a naturally occurring allotrope of carbon that consists of a series of parallel layers. It occurs naturally and significant quantities are found in China, Canada and Russia. Alternatively, graphite may be produced synthetically through the decomposition of hydrocarbons followed by heat treatment. Graphite properties can vary dramatically depending on the manufacturing or refining process and, in the case of synthetically produced graphite, the raw materials. The theoretical crystal density of graphite it 2.26 gcm^{-3} (Moore *et al.* 1962), however, the density of bulk material will often be less than this due to the presence of porosity.

The layered crystal structure of graphite has two forms; α (hexagonal) and β (rhombohedral). In both cases, each planar layer, referred to as the a-axis, is made up of carbon atoms arranged into a hexagonal structure. However, α and β forms differ in how the planes (c-axis) are arranged, as shown in Figure 1.1. The layer planes in hexagonal structured graphite are arranged in an ab ab... sequence (Bernal, 1924) whereas the rhombohedral structure is arranged in an abc abc... sequence (Lipson *et al.* 1943). Ordinarily, graphite is hexagonal in structure, although a small amount of rhombohedral structure may be found in natural graphite. Close spacing of carbon atoms in each layer (1.42Å) is a consequence of strong covalent bonds (Slonczewski, 1958), whereas the relatively large inter-layer spacing (3.35Å) results from weak van der Waals type bonding, produced by a delocalised π orbital (Franklin, 1950 and Chung, 2002). As a result of this structural arrangement, the atomic structure of graphite is highly anisotropic (Simmons, 1965).

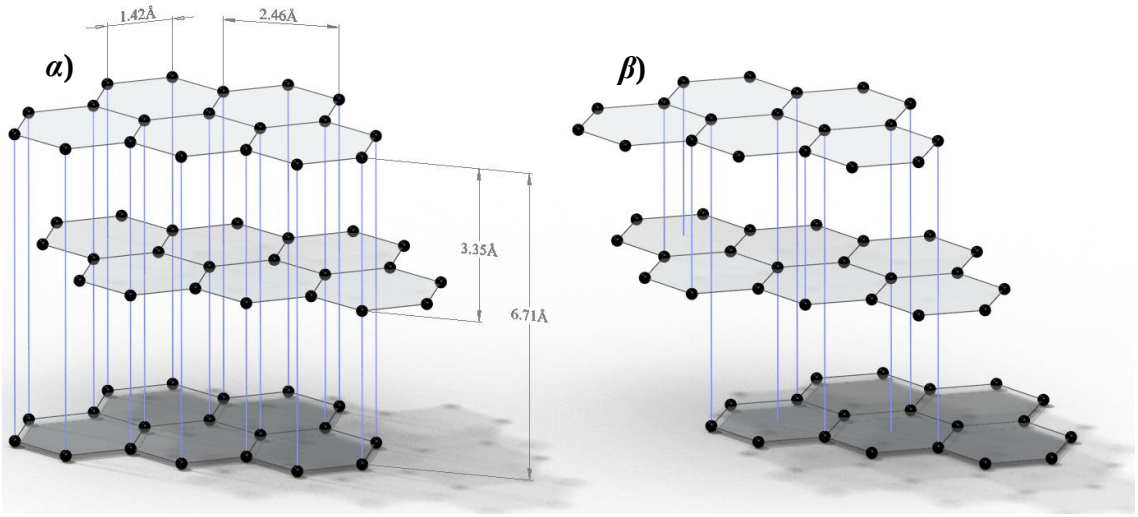

Figure 1.1: Atomic structure of α and β forms of graphite. (Based on Greenwood *et al.*, 1984)

One of the oldest widespread applications of graphite, dating back to the 16th century is its use as pencil 'lead'. This function is possible due to the inherent weak inter-plane bonds present in the material which make it easy for layers to slide with respect to one another (Chung, 2002). This property also makes graphite an excellent dry lubricant which was first used in the manufacture of cannonballs around the same time as the emergence of pencils. Graphite is an excellent conductor of heat and electricity and thus has been applied to various industries that require materials to operate in extreme conditions. Arc furnaces for melting steel use graphite electrodes due to the electrical conductivity and heat resistant properties. Similarly, nozzles and nose cones for space vehicles have also adopted the material to take advantage of the thermal properties.

1.2. Manufacture of Synthetic Graphite for Industrial Applications

In 1895, Edward Acheson submitted a patent for a method of manufacturing synthetic graphite (Acheson, 1895). This technique of synthesising graphite is commonly used to produce material for industrial applications, including the manufacture of nuclear graphite for use as a moderator. The majority of synthetic graphites manufactured through the application of this method utilise a coke 'filler' and coal tar pitch 'binder' as the primary constituents. Different graphite grades can be produced through the alteration of raw materials or manufacturing parameters, however, the general process of graphite production is described below, Figure 1.2.

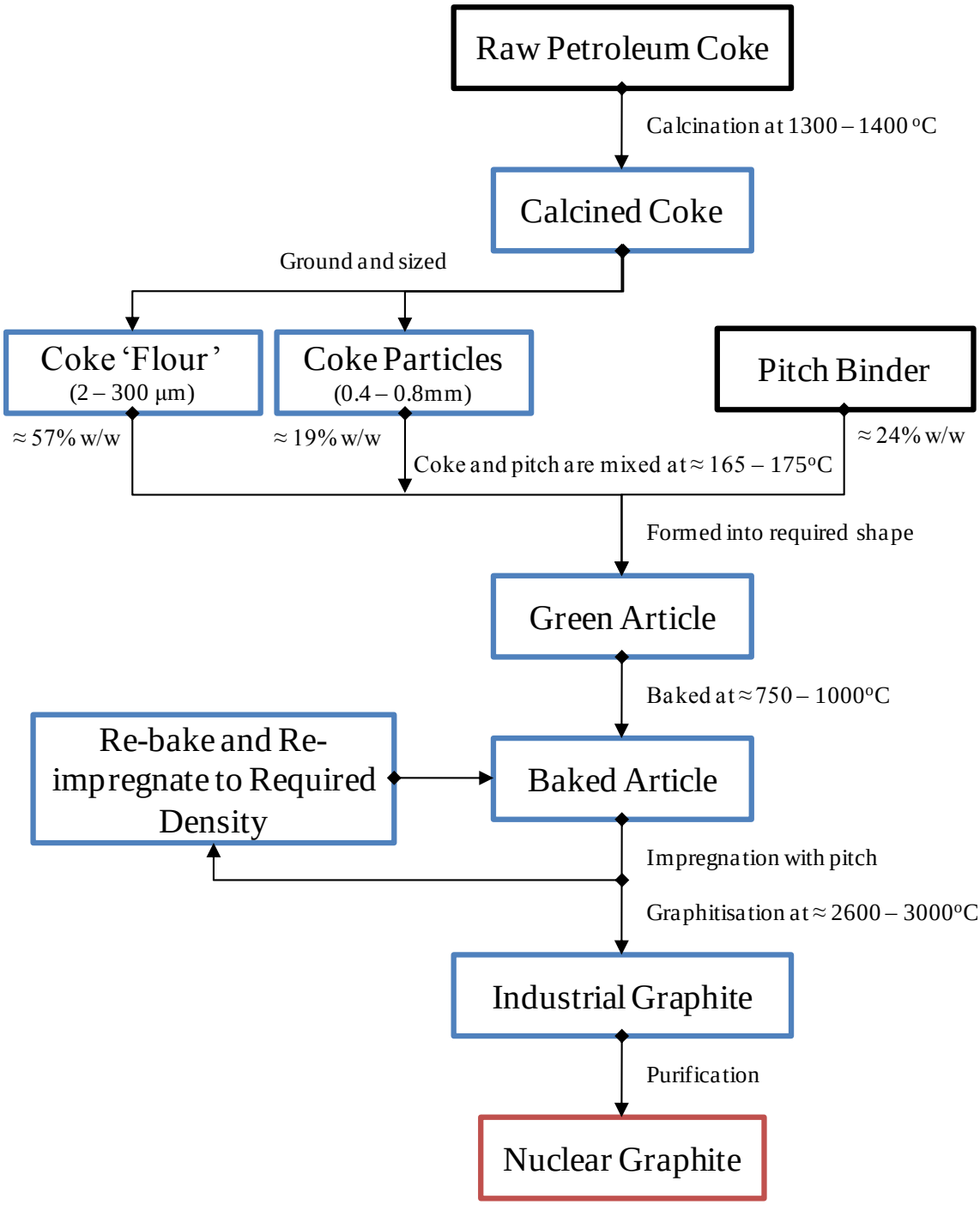

Figure 1.2: A simplified illustration to show the process of manufacture for nuclear graphites. (Based on Holt (2008), Prince (1979) and Nightingale (1962))

It should be noted that the particle size distributions in Figure 1.2 are roughly approximate to nuclear graphite used in Advanced Gas-cooled Reactors (AGR's). Other grades of graphite may utilise significantly different size distributions in their manufacture.

1.2.1. Raw Materials: Filler and Binder

Filler materials used in the manufacturing process include petroleum coke, metallurgical coke, anthracite and lampblack. The most commonly used filler materials are based on petroleum coke due to it being able to achieve a higher degree of crystallinity when it is heated to 2800-3000^{o}C. The refinement of petroleum crude oil through 'cracking' produces petroleum coke as an end product, thereby making it readily available at low cost. Coal tar pitch is often used as a binder material for the filler coke (Wen *et al.*, 2008). The exact requirements of binder material are dependent on the finished article but generally must fulfil a number of specifications. Firstly, the binder must be thermoplastic, in that it is solid at room temperature and fluid at higher temperatures (~140 to 190^{o}C). This requirement ensures that the filler and binder can be mixed at elevated temperatures whilst permitting storage and handling at room temperature without any effect to the shape of the material. A softening point of approximately 100^{o}C ensures that coal-tar pitch is an adequate choice of binder. Coal tar pitch is also a suitable choice since it has a high carbon content of approximately 93% and a high specific gravity of ~1.30 gcm^{-3} (Nightingale, 1962). A wide range of filler and binder materials are used to produce graphite with different mechanical, electrical and physical properties to suit specific applications

1.2.2. Calcination and Sizing

Calcination heats the raw petroleum coke (commonly referred to as 'green coke') to temperatures as high as 1400^{o}C in order to remove moisture and volatile matter. This process also pre-shrinks the coke to prevent excessive dimensional change later in the process (Akhmetov *et al.*, 1980). After calcination, the filler material is crushed and screened to provide the necessary mixture of coke particles and 'flour'. The coke particles typically range in size from 0.4 to 0.8 mm whereas the flour is much finer, 2 to 300 μm. The size distribution of particles in the flour mix is carefully controlled. Variations in these distributions can lead to different grades of graphite being manufactured. There are three main considerations when selecting a filler particle size distribution (Ragan *et al.* 1983):

- Through the use of an appropriate particle size distribution, it is possible to reduce the size of and overall number of interparticle voids by packing small particles between larger particles.
- Contradictory to the first point, it may be necessary to provide enough porosity to allow volatile products from the binder phase to escape during baking.
- It may also be necessary to alter the size distribution of particles to ensure that the porosity distribution and overall percentage porosity in the finished article are adequate for the application.

The shape of particles can have an impact on the packing arrangement and thereby influence the orientation of the particles. This can have an effect on the degree of isotropy exhibited by the final product. For example, the use elongated coke particles can result in a highly anisotropic finished article.

1.2.3. Mixing and Forming

After the filler particles have been crushed and sized, they are mixed with the binder material at a low intensity to ensure that they remain intact. The ratio of material is approximately three parts filler to one part binder. Mixing takes place at a temperature of ~165 to 175^{o}C so as to soften the coal tar pitch and allows for an even distribution of filler and binder phases throughout the material. The structural integrity of the finished article depends on the intergranular bonds, thus making an even mixture of binder throughout the filler coke important when considering the strength of the material. The mixture is then formed through extrusion, moulding or isostatic pressing. The purpose of forming at this stage is to increase the density of the article through contact between binder coated filler particles and a reduction in the overall porosity of the mixture. This process produces a 'green' article with dimensions that are as near as possible to the finished product, thereby reducing machining and finishing costs. The variety of different forming methods can have an effect on the material properties and isotropy. Application of either an extrusion or a moulding forming process can result in bulk anisotropy in the resultant graphite. During the extrusion process, filler particles align with their long dimensions parallel to the direction of extrusion. This process produces graphite with two across-grain directions and one with-grain direction. When the moulding process is used, filler particles will align with their long dimensions normal to

the moulding form. Thus, a moulded article will exhibit two with-grain directions and one across-grain direction which coincides with the moulding direction. Generally, it is observed that properties such as the Young's modulus, strength and thermal conductivity are higher in with-grain directions, whereas, thermal expansively is greater in the across-grain direction (Haag, 2005).

1.2.4. Baking and Graphitisation

The green article is baked to carbonise the binder pitch, thereby converting it into solid coke. Shrinkage through the volatilisation of binder is controlled by heating the material at a slow rate. This ensures that cracking of the artefact is avoided during subsequent graphitisation where the material is heated up very rapidly. Baking takes place in a furnace at temperatures of around 750 to 1000^{o}C. The heating cycle can take between 30 and 70 days due to the low thermal conductivity of the contents in the baking furnace. The baking process may volatise 30 to 40% of the binder content, resulting in an increase in porosity and thus lower density. A critical heating rate, normally in the range of 2 to 10^{o}Ch^{-1} should not be exceeded in order to avoid preferential shrinkage and potentially splitting of the product (Ragan *et al.*, 1983). In the manufacture of high performance graphites, such as those for nuclear applications, an impregnation stage is used before final graphitisation. Impregnation involves the addition of solid material; most commonly pitch, to the graphite article. The impregnant, in fluid state, is added to the material under positive pressure to fill pores in the graphites structure. Upon re-baking, additional solid carbon is deposited in the voids. The result is an alteration of the material properties through an increase in density (*i.e.* reduction in porosity) (Jäger *et al.*, 2010). At this stage the baked material is very hard, brittle, difficult to machine and may contain a significant amount of impurities (Prince, 1979).

Graphitisation is the transformation of non-graphitic carbon into a well ordered graphite structure through the movement of carbon atoms into a more thermodynamically stable graphite lattice. This process requires a temperature of around 2600 to 3000^{o}C and can take up to 18 days in an Acheson furnace. Changes to the material structure during graphitisation are a result of crystal development and have a significant effect on the properties, in particular, ease of machining and improved thermal conductivity (Prince,

1979). The high temperatures required for this process volatise much of the remaining material impurities. Once the material has cooled, it can be machined into the required shape.

In the case of nuclear graphites, steps must be taken to ensure they are refined in such a way as to make them suitable for use in reactors. Special attention is paid to the selection of high purity raw materials to minimise trace elements that have a high neutron cross section such as vanadium and boron. Thermochemical processes such as the addition of halogens during the graphitisation process may be used to remove such impurities from the graphite (Jäger *et al.*, 2010).

1.3. Nuclear Power and the Role of Graphite

In January 1939, two German scientists, Otto Hahn and Fritz Strassman, reported that they had found the element barium as a product through neutron bombardment of uranium thereby demonstrating nuclear fission (Arnold, 1979). Hahn and Strassman then went on to demonstrate that fission not only released a large amount of energy, but also released additional neutrons which could in turn sustain a nuclear chain reaction. Further research suggested that fission would be more effective with slow moving neutrons leading to the proposal of a moderator being used to slow the neutrons and thereby increase the chance of capture from other uranium atoms.

The first nuclear reactor became critical on 2nd December 1942 at Chicago University. This reactor, developed and built by a small group led by Enrico Fermi as part of the Manhattan project, was called Chicago pile 1 (CP1) (Maier-Komor, 2009). The years following this initial success lead to resources being used to develop nuclear weapons for use in World War II. However, following the end of the war, interest was expressed in using nuclear technology as a means of power generation in addition to the further development of weapons.

1.3.1. Brief History of Nuclear Power in the United Kingdom

The first commercial reactor in the United Kingdom (U.K.) and indeed the World's first nuclear power plant to generate electricity on an industrial scale was constructed

between 1953 and 1956 at Calder Hall in Cumbria and was officially opened by HM The Queen in October 1956. The first generation reactors in the U.K. were of the Magnox type, of which a total of 26 units were commissioned at 11 power stations between 1953 and 1971. Table 1.1 shows the location of the nuclear power stations currently in operation in the U.K. along with the type of reactor and expected shutdown date. Of the Magnox reactors that were commissioned only one is currently still operational. Advances in nuclear technology led to the development of the Advanced Gas-cooled Reactor (AGR). These reactors were able to run at higher temperatures and fuel ratings, thus increasing the efficiency. Construction on the first AGR power station (Hinkley Point B) began in 1965 and commercial operation was started in 1983. By the beginning of the 1990's seven power stations were in operation, each with two AGR's. Construction of a single Pressurised Water Reactor (PWR) began in 1988 and entered commercial service in 1995 (Sizewell B).

Table 1.1: Nuclear Power stations currently operating in the U.K. and their expected shutdown dates.

Reactors	Type	Expected Shutdown[2]
Wylfa	Magnox	End of 2012
Dungeness B	AGR	2018
Hartlepool	AGR	2019
Heysham 1	AGR	2019
Heysham 2	AGR	2023
Hinkley Point B	AGR	2016
Hunterston B	AGR	2016
Torness	AGR	2023
Sizewell B	PWR	2035

1.3.2. Nuclear Reactor Technology

This thesis primarily focuses on the Magnox and AGR reactors since these utilise a graphite core. Graphite's use in a reactor is primarily, but not exclusively, to provide a

[2] Expected Shutdown dates referenced from information provided by Magnox Ltd and EDF Energy Ltd. Information accessed 26th June 2012.

means for moderation of the nuclear reaction. The two main requirements for moderator graphite are that it must be effective at slowing fast neutrons down to thermal energies and that it must have a small neutron absorption cross section. Elastic collisions between the neutrons and the moderator atoms result in energy transfer. This slows the neutrons down, thereby increasing the likelihood of absorption by other uranium atoms and thus aids in sustaining a nuclear chain reaction. Parasitic absorption, when neutrons are absorbed by reactor components other than the fuel must be minimised, thereby making it important that the graphite is free from impurities (Nightingale, 1962). Graphite is by no means the only suitable moderator material, with alternative commercial reactor designs utilising, water or heavy water to achieve neutron moderation. Additionally, beryllium and lithium are possible moderator materials; however, these have not been implemented in modern commercial reactors.

An addition purpose of a graphite core is to accommodate the fuel source and allow the energetical output of the nuclear reaction to be controlled through insertion of control rods. Further, the core must be designed in such a way as to allow coolant to pass though the core and heat up sufficiently before exiting to the boiler. Although similar in their purpose and operational requirements, the designs for Magnox and AGR cores do vary. PWR technology will not be described in this section since water is used as a moderator and therefore graphite is not used in the construction of the core.

1.3.2.1. Magnox

The Magnox reactor takes its name from the Magnesium Non-Oxidising cans which are used to contain the fuel source. All Magnox reactors are moderated by a graphite core and cooled by carbon dioxide. The temperature of the CO_2 increases from 225^{o}C at the inlet to approximately 370^{o}C before it is discharged into the heat exchanger. The reactors were originally constructed with steel pressure vessels; however this design was changed for the final four reactors, which opted for a pre-stressed concrete pressure vessel. The core structure is carried on a steel diagrid via support plates. Its position and shape are maintained through a steel restraint structure. The dimensions for the Oldbury active core are 9.75m in height with a radius between 6.8 and 7.2m. The core is made up of graphite bricks, each around 81 cm in height and between 17 and 22 cm wide. The graphite used in the core is of two types, Pile Grade A (PGA) and Pile Grade

B (PGB) with the moderator being formed from PGA since it has a higher density and lower neutron capture cross-section. A mixture of PGA and PGB form the top, bottom and side reflector blocks of the core (Ellis *et al.*, 2007)

When the first Magnox reactor was designed, it was erroneously believed that the graphite would grow in both perpendicular and parallel directions to extrusion axes of the brick, with a respective ratio of 6:1. A solid structure would have become 'barrel-shaped' and ultimately would have resulted in channel distortion and thus difficulties inserting control rods and fuel elements. Early reactors overcame this problem through the use two layers of rectangular tiles interleaving the moderator bricks. Vertical keys were used to interlock the columns in later station designs. These keys extend over the complete length of each moderator brick which take the form of alternate square and octagonal shapes (Figure 1.3). This design allowed for radial and vertical movement between adjacent columns thus allowing for dimensional change (Prince, 1979).

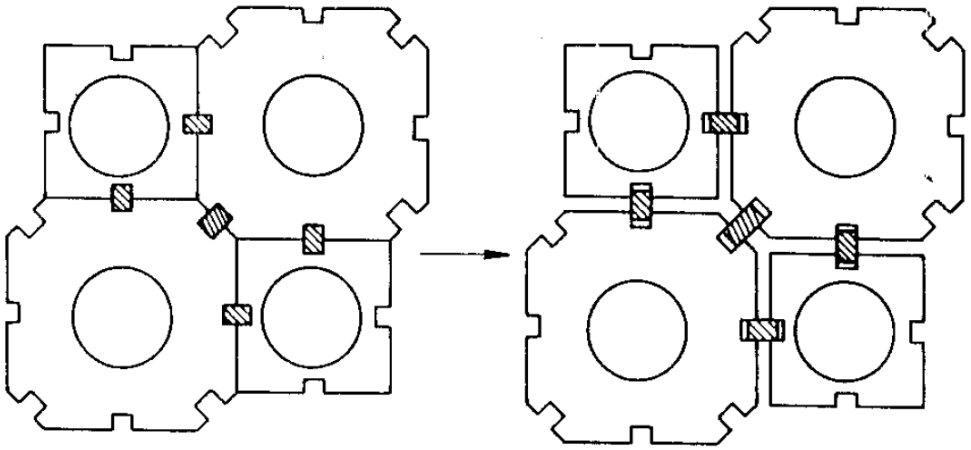

Figure 1.3: Vertical key design for interlocking adjacent columns (Carpenter and Norfolk, 1984).

1.3.2.2. Advanced Gas-cooled Reactor (AGR)

Like the Magnox reactor design, Advanced Gas-Cooled reactors use graphite for moderation and cooling is provided by carbon dioxide. As a result of operational experience from the Magnox reactors, the AGR's incorporated a number of significant changes. High thermal efficiency of the reactor (around 40%) was achieved by providing high temperature and high pressure steam conditions. Each reactor was

designed to generate 1600 MW of heat; resulting in an electrical power output of around 660 MW. Cold CO_2 at a temperature of around 285°C is pumped from the bottom of the boilers into the bottom of the core at a pressure of approximately 4 MPa. Flow of the coolant is directed beneath of the core support structure and upwards past the side of the core before re-entering the core from the top. This re-entrant flow is directed over the steel restraint structure and the inner surface of the pressure dome to prevent preferential expansion, which could potentially distort the vertical fuel paths. Additionally, the re-entrant flow feature is necessary due to the upper moderator temperature specification which requires that the flow be taken in series, opposed to parallel with the fuel channel flow, to prevent degradation of outlet gas temperature. On passing the fuel pins the gas is heated to approximately 650°C before it is discharged and enters the tops of the boilers. The core is approximately 9 metres in diameter and 8 meters in height. The permanent components of the core are made from nuclear graphite that is flour impregnated with pitch to produce near-isotropic properties. Moderator bricks are double impregnated and the reflector and shielding bricks are single impregnated (Steer, 2007). Figure 1.4 shows a simplified diagram of an AGR.

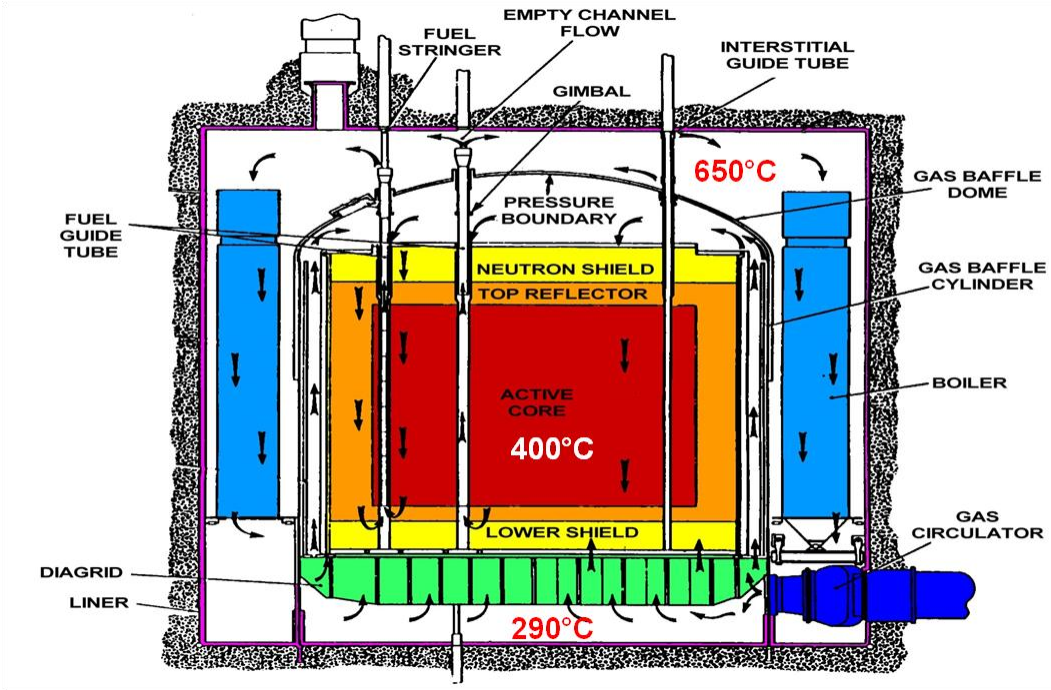

Figure 1.4: Diagram of an Advanced Gas-cooled Reactor (AGR) (Reed, 2008)

Each core is roughly circular and consists of 11-13 rings of columns made from the large bricks. The inner 9-10 columns are hollow and accommodate the fuel rods,

whereas the outmost rings are solid and act as a neutron reflector. Overall the core is made up of approximately 300 fuel channels and 80 control channels. AGR cores use large bricks that are approximately circular in shape, with smaller bricks to accommodate the interstitial positions. Filler brick accommodate any other space in the reactor and also contain cooling gas channels.

Similarly to the later designs for the Magnox reactors, AGR cores use keys to interlock the columns whilst still allowing for dimensional change of the components. Although this keying arrangement was adopted, it was necessary to make significant changes to the arrangement of the bricks and keys (Figure 1.5). The peripheral reflector bricks are connected to a steel restraint core to ensure the graphite expansion matches that of the pressure dome. Relative sliding of keyways in the core is inevitable when circumstances dictate a change in temperature (*e.g.* changes in reactor power) since the thermal expansion coefficient of graphite is approximately 1/3 that of mild steel (Prince, 1979).

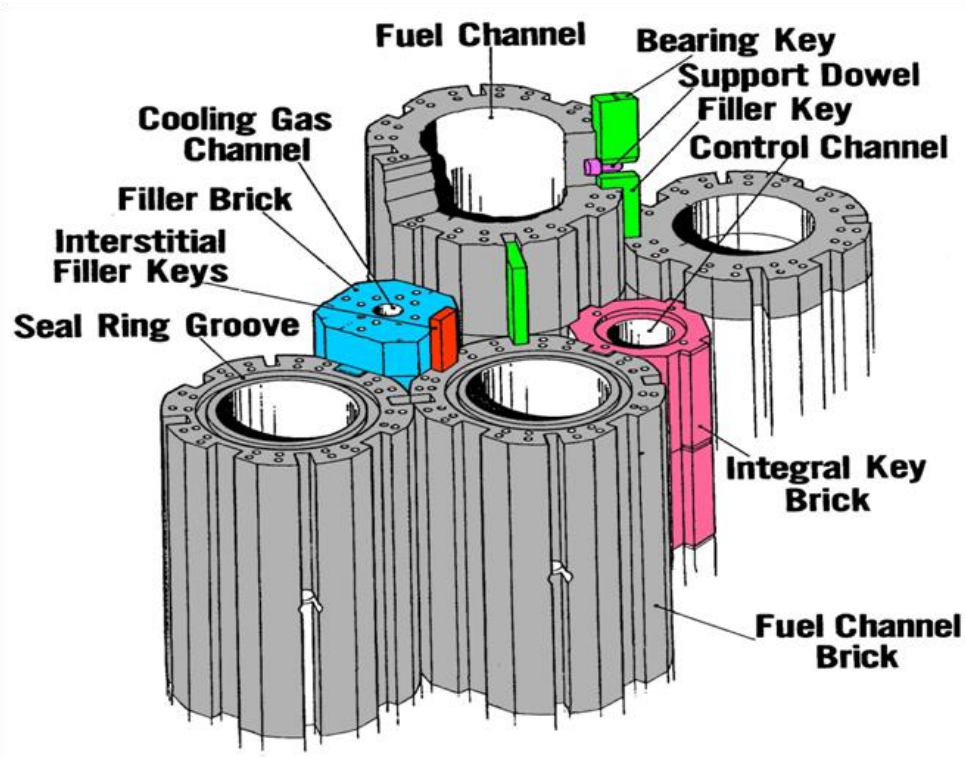

Figure 1.5: Keying arrangement in AGR core showing the large fuel bricks and interstitial/integral key bricks (Reed, 2008).

1.4. Effect of Reactor Conditions on the Physical Properties of Graphite

The mechanical performance of nuclear graphite has been the subject of a great deal of research, both during the development of reactor materials and throughout the lifetime of the power stations. Research into the development of suitable material has resulted in grades of graphite that are designed specifically to endure the conditions present in a reactor core. Since the first generation of commercial reactors went critical there have been significant advancements in reactor technology as well as an increased understanding for the operational requirements of nuclear materials. In the interests of ensuring safe performance whilst increasing the operational lifespan of reactors, development of moderator material has meant that specific grades have been utilised for each generation of graphite moderated reactors (*e.g.* the use of PGA and IM1-24/GCMB grade graphites for first and second generation reactors respectively).

Graphite components used in reactors cannot be replaced or repaired once the station begins operational service. Continual monitoring of moderator material is required due to physical changes that occur as a result of conditions present in the reactor core. Throughout the operational life of a reactor core, the graphite moderator bricks are subjected to a range of stresses, such as vibrations, thermal expansion and gas pressure. In addition to these stresses, the material undergoes physical changes induced though exposure to high levels of radiation. Over the course of the reactors lifespan, these changes have a dramatic effect on the physical dimensions and material properties of the graphite. It is therefore critical to the continued safe operation of the reactors that the current state of the graphite is understood. Exposure to the high levels of ionising radiation in a reactor core result in two main processes that contribute to material changes in graphite, radiolytic oxidation and neutron irradiation.

1.4.1. Radiolytic Oxidation

The sole source of graphite moderator corrosion in carbon dioxide cooled reactor cores is caused by radiation-induced oxidation. Radiolytic oxidation of graphite occurs when the carbon dioxide coolant is exposed to radiation energy, primarily gamma-radiation. This exposure results in the breakdown of CO_2 molecules into oxidising species (commonly represented by ‘Ox’) and additional products, including CO. If an oxidising

species makes contact with the graphite surface before is recombines into CO_2, it results in the gasification of a carbon atom to produce CO (Best *et al.*, 1985). Early work relating to the effect of radiolytic oxidation processes on single crystal graphite demonstrated that the oxidation would create vacancies in basal planes which would subsequently be expanded by mobile surface oxides (Feates, 1969). Oxidation may take place at any surface exposed to CO_2, including open porosity in the material. As a consequence, the overall porosity in oxidised graphite will increase, thereby contributing to weight loss of the material. Corrosion at the surface of pores causes them to enlarge and in some cases form interconnections to neighbouring pores, enlarging them further. The rate of corrosion in enlarged pores is likely to increase due to an increased surface area as well as a greater volume of gas contained within the pore. In addition to increasing the open pore volume of the material, closed porosity in filler particles may be converted to open porosity as the corrosive effects of oxidation form interconnections between binder and filler materials (Murdie *et al.*, 1986).

The net result of weight loss from radiolytic oxidation is an alteration in the material properties, in particular, a reduction in strength and elastic modulus. Corrosion effects from radiolytic oxidation are reduced through addition of small quantities of the gas-phase inhibitors, carbon monoxide (between 1 and 2%) and methane (0.023%) to the coolant (Minshall *et al.*, 1995).

1.4.2. Neutron Irradiation

Damage from neutrons is caused when energetic particles displace carbon atoms from their position in a lattice thereby creating a vacancy and an interstitial atom. Displaced carbon atoms tend to create a cascade effect, displacing 5-10 additional atoms in the process. Generally, a high proportion of interstitials will recombine with lattice vacancies; however, others may coalesce into less energetic linear molecules which in turn may form the nucleus of a dislocation loop (Burchell, 2002).

Neutron irradiation induces dimensional change as well as alterations to the material properties of the graphite. Initial bulk shrinkage of the components at lower neutron fluence is follow by expansion at higher neutron fluence. The initial shrinkage of the graphite is caused by the closure of small pores and cracks as a result of *c*-axis

expansion and contraction of the crystallites in the *a*-axis. The point at which shrinkage is reversed is called 'turnaround' and is believed to occur when shrinkage cracks are unable to accommodate new irradiation-induced crystalline growth. Following 'turnaround', the material begins expanding, eventually resulting in a net expansion of the graphite components.

Figure 1.6 schematically illustrates the relationship between dimensional change and increasing neutron dose as follows:

- AB – initial bulk shrinkage of the material. Pore closure due to *c*-axis growth but no pore generation.
- BC – transient pore generation. Radiolytic oxidation accommodating new c-axis growth and delaying turnaround.
- CD – pore generation from unaccommodated crystal growth.
- BF – unaccommodated c-axis growth and undelayed pore generation.
- BE – unlimited pore closure (theoretical case).

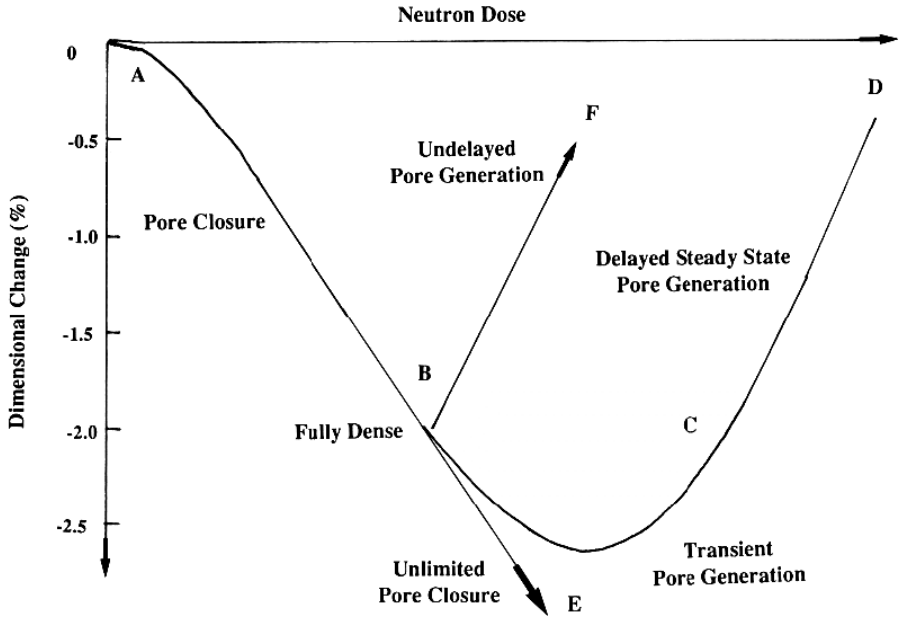

Figure 1.6: Dimensional charge as neutron dose increases (Neighbour, 2000).

The rate of dimensional change of graphite varies throughout the reactor core since material close to the fuel source (*i.e.* the bore of the moderator brick) receives a higher fluence. Internal stresses are induced in components due to this effect. Prior to turnaround, the bore of the moderator brinks shrink at a faster rate than the periphery

resulting in a tensile hoop stress at the bore and a compressive hoop stress at the periphery. After 'turnaround', this effect is reversed (Figure 1.7).

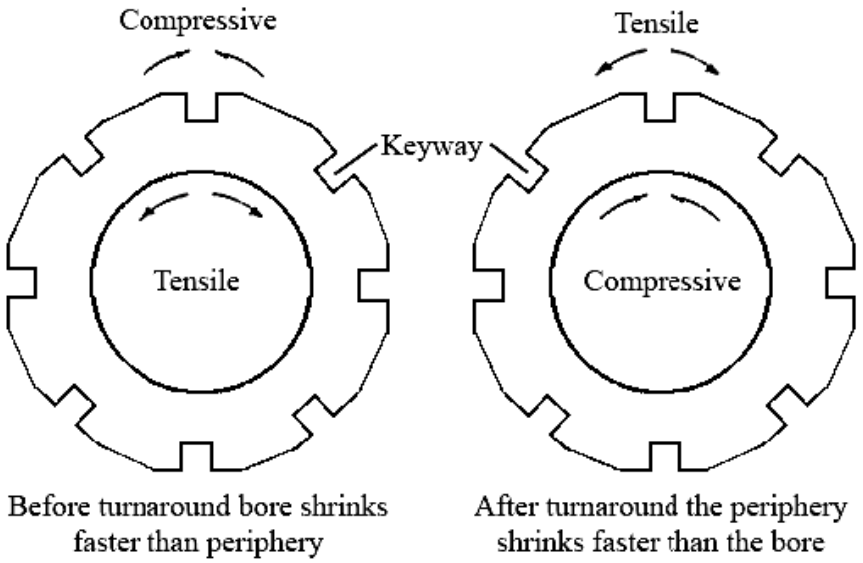

Figure 1.7: Schematic diagram of internal stress distributions in AGR moderator bricks (Carpenter and Norfolk, 1984).

Various cracking phenomena can occur in the core of an AGR due to the stress on the moderator bricks. Internal and external sources of stress are concentrated around the keyway root, making this the most likely location for crack initiation. Indeed, 'keyway cracking' has been observed in the core of some nuclear reactors. Another mechanism involves the controlled progression of cracks on the bore of the moderator bricks.

1.5. Chapter Summary

An appreciation for the intricacies of graphite and its application to the nuclear industry provides a firm foundation on which further work will be based. This chapter has briefly discussed the history of graphite as well as the manufacturing process and its applications to modern industry. The role of graphite in nuclear reactors was also discussed with an emphasis on the technology that is currently operating in the U.K. Effects of reactor conditions, radiolytic oxidation and neutron irradiation, on the material have also been detailed. Subsequent chapters will aim to explain more about the graphite from an engineering view point and outline the characteristics and properties of the material in greater detail.

Chapter 2 – Microstructural Characteristics of Nuclear Graphite

As with many engineering materials, graphite is commercially produced in numerous different grades. Material properties of graphite may be changed by altering a number of different factors such as; size of filler particles, flour and particle mix, binder type, or manufacture process (*e.g.* extrusion or moulding) to name but a few. Identifying the optimal manufacturing parameters to produce graphite with suitable material properties continues to be the subject of a great deal of research. This chapter is concerned with the bulk properties and microstructural characteristics of graphite. Additionally, the effect of microstructural features on mechanical properties will be discussed. Although nuclear graphite is the focus for this chapter, much of the information is generally applicable to industrial graphites.

2.1. Microstructural Characteristics of Graphite

Graphite is a highly heterogeneous material on a microstructural scale due to different constituent materials (*e.g.* filler, binder and impregnant) being used in its manufacture. In addition, differential thermal contraction, blow holes due to gas evolution from the volatilisation of binder material or inherent voids in the raw coke can lead to a wide spectrum pores (Brocklehurst, 1977). Due to this heterogeneity and in some instances, anisotropy, mechanical properties and hence, fracture, can be difficult to predict accurately and consistently. The quantity, size distributions and orientation of porosity or material constituents can have a significant impact on mechanical test results. This variability means that experimental samples are likely to exhibit different mechanical characteristics, even when tested under identical loading conditions. An additional complication when considering the testing of graphite is the reproducibility of results. Compositional variation on a microstructural level cannot be accurately controlled and thus results in a probabilistic pore size distribution within the material.

2.2. Binder Material

Within the microstructure of typical graphites, two distinct regions of binder phase material are commonly observed. Domains are relatively large areas (with linear

dimension more than 100 μm) of common basal plane alignment, whereas mosaics consist of small areas (with commonly oriented basal planes less than 10 μm in linear dimensions) of randomly oriented pseudo-crystallites. Domains, with their extended areas of basal plane alignment are liable to undergo cleavage at stresses below fracture stress and are likely sources of crack initiation, especially when located near pores. Conversely, mosaic regions are likely to arrest propagating cracks and will generally only fracture at stresses approaching the fracture stress of the material (Burchell, 1996).

2.3. Filler Particles

The manufacture of graphite uses a distribution of particle sizes and whilst some of the filler material is crushed and sized to provide the required distribution of small particles (*i.e.* the 'flour'), larger particles form a significant proportion of the overall volume. The selection of these particles can have a dramatic effect on the material properties of the bulk material. Moderator graphite used in the U.K's Magnox and AGR nuclear reactors is of PGA and IM1-24/GCMB grade respectively (Virgil'ev, 1997). IM1-24 and GCMB graphites have the same specification, but were manufactured by different companies. Additional grades of graphite, PGB and a singly impregnated grade of AGR graphite are used for reflector bricks around the outside diameter of the core.

2.3.1. Needle Coke

Magnox reactor graphite is manufactured using a 'needle coke' which is usually manufactured from petroleum products. The grinding process results in acicular (needle shaped) particles (Kelly, 2000) up to 1 mm in length. The 'needle' shaped particles have a tendency to align in the direction of extrusion giving rise to significant anisotropy in the material. The effect of radiation on this anisotropic material was concerning and as such it was determined that an isotropic material would be preferable for use in AGR's.

2.3.2. Gilsocarbon

A naturally occurring asphaltite called Gilsonite coke, which was mined in Utah; USA (Picard, 1985) was used as a filler material in AGR graphite. The particles in AGR

graphite are roughly spherical in shape and exhibit an 'onion skin' like structure. The diameter of these particles is approximately 0.5 mm (Ouagne *et al.*, 2002); however, it is common to identify particles of varying sizes. During moulding, the particles show no preferential alignment resulting in near-isotropic properties for the material.

2.4. Porosity

Porosity in a solid body may be defined as the fraction, *P*, of the volume of a sample which is attributed to pores:

$$P = V_p/V \qquad \text{Equation [2.1]}$$

The value of this fraction is dependent on the method used to measure the apparent volume *V*, and on which technique is applied when assessing the pore volume, V_p (Rouquerol *et al.*, 1994). Kelly (1981) explains that the manufacture of polygranular graphite can lead to the presence of different types of porosity. Porosity in virtually all polycrystalline graphite accounts for at least ~5% of the overall volume of the material, however, voids in commercial grades of graphite commonly account for ~20% of the total volume. Typical bulk densities of graphite range from 1.7 to 1.9 gcm^{-3}. Comparing the bulk densities of these materials with the theoretical value of 2.26 gcm^{-3} emphasises the large volume of porosity within the structure. Pores within the material can arise from a number of different origins, such as:

- Misfit of particles due to shape and size distribution.
- Pressure from gas evolution during heat treatment.
- Porosity in raw materials such as coke grains.
- Differential thermal expansion of crystallites upon cooling from final heat treatment temperature.
- Calcination cracks are evident in some filler particles due to volumetric shrinkage during calcination (Hacker *et al.*, 2000).
- Micro-cracks, commonly referred to at Mrozowski cracks (Mrozowski, 1954), may be formed parallel to the basal planes of the crystallites. These cracks arise during cooling of the material as a result of anisotropic contraction within the crystals (Hagos, 2010).

Complete characterisation of the pore structure in graphite is practically impossible. It has been estimated that in nuclear graphite with a grain size of ~1 mm, there are ~10^9 pores/cm^3. Further, pore dimensions may range from 1 mm down to 1 nm and have varying degrees of anisometry (Kelly, 1981). Pores is solid materials may be generally classified through a number of different criteria. This classification may be based on their origin (*e.g.* intraparticle and interparticle pores), size (*e.g.* micro-, meso- and macro-pores) or state (*e.g.* open and closed pores) (Patrick, 1995). The various origins of pore generation contribute to whether a pore is classed as interparticle or intraparticle. For example, pores within grains, such as porosity in raw coke grains or calcination cracks in filler particles would be classed as intraparticle pores. Gas evolution from volatilisation of binder material or misfit of particles due to size and shape distributions would typically be between particles and would therefore be classed as interparticle porosity. The classification of pores based on their size has been commonly applied to carbon material. The accepted range for classification by pore size is described by Sing *et al.* (1985):

- Micropores: Smaller than 2 nm
- Mesopores: Between 2 and 50 nm
- Macropores: Larger than 50 nm

The state of a pore may be simplified into whether it is open or closed. Figure 2.1 shows a schematic of a porous solid exhibiting a variety of different pore states and shapes. The following description of pore states will reference specific pores shown in Figure 2.1. Closed pores (a) are completely isolated within the material, whereas open pore (b, c, d, e, and f) have a continuous channel of communication with the external surface of the material. Open pores may be referred to as 'blind' (only open at one end like (b) and (f)) or 'Transport' (open at two ends like (c) and around (e)) pores. Roughness of the external surface may, in some instances, be comparable to porosity (g). The general convention to make the distinction between a rough surface and porosity is to consider the depth and width of the feature. The surface may not be considered to be porous unless it has irregularities that are deeper than they are wide. Pores also come in a variety of different shapes, some of which are described in Figure 2.1. (Rouquerol *et al.*, 1994).

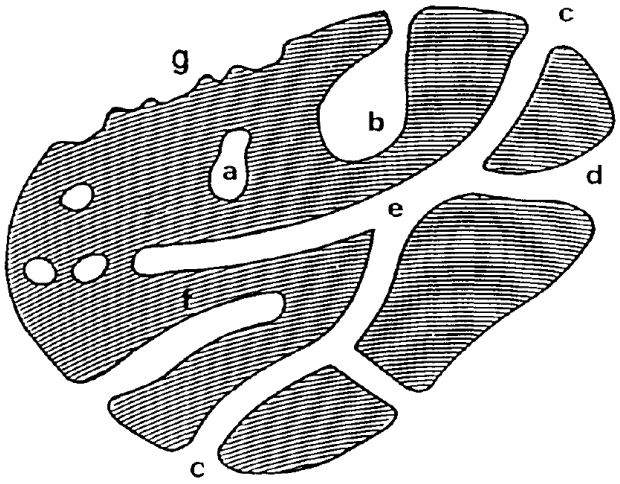

Figure 2.1: Schematic of a porous solid showing pores of different states and shapes. a) closed pore, b) open, 'ink-bottle' shaped, blind pore, c) open, 'cylindrically' shaped, transport pore, d) open, 'funnel' shaped transport pore, e) network of transport pores, f) open, 'cylindrically' shaped, blind pore. (Reproduced from Rouquerol *et al.*, 1994)

Measurement of the volumetric porosity percentage is crucial in the understanding of materials. Measured porosity values may be used for quality control purposes during manufacture or periodic inspections to ensure the material in service retains adequate integrity. The volumetric porosity percentage in a material can be simply calculated through the use of the equation:

$$P = 1 - \rho/\rho_T \qquad \text{Equation [2.2]}$$

where ρ is the apparent bulk density of a sample and ρ_T is the theoretical density of pure graphite crystals (2.26 gcm^{-3}) (Rice, 1998). As well as the overall percentage porosity, pore sizes are of great important when considering practical uses of porous materials, especially those relating to engineering applications. The method used to identify pores in the material can have a potential impact on the fractional porosity measurements. In addition to the potential problems caused through choice of method, the measurement is complicated by the presence of highly irregular and variable pores. Defining individual pores can be a difficult task in itself since pore systems are usually interconnected and form part of large networks within the microstructure. These difficulties mean that it is important to carefully select which method is used to measure the features and also consider the relative size range that is appropriate for the particular material and application.

Numerous methods may be employed to study and characterise the pore structure. The variation in physical properties of pores means that some methods are only suited to characterise larger pores, whereas others may be used to identify specific features within a certain size range or of a given type. Figure 2.2 shows some techniques for identifying pores within carbon materials and the approximate size range over which they are applicable. Additionally, this figure shows the size range of features that are of primary concern to this work, approximately 1 μm to 1 mm.

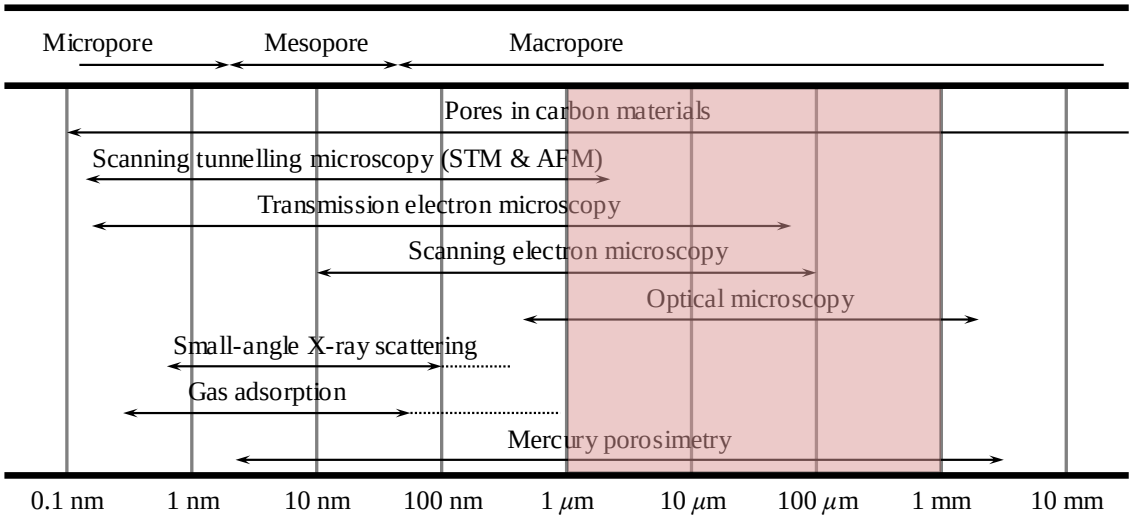

Figure 2.2: Techniques for the identification of pores in carbon materials and the approximate size range over which they are applicable (based on Inagaki, 2009). The approximate size range of features is highlighted by the red region.

The effective size range of a technique is not the only consideration when identifying pores. Some methods may be unsuitable for detecting pores of certain origins or states. Methods using a fluid only have access to open pores, whereas others such as methods using radiation may be used to identify closed porosity as well. When evaluating an identification technique it is also important to consider sample sizes requirements. Some methods have limitations on thickness, thereby making them unsuitable for identifying larger pores and ineffective at sampling large areas. Some relevant characterisation techniques are described in the following sections.

2.4.1. Stereology

Stereology is the characterisation of a material based on direct observation of cross sectional planes. Since stereology is based on the direct observations of pores it ensures

a realistic value of the pore structural parameters. It is important to examine anisotropic material in a variety of non-parallel planes in order to fully characterise the pore structure. Conversely, the pore structure of isotropic materials may be considered to be consistent irrespective of the orientation of the viewing plane. Methods that use direct observation include scanning electron microscopy (SEM) and optical microscopy. Limitations on the resolution of optical and to a lesser extent SEM methods mean that only macro pores are detected (Inagaki, 2009). The successful observation of porosity through the use optical methods is highly dependent on the preparation of the sample. When possible, samples are mounted in epoxy resin under positive pressure to 'infill' surface pores to enable a well-defined contrast between porosity and the surrounding material (Kane *et al*. (2011) and Devon (2008)). These methods are used to take micrographs of the sample before image processing and analytical techniques are applied to identify porosity (Inagaki *et al.*, 2000). When considering the characterisation of porosity networks throughout a sample, these approaches are particularly ineffective since they only detect pore entrances at the surface of the material. Transmission electron microscopy (TEM) can also be utilised, however, it is only suitable for observing very thin samples ~20 μm before ion beam thinning (Wen *et al*. (2008), Spence (2008)) and as such are not commonly applied to nuclear graphite.

2.4.2. X-ray Tomography

The use of x-ray computational tomography (CT) to characterise pore networks has numerous advantages. It enables the sample to be viewed in three dimensions allowing the structure and the interaction between pores to be better understood. Analytical methods can be applied to individual 'slices' to give a stereological interpretation. Alternatively, software can be used to construct a model from the CT data set. Analytical methods can then be applied to this model in order to characterise the pore structure in three dimensions (Sun *et al*., 2004). This method is also non-destructive and therefore allows fragile materials, such as highly oxidised graphites to be viewed without the risk of damage through sample preparation (Babout *et al*., 2005). The limitations of x-ray tomography mostly relate to the computation ability to process the large amount of data that it generates. Although micro CT scanners are able to identify very small features, the sample volume for such high magnification images is limited, thus making it difficult to view large features in high detail.

2.4.3. Additional Methods

As shown in Figure 2.2, there are numerous other methods that can be employed to characterise the porosity networks in graphite and carbon materials. However, not all of these methods are applicable to nuclear graphite due to the properties of the material or the size range being characterised. These methods will therefore not be discussed in detail here. Background information and the application of these methods to graphite and carbon can be found in following references:

- Mercury porosimetry; Washburn (1921), Ritter *et al.* (1945), Eatherly *et al.* (1958), Shibata *et al.*, (2001), Giesche (2006).
- Small-angle x-ray scattering; Warren *et al.* (1954).
- Gas adsorption; Barrett *et al.* (1951), Spalaris (1956), Rouquerol *et al.* (1994).

2.5. Microstructural Characteristics of Selected Nuclear Graphite

As previously described, the two main graphites used in the U.K. nuclear industry are AGR and PGA. Typical density and porosity characteristics of PGA and IM1-24 (used in AGR's) graphites are shown in Table 2.1.

Table 2.1: Typical density and porosity values for Pile Grade A and IM1-24 graphites (Kelly, 2000).

Property	PGA	IM1-24
Bulk Density (g/cm^3)	1.74	1.81
Open Pore Volume (%)	19.8	11.0
Closed Pore Volume (%)	1.0	8.6

Figure 2.3 show a typical microstructure for the two graphites. The PGA example shows a large elongated filler particle of needle coke along with binder phase and porosity. IM1-24 grade shows number Gilsocarbon particles of varying shapes and size. Although there is evidence of differences in the individual characteristics of the particles, it is important to note that these particles are roughly spherical and contribute the near isotropy of the bulk material.

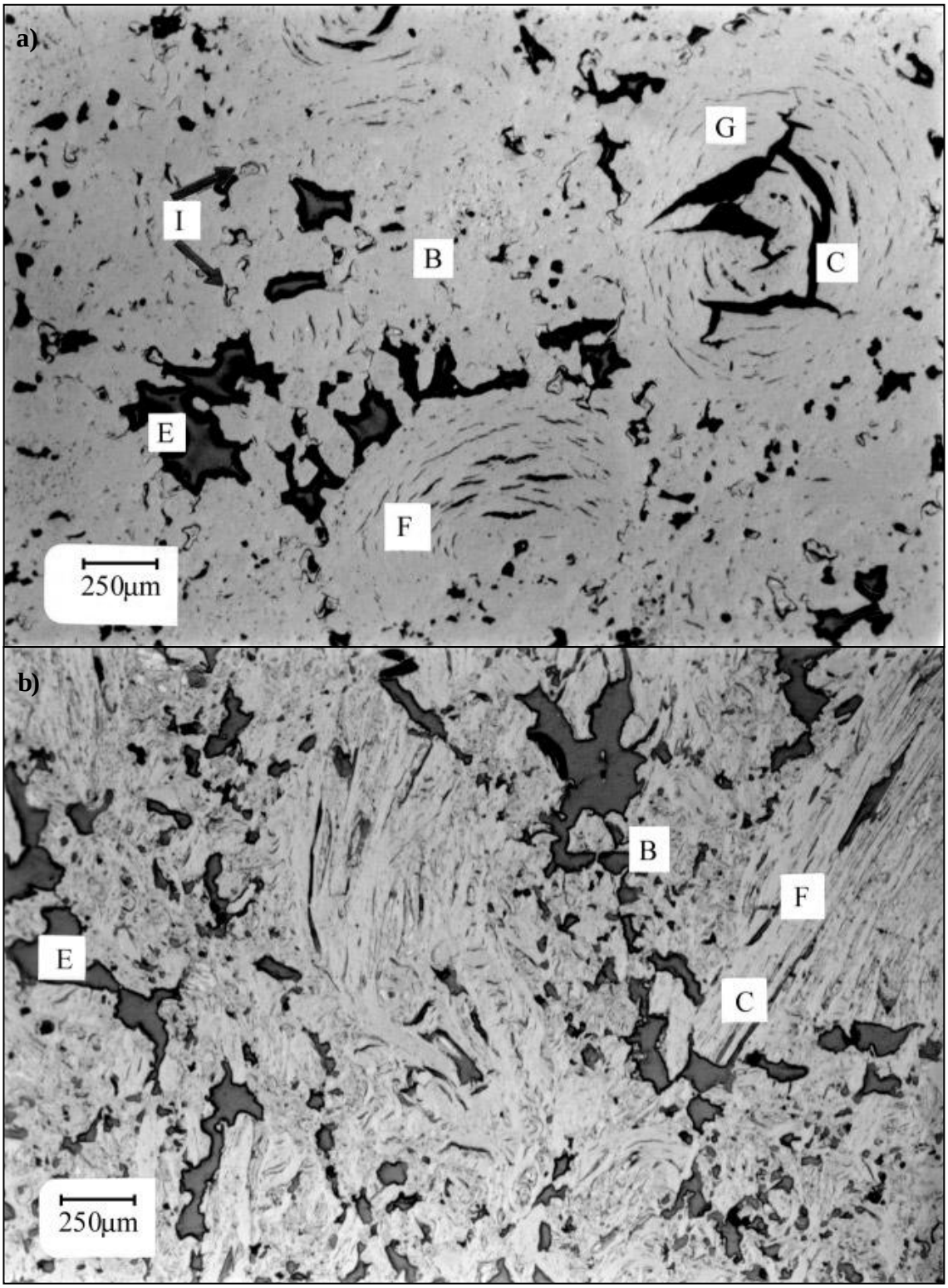

Figure 2.3: Optical Micrographs showing features of a) Gilsocarbon graphite (labels denote G, Gilsocarbon filler particle; B, binder phase; C, calcination cracks; E, gas entrapment pores; F, fragment of Gilsocarbon filler particle; and I, impregnant) and b) PGA Graphite (labels denote F, needle coke filler particle; B, binder phase, C, calcination cracks; and E, gas entrapment pores) (Reproduced from Hacker *et al.*, 2000).

2.6. Chapter Summary

Consideration of the graphite on a microstructural scale is vital in order to fully understand the properties and performance of the material. Although particular attention has been paid to porosity, other constituents such as filler and binder were also discussed. This chapter has explained the various origins and types of porosity in graphite as well as applicable methods for the characterisation of percentage content and determination of distributions. Although not all methods of pore detection are widely applicable to nuclear graphite, an understanding of these methods and the relative sizes over which they are effective is important to fully characterise the material.

The graphite grades most commonly used in the U.K. were also described in terms of their typical porosity content and their material constituents. Brief characterisation of needle coke and Gilsocarbon filler particles was also discussed.

The following chapter will discuss mechanical properties of graphite. Particular emphasis will be placed on the complexities in characterising the mechanical performance which are, in some cases, a direct result of the microstructural variations. Additionally, this chapter will outline the methods used to undertake experimental testing of graphite and discuss the fracture mechanics associated with the material.

Chapter 3 - Mechanical Performance of Graphite

Mechanical performance of graphite is a mature field due to the varied applications in engineering industries. Properties such as strength, thermal or electrical conductivity and fracture toughness are all important to consider during the development of material that will be subjected to extreme environments. Properties of graphite may be quoted when marketing a product due to competition between companies (*e.g.* when selling electrodes to steel foundries). Inherent variability in the material, as a consequence of the manufacturing process, means that reproducibility of test results with respect to mechanical performance is not realistic. It is therefore common for samples of graphite to experience a significant deviation from one another during mechanical testing. The scale of this deviation is dependent on the type of graphite. Changing the average grain size may affect microstructural variability between samples which could lead to changes in mechanical properties such as strength and elastic modulus. This is however dependent on a number of factors, such as the choice of filler particles, binder material and manufacturing conditions. Thus, the large number of variables involved in the manufacture of graphite makes it difficult to compare them 'like-for-like' and therefore different grades may be tested and characterised using different standards. However, methods used in the experimental testing of graphite are often recognised throughout different industries and certain procedures will be commonly applied in the characterisation of graphite.

For reasons discussed later in this chapter, mechanical data ascertained through experimental testing is not always in agreement. This can lead to difficulties when quoting mechanical values for graphites. It is therefore important to consider the context of the work when referencing mechanical properties from previous studies. To demonstrate this variation in experimental studies, mechanical values from a number of sources for PGA (parallel and perpendicular to direction of extrusion) and IM1-24 graphites are shown in Table 3.1.

Table 3.1: Mean values for a number of experimental studies on the mechanical properties of PGA (tested both parallel and perpendicular to direction of extrusion) and IM1-24 graphites.

Experimental Study	Graphite Grade	Property			
		Young's modulus (GPa)	Compressive strength (MPa)	Flexural strength (MPa)	Tensile strength (MPa)
Brocklehurst (1977)	PGA Para.	11	30	14	10
	PGA Perp.	6	30	9	6
	IM1-24	10	85	33	22
Neighbour (1993)	PGA Para.	14.14	34.5	20.11	11.04
	IM1-24	10.9	72.15	25.81	14.22
Vidal *et al.* (1999)	IM1-24	11.6	62.5	32.8	-
Kelly (2000)	PGA Para.	11.7	27	19	17
	PGA Perp.	5.4	27	12	11
	IM1-24	10.8	70	23	17.5
Ouagne *et al.* (2005)	PGA Para.	7.9	-	14	-
	PGA Perp.	5.6	-	5.6	-
	IM1-24	12.4	-	27	-

This table is not entirely complete due to the experimental work in each study being specifically concerned with different properties or materials. It does however, highlight the variation between experiments which attempt to characterise properties of the same material. In all the studies, the general trend of strength values is consistent. Compressive strengths are higher than flexural strengths which are in turn higher than tensile strengths, as would typically be expected from graphite (Neighbour, 1993). The discrepancies regarding mechanical properties arise when values for grades of graphite are compared between studies. For example, the flexural strength for IM1-24 grade graphite is quoted in Brocklehurst (1977) as being 33 MPa, whereas Kelly (2000) states that it is 23 MPa. Table 3.2 summarises the experimental results for each grade of graphite and mechanical property to demonstrate the deviation in values that are generated from these five experimental investigations. Considering the extensive work that has been undertaken on graphite and the number of different grades that are utilised in industrial applications, it is perhaps unsurprising that quoting mechanical properties can be a problematic.

Table 3.2: Summary of the range of mechanical properties, observed in Table 3.1, ascertained through five experimental investigations.

Graphite Grade		Property			
		Young's modulus (GPa)	Compressive strength (MPa)	Flexural strength (MPa)	Tensile strength (MPa)
PGA	Para.	7.9 – 11	27 – 34.5	14 – 20.11	10 – 17
PGA	Perp.	5.4 – 6	27 – 30	5.6 – 12	6 – 11
IM1-24		10 – 12.4	65.5 – 85	23 – 33	14.22 – 22

A degree of inconsistency between samples is expected due to the inherent probabilistic microstructure. Neighbour (1993) states that it is not uncommon to observe variations between samples of around 10%. This variation applies to individual samples within experimental test programmes, so the level of deviance between studies which test numerous samples, is unlikely to be greater than the suggested 10%. Therefore, the differences observed between studies are, in some cases, too large to be accounted for though material structure variations. The most likely reason for this disparity is the test method or sample geometry used to determine mechanical properties (Kennedy *et al.*, 1990).

3.1. Mechanical Testing of Graphite

In addition to the effect of microstructural features, it is also important to consider which test is used to determine mechanical values since the results from experimental techniques are heavily dependent on the method being used and the sample geometry. Some examples of experimental techniques commonly applied for characterising the mechanical performance of graphite are; compression, three-point flexural, four-point flexural, biaxial flexural (*e.g.* ball on three ball), single edge notched beam (SENB), brittle-ring and compact tension (CT). The principal reason for using different test methods is to ascertain different mechanical properties (*e.g.* compressive, tensile or flexural strength, work of fracture *etc*.). When considering the strength of the material, sample geometry and test setup will affect the mode of failure and thus output a corresponding strength value. As is common with many other brittle materials, such as concrete and ceramics, carbon and graphite materials generally have a high compressive strength compared to tensile strength. For graphite, it is often quoted that compressive

strength is typically 3 or 4 times higher than the tensile strength (Brocklehurst, 1977, Hindley *et al.*, 2012 *etc*.). This relationship can be explained through consideration of the model given by Griffith (1920), which states that failure of a brittle material is due to the presence of crack-like defects causing stress concentrations when a load is applied. The model commonly adopted is the weakest link hypothesis which suggests that the theoretical strength of a brittle material is dependent on a critically orientated crack. Failure of the sample will occur when the stress intensity at a flaw reaches a critical value for crack propagation (Brocklehurst, 1977). The microstructure of graphite contains an abundance of such potential defects, accounting for the inherent variability in the mechanical testing of samples. Taking into account this theory, tensile failure will normally be expected to initiate in a direction perpendicular to the applied force, thus in the plane of the critically orientated crack (Hoek *et al.*, 1965). This is caused by the 'opening' of the defect as a result of the tensile load, propagating the crack and initiating fracture of the sample. Conversely, when a compressive force is applied to the material, microstructural cracks will effectively be 'closed'.

The test method and sample geometry used in mechanical testing can have an influence on the strength values. This statement extends further than simply whether the material is subject to compressive or tensile forces. Although the failure mode associated with a testing method has a significant impact on the strength value, it is equally important to consider the stressed volume during experimental testing. The application of weakest link theory regarding brittle failure can be used to support this consideration. Samples made from a large volume of material will have a greater chance of containing a large, critically orientated flaw and will therefore be weaker. The same theory is applicable when considering relative stressed volumes. When a sample is tested in any experimental configuration, failure will likely be initiated in a region of high stress. A large region of high stress will increase the probability of a large flaw being contained within it, meaning that mechanical test methods that subject the sample to large stress fields are likely to demonstrate lower strength values.

3.1.1. Tensile Test

Tensile testing of carbon and graphite material can be difficult due to the brittleness of the material. The manufacture of samples into the complex shapes associated with

tensile tests can be problematic in both production of consistent specimens and limitation of surface flaws. The heterogeneous nature of graphites can exacerbate these surface flaws due to large particles being 'plucked' from the material during machining. These flaws can have a significant effect on the experimental results due to them acting as critical defects upon tensile loading, thereby resulting in the sample demonstrating a lower strength. Standard test methods for tension testing of carbon and graphite materials can be found in ASTM C565 as well as a more sophisticated method in ASTM C749. These standards emphasise the requirement for careful and precise manufacture of test samples. Measures should also be taken to ensure that the sample is loaded evenly, such as through the use of flexible linkages. Uneven loading of a specimen is likely to result in shear mode failure rather than tensile.

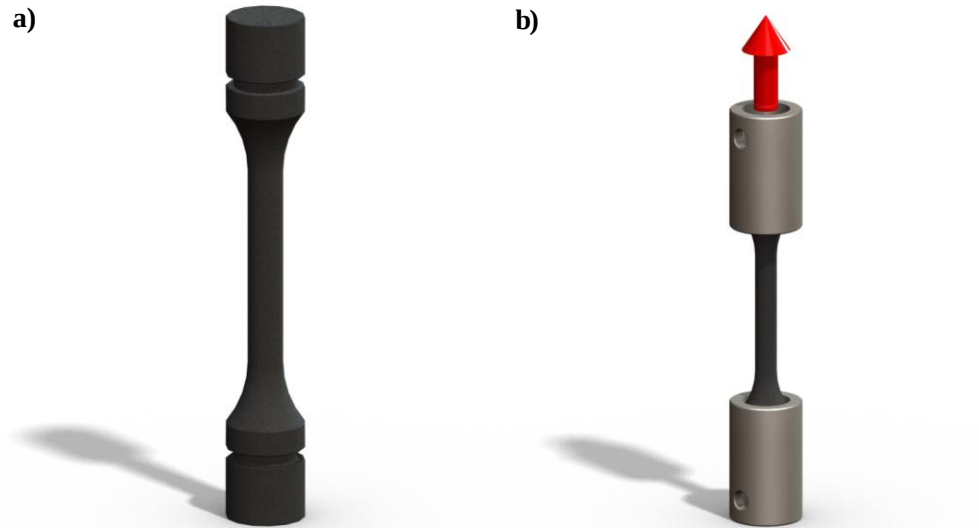

Figure 3.1: Schematic illustration of a) tensile sample geometry and b) example tensile loading scenario (reproduced from ASTM C749).

3.1.2. Compression Test

The compressive strength of graphite and carbon material is generally high when compared to the tensile strength. For this reason, compressive failure of test specimens is not commonly observed. Rather, when tested under compression, graphite often exhibits a 'shear' type failure with the fractured face angled to the applied force. Previous studies have reported fracture faces at 45^{o} (Gillin, 1967), 35^{o} (Taylor *et al.*, 1967) and also longitudinal splitting of samples (Greenstreet *et al.*, 1969). Although studies state that the fracture face is irregular, it usually occurs at an approximately consistent angle. The fracture process under compression has been described as being

due to linking of micro-cracks along a plane of maximum net shear stress (Brocklehurst, 1977). Longitudinal cracks may be due to lateral tensile failure of samples (Neighbour, 1993). Variations in graphite grades used in these test programmes likely account for the differences in failure mode. The standard test method for determining the compressive strength of graphite (ASTM C695) states that it is important to manufacture samples with parallel loading surfaces. This consideration is to limit the effect of shear forces acting on the sample. Standard apparatus for this method includes a well lubricated spherical 'bearing block' to ensure the sample surface is in full contact with the loading crosshead.

Figure 3.2: Schematic illustration of simple compressive loading scenario.

3.1.3. Flexural Test

A common alternative method for determining the strength of graphite is the flexural test (*e.g.* ASTM C651, Mostafavi *et al.* (2011) *etc.*). Due to difficulties when attempting to manufacture complex specimen shapes such as tensile samples, simple geometries such as those used for flexural tests, are more appropriate when considering experimental reproducibility. The stress distribution varies through the sample from compression at the loading surface to tension at the surface opposite the loading point, where failure of the sample generally occurs. The failure method of this test makes it susceptible to surface flaws and samples must therefore be manufactured with care to avoid critical defects at the tensile surface. Since sample failure is initiated at the tensile surface, flexural tests are often used in place of traditional tensile tests. Although it may be used as an alternative to the tensile test, flexural strengths of graphites are approximately 1.3 times greater than tensile strength (Brocklehurst, 1977), however,

this can vary depending on the loading mechanism (three or four point), sample size and grade of graphite being tested.

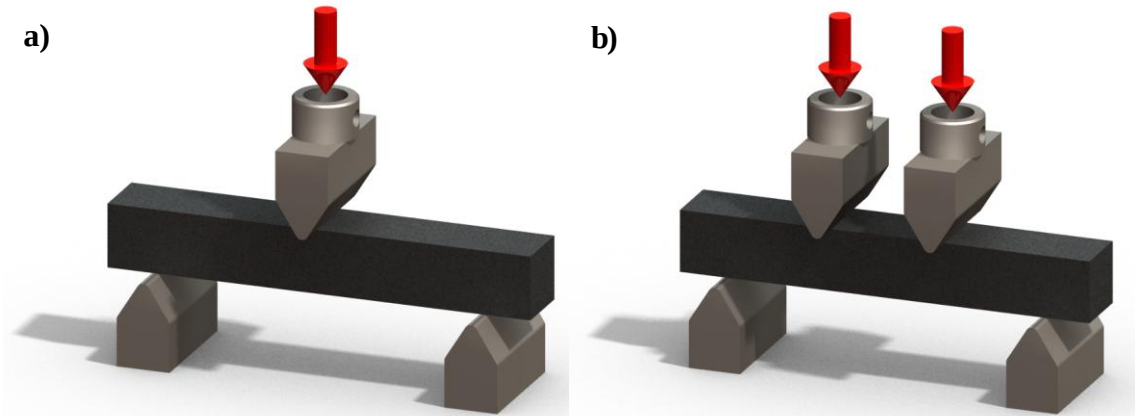

Figure 3.3: Schematic illustration of a) three and b) four-point bend loading scenarios.

Flexural strengths (σ_f) of three and four point bend specimen are determined through the use of Equations 3.1 and 3.2 respectively.

$$\sigma_f = \frac{3PL}{2bd^2} \qquad \text{Equation [3.1]}$$

$$\sigma_f = \frac{3P(L - L_i)}{2bd^2} \qquad \text{Equation [3.2]}$$

where, P is the maximum load, L is the span between support contacts, L_i is the span between loading contacts, b in the sample breadth and d is the sample depth. Studies have shown that strength values calculated using three-point flexural tests are generally higher than those from the four-point method (Rose *et al.*, 1982). This observation is a consequence of the relative stressed volume during testing. Samples in four-point configuration will have a larger volume of the material under tensile stress between the two loading points around the bottom surface of the sample. Therefore the probability of a large flaw being critically orientated to the tensile load is greater than in a three-point arrangement where the stress is concentrated in a small volume around the centre of the tensile surface.

Biaxial flexural tests (*e.g.* ball on three ball (B3B) (Godfrey, 1985), ring on ring (ROR) (Ovri, 2000), *etc.*) determine the strength of a sample that is subject to a tensile biaxial stress. Figure 3.4 shows a schematic example of a ball on three ball biaxial apparatus.

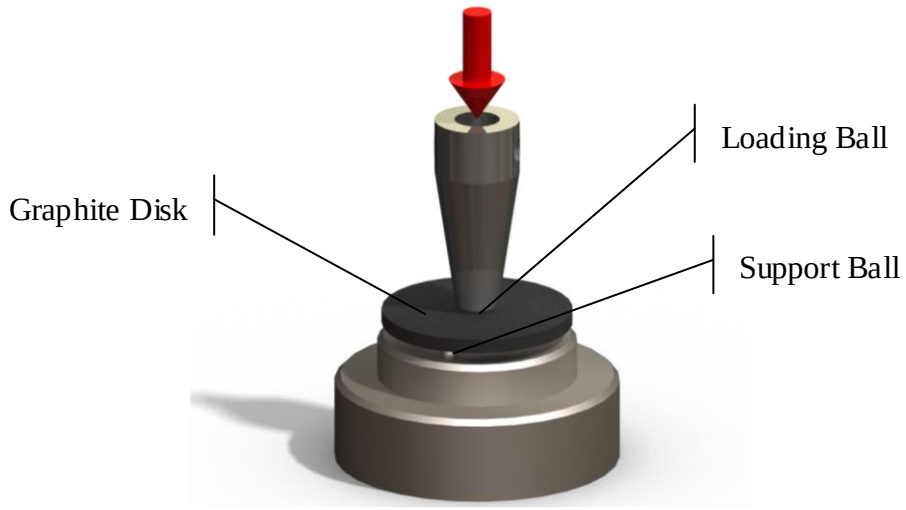

Figure 3.4: Schematic illustration of a ball on three ball biaxial loading scenario.

Various experimental studies have derived equations for calculating the biaxial strength of samples tested using the ball on three ball configuration. Although these approximations are similar in their derivation, subtle differences can have an impact on the calculated strength values. These are discussed in Kipling *et al.* (2010). Pagniano *et al.* (2005) determined the biaxial strength of disk samples using the equation:

$$\sigma = 3P\frac{(1-\nu)}{4\pi t^2}\left[1+2\ln\left(\frac{a}{b}\right)+\left(\frac{1-\nu}{1+\nu}\right)\cdot\left(1-\frac{b^2}{2a^2}\right)\cdot\left(\frac{a^2}{R^2}\right)\right]$$

Equation [3.3]

where, t is the disk thickness, a is the support circle radius, b is the loading ball radius, R is the disk radius and ν is the disk Poisson's ratio. Biaxial strengths are typically considered to be lower than equivalent uniaxial strengths due to an increased probability that flaws will be critically oriented to the applied stress (Brocklehurst, 1977).

Another flexural configuration commonly applied to graphite and carbon materials is the single edge notched beam (SENB) test (ASTM E399). Although similar in test up to the three-point flexural test, SENB samples have a deep notch cut into the centre, which is often approximately half the sample thickness. This notch reduces the energy required to initiate failure of the sample, thereby promoting controlled crack growth rather than fast fracture. Data ascertained through experiments that encourage controlled crack growth is used in the determination of fracture toughness values.

3.1.4. Brittle-Ring

Although not widespread in its use as a testing method for graphite and carbon material, the brittle-ring test (Darby (1976), Price (1979), Kennedy (1993)) offers an efficient method of determining strength values from small samples. Samples generally have an internal diameter that is approximately half the external diameter and are loaded in compression. Experimental values from this test approximate closely to tensile strengths due to failure initiation at the inner radius. Through experimental testing of several isotropic graphite grades, Kennedy determined that the results showed good agreement with four-point bend samples tested from the same material. The absolute strength values were in fact higher than four-point bend tests, however, this can be accounted for by the smaller relative stressed volume of the sample. Strength of brittle ring samples is calculated using the expression:

$$\sigma = \frac{3P(a+b)}{\pi t(b-a)^2} \qquad \text{Equation [3.4]}$$

where, a and b are the inner and outer radii of the ring respectively.

Figure 3.5: Schematic illustration of a brittle ring loading scenario.

3.1.5. Controlled Crack Growth

The primary criterion in determining fracture toughness parameters is the potential to allow for controlled crack growth through the specimen thereby preventing fast fracture. In most cases this is achieved through appropriate choice of sample geometries which

concentrate stresses into a small volume of the material (*e.g.* by using specimen manufactured with sharp notches). In addition to SENB, compact tension (CT) sample geometries are used to ascertain these parameters. Although other test configurations may be used to meet this criterion (*e.g.* Romanoski *et al.* (1991), ASTM E561 *etc.*) they are not generally applied to graphite and carbon material. The CT test method (Ouagne *et al.* (2002), ASTM E399) involves testing of notched specimen with a fine crack at the root of the notch. Cyclic loading through small increments in displacement ensures that the sample does not fail through fast fracture.

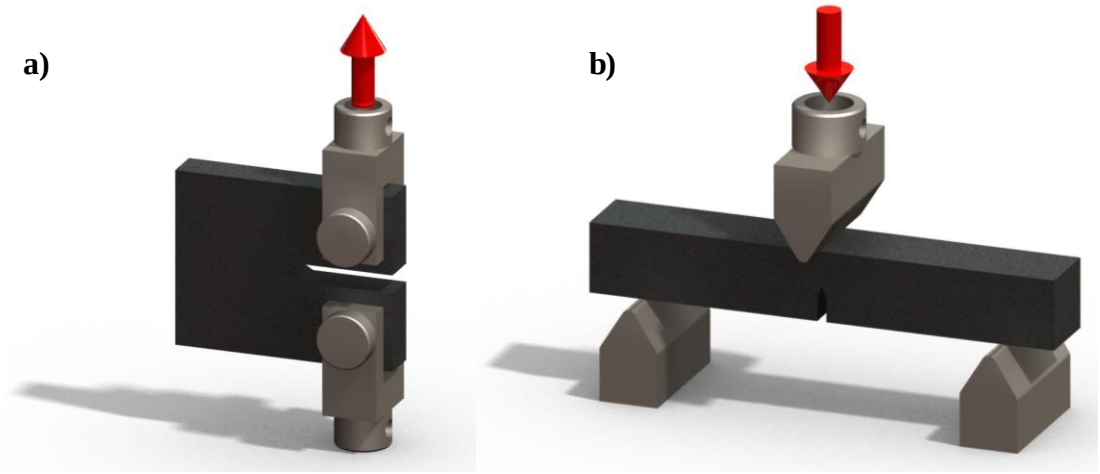

Figure 3.6: Schematic illustration of a) CT and b) SENB loading scenarios.

3.2. Fracture Mechanics of Graphite

An understanding of fracture mechanics and what conditions may lead to failure is vital when considering the lifespan of graphite components. The fracture behaviour of graphite is commonly stated as quasi-brittle. Work undertaken by Sakai *et al.* (1983b), Gopalaratnam *et al.* (1985), Allard *et al.* (1991) has shown that graphite, along with other quasi-brittle materials, exhibit a 'post-peak softening' response, whereby the material exhibits variable strain energy release rates as the crack propagates through the material. The response of graphite that is subject to extreme conditions such as radiolytic oxidation and neutron irradiation (Neighbour *et al.* (2001), Jones *et al.* (2008)) and also change in geometric factors (*e.g.* crack size and shape) further complicates the understanding of fracture behaviour. This is reflected by the relatively small amount of work that has been devoted to the subject.

Microstructural heterogeneity, which is a factor in most graphite grades, contributes to the complex failure characteristics that are commonly observed. Crack growth during failure can be heavily influenced by the size, shape and distribution of microstructural features. Additionally, the variation in material constituents and the boundaries between them can also have an impact on the fracture path. Burchell (1996) highlights the principal observations regarding how the main constituents in typical polygranular graphites may affect a propagating crack. Porosity in the material is likely to be one such contributing factor in the overall propagation characteristics of a crack. When placed under a load, graphite will exhibit localised stress concentrations around pores. Cracks may be initiated when the stress concentration at a favourably oriented defect exceeds a critical value. Interaction between the stress field and the distribution of pores may also be responsible for drawing the crack path towards pores in their vicinity. This can have the effect of accelerating propagating crack; however, it has been observed that cracks can be arrested by pores. The variety in pore shape and size within a typical graphite means that some will have a greater influence on the crack path than others. Generally it was found that larger 'slit-shaped' pores were more likely to aid the fracture of the material (Burchell, 1996).

Filler particles, depending on their alignment, can be highly susceptible to micro-cracking through cleavage along basal planes. This is primarily caused by calcination cracks in the particles, which are parallel to the basal planes. Cracks advancing though binder phases that encounter filler particles may propagate though the easily cleaved particle. This process is generally only observed in one direction as cracks do not commonly propagate from a filler particle into the binder phase. Allard *et al*. (1991) discusses the fracture behaviour of carbon materials stating that in perfectly elastic materials a crack initiates and propagates rapidly to final fracture. In the same paper, Allard goes on to discuss how mechanisms in elasto-plastic materials can lead to energy absorption such as; friction, debris, micro-cracking and crack bridging. The energy absorbed by these mechanisms is not available for creation of new crack surfaces; therefore, the crack can be controlled. Additionally the material can be characterised by the energy required for a given crack increment. Two methods are used to determine fracture energy. An energetical approach considers the energy input and the plastic energy that is dissipated in the material. The stress intensity approach considers the intensity of stress around a crack tip.

3.2.1. Energy Balance Approach

Alan Griffith (1920) developed a theory to explain the fracture in solids. He theorised that failure in a solid is due to stress concentrations caused by the presence of small cracks or flaws in the material when a stress is applied. The theory suggests that the practical strength of a material is dependent on the size and orientation of these features. It follows that the maximum stress which contributes to failure is only applied to a small volume of the material, whilst the mean stress throughout the solid may remain relatively low (Orowan, 1949). Thus, materials which experience very little plastic deformation (*i.e.* brittle materials) have a very low tolerance for stress concentrating defects. The failure strength for plane stress is given by Griffith as,

$$\sigma_f = \sqrt{2E\gamma/\pi a} \qquad \text{Equation [3.5]}$$

where σ_f is the failure stress, γ is the surface energy, and a is the crack length. Values of σ_f calculated using Equation 3.5 were found to be lower than experimental data when predicted values of γ were used (Yarema, 1995). This prompted the independent modification of Griffith's equation by Orowan (1955) and Irwin (1958). They proposed that a material will experience an element of plastic deformation during the fracture process accounting for the discrepancy between practical and theoretical values. Therefore, any crack extension will require more than just an increase in surface energy. To account for the plastic deformation energy the energy term was altered to give:

$$G_C = 2(\gamma_S + \gamma_p) \qquad \text{Equation [3.6]}$$

where G_C is the strain energy release rate and γ_P is the energy due to plastic deformation. Griffith's original equation is therefore modified to give:

$$\sigma_f = \sqrt{EG_C/\pi a} \qquad \text{Equation [3.7]}$$

In determining the mechanical properties of brittle materials, the surface energy is of critical importance and indeed there have been numerous publications relating to its calculation. It may be described as the work done to create a unit area of new fracture surface. The Griffith energy balance criterion for crack growth is given by:

$$-\frac{\partial U}{\partial A} = \gamma \qquad \text{Equation [3.8]}$$

where, U is the stored elastic energy in the structure and A is the area of the fracture face. It is not energetically possible for a crack to grow until this criterion is satisfied. The behaviour of the crack upon meeting the criterion for propagation is dependent on how the value of $-(\partial U/\partial A)$ changes as a result of crack growth. The crack will accelerate if the energy released is more than sufficient to create the new surface area (*i.e.* $-(\partial^2 U/\partial^2 A)$ is positive). Conversely, if there is insufficient energy to create new surfaces (*i.e.* $-(\partial^2 U/\partial^2 A)$ is negative), $-(\partial U/\partial A)$ may become less than γ and additional work must be done to propagate the crack further. This criterion essentially dictates whether a test sample will fail catastrophically through fast fracture or if controlled crack growth will be possible. Practical considerations to encourage crack growth are aimed at limiting the elastic energy stored in the specimen and test machine at fracture initiation. This may be achieve by using a hard testing machine and by shaping the specimen so that the stress is concentrated at the tip of a notch, thus resulting in cracks being initiated at relatively low loads (Tattersall *et al.*, 1966). The energies stored in a three-point bend specimen (with length l, thickness d and breadth b) and in the testing apparatus at the moment of fracture are derived by Nakayama (1965) as being:

$$U_s = \frac{lbsS^2}{18E} \qquad \text{Equation [3.9]}$$

$$U_a = \frac{4b^2d^4S^2}{Kl^2} \qquad \text{Equation [3.10]}$$

where, U_s and U_a are the stored energy in the sample and the test apparatus respectively, S is the tensile strength of the sample and K is the apparent spring constant which relates to the apparatus. Tattersall *et al.* (1966) investigated the work of fracture for several materials including 'reactor graphite'. Their investigation utilised three-point flexural samples with isosceles triangles cut into the square cross-section. The stress concentration at the apex of the triangular cross-section results in initiation of the crack before a sufficient elastic energy is available in the specimen or test machine to result in fast fracture. Reactor graphite is quoted as having a work of fracture value of 100 Jm^{-2}.

Davidge *et al.* (1968) investigated the surface energy of four brittle materials, including PGA graphite, using notched bar specimens in a three-point bend test configuration. Each graphite specimen was 45 mm long and had a 10 mm square cross section. They

state that the effective surface energy (γ) for a given material may vary during the fracture process and consider two particular values of γ, at the point of initiation and the average work for the whole fracture process. Surface energy leading to the initiation of fracture, denoted as γ_I, is the value of γ used in the Griffith equation (Equation 3.5). This value is related to the strain energy release rate at the point of fracture by $-(\partial U/\partial A) \geq \gamma_I$. $(\partial U/\partial A)$ can be determined theoretically through consideration of mathematically computed stress distributions around the tip of the notch or experimentally form a load-deflection curve using compliance analysis. Both methods should give consistent results and indeed Davidge *et al.* (1968) showed good agreement for all materials. The average work of fracture for the whole process, γ_F, is obtained through measuring the work required to fracture a specimen in a controlled manner and is given by the equation:

$$\gamma_F = \frac{U}{2b(d-c)} \qquad \text{Equation [3.11]}$$

where, U is the total work done (*i.e.* the area under the load-deflection curve), b is the breadth of the specimen, d is the depth and c is the crack depth. The general trend showed a decrease in γ_F and as the effective cross-section was reduced and the failure process became more controlled. Work of fracture for PGA is quoted as ranging from 227 Jm^{-2} to 84 Jm^{-2} depending on the notch depth (Davidge *et al.*, 1968). For PGA graphite the effective surface energy at crack initiation was found to be less than the average work of fracture. This has been attributed by Davidge *et al.* (1968) (as well as others, *e.g.* Knibbs, 1967) to energy absorption by subsidiary cracking that occurs during the fracture process. As a result, it is more difficult to propagate a crack than it is to initiate it. Graphite samples exhibited controlled crack growth regardless of the notch depth, including when there was no notch cut into the bar. This is contrary to similar work undertaken by Corum (1966) on notched samples of EGCR-type AGOT graphite. Corum's work demonstrated that in all cases a sample would undergo fast fracture if the notch depth was less than 20% of sample depth. This discrepancy between studies is likely due to the larger samples (32 mm wide, 25 mm deep and 300 mm long) used by Corum (1966) which would require a greater load to initiate fracture. In considering the energetical approach further, additional material characteristics for an elastic-plastic material can be derived. The energy required to propagate a crack per

unit surface area is referred to as the crack growth resistance, *R*. The total energy is the sum of elastic energy, *J* and pseudoplastic energy, ϕ_p. Methods for determining crack growth resistance parameters, J_R and *R*, are suggested by Rice *et al.* (1973) and Sakai *et al.* (1983b), respectively. Rice's method considers a cyclically loaded bar sample in three-point bend configuration. After each cycle, the sample will have a crack of size *a*, which is estimated using the compliance increase using the expression:

$$a_n = a_{n-1} + \frac{W - a_{n-1}}{2}\frac{C_n - C_{n-a}}{C_n} \qquad \text{Equation [3.12]}$$

where, a_n is the actual crack length at cycle *n*, a_{n-1} is the crack length at the previous cycle, C_n and C_{n-1} are the actual and previous compliance. The compliance is derived from the loading-unloading cycle by calculating the inverse of the average slope of cycle *n*. The elastic energy component at each cycle can be defined as twice the work of deformation divided by the remaining cross sectional area and is calculated using the expression:

$$J = \frac{2U_1}{B(W - a)} \qquad \text{Equation [3.13]}$$

where, U_1 is the area under the load-displacement curve (see Figure 3.7) , *W* is the width of the beam and $W - a$ is the remaining ligament length.

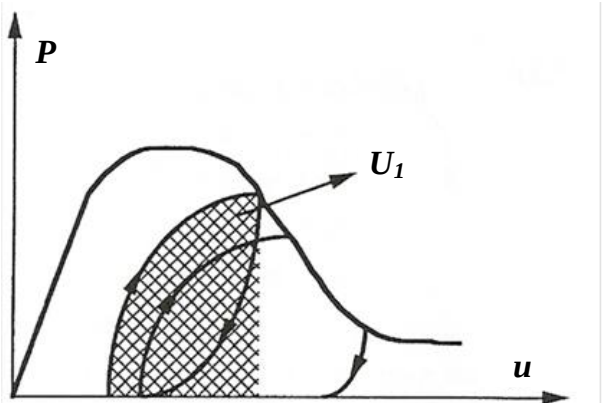

Figure 3.7: Rice's method of determining the work of deformation from a load-displacement curve generated from a cyclically loaded test (diagram reproduced from Allard *et al.*, 1991).

Sakai's proposed method allowed for the determination of the total energy, *R*, based on the assumption that kinetic energy of the sample body is negligible. To fulfil this

statement, loads must be applied to the sample slowly and in small increments. Providing this condition is satisfied the global energy of a sample is given by:

$$\frac{\partial W}{\partial A} = \frac{\partial U_t}{\partial A} + \frac{\partial \Gamma}{\partial A} \qquad \text{Equation [3.14]}$$

where, ∂A is the increment of crack surface area, W is the external input of work and Γ is the energy required to create a new cracked surface. U_t refers to the total internal energy and is comprised of the elastic stored energy U_e, and the plastic dissipation, U_P, thus:

$$U_t = U_E + U_P \qquad \text{Equation [3.15]}$$

Substitution of the components for total internal energy modifies the global energy formula into the form:

$$\frac{\partial W}{\partial A} = \left(\frac{\partial U_e}{\partial A} + \frac{\partial U_P}{\partial A} \right) + \frac{\partial \Gamma}{\partial A} \qquad \text{Equation [3.16]}$$

The energy available to create a new cracked surface is the fraction of work input energy that is not consumed in the elastic-plastic deformation. This energy may be defined as the net energy available for crack extension and is represented by $(\partial W/\partial A) - [(\partial U_e/\partial A) - (\partial U_p/\partial A)]$. This relationship leads to the derivation of the nonlinear fracture toughness parameter, $\bar{G}_c$, which is defined as:

$$\bar{G}_C = \frac{\partial}{\partial A}[W - (U_e + U_p)]_c \qquad \text{Equation [3.17]}$$

The crack growth resistance parameter, R, is defined as:

$$R = \frac{\partial}{\partial A}(W - U_e)_c \qquad \text{Equation [3.18]}$$

Sakai's experimental work involved the application of cyclic loading to chevron-notched samples. Values for nonlinear fracture toughness parameters such as $\bar{G}_c$, R, and the plastic energy dissipation rate, ϕ_p, can be attained through consideration of experimental load-displacement curves. Figure 3.8 schematically shows the quasi-static extension of a crack from point B to D, creating the area new cracked area, ΔA.

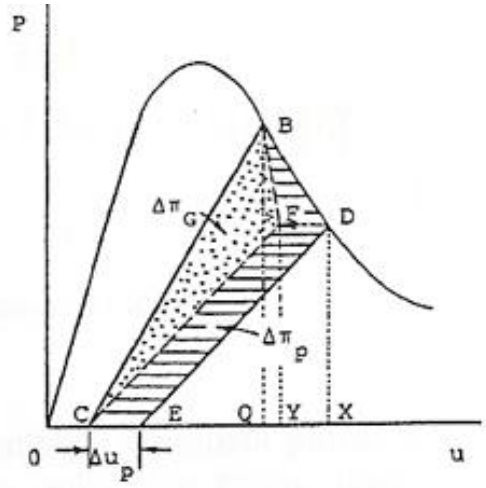

Figure 3.8: Sakai's graphical method for determination of nonlinear fracture parameters from a load-displacement curve (diagram reproduced from Sakai *et al.*, 1983b).

Unloading the sample at point D will result in additional plastic deformation at the crack tip compared to if it was unloaded at point C (shown as ΔU_p). Based on this increment of plastic deformation, the area under the load-displacement curve may be separated into two portions shown as $\Delta\pi_G$ and $\Delta\pi_p$. Assuming that the new cracked area is small, the following relations can be derived:

$$\bar{G}_C = \frac{\Delta\pi_G}{\Delta A} \qquad \text{Equation [3.19]}$$

$$\phi_P = \frac{\Delta\pi_P}{\Delta A} \qquad \text{Equation [3.20]}$$

The total area under the curve as defined in Figure 3.8 (*i.e.* $\Delta\pi_G + \Delta\pi_p$) is the additional amount of energy that is required to propagate the crack from point B to D. This irrecoverable energy is that consumed in order to create the new cracked area, ΔA. Therefore, it follows that the crack growth resistance may be determined from:

$$R = \frac{\left(\Delta\pi_G + \Delta\pi_P\right)}{\Delta A} = \bar{G}_C + \phi_P \qquad \text{Equation [3.21]}$$

Crack growth resistance parameters may be plotted as a function of crack growth to enable further characterisation of fracture behaviour. Generally, crack growth resistance curves (*R*-curves) will plot data ascertained from experimental testing (*e.g.* Rice's or Sakai's method). At each increment of crack growth, values for *R*, *J* and ϕ are

calculated. *R*-curve shapes vary depending on the parameter being plotted. Graphite and carbon materials will typically demonstrate one of the shapes shown in Figure 3.9.

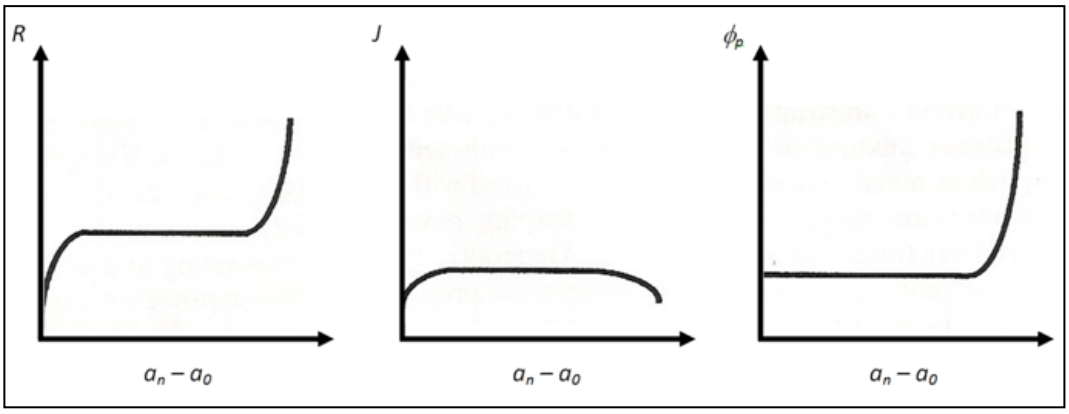

Figure 3.9: Typical shape of crack growth resistance curves for total energy, *R*, elastic energy, *J*, and pseudoplastic energy, ϕ. Plotted as a function of crack length (Allard *et al.*, 1991).

Analysis of the total energy *R*-curve reveals three distinctive regions. There is a rapid increase in energy at fracture initiation due to the onset of micro-cracking as well as the macro-crack. Subsequent increases in energy are attributed to an increase in the size of the process zone. This is followed by a 'plateau like' region (Sakai, 1988) corresponding to a constant value of crack growth resistance as the crack and process zone propagate in a steady state through the material. The final increase in crack growth resistance is due to the process zone interacting with the rear surface of the specimen. Relative to the surface increase, more energy is consumed by the process zone as it extends laterally along the specimen surface (Allard *et al.*, 1991).

3.2.2. Stress Intensity Approach

Determination of the fracture energy through the stress intensity approach hinges on the assumption that linear elastic fracture mechanics (LEFM) may be applied to the material. In the case of carbon materials subject to a cyclic loading test, the crack may be prevented from closing when the load is removed. This may be caused by the formation of debris during the test. If this residual displacement is due to the debris, then the observed plasticity of the material may be a result of the unloading and not inherent of the material, therefore allowing LEFM to be applied (Allard *et al.*, 1991). For a given structure, comparing the computed value of stress intensity at the crack tip, *K*, with the critical stress intensity value for a material, K_c, will give an indication as to

whether the component will fail (Brocklehurst, 1977). K_R-curves, which is may be used in place of an *R*-curve, correspond to the stress intensity factor plotted as a function of crack length. The magnitude of *K* is dependent on the structural geometry of the sample and the loading system. As such, different equations are used to calculate *K* depending on the experimental geometry. To highlight the different considerations for sample geometries, Equations 3.22 to 3.25 show the variations in formula for notched three-point bend and compact tension samples. Calculation of *K* values form experimental testing of bend specimens requires the formula:

$$K = \frac{PS}{BW^{\frac{3}{2}}} f_1\left(\frac{a}{W}\right) \qquad \text{Equation [3.22]}$$

where, *P* is the applied load, *B* is the specimen thickness, *S* is the span, *W* is the thickness of specimen, *a* is the crack length and $f_1(a/W)$ is a geometric factor which may be determined from:

$$f_1(a/W) = \frac{3\left(\frac{a}{W}\right)^{\frac{1}{2}}\left[1.99 - \left(\frac{a}{W}\right)\left(1-\frac{a}{W}\right)\left(2.15 - 3.93\frac{a}{W} + 2.7\frac{a^2}{W^2}\right)\right]}{2\left(1+\frac{2a}{W}\right)\left(1-\frac{a}{W}\right)^{\frac{3}{2}}}$$

Equation [3.23]

The application of a compact tension sample and therefore significantly different sample geometry necessitates the modification of stress intensity formula. Stress intensity values calculated from:

$$K = \frac{P}{BW^{\frac{1}{2}}} f_2\left(\frac{a}{W}\right) \qquad \text{Equation [3.24]}$$

where $f_2(a/W)$ is calculated from:

$$f_2(a/W) = \frac{\left(2+\frac{a}{W}\right)\left(0.886 + 4.64\frac{a}{W} - 13.32\frac{a^2}{W^2} + 14.72\frac{a^3}{W^3} - 5.6\frac{a^4}{W^4}\right)}{\left(1-\frac{a}{W}\right)^{\frac{3}{2}}}$$

Equation [3.25]

Geometries for, *B*, *S*, *W* and *a* are determined according to dimensions, conditions and experimental arrangements which relate to each particular test and are outlined in ASTM E399. In his review of fracture in polycrystalline graphite, Brocklehurst (1977) investigated the effect of specimen type and geometry on the stress intensity values of a fine-grained version of IM1-24. Compact tension and circumferentially notched round bar (CNRB) samples were tested alongside notched samples in tension and three-point bend. K_C values for the four sample geometries are shown in Table 3.3.

Table 3.3: Stress intensity values for a fine-grained IM1-24 graphite tested in four different configurations (Brocklehurst, 1977).

Sample Geometry	Loading Condition	Stress Intensity Factor (K_C) (MPa·m$^{0.5}$)
Notched bar	Three-point bend	1.4 - 1.5
Notched bar	Tension	1.3
CT	Tension	1.3
CNRB	Tension	0.8

Experimentally determined values for K_C from notched bar and compact tension samples are in reasonable agreement. However, samples tested in circumferentially notch round bar configuration gave considerably lower values. Brocklehurst noted that the estimated inherent flaw size from his data was calculated to be between 0.25 and 0.4 mm, which is comparable to the maximum grain size for this particular graphite.

The critical stress intensity factor, K_{Ic}, for pitchcoke nuclear graphite was calculated by Rose (1985) through the use of small, notched four-point bend samples and notched curved bars loaded in three-point bend configuration. Different notch depth to specimen thickness ratios (a_o/W) were tested from 0.01 to approximately 0.5. Interestingly, samples with a_o/W values of 0.01 and 0.02, which equate to 0.1 and 0.2 mm notches in the 10 mm thick sample, did not guarantee fracture initiation at the tip of the notch. This was attributed to the large cracks within the material being 'more severe' defects than the machined notch. Values for K_{Ic} obtained from his investigation were 1.20 ± 0.15 MPa·m$^{0.5}$ which is similar to typical data values for similar graphites (Rose *et al.*, 1982).

3.3. Chapter Summary

The mechanical performance of graphite as a material is dependent on a number of factors. Consideration of only the factors involved in manufacture does not fully characterise the material performance. As discussed in this chapter, determining and quantifying the performance of a particular graphite grade is not straightforward. Experimental test programmes can be expected to demonstrate a distribution of failures, thereby making them difficult to consistently and accurately predict mechanical properties of the material. Additionally, different experimental methods are liable to predict different values for mechanical performance due to the relative stress volume within a specimen. Discussion regarding fracture mechanisms of graphite again sought to highlight the number of considerations that must be taken into account when attempting to characterise the fracture of the material. Global energy balance and stress intensity methods for the calculation of fracture energies were considered along with suggested methods for their experimental determination. These complexities relating to material properties are complicated further when taking account of the operational conditions within the reactor.

Understanding the fracture in graphite is vital to ensure any subsequent modelling work is able to accurately represent microstructural mechanisms of the material. Similarly, the development of any experimental test programmes will need to consider what properties are to be determined and the most suitable method of generating relevant data.

Many of the modelling methods commonly applied to graphite are based on the fundamental principles outlined in this chapter. Chapter Four will evaluate some of these approaches whilst discussing their foundations and subsequent development. Additionally, computational models will be considered which will ultimately assist in the development of a representative microstructure model.

Chapter 4 –Modelling of Graphite

Models are advantageous when designing components to ensure the most suitable design or grade of graphite is selected. Additional advantages include the prediction of how components may interact in operational environments. Numerous models for predicting the failure of graphite have been proposed and developed since its widespread application as an engineering material. It is often the case that each theory is effective at describing a particular loading situation, but not all circumstances of interest. Heterogeneity within the material and a significant variation in structural properties between grades are a contributing factor to the lack of a universal theory. Due to these complexities, the most versatile theories are likely to be those which place an emphasis on the microstructure. These theories have an additional benefit of being more suited to describing microstructural changes as a result of environmental conditions, such as radiolytic oxidation and neutron irradiation (Tucker *et al.*, 1986).

The application of computational modelling techniques to graphite allows for predications regarding the performance of the material under conditions that represent an operational environment. The complex and probabilistic nature of the material, coupled with the large number of operational factors make providing a 'whole core' solution which accounts for microstructural (or even atomic) material characteristics unrealistic. This chapter will review a number of commonly used fracture models and evaluate their strengths and weaknesses with regards to describing loading conditions. Since this work is primarily interested in the microstructure of graphite, particular attention will be paid to how the models account for microstructural characteristics. Consideration of theories and modelling techniques will aid in the design and development of a new representative microstructure model.

4.1. Modelling the Fracture of Graphite

Early simple fracture models were based on critical stress, critical strain, and critical strain energy density. Further development and consideration of graphite fracture lead to the adoption of Weibull and fracture mechanics models. The deficiencies of these

models resulted in models being specifically developed to account for the graphite microstructure.

4.1.1. Critical Criteria Models

Traditional critical stress models assume that a component will fracture when the applied maximum tensile stress reaches or exceeds the tensile strength of the material. Similarly, a critical strain model will assume that failure occurs when the strain reaches a critical value related to the material. These simple models rely on the assumption that the material is a continuum and therefore disregard microstructural characteristics of graphite as well as the potential for localised stresses concentration at flaws or other features (Tucker *et al.*, 1982).

The critical strain energy density criterion fracture model considers the average strain energy in the volume of the sample that is subject a tensile stress. Understandably, for this criterion to be applicable, the volume of the sample over which tensile loading occurs must be well defined. Standard experimental testing does not always enable this condition to be met. Consider, for example, the three-point bend sample shown in Figure 4.1.

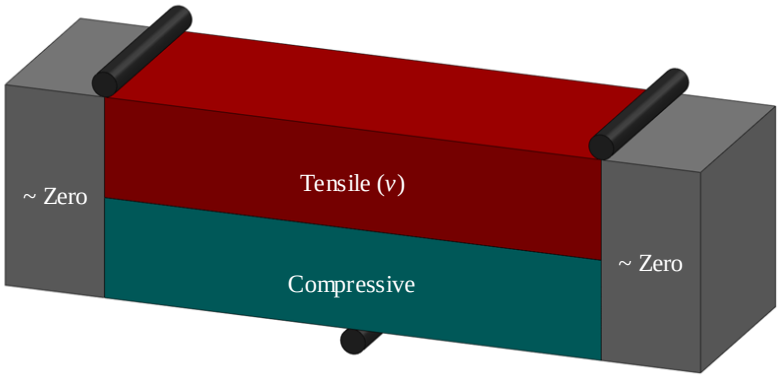

Figure 4.1: Schematic of three-point bend sample showing volumes under tensile and compressive stresses (based on Tucker *et al.*, 1986).

The magnitude of stress within the tensile volume (v) will vary from a maximum at the centre of the top surface to zero under the loading bars, as well as at the neutral axis between the tensile and compressive volumes. Calculating the strain energy density over the tensile volume would result in a density value that is much lower than near the

point of maximum stress, which is where failure tends to occur. This model does at least take into consideration that the failure strength of a component is determined by the stress state over a finite volume, rather than at a single point. Although this does not account for microstructural characteristics such as size and nature of features, it does indirectly allow for the effect of defects in the material and their interaction to cause failure.

Tucker and Rose (1982) determined that all models based on critical criteria were unsuccessful at accurately explaining experimental results. They attribute this to the models assumption that the graphite is an elastic continuum and does not take into account the heterogeneity and complexity of the microstructure.

4.1.2. Weibull Model

One of the more commonly applied theories of graphite fracture is the Weibull (1939) model. This theory takes account of flaws in the material as well as the volume of the sample being tested in order to derive a probability of failure for materials under stress. The statistical distribution function proposed by Weibull has wide ranging applicability and is therefore not specifically developed for use with graphites. Application to graphite considers the material to be made up of small elements. Failure of the sample is due to failure of the element containing the weakest defect (*i.e.* consistent with the weakest link theory). Taking into account these considerations, the probability of fracture of the material under stress, $S(\sigma)$, is given as:

$$S(\sigma) = 1 - \mathrm{e}^{-B} \qquad \text{Equation [4.1]}$$

where, B is a function relating to the risk of failure. Weibull (1951) chose the simplest expression that satisfied the general conditions of the function, which is given as:

$$B = \int_v \left(\frac{\sigma - \sigma_u}{\sigma_O} \right)^m dv \qquad \text{Equation [4.2]}$$

where, σ is the tensile stress in the element dv, σ_u is the stress below which there is a zero chance of failure, σ_0 is the normalising parameter and m is the homogeneity factor, higher values of which correspond to a greater uniformity in the flaw distribution

(Brocklehurst, 1977). Values may be determined experimentally for σ_0 and m, however, determination of σ_u is difficult to precisely define through testing. In practice, approximate values for σ_u have been shown to be acceptable, with an approximation of zero being commonly adopted. Brocklehurst (1977) explains how the Weibull theory can be used to predict the probability of failure for components with different volumes and applied stress states. When the failure probability of a component in differing scenarios is the same, values for B may be equated. One example is the comparison of tensile and simple bend samples. The risk of failure in uniform tension is given by the expression:

$$B = V_t\left(\frac{\sigma_t}{\sigma_0}\right)^m \qquad \text{Equation [4.3]}$$

and in simple flexural configuration:

$$B = \frac{V_b}{2(m+1)}\left(\frac{\sigma_b}{\sigma_0}\right)^m \qquad \text{Equation [4.4]}$$

where, V_t and V_b are the appropriate volumes for tensile and bend samples respectively. Maximum tensile stresses for tension and flexural samples are given by σ_t and σ_b respectively. A ratio between flexural and tensile strength can be formulated by equating values for B and rearranging to give:

$$\frac{\sigma_b}{\sigma_t} = \left[2(m+1)\right]^{1/m}\left(\frac{V_t}{V_b}\right)^{1/m} \qquad \text{Equation [4.5]}$$

Additionally, different volumes of the same test sample geometry V_1 and V_2 are related by the expression:

$$\frac{\sigma_1}{\sigma_2} = \left(\frac{V_2}{V_1}\right)^{1/m} \qquad \text{Equation [4.6]}$$

Work undertaken by Brocklehurst and Darby (1974) on the application of Weibull theory to different tests conditions found that it failed to give consistent values for material parameters, in particular, m. Their work, amongst others (*e.g.* Price, 1976), showed little dependence on volume indicating that the Weibull theory overestimates

the size effect by predicting theoretical strength ratios that were much lower than experimental results. Calculation of this volumetric relationship for tensile and flexural strength required a high value for *m* (approximately 18) which was consistent with the flexural strength at constant volume.

Rose and Tucker (1982) presented an assessment of the Weibull model in which they describe how it has potentially useful application to geometrical effects, however, the lack of any consideration as to the microstructural composition of graphite means that its usefulness at describing experimental behaviour in their study was somewhat limited. Despite being regarded by some reviewers as being inadequate to model graphite, is still widely used (*e.g*. Fok *et al*. (2001), Smart *et al*., (2003) *etc*.).

4.1.3. Fracture Mechanics Model

The foundation for this model is the assumption that a Griffith crack exists within the material that is positioned in the most damaging orientation and is of a characteristic length for the grade of graphite (Rose *et al*., 1982). For example, in a flexural beam test, the assumed crack would be located in the centre of the tensile surface. The actual weakening defects in the material such as pores and easily cleaved particles are analogous to this crack. These defects would, when stressed under a tensile load, interact and cause cracks within the material. The geometry of the assumed defect is, to some extent, based on the size and distribution of defects in the material, however, the microstructural processes leading to fracture are not taken into account. Unlike Weibull theory, consideration as to the microstructure of the material is incorporated into the fracture mechanics model. Consequently, Rose and Tucker (1982) state that the range of usefulness is much wider and they argue that elements of the model should be developed into a new theory for graphite fracture.

4.1.4. Microstructure Based Fracture Models

The Rose/Tucker model, which was developed and applied to nuclear graphites (Rose *et al*., 1982) expanded on a previously proposed theory by Buch (1976). Buch's physically based statistical model relates tensile failure to the microstructure of aerospace grade graphite. The failure criterion is dependent on the probability of

adjacent graphite particles cleaving along their basal planes when a load is applied. Cleavage of particles forms extended cracks that are large enough to fail through linear elastic fracture mechanics. Tensile stresses acting on the cleavage planes determine the probability of cracking. Consideration of material input parameters such as particle size, porosity volume, particle cleavage stress and critical stress intensity factor ensure that microstructural features and fracture toughness are accounted for when applying this model.

The Rose/Tucker model divides the graphite into uniformly sized cubic blocks that represent the particle size of the material. Each block is assumed to have a crystalline structure of random orientation thereby determining the direction in which the basal planes are permitted to cleave. Upon applying a load, a particle is considered to have failed when the critical tensile stress on the cleavage plane is reached. Failure of adjacent particles at the same stress results in an adjoining crack across the two particles. Pores are regarded as particle with zero cleavage strength and appropriate fractions are defined to provide the model with a representative pore volume. As with Buch's theory, failure occurs when a critical number of particles fracture to form a large enough crack to fail as a brittle Griffith crack. The probability that a component will fail is equal to the probability that a critical defect is contained within the material. Although this model accounts for mean particle size, particle orientation, and the pore volume, the size and shape distributions of microstructural features is not considered.

Having identified failings in the Rose/Tucker theory, Burchell (1986) developed a microstructurally based fracture model which was considered to be comprised of an array of cubic particles of a size equal to the mean linear dimensions of the filler particles in the graphite. Although similar to the Rose/Tucker model in terms of how particles are arranged, pores are treated as 'crack like' in nature rather than particles of zero cleavage strength. Each particle is assumed to have a randomly oriented plane of weakness (cleavage plane). Pores are randomly scattered within the conceived structure, with their cross section being log-normally distributed, as shown in Figure 4.2.

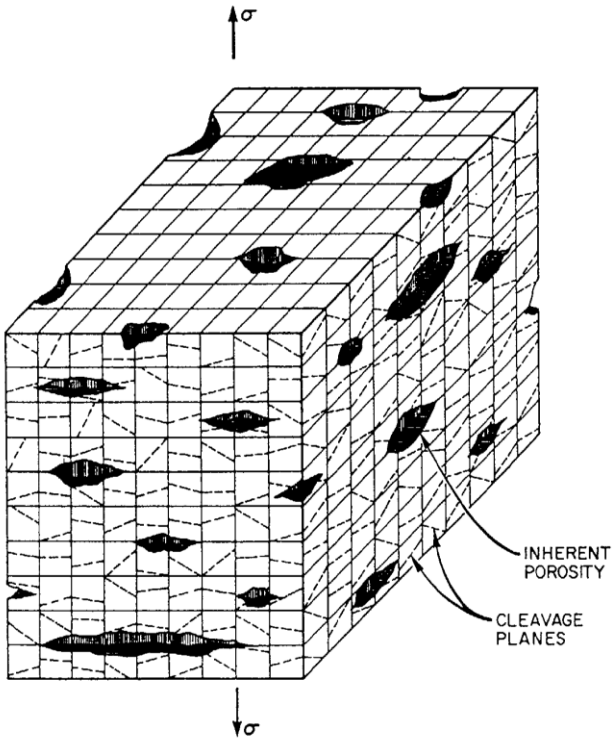

Figure 4.2: Schematic representation of a graphite microstructure as conceived in the Burchell model (Burchell, 1996)

Linear elastic fracture mechanics is used to assign a stress intensity factor (*Ki*) to the pores based on the applied stress and the length of the pore. Failure in this model is assumed to be initiated from a pore and propagate along the weak cleavage planes in the simulated graphite particles. The particle is considered to have failed when the critical stress intensity value assigned to a particle is exceeded by the stress intensity factor on the plane of weakness, which is a function of K_i and the angle at which the cleavage plane is aligned. The pore responsible for crack initiation would then increase in size from its original length, *c*, by a value equal to the size of the particle, *a*, thus growing to length $c + a$. The probability that subsequent particle failures (*n*) leads to crack propagating across the entire row is given by $P(n) = P(i)^n$. Based on this relationship, it is possible to determine the probability that the defect will result in fracture of *i* rows and thus grow to a length $c + ia$. Failure of the graphite occurs when the stress intensity factor relating to the advancing crack (K_i) exceeds the critical value associated with the particle (K_{Ic}).

There are a total of nine input parameters which are required to implement Burchell's model, they are; mean particle size, bulk density, mean pore size, standard deviation of

pore size distribution, mean pore area, number of pores per cubic meter, volume of specimen, breadth of specimen and the critical stress intensity factor of the particle. All the input parameters, with the exception of critical stress intensity factor which was published in literature, were determined by image analysis of microscopy samples.

Burchell (1996) applied his model to four contrasting grades of graphite. H-451, having an average particle size of 500 μm was selected as a relatively coarse grained graphite. Finer grained grades IG-110 and AXF-5Q, with average grain sizes of 20 μm and 5 μm respectively were also investigated. Additionally, the coarse grained electrode graphite, AGX (which has a mean particle size of 6.35 mm), was studied in order to determine the applicability of the Burchell model to graphites used in different industrial applications. Experimental tensile strength data was compared to the modelling predictions and generally showed good agreement for all four grades. Greater deviations were observed for IG-110, AXF-50 and AGX grades, although they did provide an acceptable approximation when compared to the model predictions. Failure probability distributions for H-451 graphite determined through experimental means were very close to modelling predictions. Slight deviations at low and high stress values were observed, suggesting that the model predicted pessimistic failure probabilities at low stresses and optimistic probabilities at higher stresses.

The pore size distribution used in the model is derived from image analysis of micrographs. The possible presence of large flaws could have an effect on determining the materials strength, as observed by Abe *et al.* (2003) whilst investigating the flaw size distribution in alumina. Therefore to not include them in a model could lead to optimistic strength related values derived from its use (Nemeth *et al*, 2010).

Tucker and McLachlan (1993) further expanded in the microstructurally based fracture model. The purpose of this work was to extend Burchell's model in order to account for physical properties other than fracture, primarily, stress related effects such as strain hysteresis and acoustic emission. This expansion requires a total of fourteen model input parameters to be determined (McLachlan, 1992); shear modulus, Poisson's ratio, plastic friction stress, granular critical stress intensity factor, pinning grain separation, fraction of porosity, fracture acoustic emission events per square meter, displacement acoustic emission events per square meter, defect diameter distribution, mode, defect

diameter distribution, spread, density of defects with crack geometry, lowest considered defect radius, largest considered defect radius and propagation cut-off radius. Rather than including the entire pore distribution, the Tucker/McLachlan model categorises them into 'active' and 'passive' pores based on the likelihood that they will contribute to failure initiation of the material. Pores are considered to be active if they cause localised regions of high stress when a load is applied. As such, shaper, crack like pores are generally considered to be active. Stress concentrations around these pores may effectively attract the advancing crack tip towards them thereby increasing the crack length by a value equal to the length of the pore. These passive pores can therefore be considered to be crystalline material with zero resistance to cleavage. Intersecting grains at the edge of the crack may cause it to arrest. The subsequent failure of these grains, referred to as 'pinning' grains, is dependent on their orientation. For example, individual crystallite material adjacent to active pores may fail easily if they are aligned so that their basal planes are coplanar with the advancing crack. This scenario is assumed to cause grain deformation from crystalline shear processes. Based on the probability of pinning grain failure the probability of formation of a critical defect can be calculated in a similar manner to that described by the Burchell model.

The performance of this model was assessed using VFT pitch coke and IM1-24 grade nuclear graphites in tensile and flexural (three and four point bend) configurations. This approach was reportedly successful at describing a range of fracture data. Although the model was generally able to predict an accurate failure distribution, the level of accuracy varied between materials and test geometry. Generally, the probability of failure for VFT pitch coke demonstrated a close fit and accurately predicted values for both mean and standard deviation. Failure probability curves for modelling IM1-24 graphite again gave an accurate representation. However the four-point bend configuration showed a more significant deviation from experimental data then tensile and three-point bend geometries. Sharp notches were also simulated using this model by considering them to be very large defects in the material.

Critical reviews of the Tucker and McLachlan model have stated that it deviates significantly for the simplicity of the Burchell model and can therefore be cumbersome to use (*e.g.* Burchell (1996), Nemeth *et al.* (2010)). Additionally, many of the parameter values were not determined experimentally. Rather they were derived though

a process that selected initial values before the model parameters were iteratively altered until an acceptable distribution that represented experimental data was attained.

4.2. Computational Modelling

Computational modelling of graphite and graphite components has become an important tool in ensuring the continued safe performance of nuclear reactors as well as the continued design and development of graphite components for a number of industrial applications. As previously mentioned, the scale of the modelling is dependent on the application of the study. Since it is not possible to model large components in detail, it is important to understand that the results from some types of modelling may not fully reflect the performance and variability in operational components. Conversely, the results from computational modelling on a micro scale may not be widely applicable when scaled up to represent whole components. Examples of computational studies which focus on the reactor and component scale have been undertaken by; Ahmed (1987), Taylor *et al.* (1997), Warner *et al.* (1998), Tsang *et al.* (2006), Kralj *et al.* (2007).

Computational modelling may refer to a number of approaches that can be used to determine material parameters of the graphite in service. Specific computational programs may be developed in order to simulate specific aspects that require further investigation. Alternatively, existing commercial programs may be modified to allow for graphite to be simulated more appropriately. Most computational procedures will incorporate at least some component of finite element analysis (FEA). Indeed, the versatility of FEA as a tool in simulating potential situations and events means that models are often constructed and analysed entirely within the environment of an appropriate FEA program.

FEA is the method of numerically approximating solutions to the performance of components (*e.g.* the stress distribution induced through application of a load). After constructing a model in an FEA program it is segmented into 'finite elements'. These elements are geometrically simple and create a 'mesh' of the material. Each element in the mesh contains a quantity of 'nodes' which provide a discrete number of points at which partial differential and integration calculations take place. Considering the

calculated values at the nodes in relation to adjacent ones allows for distributions showing the response to a loading scenario to be determined. Each model can contain thousands of nodes and as such, it is perhaps unsurprising that calculations are liable to require a significant amount of computing power and can take a great deal of time to complete. For this reason, the use of FEA methods has become more common since computing power has become more economical and readily available. Advantages to the use of FEA include the ability to construct and simulate the response of geometrically complicated components. These solutions may then be used to better understand the response of a component under operational conditions. At the design stage this information may be used to further optimise the component to enhance performance or optimise construction parameters. Alternatively, FEA methods may be used to satisfy that the continued use of a component in a given scenario satisfies safety regulations (Reddy, 2004). Simulation of a model in an FEA environment depends on a number of input parameters and the success depends on the accurate determination of the following factors:

- Accurate representation of the model. This consideration often refers to the accurate geometric reproduction of the component or experimental specimen. However, when modelling highly heterogeneous material such as graphite, it may be advantageous to consider additional factors such as the microstructure.
- Appropriate input of relevant material properties to the model. This is highly dependent on the desired outputs for the simulation. This may include but is in no way exclusive to parameters such as elastic modulus, poisons ratio, density or thermal conductivity.
- Consideration of element type and application. The choice of elements used in a model can have an effect on the overall solution. To ensure the most accurate solution elements that are suitable for the modelling parameters and loading conditions should be utilised.
- Simulation of loading factors. In order to correctly simulate the experimental or operations conditions of a component, the loads and constraints must be correctly represented. This could be simply achieved through application of a suitable tensile or compressive load or displacement to the surface of an experimental specimen. Alternatively, complex situations involving the

interactions between engineering components may be required to fully simulate an operational environment.

- Understanding of applicable post processing tools. Simulation using FEA methods can provide a great deal of information regarding the performance of the model based on the input parameters. Successfully solving an FEA model will enable complex stress distributions of the entire model or individual values to be output. The correct implementation of such tools is vital in ascertaining meaningful data from the model.

4.2.1. Microstructure Modelling

Incorporation of microstructural features and processes into a computational model would provide a description of material behaviour under different loading scenarios. Accurate modelling of a representative microstructure needs to take account of the probabilistic nature of the material and as such should consider microstructural variations which cause stress concentrations that could potentially lead to failure.

Holt (2008), whist investigating issues of scale relating to nuclear graphite, investigated methodologies that would enable a probabilistic microstructure to be created in the FEA environment, ANSYS. Upon loading the model, the influence of microstructural features on the bulk material properties could be determined through analysis of post processing distributions (*e.g.* stresses and strains *etc*.). In order to best represent the microstructure of graphite, the model needed to incorporate the three fundamental features of the material; Gilsocarbon coke particles, matrix material (including binder phase and flour) and porosity. Holt (2008) determined that the most appropriate method to represent particles and porosity whilst simplifying construction was to use hexagonal shapes to create the models. Figure 4.3(a) shows a simple model with a uniform pore distribution to demonstrate the methodology. Hexagonal shapes have the added advantage of allowing models of various sizes to be constructed by simply increasing the number of 'particles'. The model was refined to incorporate the microstructural features of the graphite and thereby make the model more representative. Computational codes were written to generate the model and set appropriate material parameters. Suitable input values for model size as well as a percentage value for porosity were entered into the model generation programme to generate an *.lgw file

which could then be used with the ANSYS software. The material setter program gave a simple representation for the properties of Gilsocarbon filler particles and binder phase within the graphite as shown in Figure 4.3(b).

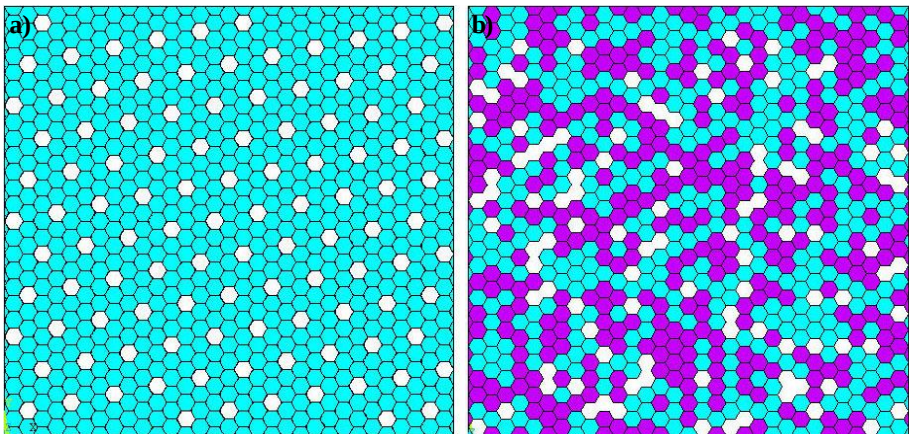

Figure 4.3: Simple hexagonal models showing a) uniform pore distribution (pores are indicated by white 'voids' in the model) and b) further developed model random pore distribution with simulated Gilsocarbon filler particles (purple) and binder material (light blue) (Holt, 2008).

Porosity in the model was generally fixed at 20% since this is approximately typical for nuclear graphites. To account for the Gilsocarbon and binder material in this model, two sets of material properties were defined. Values of density, Young's modulus and Poisson's ratio were determined through consideration of single graphite crystal properties as shown in Table 4.1.

Table 4.1: Determined properties for Gilsocarbon and binder material (Holt, 2008)

Material Property	Determined Model Property	
	Binder	Gilsocarbon
Young's Modulus (GPa)	692	18.82
Density (Kgm^{-3})	2260	1849
Poisson's Ratio	0.23	0.33

Porosity was simulated by effectively creating voids in the model and therefore did not require any consideration for material parameters. Binder regions were considered to be mosaics of randomly oriented crystallites and values were therefore considered to have similar density and Young's modulus to single graphite crystals. The binder Poisson's ratio was calculated based on the input parameters of 0.2 for bulk IM1-24 grade graphite and a porosity value of 20.12%. Image analysis of Gilsocarbon particles

determined an average porosity percentage of 15.203%, which was used to estimate the density and Poisson's ratio. Young's modulus of these particles, E_0, was estimated through simple modification of the Knudsen's relationship:

$$E = E_0 e^{-b\eta} \qquad \text{Equation [4.7]}$$

where, E is the Young's modulus of bulk IM1-24 graphite, η is the porosity ratio, as determined through experimental observations and b is a constant derived from experimental values. The calculated value of 18.82 GPa was determined by using the variables E = 10.89, η = 0.15203 and b = 3.2 (Rice, 1996).

Since this work was primarily concerned with the issues of scale inherent to nuclear graphites, a total of seven different model scales were constructed ranging from 5 x 5 to 400 x 400 hexagons. Figure 4.4 shows two examples of the constructed models before loading. Generally, there will be a higher probability of long pore 'chains' in larger models. This is analogous to larger volumes of graphite being more likely to contain large, potentially critical defects.

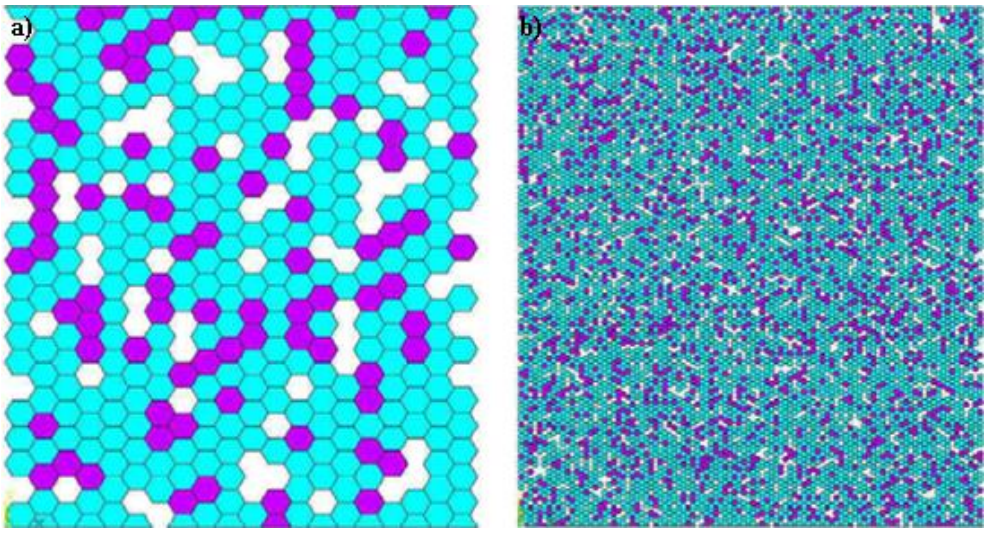

Figure 4.4: Example models showing the distribution of porosity, filler particles and binder phase for a) 20 x 20 and b) 100 x 100 hexagon models.

Simulated loading of the model was achieved though constraining the bottom surface and applying either a tensile or compressive displacement in the y-direction at the top surface. Consideration of parameters (*e.g.* stresses, strains strain energy *etc*.) allowed for determination of the relative performance of each model. Direct comparisons

proved problematic since the larger models required a greater displacement to be applied which in turn has an effect on the distributions. Further issues arose when trying to create and analysis 400 x 400 hexagon models which required a significant amount of time to solve. Only two of these large models were tested due to this restriction.

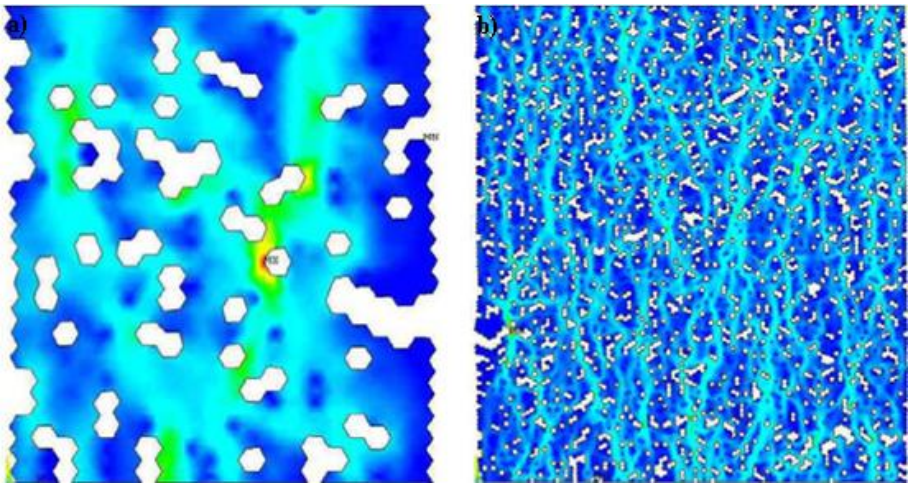

Figure 4.5: Example first principal stress distributions under tensile loading for a) 20 x 20 and b) 100 x 100 hexagon models.

Although this model was able to simulate the tensile and compressive responses for a porous material, the simulated structure is not representative of graphite. Porosity distribution were shown to have a significant effect on modelling results, however, the size, shape and distribution of simulated pores is purely random and does not accurately characterise what would typically be observed in a graphite microstructure. Further, the incorporation of material properties for Gilsocarbon and binder constituents does not take into account their relative sizes. It could be argued that considering of the binder phase as discrete mosaic areas of material means they do not have a defined size, however, accurate characterisation of Gilsocarbon would require a great deal more consideration. Generally these particles are observed in a range of sizes and shapes and will tend to be evenly dispersed through the material. Another concern regarding the modelled 'particle' is the relative size between Gilsocarbon and porosity. A single pore in the model is equivalent in size to a filler particle; therefore it follows that any pore chains will be larger than the modelled filler particles. However, a typical microstructure may observe Gilsocarbon particles up to 1 mm in diameter, whereas

pores will normally be far smaller, therefore it is clear that this scale is not representative.

Lynch *et al.* (2007) developed an abstract model to computationally predict the microstructure of graphite as a function of increasing weight loss from radiolytic oxidation. Constituent material parameters for binder matrix, filler particles and porosity were simulated in the model using appropriate proportions typical of IM1-24 graphite. Randomly generated porosity in the model was created though application of 'circles within circles' method. This method enables the formation of complex shapes by packing circles according to geometric relationships. Pore sizes were controlled through a random number generator to ensure a probabilistic distribution. Radiolytic oxidation of the model was modelled by simulating degradation at the pore walls within a set distance from the creation of oxidising species (shown in Figure 4.6(a)). Fracture of the model was based on the path of least resistance through the material (Neighbour, 2008). Figure 4.6(b) shows the microstructure model with a simulated crack path. The generation of a probabilistic microstructure model that incorporates a wide range of porosity/particle sizes and shapes is beneficial since simulations do not require the input of extensive parameters from observed microstructures.

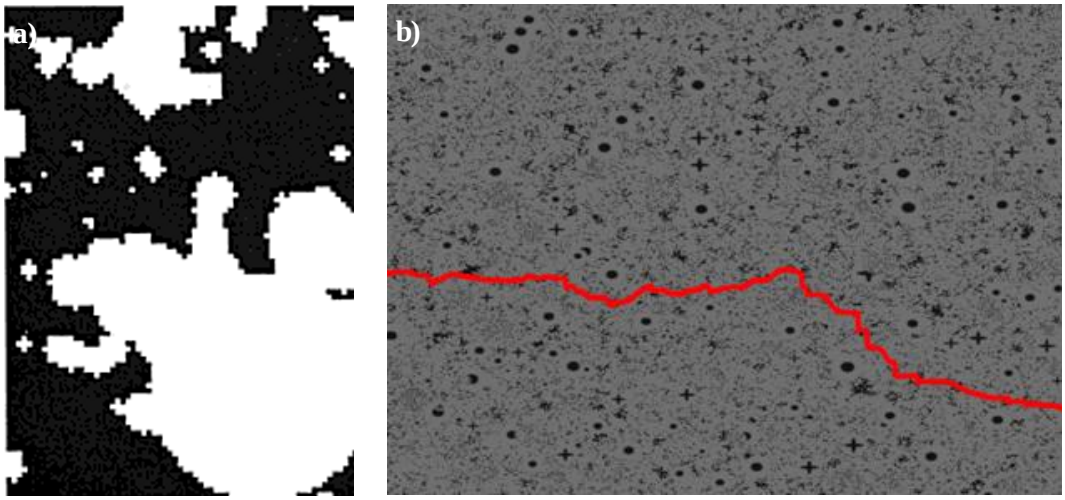

Figure 4.6: Abstract model showing a) simulated microstructure and the effect of oxidation (Lynch *et al.*, 2007) and b) crack path through simulated microstructure (Neighbour, 2008).

Micro scale x-ray tomography was used by Berre *et al.* (2006) to create three-dimensional models with a representative Gilsocarbon graphite microstructure. The image processing and analysis software Simpleware was used to reconstruct CT scan

image 'slices' into a volumetric model, as shown in Figure 4.7(a). Segmentation of the pores and solid material in the reconstructed image enabled the pore sizes and distributions to be defined. The segmentation process was dependent on the correct determination of a suitable greyscale value for the image that corresponds to the boundary between relatively dark pores and light filler/binder material. Another software package, ScanFE, then uses the segmentation data to automatically create an optimum voxel based FE mesh using both tetrahedral and hexahedral elements (Figure 4.7(b)). Exportation of this model in the software package ABAQUS allowed the sample to be analysed.

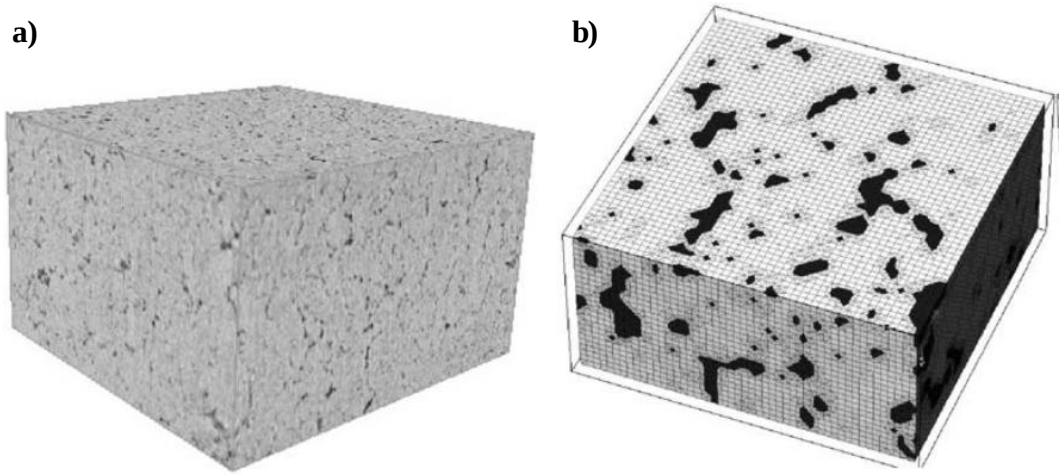

Figure 4.7: a) CT scan images reconstructed to generate a 3D volume (14 x 14 x 9 mm) and b) voxel based element mesh created through segmentation of solid and porous volumes (2 x 2 x 1 mm) (Berre *et al.*, 2006)

Weight loss simulations were made by varying the greyscale threshold level. Increasing the pore threshold to a higher greyscale value would result in an increase in pore volume within the model. Fractional weight loss due to oxidation, x, is related to material density, ρ, and the porosity ratio, η, by:

$$x = 1 - \left(\frac{\rho}{\rho_0}\right) = 1 - \left(\frac{1-\eta}{1-\eta_0}\right) \qquad \text{Equation [4.8]}$$

where, the subscript '0' indicates a value for virgin graphite before oxidation. Although this is an effective method for systematically modelling various degrees of weight loss, it does not necessarily represent the process of radiolytic oxidation in a nuclear reactor. Radiolytic oxidation only affects open porosity since it relies on the close proximity of

the CO_2 coolant to the surface. Due to the relatively similar densities of filler and binder material in the graphite, they are difficult to identify in a CT scan image. As a result, identifying the type of porosity (*e.g.* open gas evolution pores in the binder or closed filler particle calcination cracks) in the volumetric model is problematic. Failure to discriminate between the open and closed porosity when increasing the threshold results in an increase of both pore types.

Since this work was attempting to model graphite at varying degrees of weight loss, a relationship between material property and the fractional porosity was required. Berre *et al.* (2006) states that the Young's modulus, *E*, can be determined from the Knudsen relationship (see Equation 4.7). For Gilsocarbon graphite subjected to radiolytic oxidation, a constant value, *b*, of 3.6 was determined for weight losses ranging for 0 to 30% (Brocklehurst and Adam, 1983). Input data for use in predictions was obtained through nano-indentation experiments which suggested the Young's modulus of a single graphite crystal (*i.e.* 0% porosity) was 15GPa. Predicted values for Young's modulus at weight losses ranging from 0 to 45% were shown to be consistent with Knudsen's law. The model effectively demonstrated a decrease in stiffness as the weight loss increased. Using the predicted Young's modulus values, the stress distribution in the material can be simulated. Critical stress values for failure initiation were shown to decrease, indicating a reduction in tensile strength, with increasing weight loss. Validation of these results is difficult due to a lack of comparable experimental data and the small scale of the model. Further difficulties arose when considering the mesh density of the model. Increasing the density from the initiation element size was found to output different stress values. The authors stated that this dependence on mesh density requires further investigation to determine the ideal element size for the model.

Further work on tomography based modelling techniques involved its application to thermally oxidised samples of Gilsocarbon (Berre *et al.*, 2008). Figure 4.8 shows an example of a finite element mesh used in this work. Bulk tensile strengths predicted using the oxidised CT models showed an exponential decrease as the pore volume increased adding credence to the conclusions from previous work.

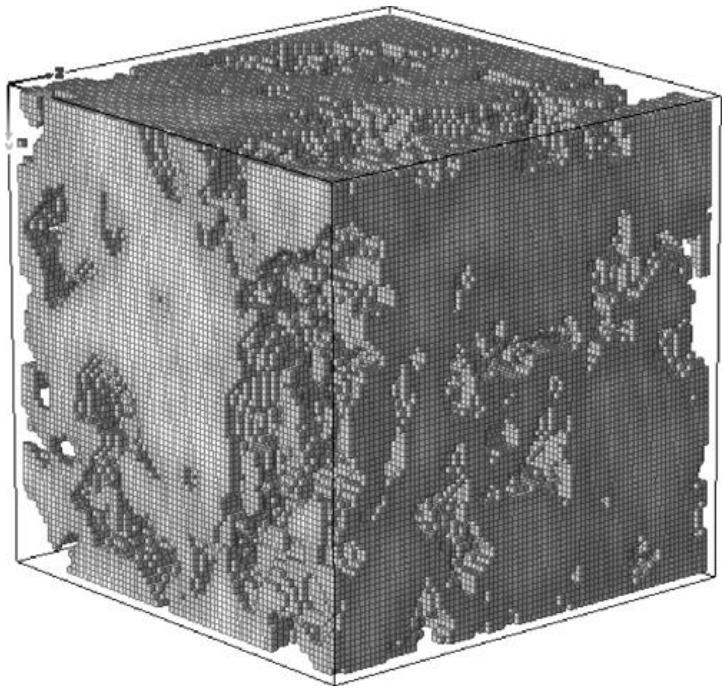

Figure 4.8: Finite element mesh generated from CT scan of thermally oxidised Gilsocarbon graphite (Berre *et al*. 2008)

Schlangen *et al*. (2011) studied the crack propagation in reactor graphite through the development of computational models. The three-dimensional models were constructed to give an accurate representation of PGA graphite on a microstructural scale accounting for filler particles, matrix and porosity. Matrix and porosity in the material was randomly distributed in the appropriate proportions. Porosity values of 20, 40 and 60% were investigated to simulate weight loss due to radiolytic oxidation. Filler particles were represented by cylinders aligned within the simulated microstructure, thus representing the needle coke particles used in the manufacture of PGA graphite. Analysis was undertaken in a custom FEA environment which utilised a 'lattice' model to simulate crack propagation. The lattice model consists of beam elements which are removed from the network when they are deemed to have 'failed', thereby simulating a crack in the mesh. Upon loading the model with a tensile strain, the beam element that experiences the highest stress is removed. Subsequent analysis is performed on this 'cracked' model and the process repeated. Progressive removal of elements allowed for detailed stress-strain and fracture characteristics to be determined on a micro scale. Simulation results showed a strain softening response indicating progressive crack propagation through the material. As would be expected from experimental testing or

theoretical predictions regarding this material, the stiffness and strength of the model was shown to decrease as the porosity increased.

Ensuring a characteristic size and shape distribution for porosity was not of primary concern when this model was constructed. Although the random pore distributions are representative of the overall percentage, there is no control over the pore sizes and shapes. Additionally, the filler particles were only representative in their basic aspect ratio. Details such as the 'needle' shape of the particles or indeed a variation in the size and shape that would be expected in the material. The filler particle porosity content was also not considered in the modelling solutions.

This thesis aims to expand on the work that has been undertaken on microstructural modelling. The particular focus of this research is in using the developed models to generate representative mechanical data on a microstructural scale. Further, this data will be used to consider how the microstructure influences the mechanical performance of the material as well as determining properties as a function of increasing crack length.

4.3. Modelling Complexities and Considerations

The level of detail that a model can simulate has a limiting factor based on time and in the case of FEA models, processing power. Consideration of modelling approaches at different scales is generally due to these complexities. Take, for example, the microstructural FEA approaches suggested in this chapter. Without exception, they all simulate very small areas or volumes of material. In order to solve larger models, greater computational resources or a reduction in detail would be required. This balance between size and detail is the reason core components are generally not modelled with detailed consideration for the material microstructure.

It has been stated throughout the previous chapters that porosity can have a major effect on the material properties of the graphite. It is therefore perhaps of little surprise that these microstructural models generally place a significant emphasis on creating a pore distribution. The two most common approaches to modelling porosity, probabilistic and observed distributions, both have advantages and disadvantages. Generating a pore

distribution based on randomly generated shapes within the structure allows for a greater number of models to be solved. Rather than requiring experimental observations, any number of models can be generated by running a computational algorithm. However, these algorithms can be time consuming to write and do not necessarily generate a representative distribution. The highly complex pore networks and large variety of shapes within the material mean that a large number of parameters need to be considered to ensure probabilistic pore distributions accurately represent the graphite microstructure. Modelling representative structures based on observations requires accurate determination of pore distributions in material samples, generally though the application of microscopy and image analysis techniques. Although this is far more time consuming than probabilistic modelling, the distribution is likely to be representative of the material, providing the image analysis is performed correctly.

Some models have attempted to include consideration as to the relative material properties of filler and binder material, which as some work has shown can be problematic. Firstly, the distribution of material is of importance and the same issues regarding porosity apply to the constituent materials. In addition, the input parameters for material properties that are required for effective application of FEA techniques need careful consideration. Experimental determination of these properties is not possible using traditional techniques. Micro or nano-indentation tests may be used to establish a rough estimate of relative material properties of the two constituents; however, these tests will generally not provide reliable data.

Three-dimensional models based on observation of microstructural features are likely to utilise CT techniques to generate data sets. The images generated through the application of CT scans are based on material density which appears as a variation in brightness. Image analysis thresholding relies on a clear distinction in brightness (*i.e.* greyscale) value between two components to effectively segment the image. Since binder and filler have a relatively similar density they will have a similar greyscale thereby making segmentation based on thresholding difficult.

4.4. Chapter Summary

This chapter briefly reviewed theoretical techniques for modelling the fracture of graphite. Generally, the common consensus regarding the success of a particular model is dependent on its ability to account for microstructural variations. For this reason, the development of the Rose/Tucker (1982) model was regarded as an appropriate benchmark for further model development. Although this technique was in itself an extension of the method proposed by Buch (1976), subsequent modifications by Burchell (1986) and Tucker/McLachlan (1993) are generally compared to the Rose/Tucker model.

Theoretical models are vital in providing an understanding of the failure characteristics of graphite and indeed a basis for computational methods. However, the primary focus of the chapter was the application of computer based models, in particular FEA approaches, since the development and implementation of a representative model is one of the main objectives of this investigation. Given the extensive amount of research on computational approaches, this chapter has reviewed a relatively small number of models.

Some theoretical techniques are based on fundamental material science and are therefore not widely applicable to graphites (*e.g.* critical stress/strain models). Indeed, it is stated that due to the heterogeneity of the material that in some cases they are inadequate for predicting the performance of graphite. Although these theories may not be directly relevant to bulk material, computational models incorporating microstructural features have demonstrated some merit in using them as a criterion for the failure of individual elements. The review of microstructural modelling techniques gave an insight into possible techniques that could be applied in developing a representative model and test programme. In addition, potential issues and complexities that will require consideration through the development of a representative model have been highlighted.

Chapter five discusses the development of an experimental test programme. In addition, experimental results will be present and discussed.

Chapter 5 – Experimental Programme Development and Details

Throughout the previous chapters, particular emphasis has been placed on the inherent variability of graphite. Raw ingredients and manufacturing methods are responsible for the material heterogeneity which results in significant variations in the microstructure resulting in a considerable effect on the mechanical performance of the material. Further, it has been discussed the variation in microstructure can result in a population of very large flaws that contribute to some test samples failing at low loads. The distribution of such flaws is referred to as the disparate flaw population (Kennedy *et al.*, 1986). This distribution is analogous to the 'infant mortality' portion of a classical bathtub curve (see Figure 5.1), which represents premature failure due to manufacturing defects. It has been suggested that the presence of such a population may contribute to a bimodal failure model, with a statistically significant distribution of failures occurring at lower loads (*i.e.* demonstrating strengths less than two standard deviation from the mean ($\mu - 2\sigma$)). Disparate mode failures are considered to account for only 3 to 5% of the entire distribution (*e.g.* Kennedy *et al.* (1986), Maul *et al.* (2010)). Since the probability of observing such failures is relatively low, a large batch of samples must be tested to increase the likelihood of observing the effect of a disparate flaw population. This chapter explains the selection of experimental methods with the objective of observing such distributions in a range of suitable materials.

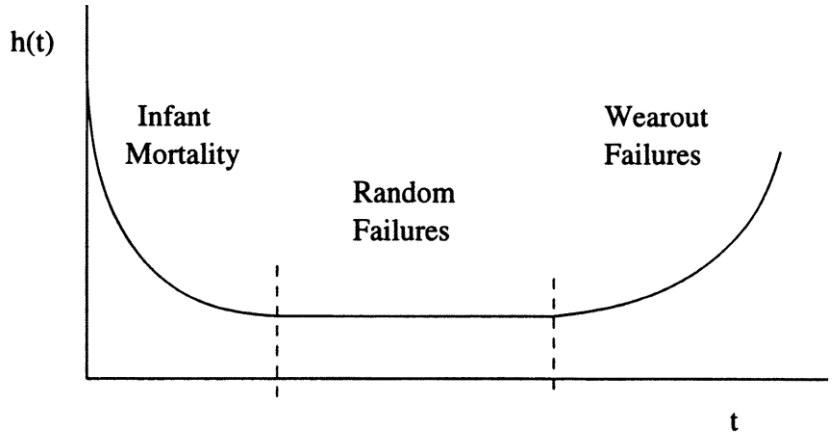

Figure 5.1: Classical bathtub curve showing probability of failure plotted as a function of time (Reproduced from Klutke *et al.*, 2003)

5.1. Experimental Selection

Due to the small proportion of disparate mode failures in a batch of samples, the primary consideration of these experimental tests is ability to produce a large quantity of samples. Additionally, the samples must be consistent in both geometry and experimental loading. Further considerations when identifying suitable experimental geometries relate to the relative stressed area of the sample when under load. The disparate flaw population is potentially volume dependent since larger regions of high stress have a greater probability of containing such a flaw. An example of an ideal experiment to stress a relatively large volume of material would be a tensile test. However, due to the intricate nature of tensile sample geometries, it is not feasible to test a large number of samples. Additionally, the complex geometry increases the likelihood of machining flaws. It could be argued that the presence of such flaws is analogous to any manufactured engineering component and that the disparate flaw population is inclusive of such defects. However, for the purposes of this experimental study, sample consistency is vital to ensure that distributions are solely representative of the material and not a result of manufacture. Experiments that utilise a simple geometry such as three-point, four-point and biaxial flexural tests are more suited to testing a large quantity of specimens. The relative stressed volume in such samples is lower than tensile tests, however, they are simple to manufacture and are less likely to contain significant machining flaws.

Consideration of available test methods suggests that flexural samples are the most suitable for the experimental programme since they enable manufacture and testing of hundreds of experimental samples with consistent geometries. From the suggested flexural tests, biaxial experiments, such as the ball on three ball (B3B) experiment (Godfrey, 1985), have the additional benefit of producing a tensile stress in two directions. As such, this increases the possibility that a sample will contain a disparate flaw that is critically oriented to the applied stress (Brocklehurst, 1977).

5.2. Material Selection and Sample Preparation

In addition to investigating graphite, experimental testing of glass will establish the failure distribution of a more homogeneous (*i.e.* ‘fully dense’) brittle material.

Explanations as to the bimodal failure distribution in graphite typically reference probabilistic porosity distributions and the presence of exceptionally large flaws (Kennedy *et al.*, 1986). Analysing the failure distribution of glass will determine whether similar distributions may be observed in a material that does not contain such a significant variety of microstructural flaws. That is, would it be expected that disparate flaws can be expected in a 'fully dense' material? Additionally, testing a material with the potential to contain a substantially larger variation in structure will demonstrate the relative effect of flaw size in a highly porous material on the failure distribution. This highly porous material is analogous to highly oxidised graphite.

5.2.1. Graphite

The existence of a bimodal distribution in graphite has been reported in a range of different material grades (*e.g.* NBG-18 (Hindley *et al.*, 2012), AGR graphite (Maul *et al*, 2010), H-451 (Kennedy *et al.*, 1986). The graphite material used in the experimental testing was EY9 grade, a fine grained material manufactured by Morgans through extrusion. Utilising fine grained graphite such as EY9 is preferable since the manufacturing process is less likely to induce significant surface defects. It is not uncommon to 'pluck' particles from the surface of the graphite during sample preparation. Depending on the grain size and the location of these plucked particles, substantial damage can be introduced to the sample which could be interpreted as disparate mode failures. Since EY9 has a small particle size, the potential for significant machining flaws is reduced. Typical properties of this material are shown in Table 5.1.

Table 5.1: Mechanical properties of Morgans EY9 grade graphite (Cowlard *et al.*, 1967).

Morgans EY9		
Density (gcm^{-3})		1.7
Porosity (%)		17
Flexural Strength (MPa)	With Grain	39.99
	Across Grain	13.1
Compressive Strength (MPa)	With Grain	51.02
	Across Grain	22.75
Young's Modulus (GPa)	With Grain	13.1
	Across Grain	4.83

The availability of this material in the form of extruded rods also made it favourable since it could be readily manufactured into large quantities of biaxial test samples. Two different sized rods of material, approximately 27 mm and 67 mm in diameter, allowed for different specimen geometries to be tested. The thickness of biaxial flexural samples can have a significant effect on the mechanical characteristics of the material. Thicker samples show significant compressive effects at the load point which can invalidate the flexural test (Kipling *et al*., 2010). As such, the samples thicknesses were 2 mm and 4 mm for the 27 mm and 67 mm diameter specimen respectively.

Prior to sectioning the material into samples, a longitudinal cut along the bar stock was made using a lathe to ensure the samples had a consistent diameter. Although edge effects in B3B tests are minimal, strength calculations do require the input of a diameter value. The material was then sectioned by making transverse cuts to give a suitable specimen thickness. A suitably slow feed rate was required to ensure defects were not introduced to the sample surface as it separated from the bar. Each sample was finished using a fine silicon carbide paper (1200 grit) on both the top and bottom surfaces to provide flat load application and support faces. Samples were cleaned in an ultrasonic bath for one minute to remove any debris for the pores before being thoroughly dried in an oven at 105^{o}C for a minimum of one hour. Since the sample surface required preparation after sectioning, the average thickness of the Ø 67 mm samples was 3.96 mm with a standard deviation of 0.061 mm. The Ø 27 mm samples had an average thickness of 1.97 mm and a standard deviation of 0.047 mm. The nominal dimensions of both manufactured sample sizes and testing apparatus are shown Table 5.2 and schematically represented in Figure 5.2. Due to a lack of data regarding the Poisson's ratio of EY9, the value is approximated as being 0.21, which corresponds to fine grained graphite with similar properties, ATJS (Marlowe, 1970).

Table 5.2: Sample and apparatus dimensions for B3B tests.

Property	**Sample Value**	
	Ø 67 mm	Ø 27 mm
Thickness of disk (mm)	4	2
Radius of disk (mm)	33.5	13.5
Poisson's ratio	0.21	0.21
Support radius (mm)	21.6	9.5
Radius of loading ball (mm)	6	6

A total of 300 Ø 27 mm samples and 298 Ø 67 mm samples were tested in the ball on three ball configuration.

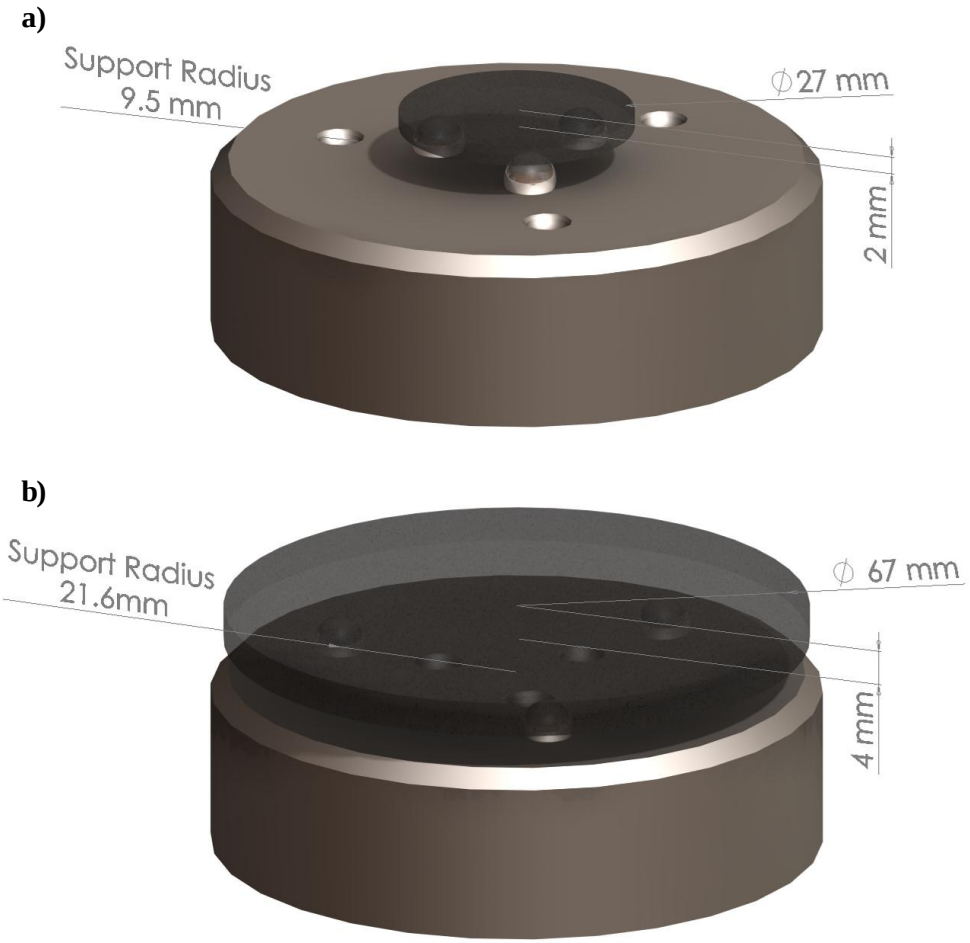

Figure 5.2: Schematic representation of the Ball on three ball configuration for a) Ø 27 mm and b) Ø 67 mm specimen.

5.2.2. Glass

Since the primary requirement of this experimental programme is to test a large number of samples, glass microscope slides were chosen to ensure that the samples are consistent in geometry. Due to the geometry of the glass slide, it is not possible to test them in a biaxial configuration. Standard three-point flexural tests were instead employed for the testing of this material. Three-point bend rather than four-point was selected since this configuration is more analogous to the B3B method (*i.e.* one point of contact). Nominal dimensions of the glass slides were 76 x 26 x 1 mm. The thickness

and width of each slide was measured and demonstrated very little variation within batches (maximum variation of 0.01 mm in both width and thickness). Between batches the slide thicknesses did vary between 1.02 mm and 1.11 mm, however, sample width remained consistent with a maximum variation of 0.01 mm. The support span for this experiment was 36 mm.

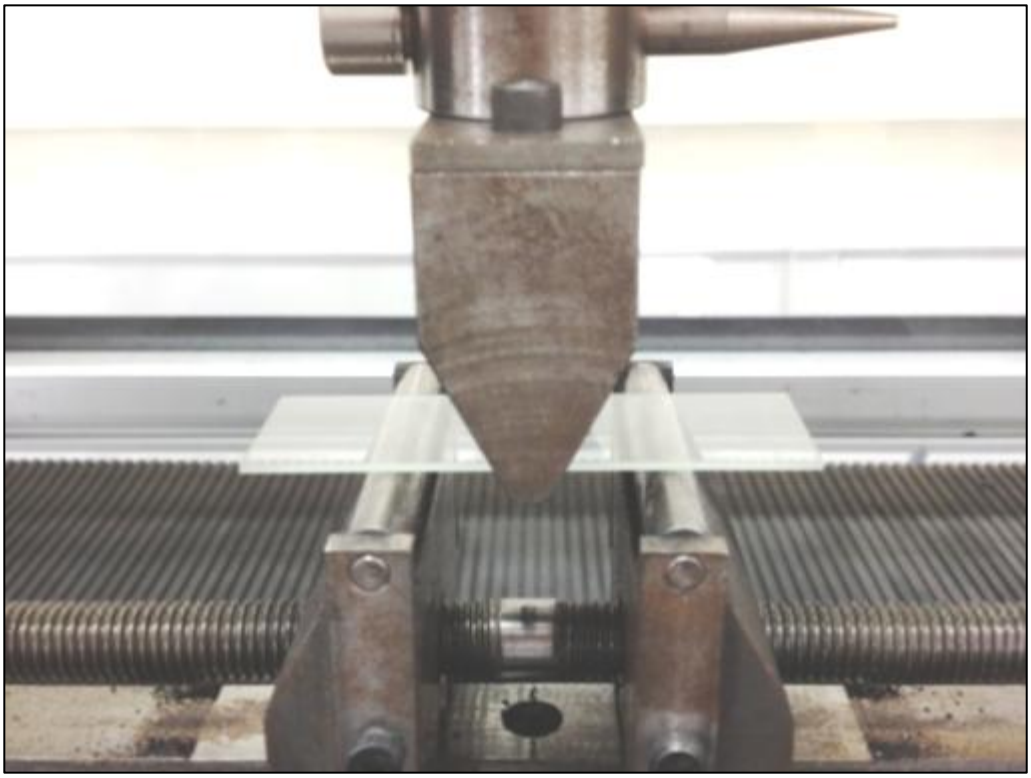

Figure 5.3: Three-point bend experimental configuration for glass slides.

5.2.3. Ligament Material

Selection of a material that potentially exhibits 'extreme' microstructural variations initially proved problematic. Initial investigations focused on identifying materials with a large amount of porosity such as foams. However, many materials that utilise a highly porous foam structure are not brittle and would be difficult to compare with graphite and glass. Further investigation identified a carbon based material with a very 'coarse' ligament structure which is both brittle and readily available in large quantities. The name of this material is a registered trademark and due to a confidentially agreement it will hereafter be referred to as 'ligament material'. Material was supplied in blocks with dimensions of 100 x 100 x 24 mm (Figure 5.4).

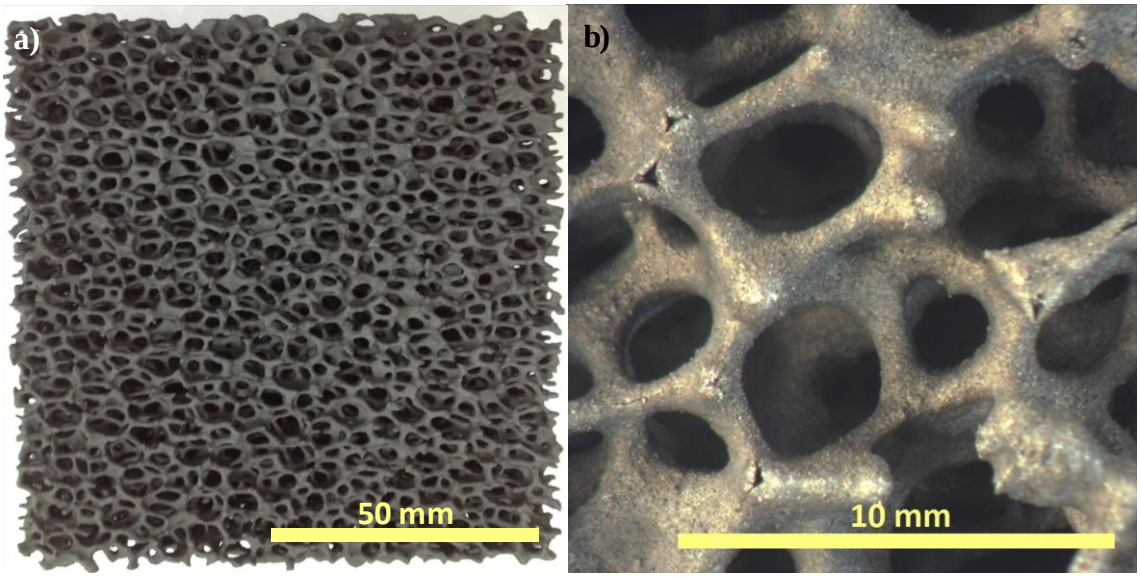

Figure 5.4: example images of ligament material showing a) supplied material block (100 x 100 x 25 mm) and b) stereo micrograph of the ligament structure.

Due to difficulties in manufacturing circular samples from available material and the small load application point inherent in B3B testing, the experimental geometry chosen to test this ligament material was three-point bend. Blocks of material were cut into three flexural samples, each with the dimensions 100 x 24 x 24 mm as shown in the sectioning diagram (Figure 5.5).

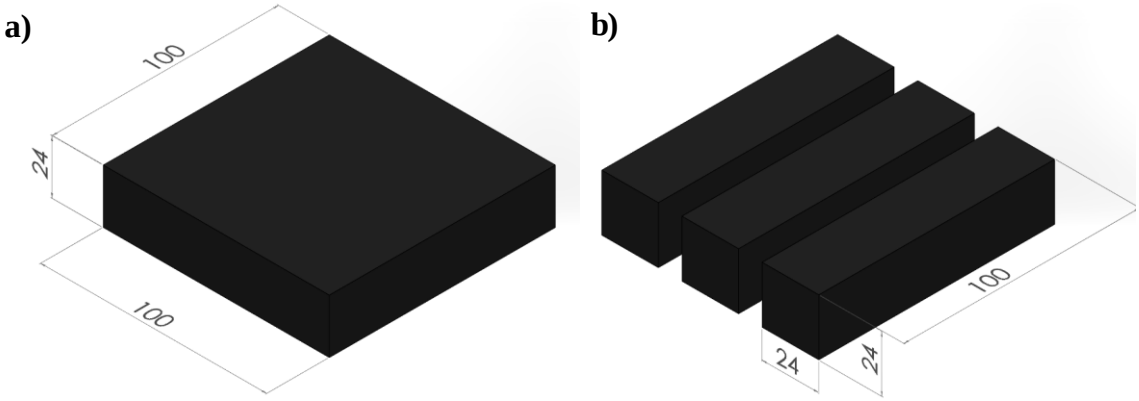

Figure 5.5: Sectioning diagram for manufacture of ligament material test samples showing a) original nominal dimensions of supplied material and b) prepared samples for experimental testing.

Samples were sectioned using a ceramic tile cutter fitted with a 2 mm cutting disk. Firstly, a thin strip of material (5 mm) was removed from one edge of the material block

to provide a flat surface. This surface provided a reference face from which additional cuts are measured and also a loading/support surface for the flexural sample. Three further cuts are made 24 mm apart on each material block to produce the flexural samples. A total of 626 flexural samples were manufactured using this method. The experimental configuration for the three-point testing of ligament material is shown in Figure 5.6. Note that the support span was set to 70 mm.

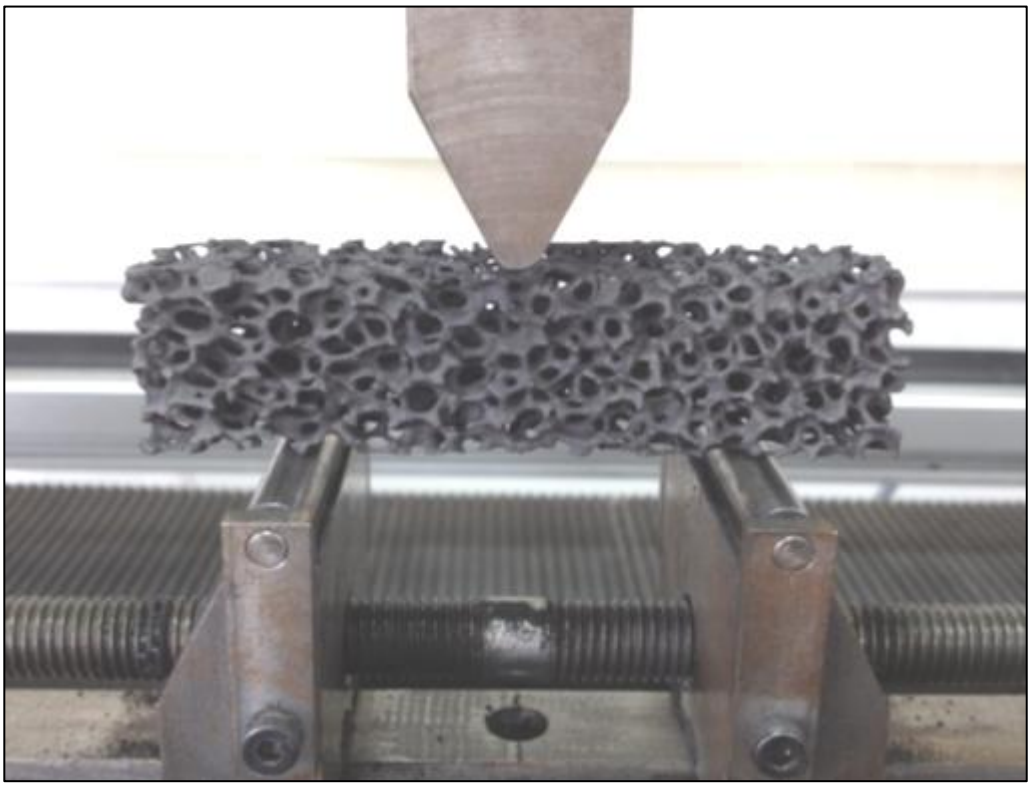

Figure 5.6: Three-point bend experimental configuration for ligament material.

The structure and thicknesses of the individual ligaments varies as a result of the manufacturing process which contributes to a deviation in sample 'bulk density' (ρ) (*i.e.* the material contained within the 100 x 24 x 24 mm bulk volume). The bulk density of the samples is determined by weighing them prior to testing (*i.e.* ρ = mass/bulk volume). The average bulk density of the flexural samples was 0.269 gcm^{-3} with a standard deviation of 0.014 gcm^{-3}. Due to the ligament structure, the bulk density is very low, which is highlighted by the estimated average 'porosity' value of 88 %.

5.3. Experimental Results

Details regarding the quantity of samples and geometric factors for all the experimental testing of is summarised in Table 5.3.

Table 5.3: Summary of details for the experimental testing of three different materials.

Material	Experimental Test		Number of Samples	Dimensions (mm)
EY9 graphite	Ball on three ball	Ø 27 mm	300	Ø 27 x 2
		Ø 67 mm	298	Ø 67 x 4
Glass slide	Three-point bend		523	76 x 26 x 1
Ligament material	Three-point bend		626	100 x 24 x 24

5.3.1. Graphite Ball on Three Ball

Biaxial flexural strength for the ball on three ball samples was calculated using the solutions given by Pagniano *et al.* (2005). Strength data for the Ø 27 mm and Ø 67 mm batches in presented in Table 5.4.

Table 5.4: Strength data for ball on three ball testing of EY9 graphite.

Sample Geometry	Strength (MPa)			
	Mean	Standard Deviation	Minimum	Maximum
Ø 27 mm	12.33	0.91	9.81	15.18
Ø 67 mm	15.66	1.72	11.31	20.71

Strength distributions for the two sample dimensions are shown in Figure 5.7 along with corresponding normal distributions. Normal distribution curves for both sample geometries are plotted using respective mean and standard deviation data.

Although both data sets do include a number of 'weak' samples, the frequency of these is not statistically significant when attempting to identify disparate mode failures. Indeed, further analysis of the data reveals that only 2.67 % of the Ø 27 mm and 1.34 % of the Ø 67 mm samples demonstrated strength values less than $\mu - 2\sigma$. A data set that conforms to a typical bell curve would anticipate 2.1 %, whilst a disparate flaw population would be expected to account for approximately 4 % of failures (Maul *et al.*, 2010). Interestingly, the data set for Ø 27 mm demonstrates a statistically significant

number of samples, 6.33 %, above $\mu + 2\sigma$. This observation could potentially be due to sample thickness or diameter since it has been demonstrated that the B3B test is sensitive to changes in geometric factors (Kipling *et al.*, 2010).

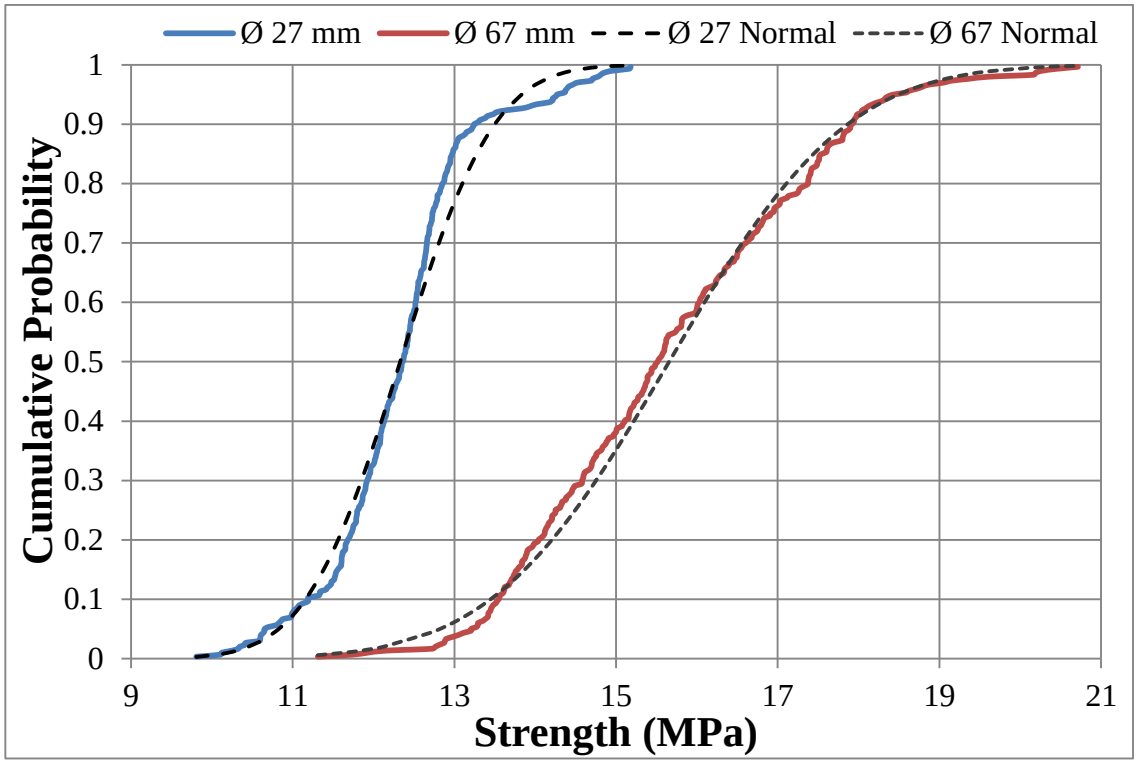

Figure 5.7: Cumulative probability distribution and corresponding normal distributions for strength of EY9 samples tested in B3B configuration.

This data suggests that the prominence of disparate flaws is insufficient to be observed. These distributions may be a consequence of a number of different factors (or a combination of factors):

- Material. The fine grained microstructure of EY9 graphite may not contain a sufficient number of potential defects to cause a significant number of premature failures.
- Experimental method. The B3B experiment only stresses a small volume of the sample, thus reducing the probability that a disparate flaw is contained within the high stress region.
- Manufacturing method. Significant efforts were taken to prevent any surface defects occurring during sample preparation. Manufacturing defects may be considered to be disparate flaws when interpreting a failure distribution curve. It

is likely that the manufacturing process of these samples did not introduce any significant flaws that would appear as a disparate flaw population.

Comparisons between normalised data for the two geometries indicate an increased strength for the larger samples (Figure 5.8). This is contrary to the expected relationship that suggests an increase in sample volume leads to a lower strength due to a greater probability of critically oriented flaws in the material. Possible explanations for this observation relate to the sample geometry and the biaxial test configuration.

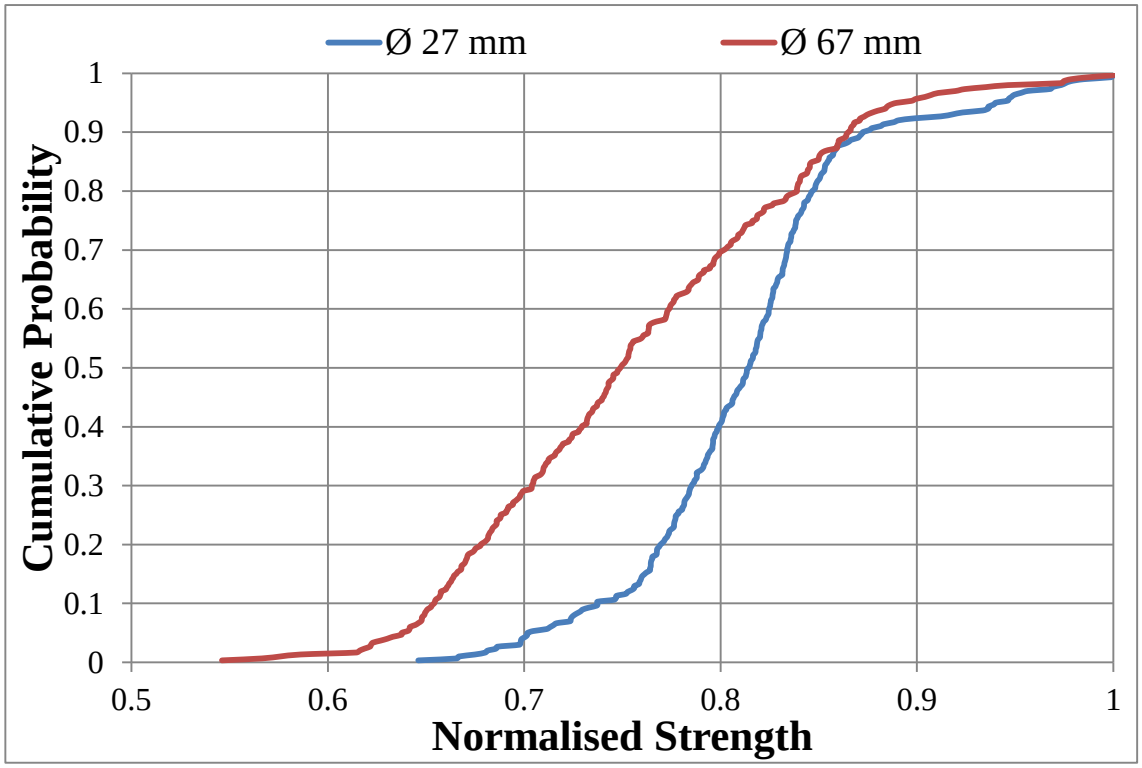

Figure 5.8: Cumulative probability distribution for normalised strength of EY9 samples tested in B3B configuration.

Sample strength derived using the B3B method is dependent on the sample geometry. Indeed, the test has been shown to have geometric limitations regarding diameter and thickness dimensions. Samples with geometries that exceed these limitations do not yield valid strength values (Kipling *et al.*, 2010). Although these geometries were chosen to ensure valid flexural results were obtained, it is important to recognise that strength values attained using this experimental method are intrinsically linked to the respective sample geometry. The larger geometry batch shows more significant

variation in determined sample strengths. This is demonstrated by the larger relative standard deviation which is approximately 11.0 % of the mean strength, whereas, the data from the smaller samples have a standard deviation that is approximately 7.4 % of the mean strength. Larger specimen volumes may contribute to this increased variability since they are more likely to contain critically oriented flaws that contribute to fracture.

Fracture is initiated at the tensile surface of the samples and causes the sample to break into two or three pieces. The fracture of samples is not consistent as three different fracture patterns are observed in both the Ø 27 mm and Ø 67 mm samples. These observations are typical of the B3B test and similar results are presented in Easton (2007) and Kipling (2008) for graphite as well as in alumina by Börger *et al.* (2002) and Jeong *et al.* (2002). Examples of the three fractured samples are presented in Figure 5.9.

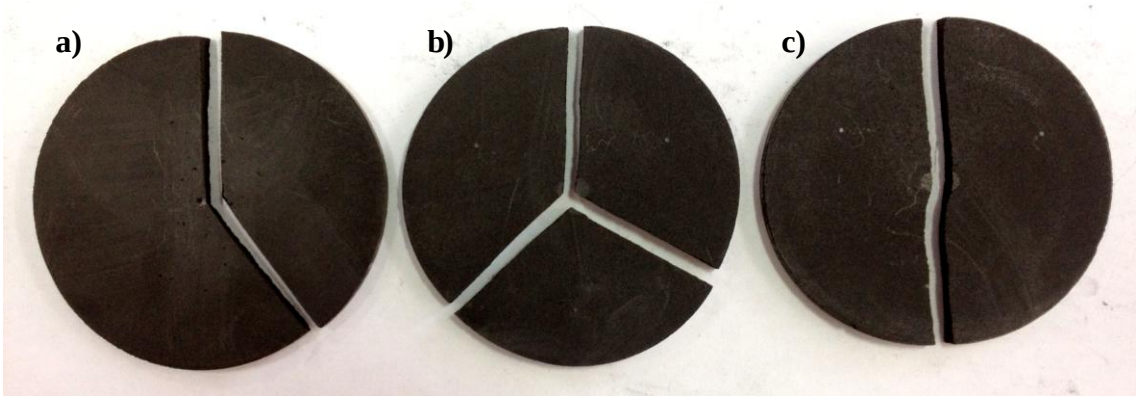

Figure 5.9: Three examples of fractured biaxial samples, a) sample fractured into two unequal pieces, b) sample fractured into three roughly equal pieces (approximately 120^{o} each) and c) sample fracture into two roughly equal halves.

Two contrasting load-deflection responses were observed for the B3B configuration as shown in Figure 5.10. The samples would either fail instantly from a peak load or undergo sub critical cracking before further extension and finally sample failure. Instant failures are associated with samples that fracture into two halves (*e.g.* Figure 5.9 (c)) when crack propagation through the sample is continuous. This is also observed when samples fail into three equal pieces since crack initiation occurs at the centre of the tensile surface and propagates in three directions simultaneously (Figure 5.9 (b)).

Sub critical fractures are due to the crack being interrupted (*e.g.* when samples break into unequal pieces Figure 5.9 (a)). In this scenario, the crack first extends from the centre to the edge of the sample in one direction. An increased displacement is then required to causes additional crack extension in a separate direction (usually ~120^{o} from the initial failure).

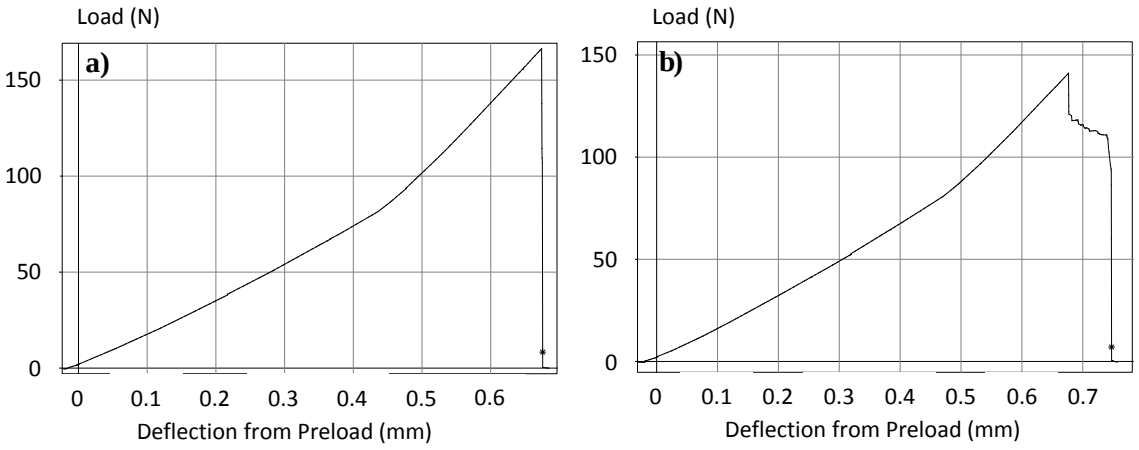

Figure 5.10: Typical load-deflection plots for the ball on three ball experimental configuration showing a) fast fracture from peak load and b) post peak extension**.**

Flexural strength of EY9 is given in literature as being 13.1 MPa (*e.g.* Cowlard *et al.*, 1967). Biaxial strengths are typically considered to be less than than uniaxial (Brocklehurst (1977) states that $\sigma_{\text{Biaxial}} \approx 0.85\sigma_{\text{Uniaxial}}$) which would suggest calculated B3B strengths in the range 11.14 to 13.1 MPa. Taking into account this expected relationship, the Ø 27 mm samples compare very favourably with the literature in having an average biaxial strength that is approximately 94% of the uniaxial strength. The larger samples do not conform to this relationship since the calculated biaxial strength is greater than the uniaxial strength from the literature. This does not necessarily indicate an invalid biaxial test since the apparent strength of these samples is a function of the geometry, as previously discussed. As such, this apparent discrepancy indicates that this geometry does not allow for a direct comparison between the published uniaxial and biaxial strengths. Similar observations were made by Börger *et al.* (2002) when comparing the uniaxial and biaxial strength of alumina. When considering this discrepancy it is important to consider the relative geometries and experimental configurations from which the uniaxial data is derived. This information is not provided by the author and therefore it is not possible to definitively identify a relationship.

5.3.2. Glass Three-Point Bend

Typically, fracture of the glass slides was initiated at the tensile surface into two roughly even halves. Due to the relative homogeneity (*i.e.* in comparison to graphite) the observed fracture path of the samples was consistent. An example of a failed sample is shown in Figure 5.11.

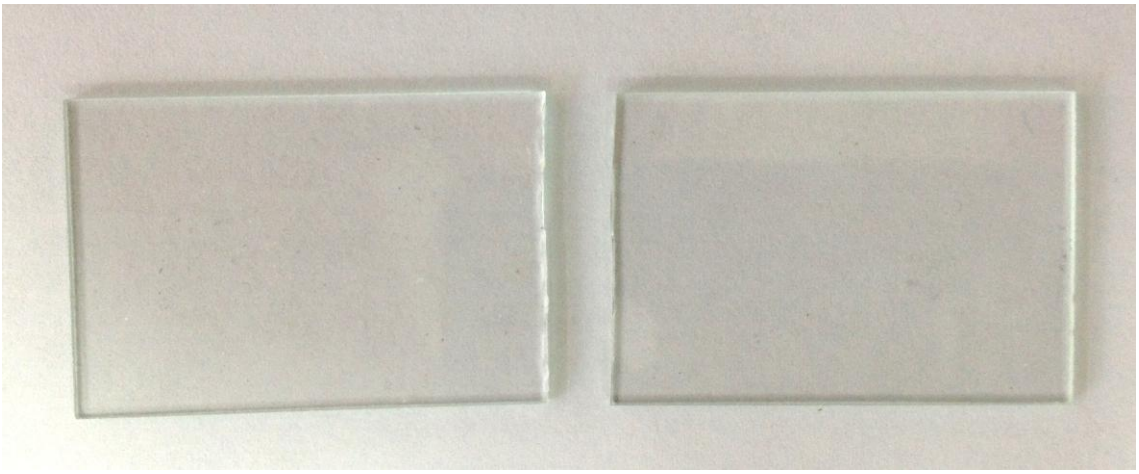

Figure 5.11: Fractured glass slide sample tested in three-point flexural configuration.

The failure distribution data is shown alongside a plotted normal distribution curve in Figure 5.12. Mean flexural strength of the 523 glass slides was 99.97 MPa with a standard deviation of 17.51 MPa. Since mechanical data for the glass slides was not available the determined strengths cannot be compared to published values. Strength values for the glass slides demonstrates a very close fit to the normal distribution curve, albeit, over a wide spread of data. This large variation in strength is likely due to the surface quality of the glass (Holloway, 1968). Although defects in the material are small (in order to maintain optical transparency), their influence on the fracture strength is exacerbated by the geometry of the samples (*i.e.* thin slides). Additionally, the most probable source of such defects is the manufacturing process, which will introduce surface flaws which can have a significant effect on the strength. Strength of glass slides is not imperative to the manufacturer and as such they are likely to disregard mechanical consistency in favour of optical properties and ease of manufacture. Indeed, although the slides were produced by the same supplier, manufacturing conditions may vary between batches, thus inducing further variations in mechanical properties.

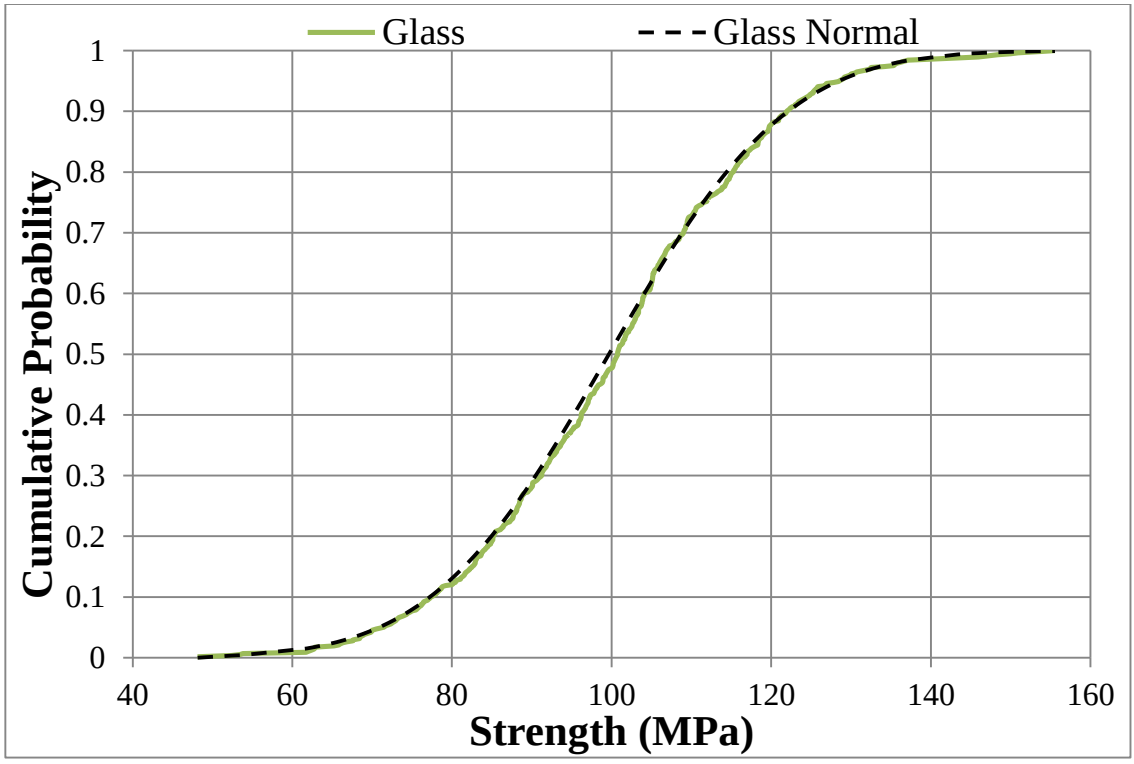

Figure 5.12: Cumulative probability distribution and corresponding normal distribution for glass slides testing in three-point bend configuration.

5.3.3. Ligament Three-Point Bend

Bulk strength of the ligament material is defined as the required stress to initiate failure of the flexural sample. These strength values take into account large voids in the material and are not necessarily representative of the individual ligaments. Mean bulk strength for the ligament material was 0.59 MPa with a standard deviation of 0.095 MPa (Figure 5.12). Although this strength data is extremely low compared to the previously described graphite and glass samples, it is important to consider the effect of 'porosity' on the material. Increases in porosity generally result in a decrease in strength, thus accounting for the low strength ligament material. The difference in strength between the three materials is not a concern since it is the relative distribution of sample failures that is primarily of interest. Bulk fracture of the samples was typical of a heterogeneous flexural test. Failure was initiated at the tensile surface and exhibited a tortuous fracture path through the sample, as shown in Figure 5.13. Crack path tortuosity is likely to be dictated by the path of least resistance, which for this material is determined by the weakest ligaments.

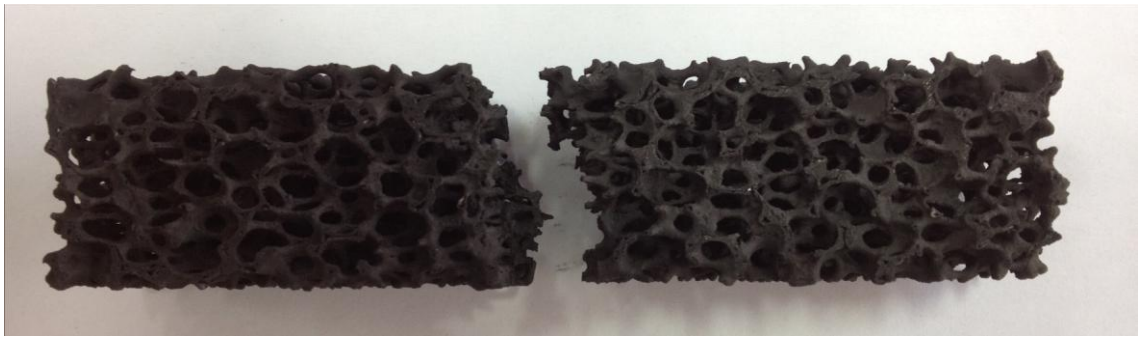

Figure 5.13: Example of a fractured ligament sample tested in three-point flexural configuration. Note the tortuous crack path through the structure.

The cumulative failure probability graph for the ligament material is shown along with a normal distribution curve in Figure 5.14.

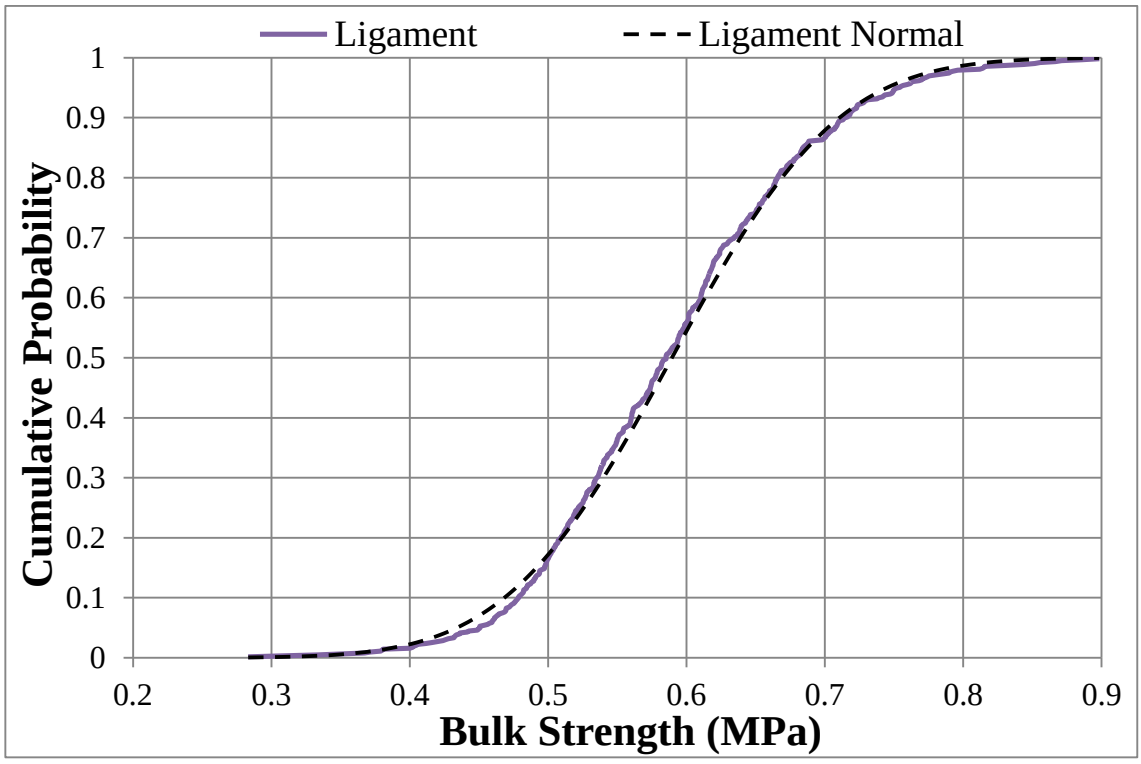

Figure 5.14: : Cumulative probability distribution and corresponding normal distributions for ligament material tested in three-point bend configuration.

The cumulative bulk strength distribution for the ligament material demonstrates a close fit to the normal distribution curve. As is perhaps expected from a material with such a varied structure, there is a very wide spread of bulk strength values with the 'weakest' sample having a strength that is less than 32 % of the 'strongest'. Although this data set contains a number of samples that fail at very low stresses (relative to the mean), the

frequency is not significant enough to suggest the presence of a disparate failure mode. Additionally, a number of samples record a high strength which suggests a highly spread normal distribution of failures. The extreme structural variations in the ligament material increase the likelihood of disparate flaws which could contribute to premature failure of the material. However, in this structure, disparate flaws may be physically represented by critically oriented weak ligaments rather than large pores. As such, the opposite is also true; in that critically oriented 'strong' ligaments may contribute to bulk failure at higher stresses. Such a hypothesis is consistent with the observed data and would also account for the apparent normal distribution. The primary factor that dictates the bulk strength of the material is the ligament structure. If the strength of individual ligaments is considered to be constant, then it follows that thicker ligaments will contribute to higher bulk strengths. Since the volume remains constant between samples, the bulk density give a reasonable indication of the ligament thickness (*i.e.* samples with thicker ligaments contain more material and thus have a higher bulk density). The relationship between bulk strength and sample weight is shown in Figure 5.15.

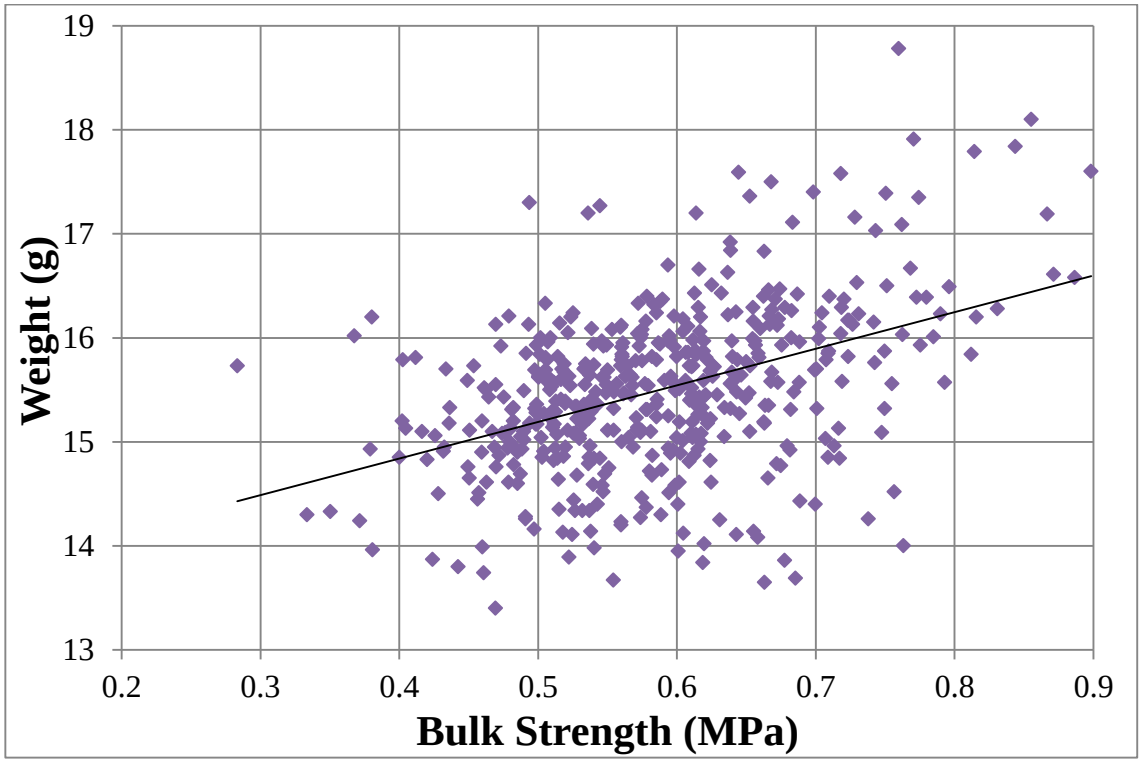

Figure 5.15: Relationship between sample weight and bulk strength.

The calculated Pearson's correlation coefficient for this set of data is 0.434, which suggests a moderate positive correlation between sample weight and bulk strength (Rodgers *et al.*, 1988). This relationship is expected since heavier samples contain more material and as such are likely to require a greater load to cause failure. The large spread of this distribution is indicative of the highly variable material structure. Although samples with higher bulk densities are likely to contain thicker ligaments, this is not the only factor that determines the bulk strength. Additionally, localised concentrations of material or the orientation of ligaments could affect the bulk strength. For example, a sample with a localised concentration of material at the tensile surface could result in high bulk strength for a sample with a relatively low bulk density. Typically, the failure mechanism for the flexural testing of ligament material was fast fracture. Samples would generally reach a peak load before failing catastrophically. However, the low strength of the ligament material and the variability in the structure caused pre peak failures (*i.e.* micro-cracks) which were observed in all the samples. The extent of micro-cracking varied significantly between samples in terms of both quantity and severity. Micro-cracking in this structure primarily occurred as a consequence of compressive forces acting on the loaded surface and some samples did demonstrate an 'indent' at the contact point. Such samples required a greater deflection to failure; however, catastrophic failure did still occur when peak load was reached. Two contrasting examples of sample load-deflection plots are shown in Figure 5.16.

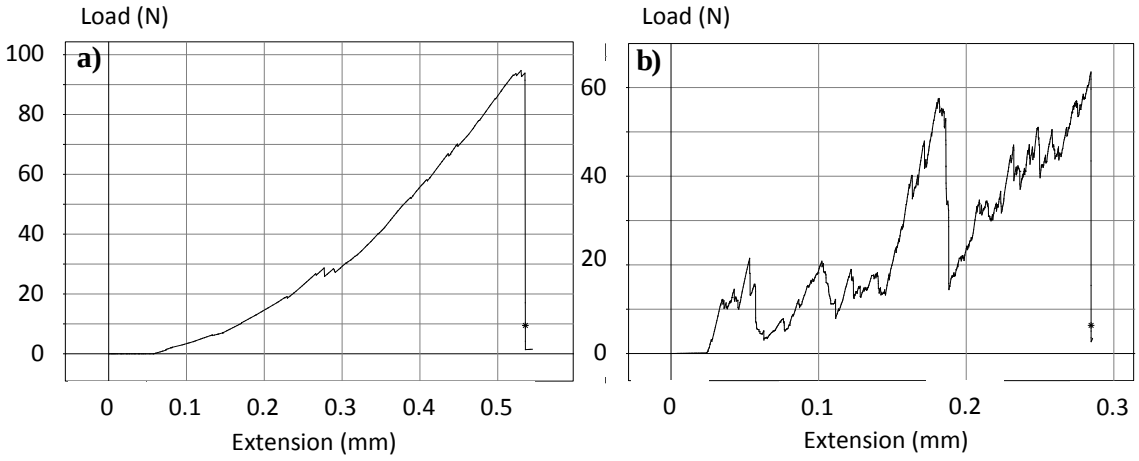

Figure 5.16: Examples of load-deflection plots for ligament material showing a) a sample that experiences minimal pre peak micro-cracking and b) a sample that has significant sub critical failures prior to fracture.

5.3.4. Relative Comparisons

Normalising data from each test enables a comparison between materials. Figure 5.17 shows the normalised strength distribution data form the two graphite geometries, glass slides and ligament material on a single plot.

EY9 showed the least variation in failure strength with the Ø 27 mm samples deviating less than the Ø 67 mm samples, as previously discussed. Although these samples appear to be the most 'consistent' there is still a significant variation with the minimum recorded strengths for the Ø 27 mm and Ø 67 mm samples being approximately 65 % and 55 % of the maximum values respectively.

Initially, expectations regarding the glass failure data were that it would demonstrate less variation than graphite due to the relative consistency of the glass structure. It is not suggested that glass is free from microstructural flaws; however, the potential for defects of varying sizes and orientations is considered to be greater in graphite than a 'fully dense' material. This hypothesis does not take into account the relative effect of flaws on the respective samples. Flaws, such as inclusions or surface scratches in the glass have a greater effect on the strength of the samples due to geometry of the samples. Shallow surface scratches or small inclusions may account for a substantial proportion of the sample depth and thus their influence on the strength is more significant than in thicker samples (*e.g.* the graphite samples). Additionally, surface defects introduced during manufacture are minimised in graphite samples though careful preparation.

Normalised cumulative probability curves show greater variability in the ligament material than in the graphite. This observation is likely due to an increased potential for variability in the ligament structure. Interestingly, the glass slide and ligament material data show similar distributions with regards to cumulative failure probabilities and the range of normalised strengths. Possible reasons for the dispersed nature of these distributions have been discussed individually.

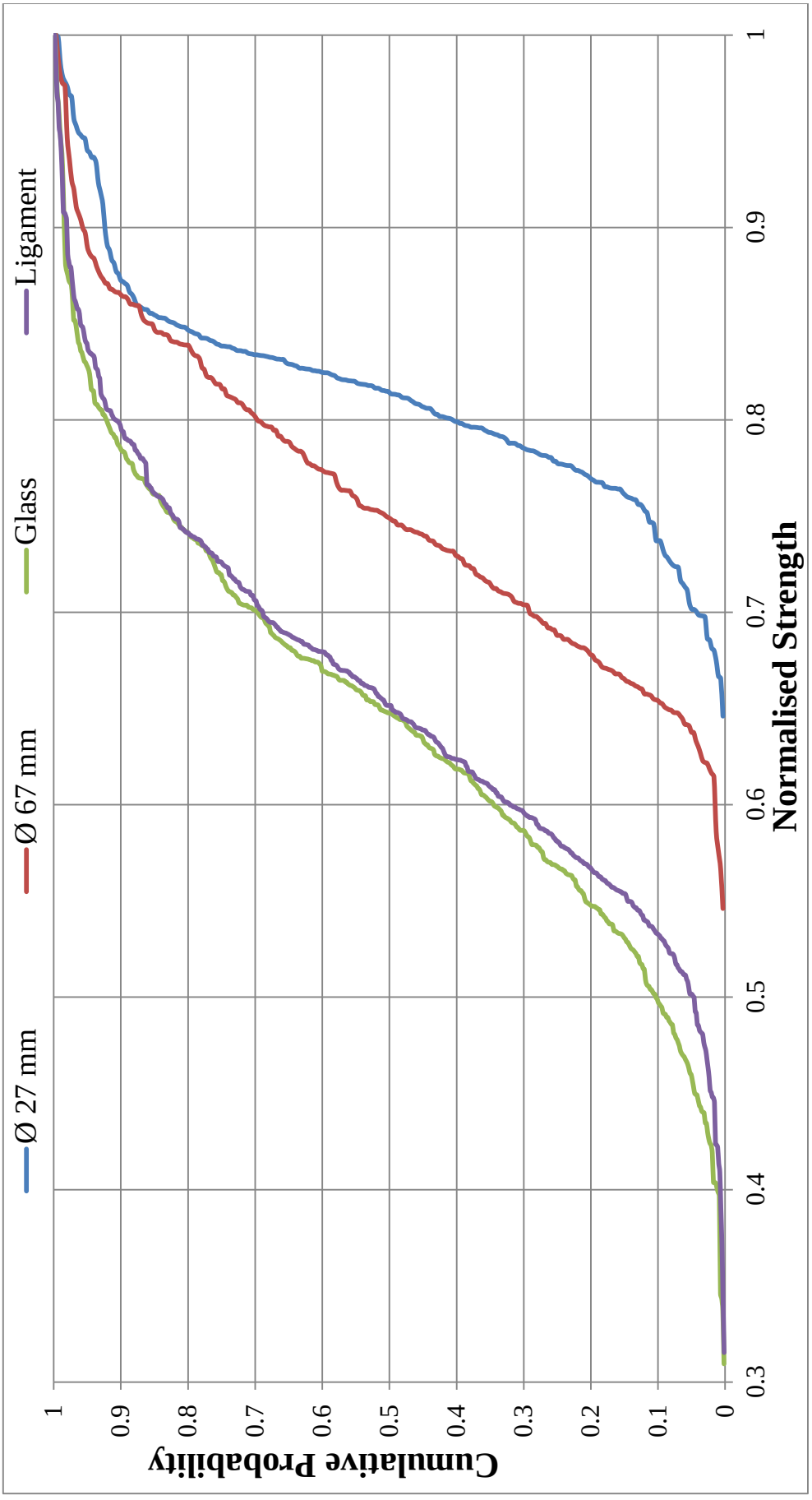

Figure 5.17: Normalised strength data for three different materials.

Comparisons of the frequency and percentage of samples that failed two standard deviations away from the mean strength are shown in Table 5.5. Note than for a normally distributed data set the proportion would be expected to be 2.1%.

Table 5.5: Frequency of samples failing two standard deviations away from the respective mean strength value.

Material		Mean (MPa)	Standard Deviation (MPa)	μ-2σ			μ+2σ		
				Range (MPa)	Freq.	%	Range (MPa)	Freq.	%
EY9	Ø 27 mm	12.33	0.91	< 10.51	8	2.67	> 14.15	19	6.33
	Ø 67 mm	15.66	1.72	< 12.22	4	1.34	> 19.1	8	2.68
Glass		99.97	17.51	< 64.95	10	1.91	> 135.0	13	2.49
Ligament		0.59	0.095	< 0.4	10	1.60	> 0.78	17	2.72

As demonstrated by the data in this table, the only experiment that showed a statistical significant number of samples failing at $\mu \pm 2\sigma$ was the high strength Ø 27 mm EY9 samples which were discussed earlier in this chapter. Relevant ranges in the other distributions were between 1.34 and 2.72 % of the sample batch. These proportions show little deviation from the expected 2.1 % and are not as significant as the 4 % 'outlier' population identified in literature (Maul *et al.*, 2010). This provides further evidence to suggest that a disparate flaw population is not observable in any of the experimental tests. Relative comparisons between $\mu - 2\sigma$ and $\mu + 2\sigma$ data also reveals that there is greater probability of failure at the high end of the distribution which is contrary to the effect expected of a disparate flaw population (Hindley *et al.*, 2012)

5.4. Determination of Mechanical Properties for Application to Models

In addition to the failure distributions described in this chapter, a number of experimental tests were undertaken to determine suitable parameters (*e.g.* strength values and representative deviations between samples) for computational models. In addition, these tests should give a broad indication as to what should be expected from the model simulations in terms of mechanical performance. Samples from six of these tests were prepared for microstructural characterisation through optical microscopy (discussed in detail in Section 6.3). Each test specimen had a square cross sectional area with sides of approximately 15 mm and an overall length of 100 mm. Flexural

samples had a support span of 70 mm. Compression samples were manufactured from the broken flexural tests and had an overall height of 37.5 mm. A total of 12 three-point flexural tests (13 sample were tested however, one was found to have a pre-existing crack and was therefore excluded from analysis) and 18 compression tests were undertaken. Experimental configurations for the flexural and compression tests are shown in Figure 5.18.

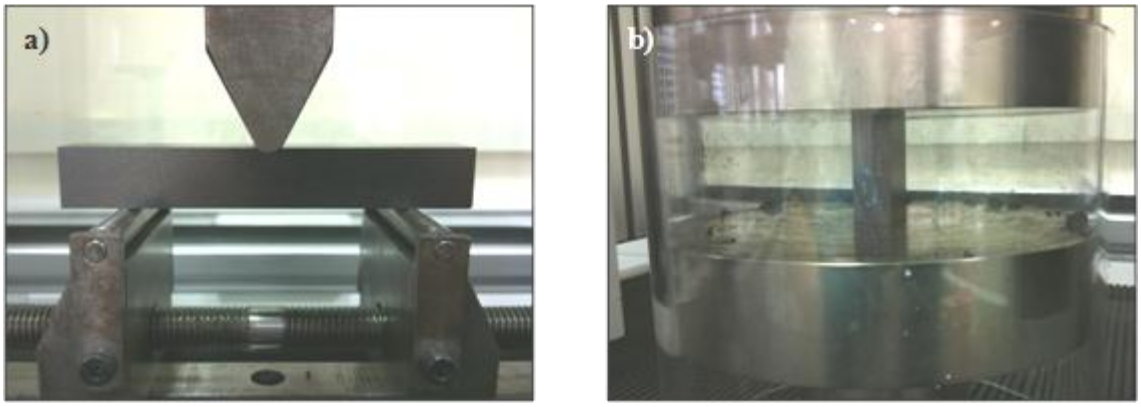

Figure 5.18: Experimental configurations for a) three-point bend and b) compression test.

Table 5.6 shows the average strength values for the 12 valid flexural tests and 18 compression tests along with the strength data for each of the six samples. Note that the compression test for sample one was invalid so is not included in the data table or average values.

Table 5.6: Flexural and Compression test results for IM1-24.

Sample	**Strength (MPa)**	
	Flexural	Compression
1	34.45	N/A
2	28.58	74.85
3	30.86	76.53
4	31.09	78.35
5	27.97	75.59
6	28.14	75.09
Mean	31.19	77.02
Standard Deviation	2.49	3.97

The experimental load-deflection plots for the 12 flexural samples are shown in Figure 5.19. These plots effectively demonstrate the variations in both peak load and deflection to failure for the flexural tests.

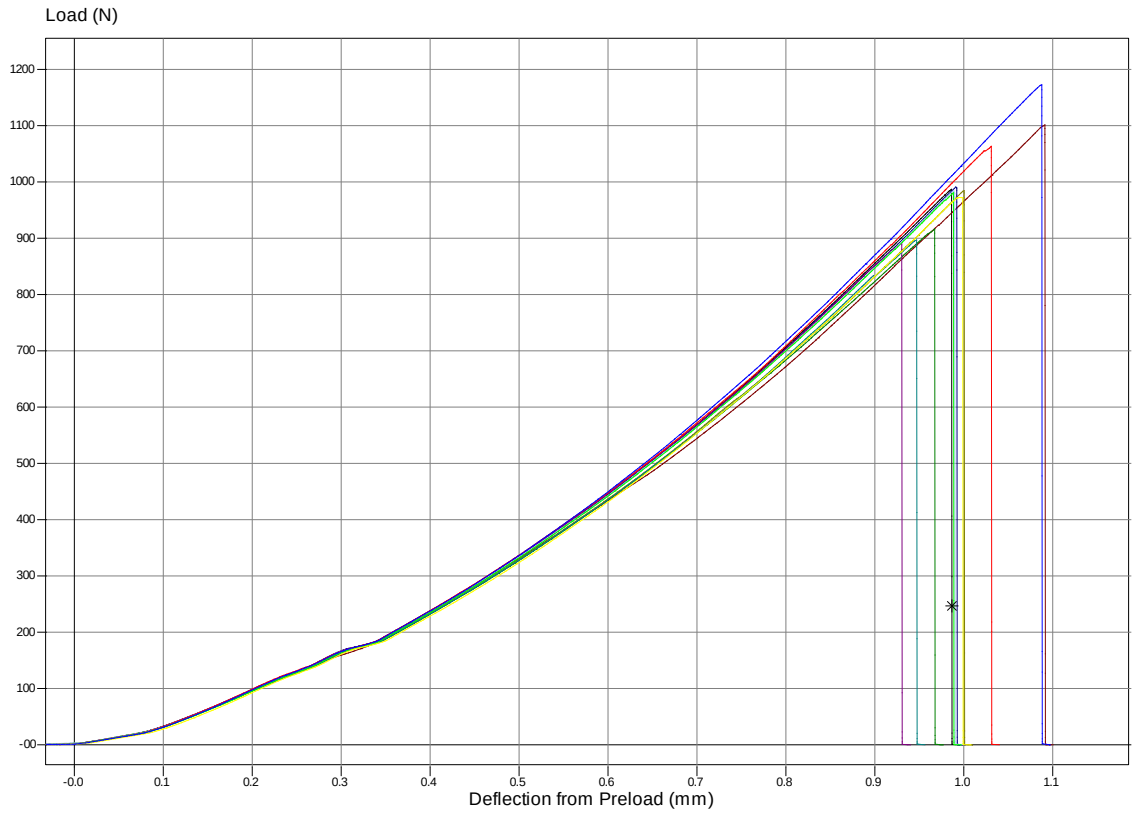

Figure 5.19: Load-deflection plots for twelve three-point bend flexural tests.

Experimental determination of mechanical values may prove to be useful in determining modelling parameters; however, it is important to consider the relative differences between experimental testing and computational predictions. Strength values from these experiments only apply to the bulk material, that is, with the inclusion of porosity. Therefore, it cannot be directly integrated into models as a threshold for predicting mechanical performance. For example, if crack propagation though the model was dependent on a critical stress criterion, individual elements would 'fail' at a higher stress than that determined though experimental testing since they are effectively free from porosity. However, determination of computational 'bulk' strength that takes into account the whole model would be expected to demonstrate similar strength values and standard deviations to the experimental data.

5.5. Chapter Summary

This chapter has presented the considerations associated with the development of an experimental testing programme. The choice of material and selection of experimental methods was individually justified in an attempt to identify how the microstructure affects the strength distribution. The primary consideration for all experiments was the ability to test a large number of samples in order to better characterise the strength distributions.

EY9 was selected as a suitable grade of graphite due to its relatively fine microstructure. This minimised the possibility of surface flaws during manufacture and ensured that strength distributions were representative of the material and experimental configuration. Graphite was tested in ball on three ball configuration since this increased the probability that a flaw would be critically oriented to the applied stress and would thus increase the likelihood of identifying disparate mode failures. Additionally, this configuration allowed for large numbers of samples to be manufactured with consistent dimensions. Strength distributions for graphite showed close agreement with a normal distribution and did not provide any conclusive evidence for disparate mode failures, despite a number of samples recording relatively low strengths. This distribution did however, demonstrate the variability of graphite when characterising large quantities of material. These observations are likely due to number of factors, namely, the small stressed volume in the sample, material selection and sample preparation. The B3B test was selected to allow a large number of samples to be tested, a critical consideration for this experimental programme due to the low probability of disparate mode failures. However, this test only stresses a relatively small volume of the material, thus decreasing the probability of a flaw being located in the high stress region. Alternative methods (*e.g.* tensile test) would stress larger volumes of material (relatively), however, complexities relating to sample preparation and testing would limit the number of samples and reduce the consistency as well as increasing the probability of manufacturing flaws. The simplicity of the sample geometry combined with careful manufacture of samples limits surface defects caused by machining. These defects could be interpreted as a potential source of disparate flaws and are limited in this experimental programme.

Glass microscope slides were tested in three-point flexural configuration to determine the failure distribution of a material with a more continuous microstructure than that typically associated with graphite. Microscope slides were selected due to their availability and consistent geometry. Cumulative probability curves for glass showed a close fit to a normal distribution. The variability in strength was however, very large. This observation may be explained through consideration of the relative effects of flaws within the glass. The effects of defects such as inclusions or surface scratches will be exacerbated in a thin sample and thus result in an extremely variable strength distribution.

Characterisation of a microstructure with potential for extreme variations was achieved through three-point flexural testing of a ligament material. As would be expected from this extreme material, the strength distribution has a large spread. The data was consistent with a normal distribution, suggesting that although there may be some very weak samples within an experimental batch (as a result of critically oriented thin ligaments) there are roughly equal quantities of strong samples (*i.e.* thick ligaments which are critically oriented).

Additionally, a number of experimental tests were undertaken on IM1-24 nuclear graphite to determine parameters for use in computational models. Application of these data is explained in subsequent chapters when discussing the development of computational techniques and associated considerations.

The following chapter will focus on the microscopy of graphite with an emphasis on characterisation techniques. Utilisation of the attained data with regards to the development of representative microstructure will be discussed.

Chapter 6 – Microscopy

Microscopy has widespread applications in numerous research fields (Russ, 1990). When considering engineering material science, its applications can range from quality control to failure diagnosis. An understanding of the material structure can be ascertained through the use of microstructural methods. Some methods relating to the identification of porosity in carbon materials are briefly described in Section 2.4.1. Each microscopy technique is used to view samples of a given size or identify specific features. For this reason, microscopy types tend to be specialised to scientific fields. In the case of engineering material science, optical and SEM techniques are most commonly utilised.

With regards to the application of microscopy techniques in this work, there are two main areas of interest. Firstly, to understand the structure of the materials being investigated and identify microstructural features. Secondly, to quantify these features through image analysis techniques for use in generating data sets, from which, representative models may be developed, which is a key aim of this work. When considering the suitability of microscopy methods, the size of features must be taken into account. Additionally, the size of the sample being investigated and the area of observation that is required are further considerations. Features such as filler particles and macropores in nuclear graphite are generally in the range of micrometres, thereby making optical microscopy a suitable method for identification and analysis in this work. Although smaller scale features will be present in any sample of nuclear graphite, such as meso and micropores, it is beyond the scope of this work to include such small defects in a computational model.

6.1. Optical Microscopy Samples

To ensure quality images, due to the limited depth of field, samples must be prepared to ensure a flat, defect free viewing surface. A correctly prepared sample will preserve a higher level of detail within the microstructure which is critical in obtaining a robust data set for subsequent modelling work.

6.1.1. Sample preparation

Preparation of microscopy samples was based on a standard metallographic methodology devised by Struers Ltd. Samples were first sectioned using a 1.05 mm thick diamond abrasive disk fitted to a Materials Research Microslice 2 cut-off machine. The sample surface was manually smoothed using a polishing wheel with fine silicon carbide paper (1200 grit). Samples were then cleaned in a warm (60°C) ultrasonic bath of distilled water to remove debris from both the surface and any particles that may have accumulated in surface pores. The samples were finally rinsed with distilled water and then ethanol before being dried in an oven at 60°C for two hours. Prior to the polishing process the samples were vacuum impregnated with epoxy resin. Epoxy resin and a hardening agent were mixed together in a container and placed in a Buehler vacuum impregnation chamber. The mixture was out gassed to remove air before being poured onto the samples in the moulds. After the impregnation process the samples and moulds are transferred to a Heraeus Kulzer positive pressure chamber. The chamber is pressurised to between two and three bar to further ingress the resin in to the pores of the materials. This ingression of resin ensures that the pores maintain their structure during grinding and polishing. The moulds are left to harden for at least 24 hours before being ground and polished according to the method outlined in Table 6.1.

Table 6.1: Typical grinding and polishing procedure for graphite samples (based on Struers (2011) and Robinson (2011)).

Step	Process	Surface	Abrasive Size	Force/ Sample (N)	Speed (RPM)	Time (s)	Rotation
1	Grinding	SiC Paper	1200 Grit	20 N	240	Until Plane	Comp.
2	Coarse Polishing	Chemotextile Cloth (Napless)	6 um Diamond Suspension	20 N	120	300	Comp.
3	Fine Polishing	Napped Cloth	1 um Diamond Suspension	20 N	120	60	Comp.
4	Final Polishing	Napped Cloth	0.1 um Colloidal Silica	10 N	120	30	Cont.

The grinding and polishing processes used in the preparation of samples for microscopic examination takes place over four stages. All stages are carried out using a Beuhlar Metaserv Motopol 12 polishing machine. The conditions (surface material, abrasive size, force, speed, time and rotation direction) of each stage are varied to ensure the sample is prepared efficiently and to a high standard. The grinding stage ensures that the sample is level and that the viewing surface will be flat. A complementary rotation direction (*i.e.* both surface and sample holder rotate in the same direction) is used since this is less aggressive than a contrary rotation and is therefore less likely to 'pluck' material from the surface during grind. The coarse and fine polishing stages use a diamond solution and complementary rotation. The short final polishing stage uses a softer solution of silica and a contrary motion (*i.e.* surface and sample holder rotating in opposite directions to each other) to give the best possible finish to the viewing surface.

6.1.2. Examination and Image Capture

The mounted and polished samples are placed on glass slides using a custom press which ensures that the viewing surface is parallel to the microscope stage. Samples are inspected using a Nikon Opiphot-2 optical microscope. Images are recorded using a Q-imaging 3.3 megapixel camera mounted above the microscope.

Images are commonly captured under bright field and polarised light conditions. When compared to bright field microscopy, the use of polarised light can allow for a more quantitative evaluation of the image since the observed effects may be easier to identify and measure. When examining graphite under polarised light, optically anisotropic areas of the structure, such as prismatic edge alignment of basal planes, will appear yellow or blue depending on their orientation to the polariser and microscope optics. If the basal plane orientation is such that it is perpendicular to the light source (*i.e.* it resembles an isotropic structure), it will appear purple regardless of its orientation. This effect is shown schematically in Figure 6.1. Individual crystallites may be too small to be examined due to limitations with regards to the magnification and optics of the microscope. In this case, anisotropic regions may appear a rose colour due to the merging of yellow and blue (Neighbour, 1993).

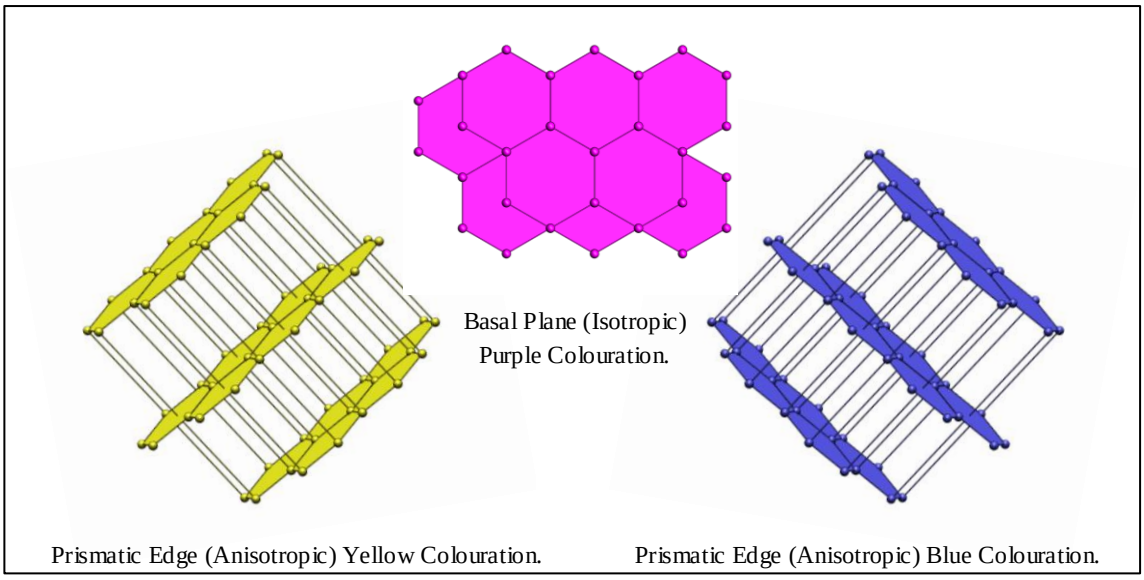

Figure 6.1: Schematic representation of an example interpretation of colours in a graphite microstructure. Colour is dependent on the direction of basal plane alignment (based on Evans, 1978)

Figure 6.2 and Figure 6.3 show the same image of IM1-24 graphite under bright field and polarised light conditions respectively. In addition to allowing isotropic and anisotropic materials to be distinguished from one another, polarisation will give an indication as to the orientation of the material (Bousfield, 1992). If an anisotropic material is rotated under polarised light, a variation in intensity and colour of the reflected light will be observed. Through 360°, the reflectivity of anisotropic material will vary between two extremes, which are called uniradial reflectivities. The difference between these two extremes is called bi-reflectance (Amelinckx, 1997).

Figure 6.4 to Figure 6.9 show graphite under polarised light conditions at various magnifications. Filler particles and large areas of porosity are visible at the lowest magnification, as are some large crystalline areas (blue or yellow isochromatic regions). Increasing the magnification allows the microstructure to be examined in greater detail. Pore shapes and sizes can be more accurately characterised as can individual crystallites.

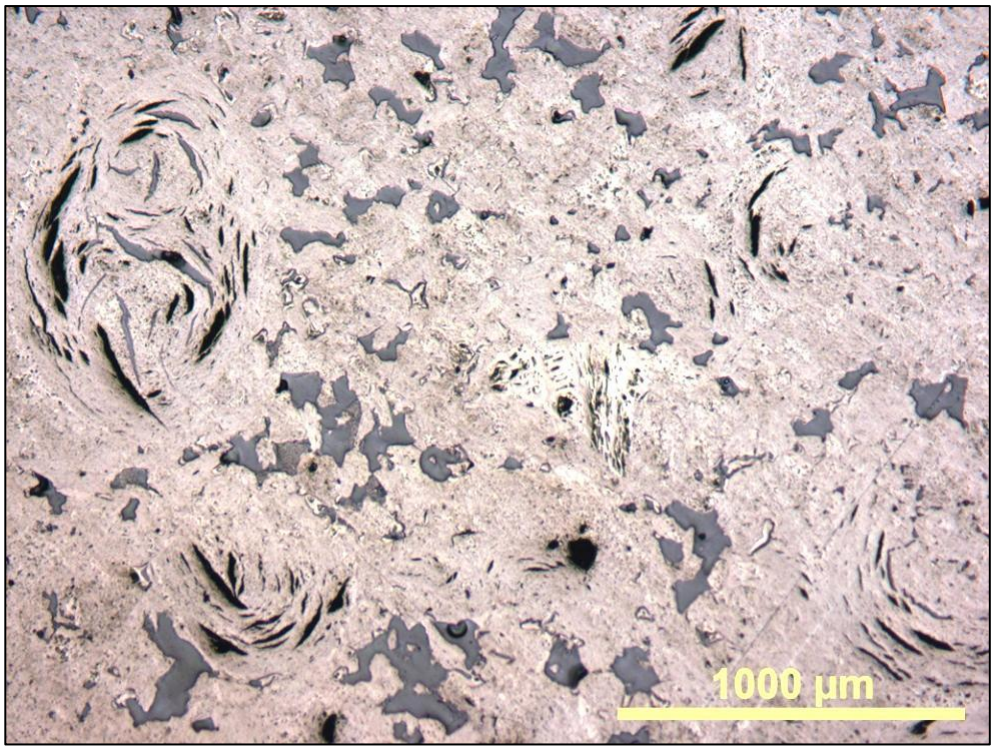

Figure 6.2: Bright field image of IM1-24 nuclear graphite at 50x magnification.

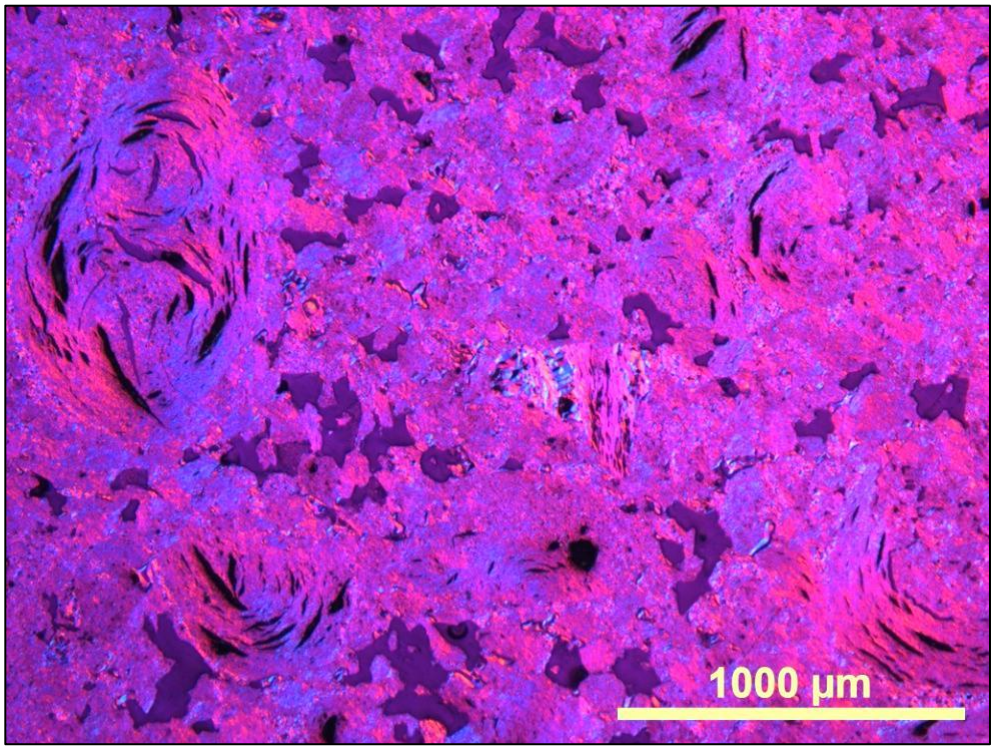

Figure 6.3: Polarised light image of IM1-24 nuclear graphite at 50x magnification.

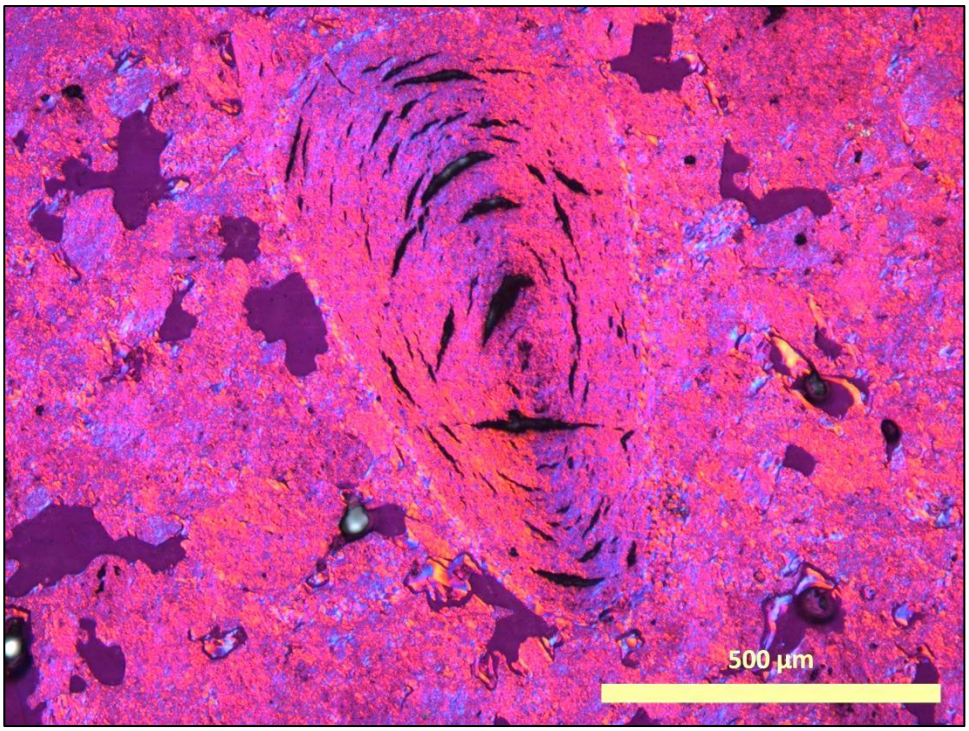

Figure 6.4: Micrograph of IM1-24 graphite at 100x magnification showing a large Gilsocarbon particle is in the centre of the image.

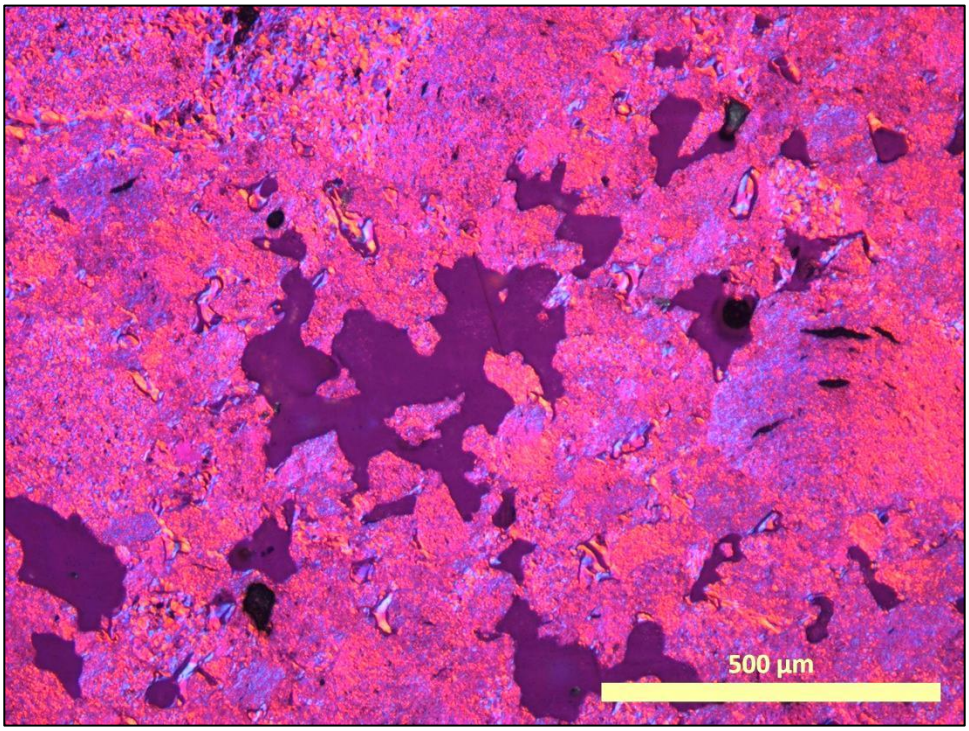

Figure 6.5: Micrograph of IM1-24 graphite at 100x magnification showing of pores (mostly a result of gas entrapment during manufacture) of various shapes and sizes.

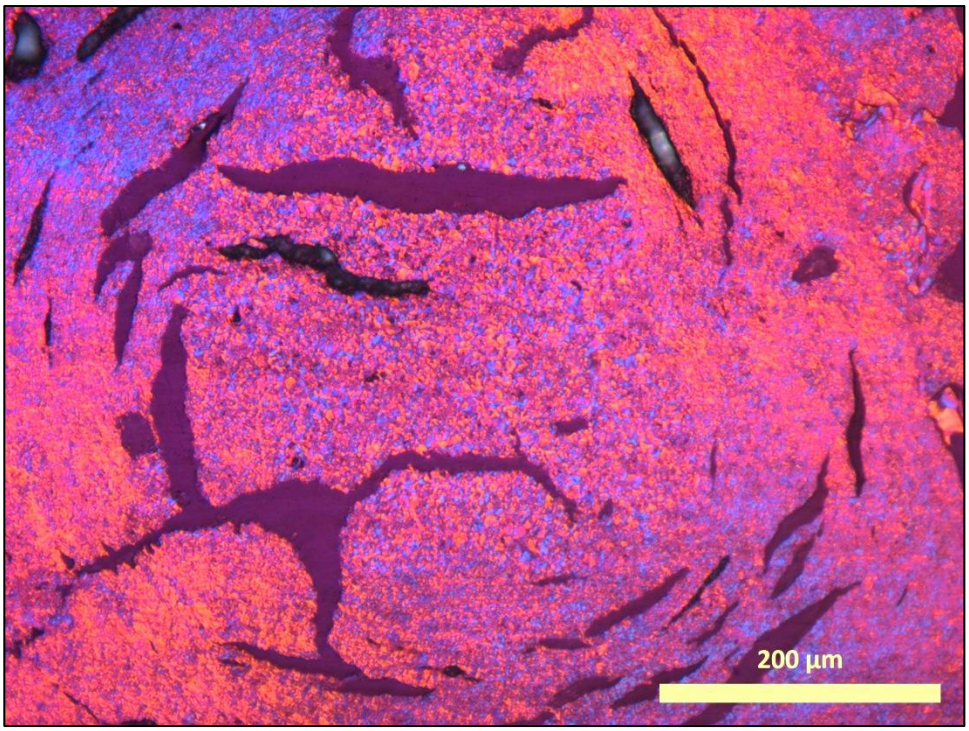

Figure 6.6: Micrograph of IM1-24 graphite at 200x magnification showing the centre of a large Gilsocarbon particle and calcination cracks within the particle.

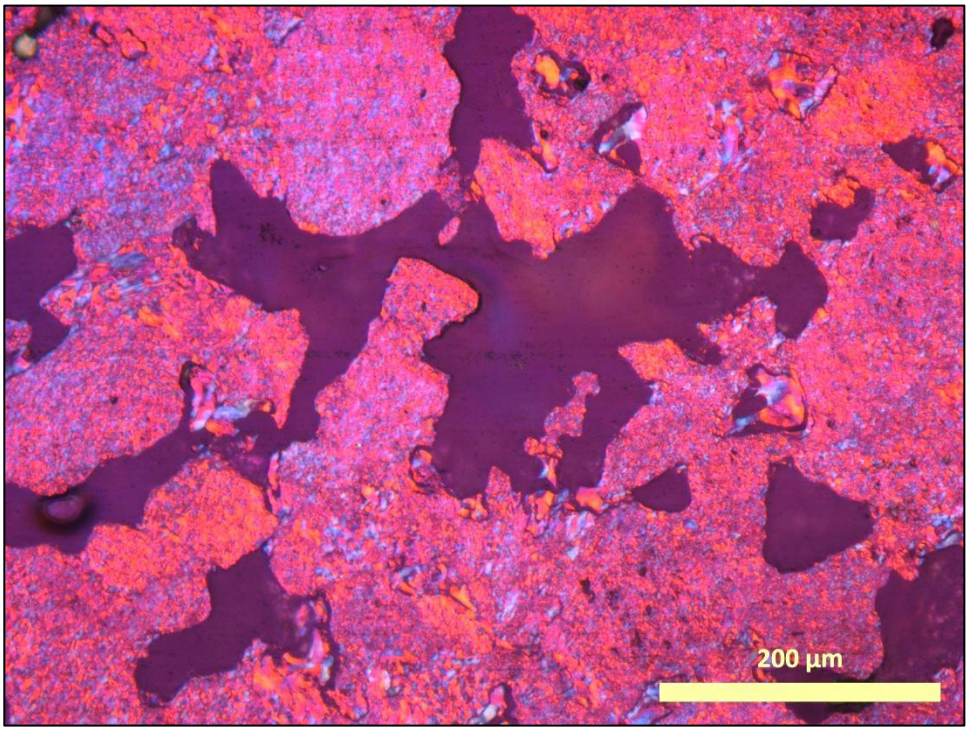

Figure 6.7: Micrograph of IM1-24 graphite at 200x magnification showing porosity of various sizes including a particularly large pore in the centre of the image.

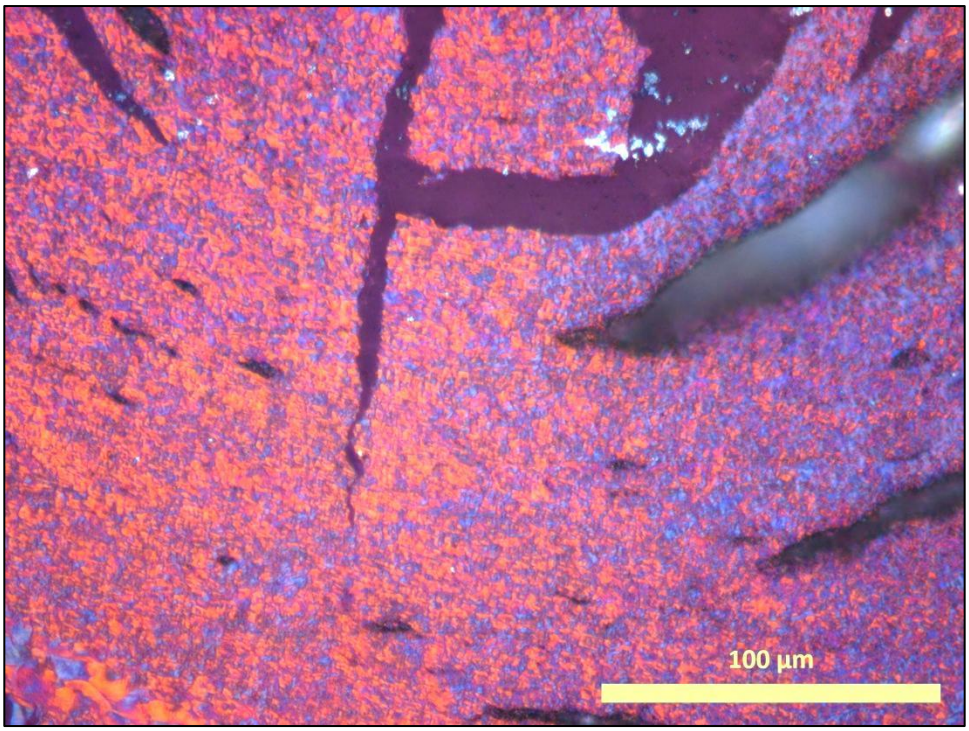

Figure 6.8: Micrograph of IM1-24 graphite at 500x magnification showing part of a Gilsocarbon particle.

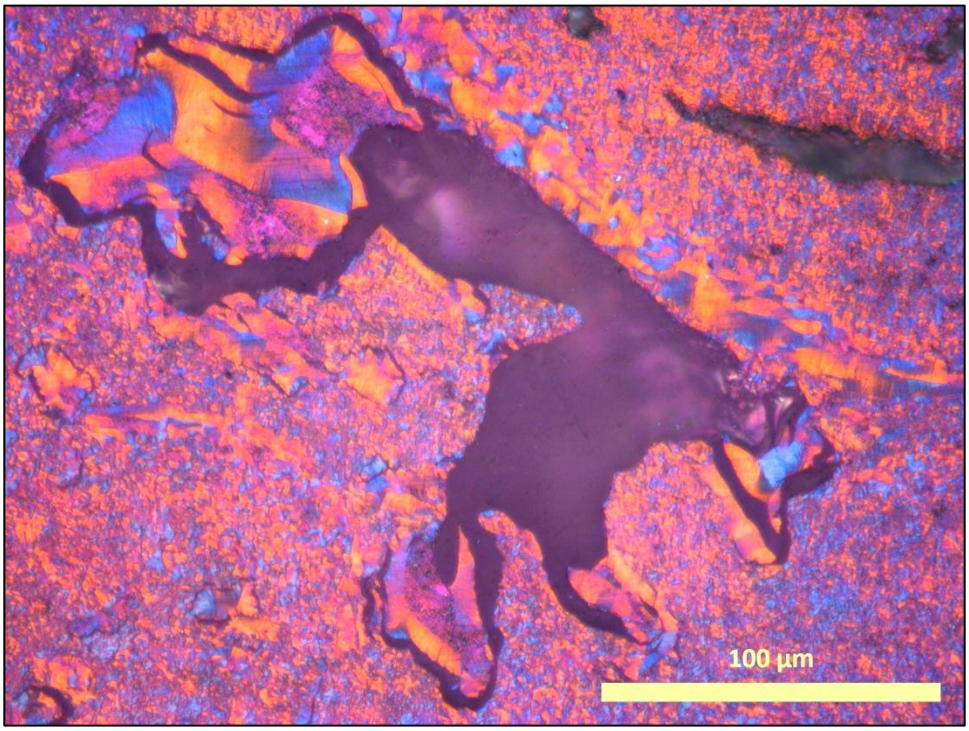

Figure 6.9: Micrograph of IM1-24 graphite at 500x magnification showing a pore surrounded impregnant.

6.2. Image Analysis and Applications to Nuclear Graphite

In the course of this work, an image analysis technique was developed using the software Image Pro Plus 7.0 (IPP), which is used in conjunction with optical microscopy to enable detailed examination of materials. Image analysis refers to the extraction of meaningful information from an image. Quantitative analysis may be carried out on an image that would otherwise be primarily used for qualitative studies. Measurements made using image analysis can be done individually or through thresholding. Individual measurements are manually selected on the image using a variety of inbuilt tools such as length, area, radius *etc*. Thresholding is used to identify and measure a large number of objects and is particularly useful when attempting to characterise a property of the material (*e.g.* porosity). Figure 6.10 illustrates a typical methodology which may be utilised when applying image analysis techniques through thresholding.

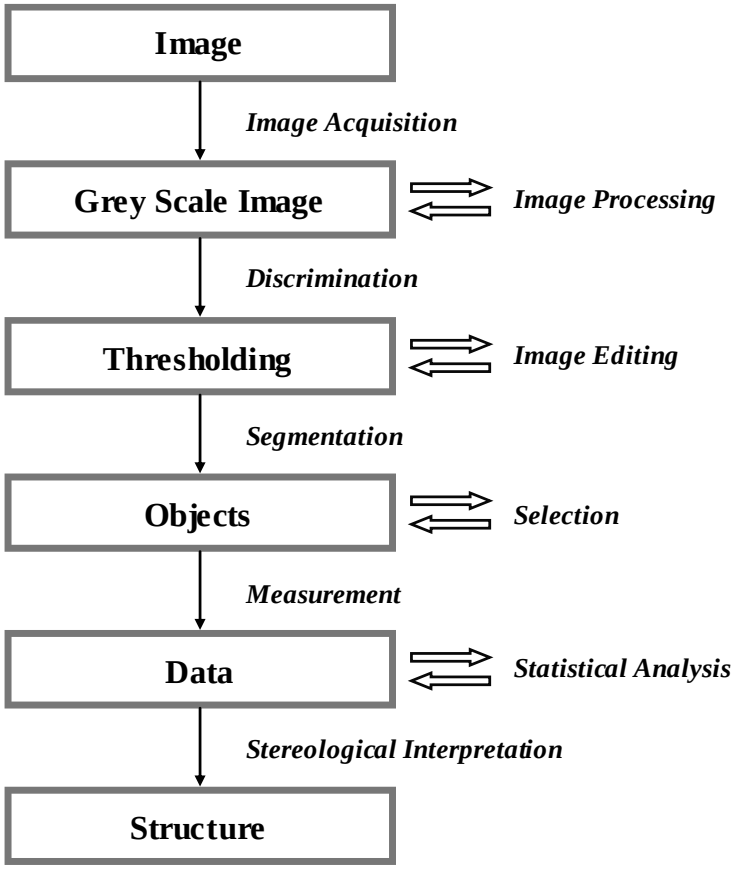

Figure 6.10: Overview of typical thresholding methodology (reproduced from Russ, 1990).

Captured images, whether taken under bright field or polarised light, are first converted to an 8-bit greyscale. An 8-bit greyscale has 256 possible grey values ranging from black (value of 0) to white (value of 255). Alternatively, an image may be converted to a 12 or 16-bit greyscale, which have 4,096 and 65,536 'levels' respectively; however, in most cases this does not give any discernible advantage when applying the methodology. A threshold range, which relates to a feature of the material, is applied to the greyscale image. When characterising porosity in a sample of graphite, pores will generally be darker than the surrounding material as shown in Figure 6.11 (a and b). The threshold range would therefore generally be applied between zero and a value which corresponds to the lightest grey level associated with pores in the particular image. Figure 6.11 (c) shows an appropriate threshold applied to the image which is in turn converted to a 1-bit image (Figure 6.11 (d)) in order to discriminate between porosity and surrounding material. Objects form the image, in this case the porosity can then be measured and analysed as per the requirements of the investigation. Although this methodology is typical of image analysis, the exact procedure is heavily dependent on the material and the type of analysis that is required. Additional stages may be required to enhance the visibility of some features or remove contaminants in the image.

Defining a precise and reliable range is somewhat subjective and can vary between images due to its dependence on lighting, polarisation and exposure conditions. Further difficulties may arise when attempting to define pore boundaries in the image. Although the pore boundary may be atomically sharp, there is a gradual transition from relatively bright surrounding material to the darker region of the pore. Figure 6.12 (b) demonstrates the variation in greyscale values along the defined line (Figure 6.12 (a)). The 'pore region' is indicated by the decrease in greyscale intensity from approximately 110 to 40 at the left side of the image. However, the pore boundary is not clearly defined on the plot since this decrease occurs over a distance of approximately 7 μm, thereby demonstrating a gradual transition. This effect may be attributed to a difference in optical reflection of the epoxy resin at different 'depths'. It is therefore important to validate this limit and attempt to quantify the value that is most appropriate for each image.

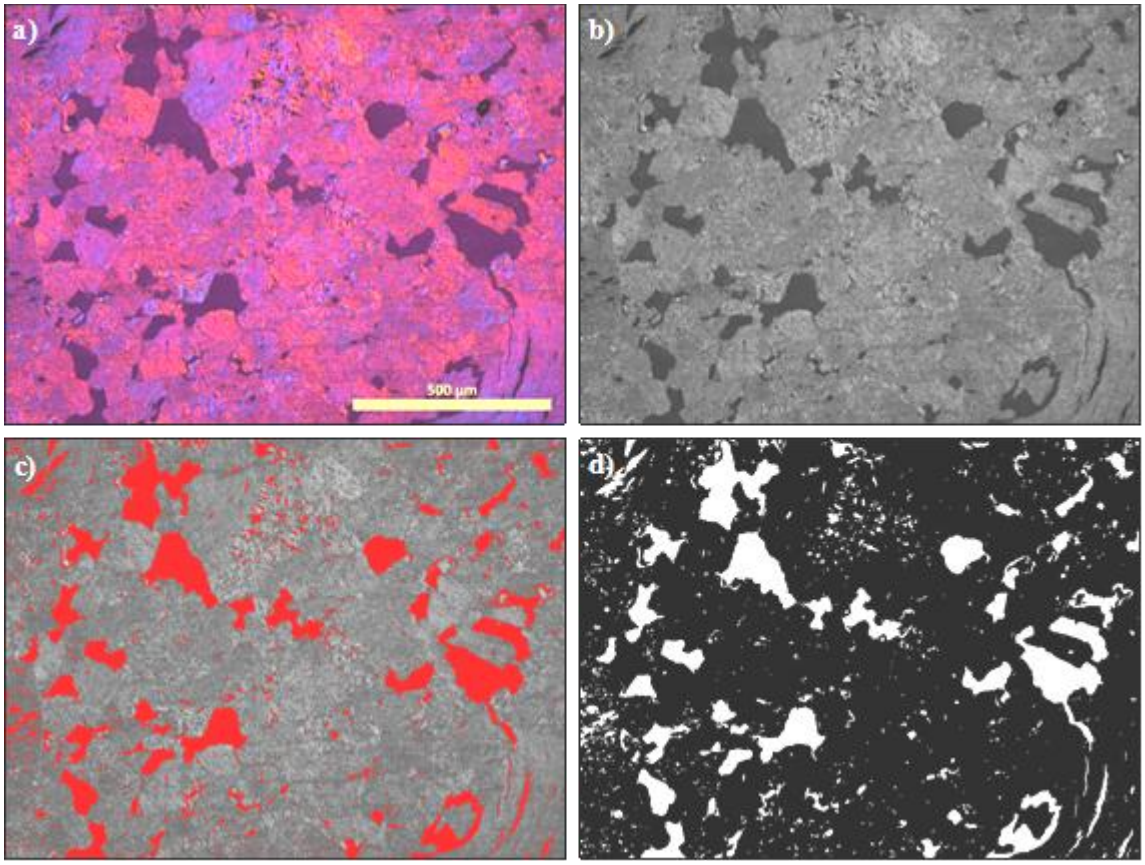

Figure 6.11: Thresholding methodology applied to example image of IM1-24 grade graphite. a) Polarised light micrograph taken at 100x magnification. b) 8-bit greyscale image conversion. c) Threshold applied to greyscale image. d) Selection of pores through conversion to 1-bit image.

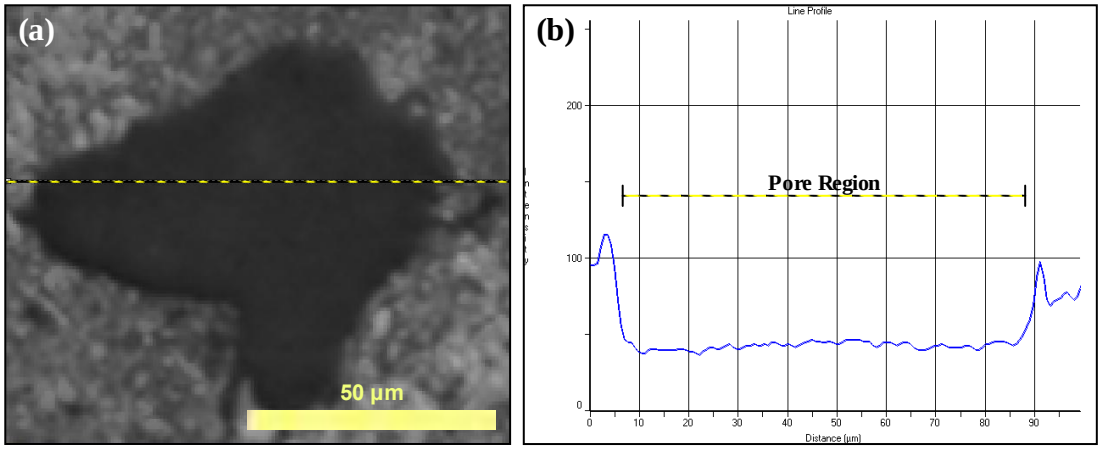

Figure 6.12: Example of a) a greyscale image of a single pore and a b) lateral greyscale variation plot showing the transition between the pore and surrounding material.

An example of determining the appropriate threshold level for a microscopy sample is given in Figure 6.13. Increasing the greyscale intensity threshold yields an increase in

segmentation area. The most appropriate greyscale intensity is the one that 'fills' the pores without including any surrounding material. Wong *et al*. (2006) uses the analogy of filling the pore with a fluid. The critical point is reached when liquid overflows into the surrounding areas, leading to a rapid increase in segmentation area. It is suggested that this 'overflow' point may provide a good estimate as to the pore threshold level for the image. Figure 6.13 demonstrates the subjectivity of the manual segmentation process since values between 55 and 65 may be suitable for this example. The segmentation area at an intensity value of 70 shows signs of the aforementioned 'overflow' into the surrounding material. Therefore, for this example an intensity threshold of 65 would provide the most appropriate estimation.

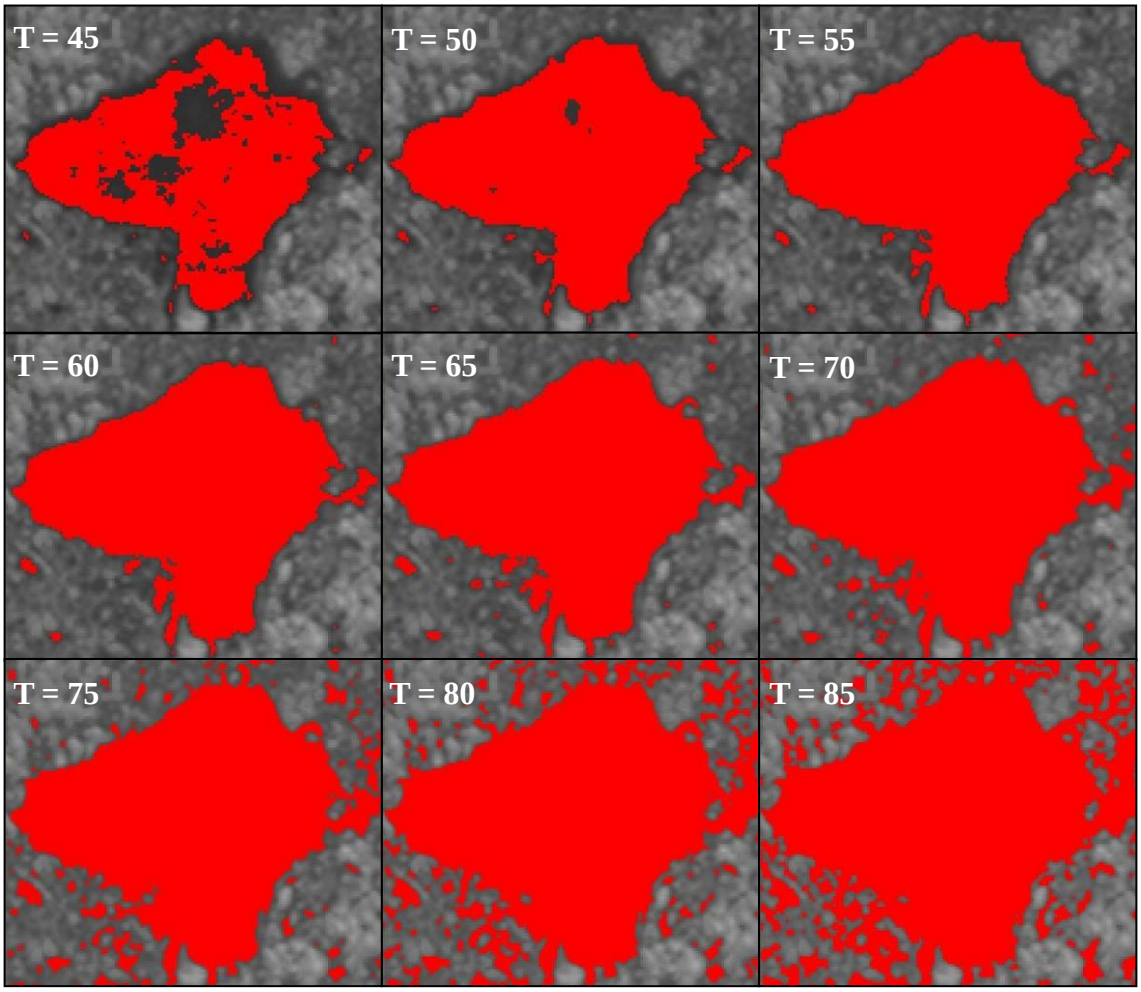

Figure 6.13: Effect on segmentation area when the greyscale intensity threshold level is varied between 45 and 85.

Through careful determination of a threshold value from an example pore, the segmentation of the whole image is likely to be representative of the pore network. However, this is not always the case and a number of factors can have an effect on the segmentation when applied over a large area, such as:

- Dark contaminants on the sample being characterised as pores when segmented.
- Light contaminants on the sample surface disguising pores or altering pore shapes by partially concealing them.
- Inadequate infilling of pores with resin can result in reflections that alter the shape of a pore or hide it entirely.
- Certain levels of polarisation may result in dark areas of filler or binder that are included in image segmentation.

It is important that these factors are considered when segmenting the image to ensure that the data accurately characterises the material. Measures are taken during the preparation stage (Section 6.1.1) to ensure that the samples retain all their key features and do not contain any contaminants. However, it is not uncommon for partially infilled pores or other artificial features to be observed. Due to the nature of the threshold segmentation methodology, it is generally not possible to automatically correct such features and as such must be done manually.

In addition to providing a means for examination, Image Pro Plus has numerous features that enhance the acquisition of images. Single images captured through optical microscopy will be limited by the resolution of the camera. At low magnifications the camera will capture a large area of the sample; however, small details will not be visible. Conversely, higher magnifications will allow smaller details to be identified but only a small field of view will be captured. In order to analyse a large area of the sample in high detail, several captured images can be 'tiled' to create a composite image. Firstly, the images must be captured manually in such a way as to ensure they overlap one another. The software is then able to automatically tile the image using a Fourier correlation method (Media Cybernetics, 2012). Figure 6.14 shows two polarised light images of IM1-24 grade graphite.

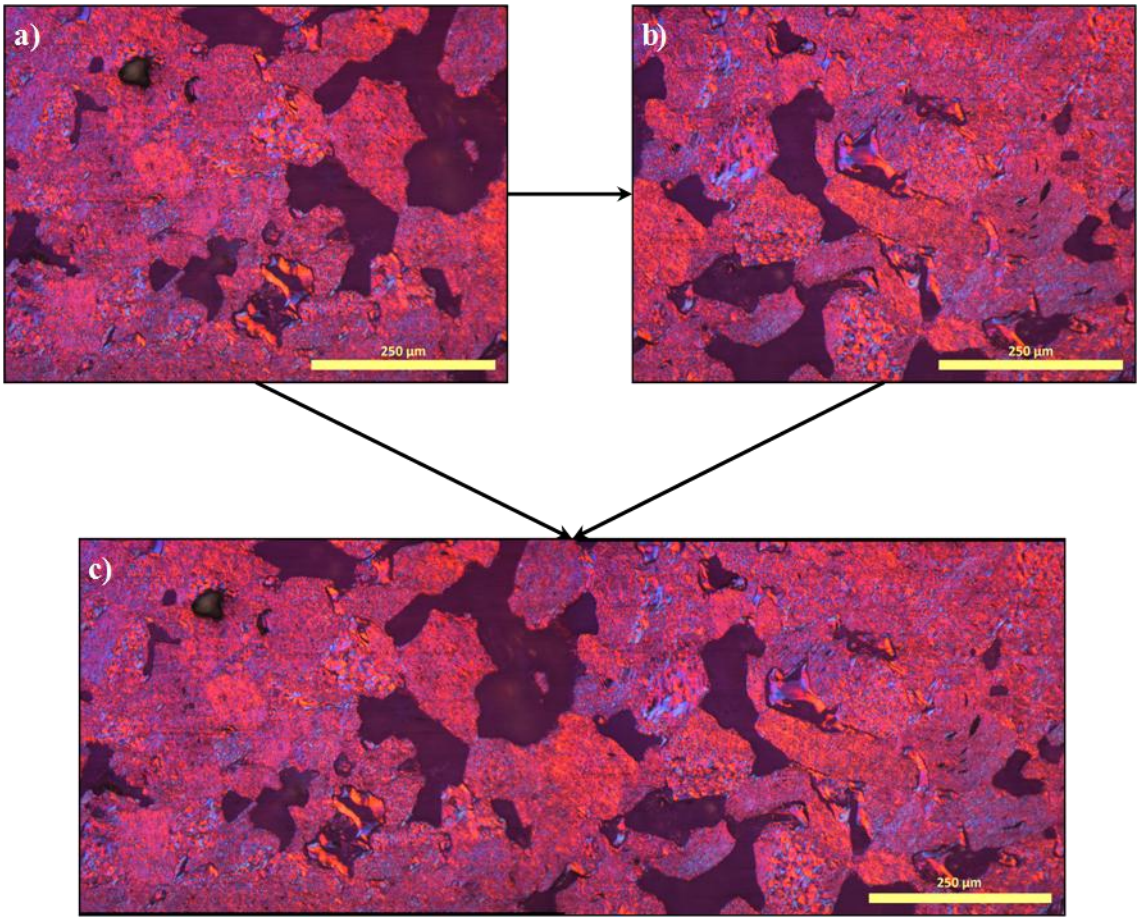

Figure 6.14: Tiling procedure applied to two images of IM1-24 grade graphite (a and b) to create a composite image (c).

The two raw images (Figure 6.14 a and b) are captured so that they are slightly overlapping. This is achieved by identifying a feature on the first image before moving the traverse table on the microscope, ensuring the identified feature is still visible on the second image. The software uses a tile function to determine the position at which the micrographs overlap and then stitches the images together to generate the tiled composite. The resulting tiled image (Figure 6.14(c)) allows a larger area to be analysed than a single image whilst retaining the same level of detail. This technique is particularly useful when analysing pores and other microstructural characteristics over a large area. The tiling procedure can be repeated for any number of images in both x and y directions in order to suit the requirements of the analysis.

6.3. Characterising the Microstructure of IM1-24 Graphite

Characterisation of the material is required to ensure that any models are representative of the material. The data from image analysis may be used to computationally reproduce a microstructure or to validate a microstructure that is generated through probabilistic algorithms. As previously mentioned in this chapter, one of the most important considerations is the porosity within the material. However, it is not enough to simply know the percentage content. Variations in pore size and shape as well as quantifiable knowledge for the distributions are also necessary. Typically, quantifiable characterisation may include statistical data such as mean, standard deviation *etc*. Although these values may be useful to some extent, it is important to realise that they are likely to be heavily skewed when analysing the microstructure of graphite. For example, a very large number of small pores may be detected that account for a small percentage of the overall porosity. Conversely, a large proportion of the porosity may be attributed to a relatively small number of larger pores. In this instance, the large quantity of smaller pores will mean that the average pore size is relatively small and does not, in any way, represent the larger pores. Larger pores in the material are likely to have a greater effect on the material properties than the smaller 'background' pores, therefore making it imperative that they are accurately represented by any analytical data. As such, the pore size distribution is generally a far more useful analytical tool for the characterisation of porosity, and thus for the purposes of modelling and ultimately for the prediction of fracture.

Quantifiable data regarding filler particles cannot be automatically generated using the thresholding technique due to it having similar optical properties to the binder phase. As such, determining size and shape distributions of filler particles is more problematic than for porosity. Tools within the image analysis environment can be used to identify and characterise basic properties of these particles such as area and aspect ratio. Further complications arise when considering the three-dimensional nature of these particles. Since a micrograph is a two dimensional cross-section of the material, there is no way of accurately determining the 'true' size of the particle (*i.e.* its maximum radius). For example, what is observed on an optical micrograph as a small particle cross-section may actually be far larger than it appears. Porosity within filler particle can be determined by isolating them before applying the image segmentation methodology.

6.3.1. Material and Acquisition Conditions

The IM1-24 material used for microstructural characterisation was taken from the batch of thirteen three-point bend specimens (Section 5.4). Utilising this material for microstructural characterisation and subsequent modelling work ensures that experimental and computational results are comparable.

Six microscopy samples were prepared through application of the procedure outlined in Section 6.1.1. Samples cross-sections were approximately 15 x 15 mm, which was large enough to enable the capture of a significant amount of microscopy data. Images were captured at a magnification of 100x to allow for a sufficiently large viewing area whilst still acquiring all the relevant microstructural data. Calibration of the image analysis software was undertaken using a 1 mm micro graticule before any images were captured. Calibration determined that each pixel has a dimension of 0.6702 μm (4 S.F.). This process was repeated for each subsequent sample to ensure validity of the measurements. Images have a resolution of 2048 x 1536 pixels which at this magnification corresponds to an image capture area of approximately 1370 x 1026 μm. Considering the relative size of features in the graphite microstructure, an image area of 10 x 10 mm is sufficient to enable a detailed characterisation to take place. Image tiling was used to stitch together micrographs in a 9 x 11 grid. This geometry allows for a total area of 10 x 10 mm to be created whilst accounting for the necessary overlap of images. Once the images are captured and tiled to form a composite image it is cropped to the determined size. Composite images with an area of 10 x 10 mm have a resolution of 14924 x 14924 pixels.

Images were initially captured under polarised light conditions, such as the tiled image of Sample one that is shown as Figure 6.15. Additional micrographs for all samples are shown in Appendix A. Note that the example image resolution is scaled down considerably. Higher resolution images for microscopy samples may be found on the attached DVD (see Appendix A, Table A.1, for image registry).

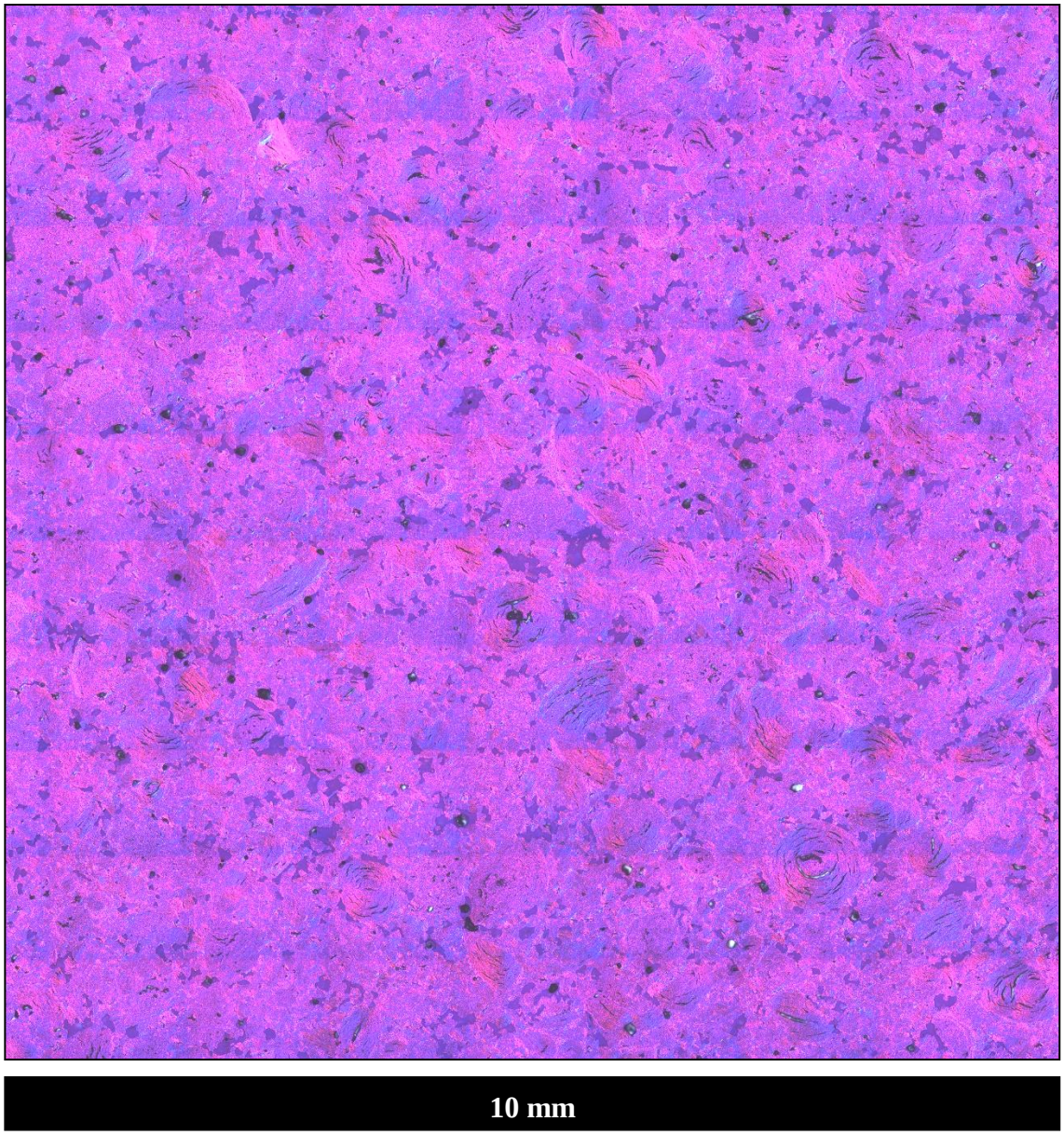

Figure 6.15: Polarised light micrograph (10 x 10 mm, 14924 x 14924 pixels) of IM1-24 Sample one captured at 100x magnification.

Upon preliminary analysis of these polarised light micrographs it became apparent that dark bands were visible at the periphery of the individual images. This effect, commonly referred to in photography as vignetting, is likely due to the optics of the microscope and the camera which combine to cause a drop in brightness at the edges. Imperfect optical alignment between the microscope lenses, camera lenses and image sensor result in the non-uniform distribution of a light and thus the observed dark areas. For a single image, this is not particularly problematic unless the difference in brightness is very severe. However, upon thresholding of this image, the observed pore

distributions may be skewed by the dark areas being characterised as pores. Polarisation of the image seems to exacerbate this effect since the observed shift in relative brightness between the centre and periphery of the images is greater. In an effort to reduce this effect and ensure an accurate pore distribution may be determined from the image, a bright field comparison was captured, as shown in Figure 6.16.

Figure 6.16: Bright field light micrograph (10 x 10 mm, 14924 x 14924 pixels) of IM1-24 Sample one captured at 100x magnification.

There is still evidence of some vignetting in the individual images before they are tiled. However, the effect is reduced and should therefore not interfere with the pore

thresholding procedure as much as if the material was characterised through analysis of the polarised light image. Although it is apparent that the thresholding of the material may be better suited to a bright field image, polarisation is still a useful tool for general observational analysis of the material (*e.g.* identification and characterisation of filler particles).

6.3.2. Characterisation of Porosity Distributions

The characterisation of porosity distributions with the material needs to include the consideration of a number of factors:

- Pore size distribution will give an indication as to what fraction of the porosity may be attributed to pores of a given size.
- Pore shape and aspect ratio. Considering that fracture is often quoted as being initiated from 'crack like defects' it is important to identify the size and aspect ratio distributions.
- Largest pores in the sample will be recorded to identify potential sources of failure initiation. Additionally, the size and aspect ratio of such defects will be considered.

As previously mentioned, microscopy images do, in some instances, require some minor editing to remove artefacts. Due to the scale of the tiled images, it was always a strong possibility that the samples would require some minor editing. Each composite image was carefully checked and minor adjustments were made when necessary to ensure that the characterisation was accurate and that any data ascertained from their analysis would be valid. Most items requiring correction related to the incomplete ingress of resin into pores which results in bright areas that are subsequently not included in pore segmentation.

A benchmark value for the porosity content expected in a sample is useful when attempting to segment the image. Percentage porosity values in graphite can be calculated using the equation:

$$P = (1 - \rho/2.26) * 100 \qquad \text{Equation [6.1]}$$

where, ρ is the density of the material and 2.26 gcm^{-3} is the theoretical density of solid graphite crystals (*i.e.* without the inclusion of porosity in the material). Using this equation, porosity percentages of the six microscopy samples were estimated. The results of these calculations are shown in Table 6.2.

Table 6.2: Measured density and calculated porosity percentage for six IM1-24 samples.

Sample	Measured Density (gcm^{-3})	Calculated porosity (%)
1	1.830	19.04
2	1.819	19.51
3	1.828	19.11
4	1.821	19.44
5	1.829	19.06
6	1.810	19.93
Mean	1.823	19.35
Standard Deviation	0.007	0.32

The bulk material density and thus the calculated porosity showed very small variations between the samples, as shown by the standard deviation for the two properties. These variations are likely due to the probabilistic nature of the material and the pore distributions.

Upon segmentation, the image analysis software allows appropriate features to be identified, which can then be measured for inclusion in further analysis. For example, an area of 1 pixel (approximately 0.49 μm^2) is too small to be conclusively deemed to be a pore and should therefore be excluded from analysis. Exclusion of very small features may result in many pores not being counted; however, it will also help to ensure that all the features that are included are relevant to the analysis. For the purposes of the pore distributions, an artefact may be classified as a pore if it has an observed area greater than 5 μm^2 (*i.e.* approximately 10 pixels or more).

One consequence of the material preparation stage is a non-uniform optical viewing surface between samples. Despite measures being taken to prepare the samples under the same conditions, a number of factors can contribute to a change in optical properties. Impregnation of the epoxy resin is dependent on the surface pore structure and can have an effect on the subsequent grinding and polishing stages. As a result,

some samples may require more polishing time to provide a suitable viewing surface thereby altering their reflectivity. Careful consideration with regards to the application of thresholding to each image is required in order to characterise the samples.

Initially, threshold values for pore percentages ranging from 17 to 20% were investigated to allow quantitative analysis of distributions with a representative pore fraction. The threshold values required to yield a segmentation percentage within this range varied between samples. Greyscale thresholding has a finite number of possible segmentation values and it is therefore not feasible to define a universal porosity value across all the samples. To demonstrate this effect, Table 6.3 shows the threshold values defined for each sample at a total segmented area percentage that relates to the calculated values. These percentages are based on a minimum object (*i.e.* pore) size of 1 μm^2.

Table 6.3: Segmentation threshold values that most closely represent the calculated percentage porosity for the six samples.

Sample	Calculated Porosity (%)	Segmentation Threshold	Observed Porosity (%)
1	19.04	117	19.26
2	19.51	166	19.35
3	19.11	221	19.14
4	19.44	170	19.24
5	19.06	167	19.14
6	19.93	172	19.96

Initial attempts to acquire micrographs of sample three using bright field illumination proved problematic. It was noted that the epoxy infilling of the pores did not demonstrate a significant deviation in greyscale value from the surrounding material. Therefore the porosity could not be effectively distinguished from solid material using the segmentation methodology. Polarised light did enable a better contrast between the pores and material, however, the aforementioned vignetting effect was too significant to provide the required uniformity across the composite image. The likely cause of this low contrast is due to an enforced modification in the preparation procedure for this particular sample. After initial polishing, scratches were visible on the surface of this sample. In an effort to remove these scratches, the sample was re-polished. However, this additional preparation stage may have contributed to 'polishing relief'. Polishing

relief occurs when the material is removed at different rates due to a varying hardness of the phases (*e.g.* between the epoxy resin infilling and the graphite) (Robinson (2012), Bjerregaard *et al.* (2000)). This variation in sample topography can potentially result in only part of the image being in focus. The depth of field of the lenses used to capture images is sufficient to negate these topographical effects; however, this preferential polishing had a detrimental effect on the contrast between the graphites and epoxy resin. Having identified this effect, the grinding the polishing procedure was repeated to ensure the sample surface was of suitable quality to ascertain the required pore data. As a consequence of this, images for sample three are brighter than the other samples and as such a higher threshold value is used to generate a representative segmentation of porosity.

Although a pore fraction that corresponds to the calculated value could be applied using the image analysis software, it was not representative of the pore distribution. Segmentation area of each sample at this percentage included a significant amount of surrounding material. In addition to this 'overflow' into the material, it was observed that some dark regions of solid material, which were clearly not pores, were also included in the segmentation. This is demonstrated by isolating a large pore from the micrograph of sample two (Figure 6.17 (a)). When a representative pore fraction is applied to the micrograph the segmentation area accounts for the whole pore as well and some surrounding material (Figure 6.17 (b)). The inclusion of solid material can be readily identified by the 'rough' boundary edges of this pore, which does not occur when the pore is correctly segmented. Application of an appropriate segmentation methodology to this image results in a well-defined pore boundary (Figure 6.17 (c)). Indeed, for this example, it is clear that there are in fact two separate pores which were joined by solid material when the initial threshold value was used.

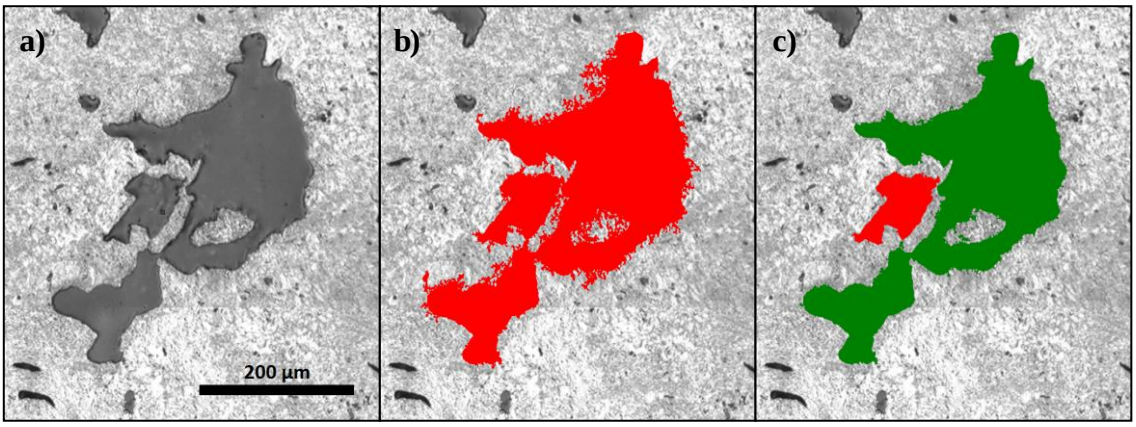

Figure 6.17: a) Example of an isolated large pore from micrograph of Sample two. b) Threshold segmentation of image using a representative pore fraction (greyscale intensity of 166). c) Threshold segmentation through the application of a more appropriate methodology (greyscale intensity of 136).

The calculated values should give a good indication of what percentage porosity can be expected to be observed in the material, however, it is important to consider how they apply to the micrographs. This amount of porosity is averaged over a relatively large volume and may contain regions of large porosity or solid material which could skew the calculated values, thereby making it inaccurate to simply apply a corresponding value when segmenting the image. Additionally, it is important to consider the scale of the micrographs, which have a maximum resolution of approximately 0.7 μm. Any pores smaller than this will have dimension less than 1 pixel and will therefore not be detected during the analysis. Porosity calculations take account of the bulk material and thus the entire pore distribution, regardless of size. As such, it is highly likely that the observed porosity in the micrograph will be less than that derived from the equations. Quantifying this reduction in observed porosity is problematic since alternative methods are not available to characterise the sub 1 μm pore distribution. Therefore, meticulous application of image segmentation methodology to the micrographs is required to ensure that any pore data is relevant to the applicable size range.

The application of the methodological procedure is somewhat subjective and requires a great deal of consideration for the image. Each image was considered independently to ensure that representative pore distribution data is generated from the image segmentation. Table 6.4 outlines the observed porosity in the micrograph along with

the respective segmentation threshold. As with the initial studies, a minimum object area of 1 μm^2 was utilised for the characterisation of pore distributions.

Table 6.4: Segmentation threshold values and observed porosity for the application of an appropriate methodology.

Sample	Segmentation Threshold	Observed Porosity (%)
1	105	14.05
2	136	11.53
3	190	12.25
4	136	12.05
5	143	13.09
6	136	11.72

The observed segmentation area and thus, porosity, of the samples varies between 11.53 and 14.05%. This range may be attributed to the probabilistic nature of the material. Observations based on a two-dimensional cross section of the material are liable to exhibit a relatively large range of values between samples. This is particularly relevant when considering the relative quantity of large pores in each sample. These pores can account for a significant percentage of the overall porosity and thus have a large influence on the percentage values. In addition to this consideration, the range of porosity values could also potentially be attributed to the preparation of the samples. When an appropriate methodology is applied to the micrographs for samples one and five, the overall pore area is characterised as being greater than the other images. Identifying the specific reason for this observation is problematic.

One possible explanation could be that smaller pores are obscured in highly reflective samples due to the relative brightness. Such a phenomenon could occur in Samples two, four and six resulting in an overall lower segmentation area. However, this theory does not account for Sample three which is the most reflective (indicated by the highest threshold value). Regardless of the reason, it is clear from qualitative analysis that the difference is pore distribution can be attributed to the small pore distributions. Although this could, in theory, affect the overall porosity values, it will be limited to smaller pores and will not influence the large pore distribution in the sample. Increasing the minimum object size threshold disregards these small pores and allow for a more direct comparison of the samples. Since this work is primarily focused on the

effect of large pores within the material structure it is important to prioritise their accurate characterisation over the inclusion of smaller features. Comparison of larger pore distributions may be achieved through increasing the threshold further still. As well as the variations in relative porosity percentage between samples, the number of objects characterised by the segmentation methodology also differs. Table 6.5 shows the porosity percentage and number of objects at different minimum size thresholds.

Table 6.5: Porosity percentage and number of objects for minimum area thresholds of 10, 100 and 1000 μm^2.

Sample	Minimum Area Threshold (μm^2)					
	10		100		1000	
	Porosity (%)	Objects (Pores)	Porosity (%)	Objects (Pores)	Porosity (%)	Objects (Pores)
1	11.81	93130	9.94	6365	8.57	1500
2	10.75	40729	9.86	6273	8.43	1428
3	11.46	54051	10.25	7677	8.52	1482
4	11.37	35044	10.47	5098	9.44	1065
5	11.53	67435	10.13	5643	8.89	1368
6	10.72	37079	9.96	4815	8.90	1341

When a minimum size threshold of 10 μm^2 is applied, samples one and five show a significantly larger number of objects than the other micrographs. It is clear from subsequent increases in the minimum area threshold that the majority of 'additional' objects defined in these images are relatively small (*i.e.* between 10 and 100 μm^2). Minimum areas of 100 and 1000 μm^2 do not demonstrate such a variation in segmented objects between samples. Characterisation of these smaller features does have an effect on the determined porosity percentage. For example, Sample one demonstrates a sharp decrease in porosity percentage as the minimum area threshold is increased. Indeed, comparisons of the relative difference in percentage porosity and object quantities are inconsistent between minimum threshold values. The relative variation between samples decreases when the minimum area threshold is increased. For example, at a minimum threshold area of 10 μm^2 Sample four was characterised as containing fewer pores than Sample one (approximately 38%). However, increasing the area threshold to 100 and 1000 μm^2 reduced this variation to 80 and 70%, respectively, thereby making the micrographs more directly comparable. Relative variations in the porosity percentage are erratic and do not indicate anything with regards to sample

comparability. Observations of this nature are likely due to the probabilistic variation in the graphite microstructure. Sample one shows the greatest porosity percentage at 10 μm^2 threshold whereas at 100 and 1000 μm^2 threshold area, Sample four demonstrates the highest percentage. These observations may bring into question the validity of pore distributions that account for small pores; however, it adds credence to distributions that only consider the larger pores in the material (*e.g.* greater than 100 μm^2). This scenario is not ideal for complete characterisation of the material; however, regardless of these difficulties this is not an entirely attainable goal due to a large proportion of the pores being smaller than the camera resolution. Direct comparisons of pore size distributions can be made between samples providing the area threshold is high enough to 'filter' out the numerous small pores that are characterised in some micrographs. Initial consideration of these distributions based on the relative sample data suggests that they are not uniform and will show a significant variation between samples.

Cumulative probability curves may be used to visually represent the pore distribution in the sample and allow for comparisons to be made. The property of interest is the area of the pores; however, a more suitable dimension for these plots is the equivalent pore diameter (EPD) (Diamond, 1970). The EPD is related to the area through the simple expression:

$$EPD = \sqrt{\frac{4A}{\pi}} \qquad \text{Equation [6.2]}$$

where, A is the area of the pore. EPD's for each pore are calculated and sorted from smallest to largest. In addition, the fractional porosity for each pore is calculated and the cumulative probability determined. Plotting of EPD against cumulative probability will create a curve that shows what fraction of porosity is accounted for by pores of a given size. Figure 6.18 shows the size distribution of pores with a 10 μm^2 minimum area threshold. The large quantity of small pores in Samples one and five is demonstrated by the initial steep gradient of the curve. After this initial rise, a similar distribution is exhibited until around 150 μm EPD when they begin to separate due to larger random pores in the material. Smaller pores are 'filtered' out when the minimum area threshold is increased to 100 or 1000 μm^2 as shown in Figure 6.19 and Figure 6.20 respectively.

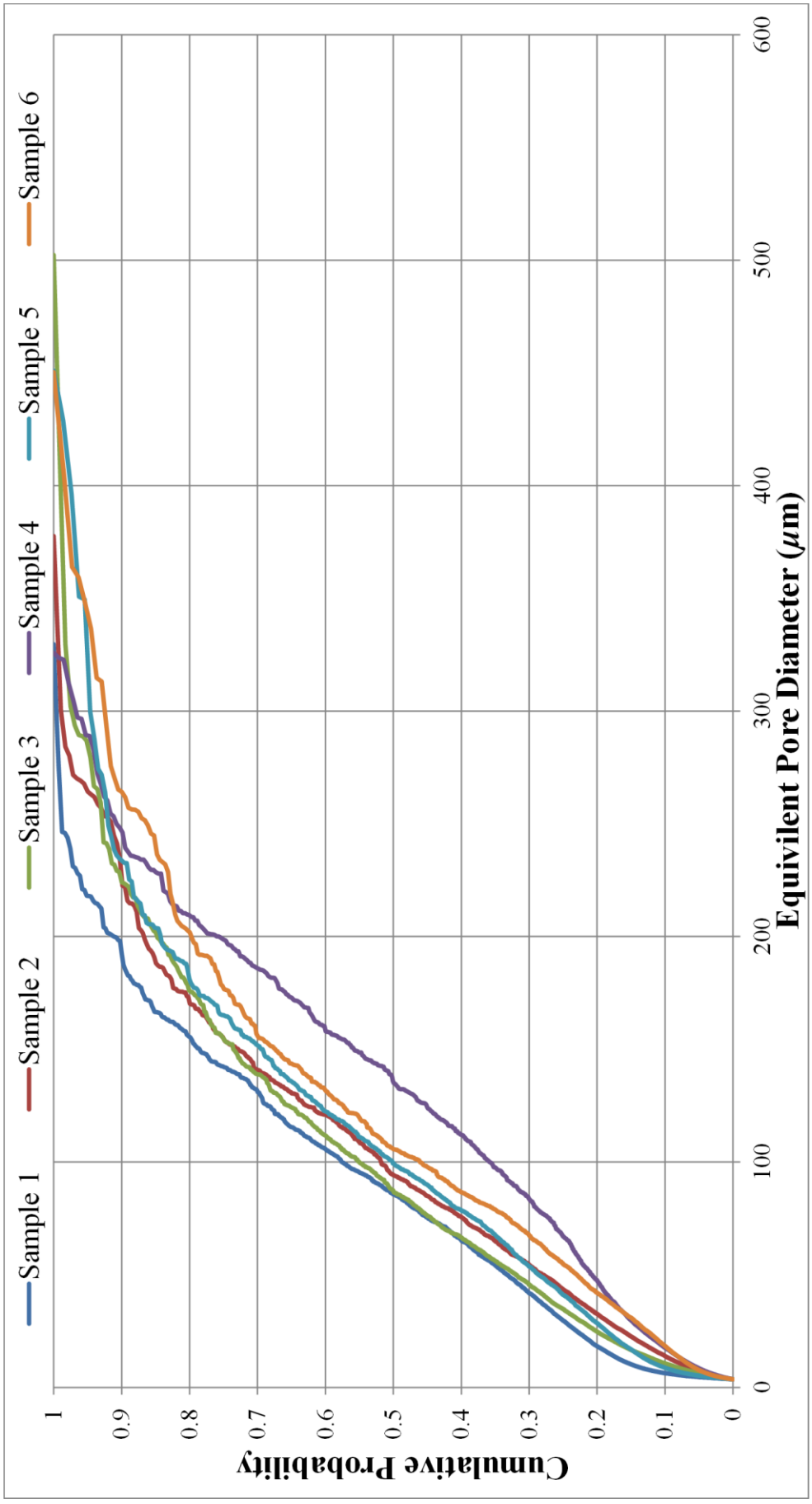

Figure 6.18: Size distribution for pores with an area over 10 μm^2.

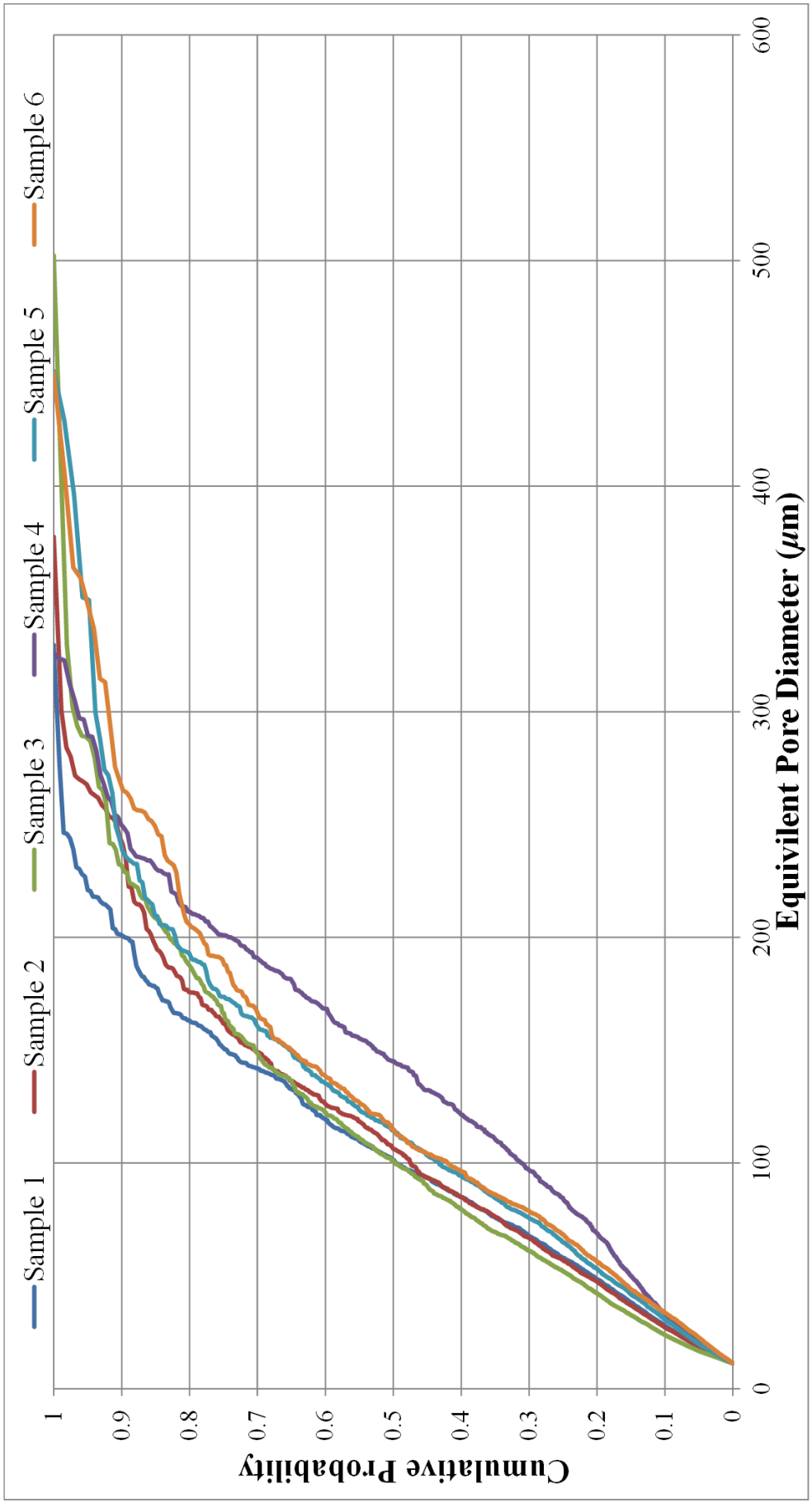

Figure 6.19: Size distribution for pores with an area over 100 μm^2.

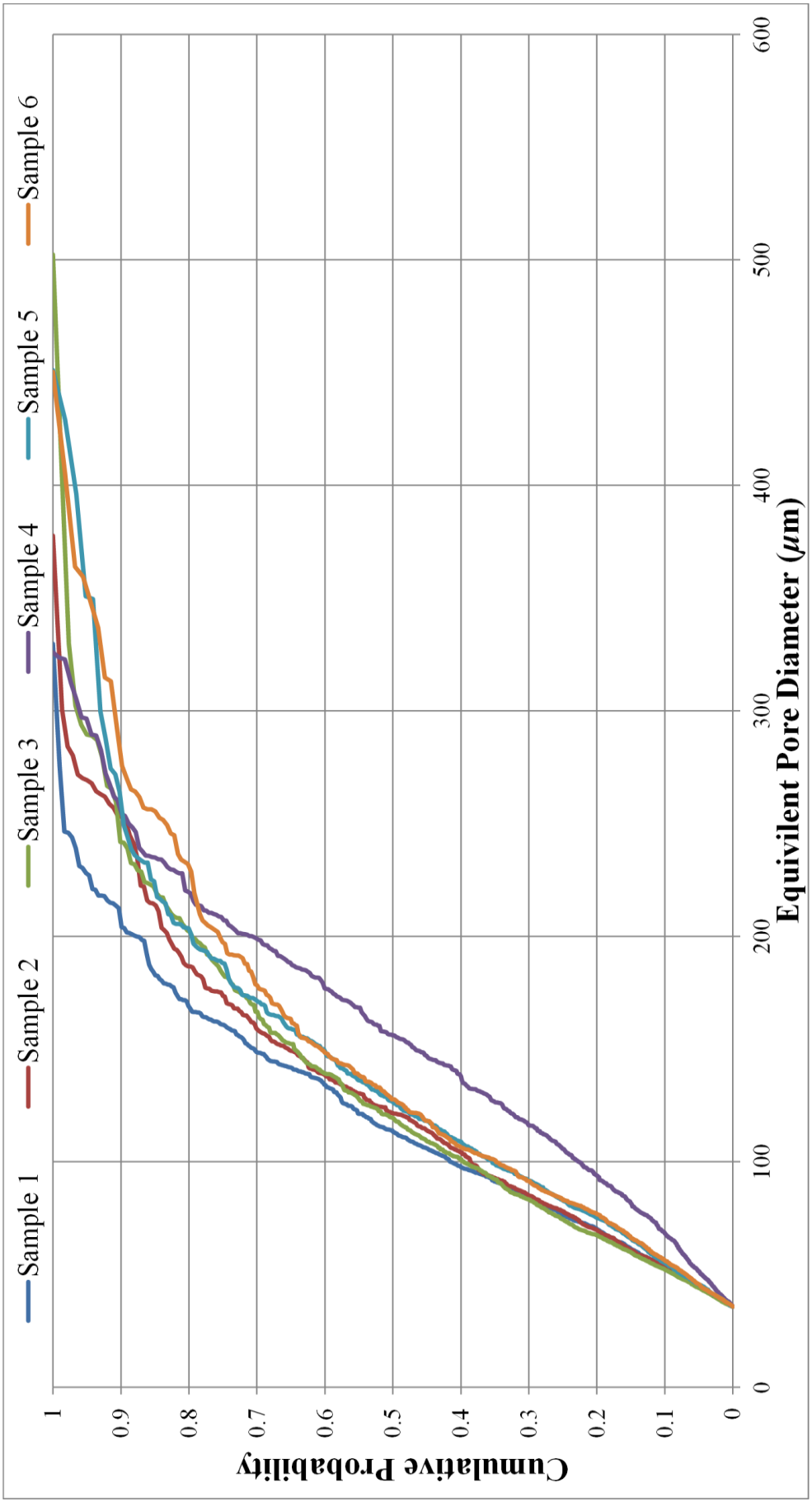

Figure 6.20: Size distribution for pores with an area over 1000 μm^2.

Distributions in the larger area plots show a far more uniform shape between samples at the smaller pore EPD's before again dispersing as the EPD increases. Sample four is shown to deviate significantly from the other distributions in all the plots. Such nonconformity from the other distributions may be attributed to a larger or smaller quantity of pores in a particular size range. Larger pores, which are relatively few in number, account for a significant amount of the total porosity in all the samples. However, through consideration of the data in Table 6.5, there is evidence to suggest that Sample four contains a particularly significant distribution of larger pores. Although few in number (1065 pores) they account for a large porosity percentage (9.44%). In order to better characterise the very large pore distributions in the samples, data for a minimum threshold value of 10000 μm^2 is presented in Table 6.6.

Table 6.6: Porosity percentage and number of objects for the very large pore distribution (minimum area threshold of 10000 μm^2).

Sample	Porosity (%)	Objects (Pores)
1	4.32	225
2	4.70	231
3	4.53	204
4	6.77	287
5	5.04	231
6	5.03	209

Consideration of only very large pores (above 10000 μm^2) shows that Sample four has a significantly larger amount of porosity attributed to this size range. This is due, at least in part, to the fact it contains the most pores in this range. The inclusion of such data in distributions will effectively skew the plot since the smaller pores will have less influence on the cumulative porosity values (indicated by the initial shallow gradient on the curve for Sample four), thereby accounting for the initial deviation from the other samples.

The relative proportion of pores within discrete size ranges can be demonstrated by calculating the mean pore size in each sample as the minimum threshold is raised. Although average values are generally not applicable to such data, they do clearly show how the porosity is distributed in the sample. Average fractional porosity data for minimum threshold areas of 100, 1000 and 10000 μm^2 are presented in Table 6.7.

Table 6.7: Average fraction porosity per pore for area threshold of 100, 1000 and 1000 μm^2.

Sample	Minimum Area Threshold (μm^2)		
	100	1000	10000
	Mean Fractional Porosity Per Pore (%)		
1	1.6×10^{-3}	5.7×10^{-3}	19.2×10^{-3}
2	1.6×10^{-3}	5.9×10^{-3}	20.4×10^{-3}
3	1.3×10^{-3}	5.7×10^{-3}	22.2×10^{-3}
4	2.1×10^{-3}	8.9×10^{-3}	23.6×10^{-3}
5	1.8×10^{-3}	6.5×10^{-3}	22.1×10^{-3}
6	2.1×10^{-3}	6.6×10^{-3}	24.1×10^{-3}

The general increase in fractional porosity per pore as the minimum area threshold is increased is indicative of the increase in pore size that these ranges consider. More useful considerations are with regards to the relative changes between samples. Although Sample four does have the largest percentage porosity at a minimum threshold area of 10000 μm^2 it does not exhibit the largest fractional porosity per pore. Therefore it can be concluded that the large quantity of pores in the range is primarily responsible for the overall higher percentage porosity.

Identifying pores within a given size range can be achieved by defining a 'single variable class'. Once a size range is defined, the image analysis software characterises the pores accordingly. Colour coordination allows for easy identification of each pore class. Figure 6.21 and Figure 6.22 illustrate the classes from minimum pore areas of 1000 and 10000 μm respectively. Table 6.8 and Table 6.9 accompany the images to show the statistics for the area classes. Images and tables showing the area classes for the remaining images are shown on the accompanying DVD (see Appendix A for details).

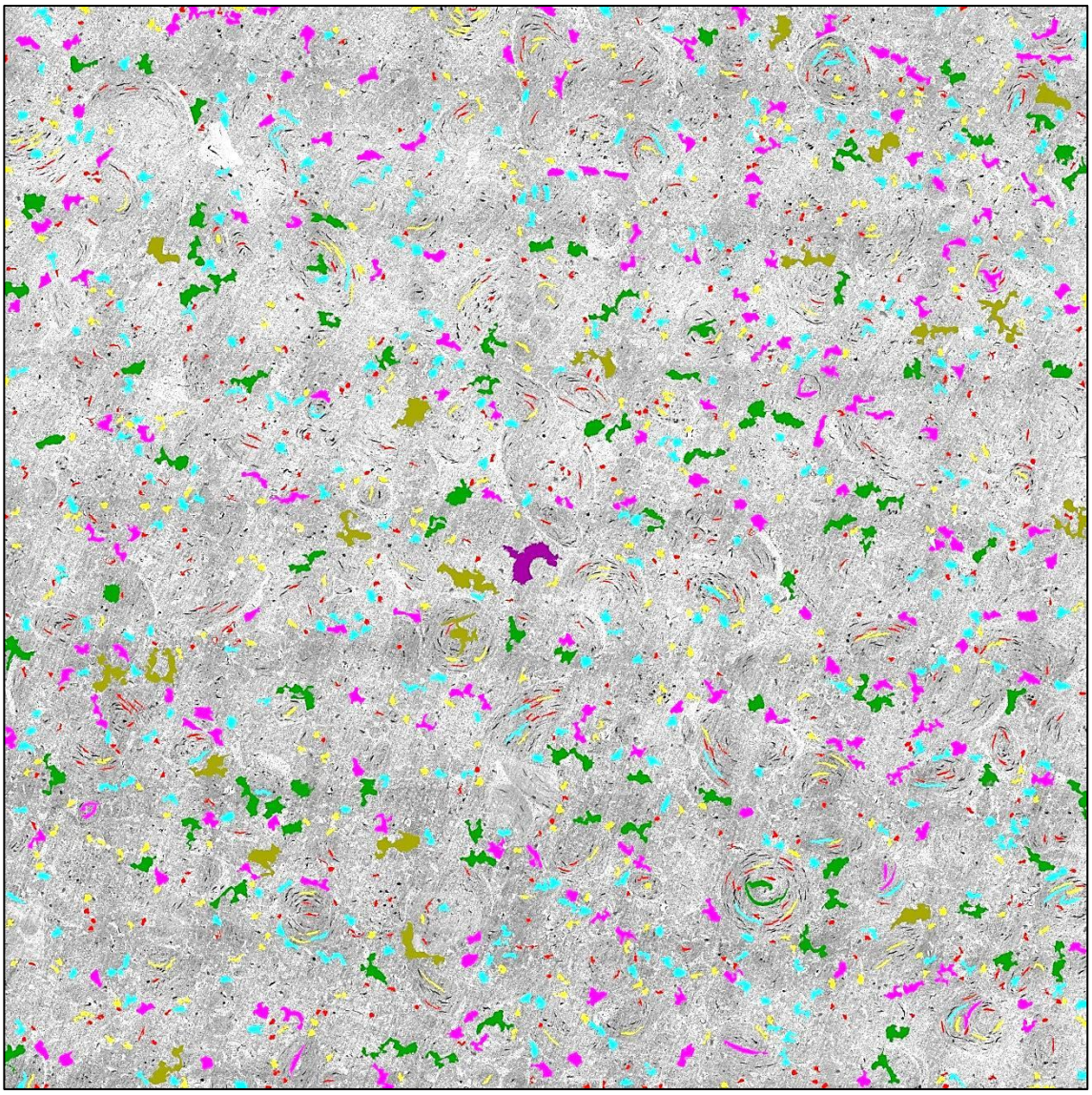

Figure 6.21: Sample one (10 x 10 mm) area classes for pores over 1000 μm^2.

Table 6.8: Sample one area class statistics for pores over 1000 μm^2.

Sample 1. Minimum Area 1000 μm^2			
Area Range (μm^2)		Objects	Mean Area (μm^2)
Start	End		
1000	2000	501	1419.60
2000	4000	375	2812.77
4000	8000	323	5594.10
8000	16000	187	11207.97
16000	32000	92	21443.00
32000	64000	21	40255.17
64000	-	1	85352.32

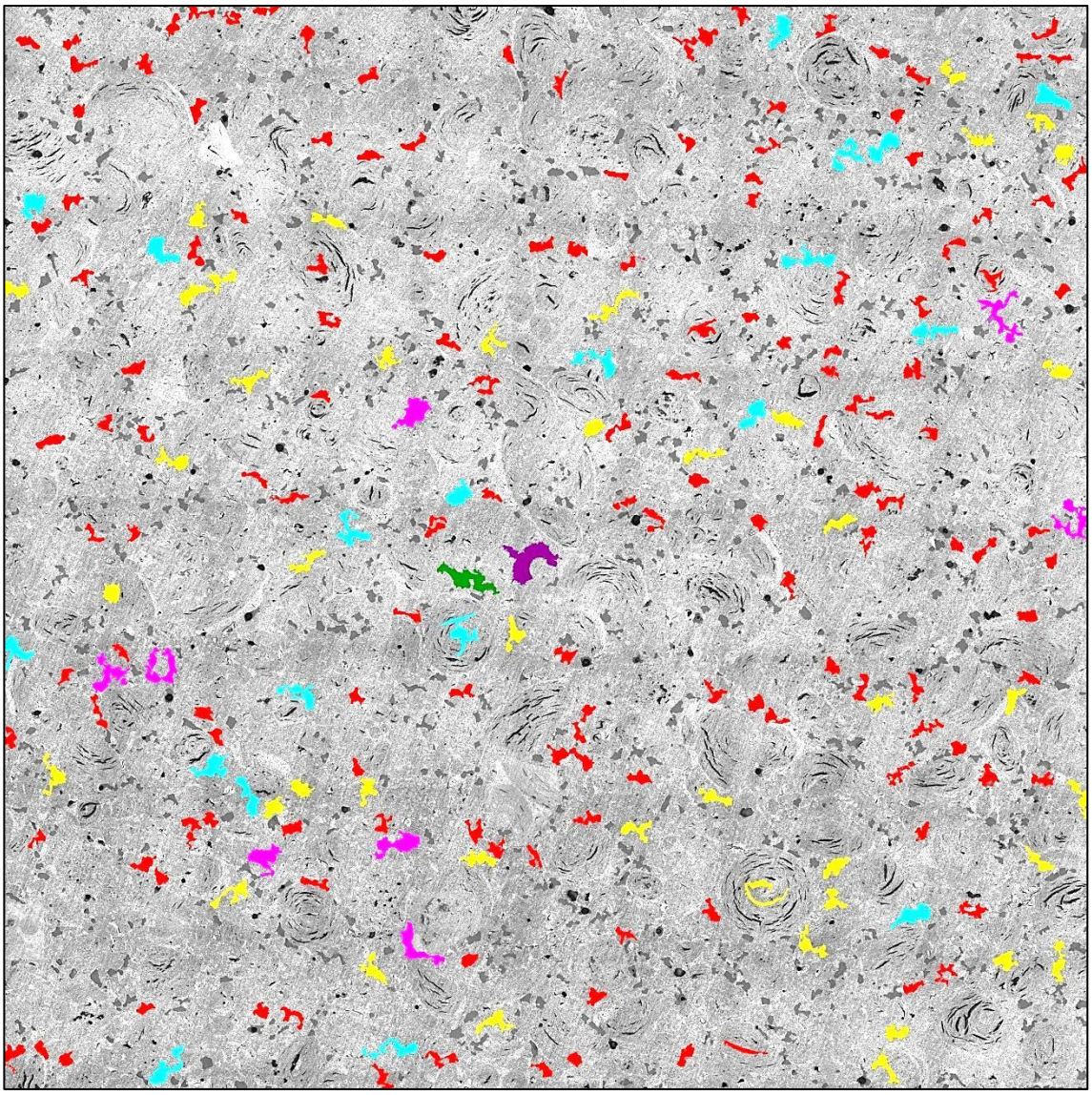

Figure 6.22: Sample one (10 x 10 mm) area classes for pores over 10000 μm^2.

Table 6.9: Sample one area class statistics for pores over 10000 μm^2.

Sample 1. Minimum Area 10000 μm^2			
Area Range (μm^2)		Objects	Mean Area (μm^2)
Start	End		
10000	20000	151	14074.53
20000	30000	44	23019.41
30000	40000	20	34270.10
40000	50000	8	43962.11
50000	60000	1	59626.82
60000	70000	0	0.00
70000	-	1	85352.32

The distribution of very large pores shows considerable variation between samples, as demonstrated by the separation of curves on the size distribution plots. However, it is clear that in all the samples a significant proportion of the overall porosity can be attributed to a small quantity of very large pores. Accurate characterisation of the large pores in the material is important since they are the most likely sources of variation when considering mechanical properties of graphite. Although the size distribution is a necessary consideration, the shape and location of pores can also have an influence on the mechanical performance of graphite, especially when applied to engineering applications. Figure 6.23 shows the two largest pores observed in each sample so as to give some examples of the variation in pore size and shape in graphite.

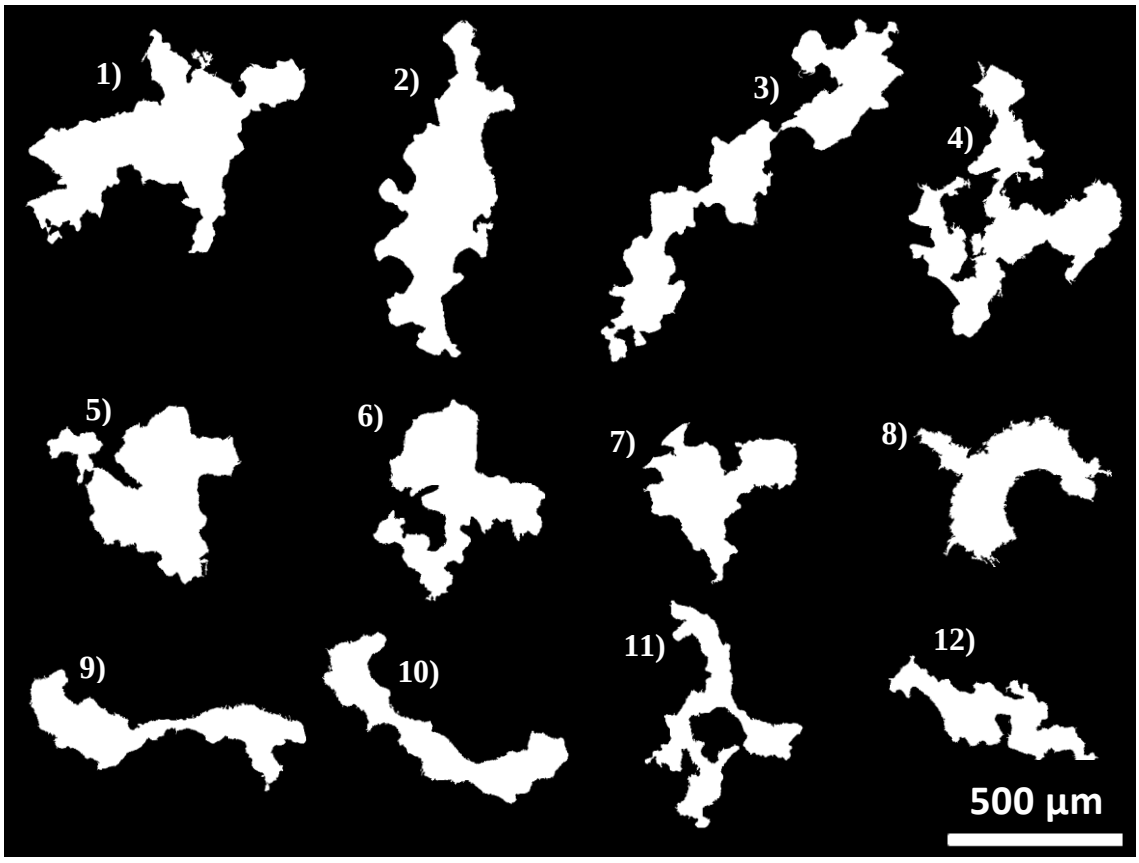

Figure 6.23: Largest pores characterised through segmentation of six micrographs.

The probabilistic nature of pore generation during the manufacture of graphite is responsible for the creation of such varied geometries. Table 6.10 presents the area of each pore and the sample in which it was observed. It also shows the variation between the largest pores in each sample. Although these only account for the two largest pores

observed in each of the micrographs, the area values between samples show a great deal of variation. For example, the overall largest pore is observed in Sample three with an area of 198169 μm^2, whereas the largest in Sample four is less than half this area with a value of 83396 μm^2.

Table 6.10: Area of each pore shown in Figure 6.23 and the sample in which it was observed.

Pore	Sample	Area (μm^2)
1	3	198169
2	5	159790
3	6	159263
4	5	144586
5	6	128876
6	2	111988
7	3	85416
8	1	85352
9	4	83396
10	4	82267
11	2	70814
12	1	59625

6.3.3. Microstructural Data for use in FEA Models

In order to create a representative graphite structure in an FEA environment, microstructural data ascertained from optical microscopy is refined and processed to create models of appropriate detail (discussed in Chapter 7). The six samples used to characterise the pore distribution in the material are used to achieve this. As already discussed in this chapter, the application of appropriate threshold values to the samples will create a representative distribution of porosity. These distributions can then form the basis of the microstructural models. Successful integration of this data into models will enable the effects of the relative differences in microstructure to be determined. Property distributions (*i.e.* stress, strain *etc.*) should demonstrate the effect pores of different geometries have on the mechanical performance of the material. In addition, quantitative analysis of modelling data should enable a comparison between samples. Detailed information regarding the computational procedures to create such models is described in Chapter 7.

6.4. Chapter Summary

This chapter has briefly described a number of microscopy approaches and identified methods that are of particular use in the field of material science and applicable to the size range being investigated. Optical microscopy was described in general terms as well as considering specific methods that are applicable to this study. The relevance of careful sample preparation in attaining accurate and reliable data was also outlined. Image analysis methods to capture, enhance and characterise micrographs were discussed in detail with particular emphasis on the most useful tools for characterising porosity in graphite, namely threshold and segmentation procedures.

An extensive investigation into the microstructural characterisation of pore distributions in six graphite samples was undertaken in 2D. Each sample micrograph was comprised of 99 individual images tilted to create a composite image. Composites image had approximate dimensions of 10 x 10 mm enabling a large area of the material to be captured and analysed. Appropriate methods to ensure the accurate characterisation of distributions were applied and data was ascertained from the six samples. A number of minimum pore thresholds were considered to identify the amount of sample porosity that is attributed to various pore size ranges. Additionally, pore size distribution plots were created to identify the effect of pore size on the overall porosity in the sample. These plots also allowed for a comparison between micrographs.

Characterisation of the small pores in the graphite was shown to be potentially inaccurate due to the relative differences in the preparation of samples. However, increasing the minimum threshold area to 100 μm^2 or greater was effective in disregarding these inconsistences and enabled a direct comparison of all six samples at a number of different pore size ranges. Additionally, examples of pore geometries showed a large variation in both size and shape and highlighted the relative disparity between samples.

Chapter seven will discuss the development of a microstructure model which utilises the characterisation data presented in this chapter. Integration of microstructural data into an FEA environment will enable a representative microstructure model to be created and computational data to be generated from simulations.

Chapter 7 – Development and Implementation of a Microstructure Model

The previous chapter, relating to the capture of high resolution 2D images provided a large data set from which models can be built. This chapter will detail some potential modelling methods that were considered before explaining and justifying the chosen methodology. The processes, inputs and outputs relating to the application of ANSYS FEA software are also outlined in this chapter.

7.1. Preliminary Model Considerations

Prior to considering any practical aspects of model development, it is important to understand how it may be used in the context of the work and what it needs to achieve. The following list highlights some key aspects that the model should aspire to:

- It should be representative, as far as reasonably practical, of a graphite microstructure[3].
- Loads and constraints must be applied to the model to allow a solution to be determined and provide a realistic assessment of the model performance.
- The model should allow for a range of loading scenarios to be simulated.
- Post processing distributions (*e.g.* stress, strains *etc*.) should demonstrate the influence of microstructural features on the intensity of the applicable parameters.
- Failure criteria are derived from calibration and normalisation of output results.
- Cracks propagation should be simulated upon satisfying the predetermined failure criteria.
- The performance of the material (*e.g.* load-deflection response, crack growth resistance *etc*.) should be determined as a function of crack propagation.

[3] The specific context of the work relates to IM1-24 graphite, however, the methodology should be applicable to other materials.

7.2. Model Development

Initially, several modelling approaches were identified, three of which are briefly summarised in this chapter. Namely:

- A probabilistic pore distribution model based on a randomised algorithm approach involving the removal of areas from a solid model that correspond to pores in the microstructure (similar to Holt, 2008).
- Removal of elements from a solid model that relate to a probabilistic pore distribution as defined by an algorithm.
- An observed distribution model created from microscopy data.

Probabilistic methods were initially considered to be preferable due to their versatility and the ability to model a large number of different microstructures with a relatively small amount of experimental data. As such, early models focused on methods to define shapes within the ANSYS environment that would accurately represent a graphite microstructure. The simplest method of simulating porosity in the model is to create voids in a solid model. This can be achieved through use of the ANSYS 'subtract' command. Careful consideration of sizes and shapes to remove from the model should enable a representative microstructure to be simulated. A very simple example of this technique, which involved the removal of different sized circles, is shown in Figure 7.1(a). This model does not take into account any size considerations or any size or shape distributions, however, these factors could potentially be incorporated if the model was developed further. An alternative method for creating voids in the model is shown in Figure 7.1(b). Rather than removing areas from a solid model, this method creates a solid mesh before removing elements. This method has the advantage of ensuring the model has an even and consistent mesh before microstructural characteristics are applied. However, the 'resolution' of these features is effectively limited by the mesh size applied to the model.

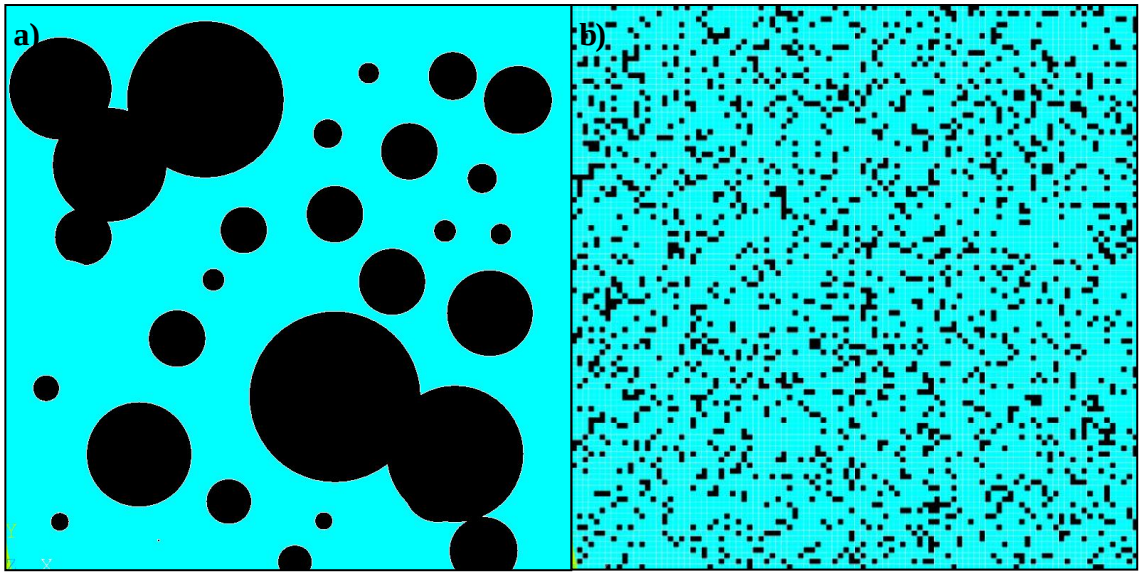

Figure 7.1: Examples of preliminary investigations into microstructural models showing a) removal of circular areas and b) removal of elements.

Further development of both models could potentially enable a representative microstructure to be generated through probabilistic methods. Indeed, some efforts were made to create computational codes that would take the preliminary techniques and apply a more structured consideration to the pore distributions. These codes showed some promise, however, it was determined that utilising data ascertained through microscopy would produce a more representative microstructure, thereby, satisfying a key aspect of this work. This method involved the utilisation of existing micrographs to effectively mirror the pore networks in an FEA model. Due to the ability to accurately model these features, this technique was selected as the most appropriate to develop and eventually use in computational simulations.

Microscopy data in the form of an image cannot be readily manipulated into a working model. It was therefore necessary to develop a methodology to convert microstructural data into a useable ANSYS format.

Image analysis is first used to acquire microstructural data through application of the defined methodology (as shown in Figure 6.10). The image is then segmented into areas representing pores and solid material. The high resolution of the micrographs means that they must be resized to a more appropriate scale. This stage does detract from the detail in the model and results in some smaller pores being effectively

removed from the analysis. However, the primary interest is with regards to large pores and the overall distribution, which is still representative after the resize. A bitmap matrix is then output from the resized image. This matrix characterises each pixel in the image as being either black or white and this information is used to create the model. White pixels in the binary images are pores and will be represented as such when the model is created.

Conversion of this information into a workable ANSYS format is achieved through the application of custom written macros. These macros take account of the matrix and the representation of each pixel. Rearrangement of the matrix into a column of data allows a number to be assigned to each pixel. This is followed by an 'if' command which differentiates between solid material and pores. If the pixel is regarded as being a pore (*i.e.* it is white) the corresponding number is preceded by the ANSYS element unselect command 'ESEL,U'. These pixel numbers and commands are collated to create a *.lgw file which can be integrated with the ANSYS FEA program.

Construction of the ANSYS model first requires a solid area representing the material to be defined. It is crucial that the dimensions of this area correspond to the image resolution. For example, if the image has a resolution of 150 x 100 pixels, the ANSYS model must also have dimensions of 150 x 100 (note that units in ANSYS are arbitrary). Meshing of this model with an element edge length of 1 will result in a mesh density that exactly relates to the pixels in the image. Running the *.lgw file in ANSYS will remove elements from the model that correspond to pores in the initial image. This methodology is outlined in Figure 7.2.

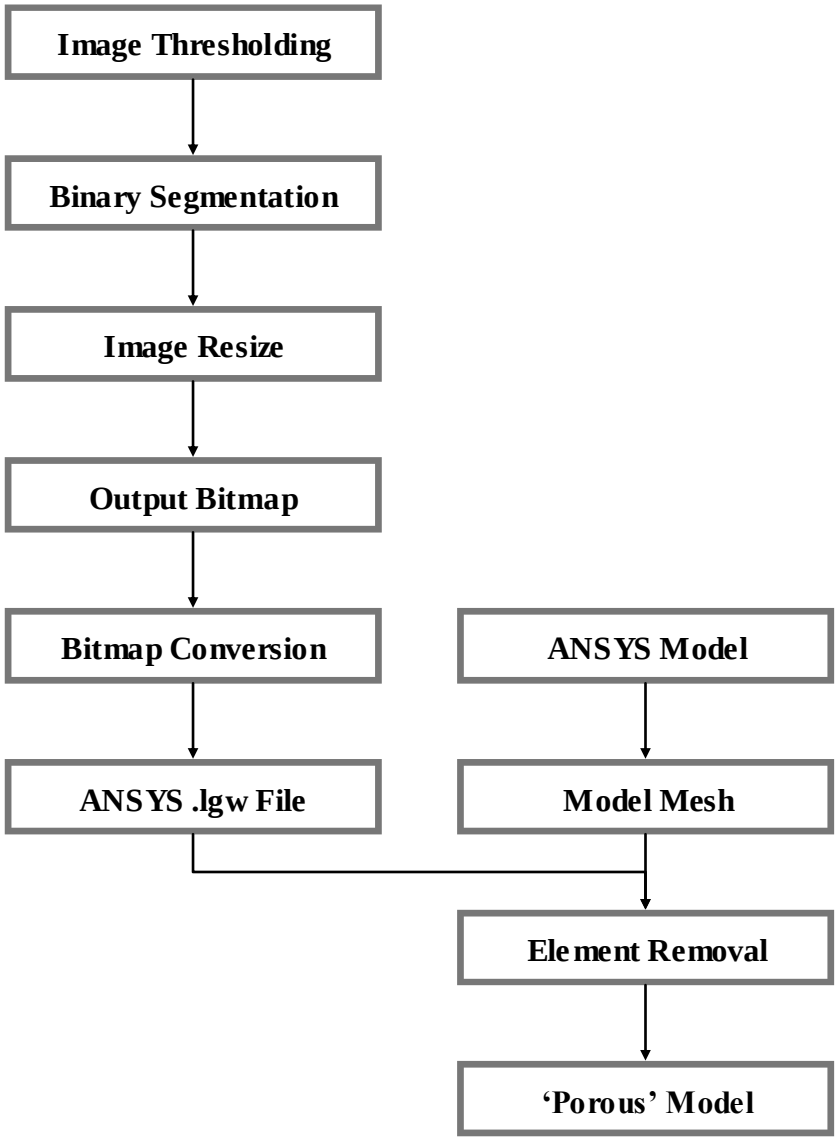

Figure 7.2: Methodology to generate a 'porous' microstructure in ANSYS from image analysis of graphite microstructures.

As a consequence of the order in which pixels in the bitmap and elements in the ANSYS environment are defined, they are not directly relatable without some further pre-processing. This problem can be rectified by rotating the image clockwise through 90^{o} before applying the macros. Alternatively, using square images would negate the requirement to rotate that image. This would effectively rotate the model when it is created and therefore careful consideration of constraints and loads would be required if a particular orientation was to be tested. An example of the conversion from a binary image to an ANSYS model is shown in Figure 7.3

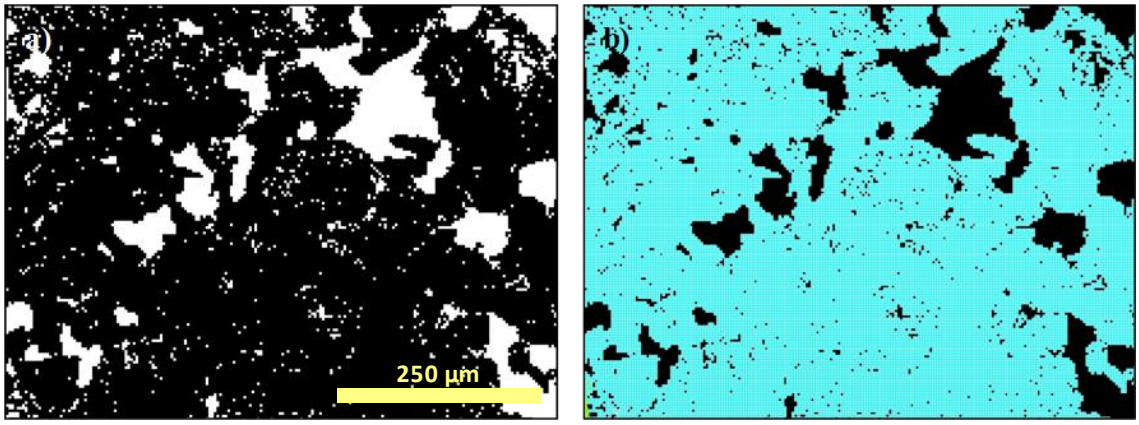

Figure 7.3: Example images showing the conversion from a) binary image detailing porous (white) and solid (black) areas to b) representative ANSYS FEA model (blue areas are elements (*i.e.* solid material) and black areas represent pores).

Loads and constraints in a two dimensional model can be applied to individual nodes or elements, however, lines are more commonly used. This could potentially be problematic due to the presence of pores at the model boundaries. Incorporating a thin continuum region at the top and bottom surfaces enables the uniform application of loads and constraints to the model. This continuum region is shown in Figure 7.4 along with the first principal stress distribution for an example model. An alternative method for applying loads to the model is to use a 'clean borders' command when attaining microstructural data. This will not include any pores that are in contact with the image boundary ensuring that loads may be applied to solid surfaces. The example model (Figure 7.4) has a tensile displacement applied in the y-direction. Although this model is purely schematic, it does show how the porosity distribution affects the stresses in the microstructure. Overall, this model shows a concentration of stresses around the pores in the microstructure with relatively large regions of low stress where the material is free from porosity. Pores oriented in the direction perpendicular to the applied load show stress concentrations at their boundaries.

Whilst initial models were constructed in 2D, if mechanical data such as strength values are to be determined, the model must have a depth (*i.e.* 3D). As such 'pseudo 2D' models, which have a depth of one element, allow the continued use of the established methodology whilst modelling a volume from which properties can be calculated.

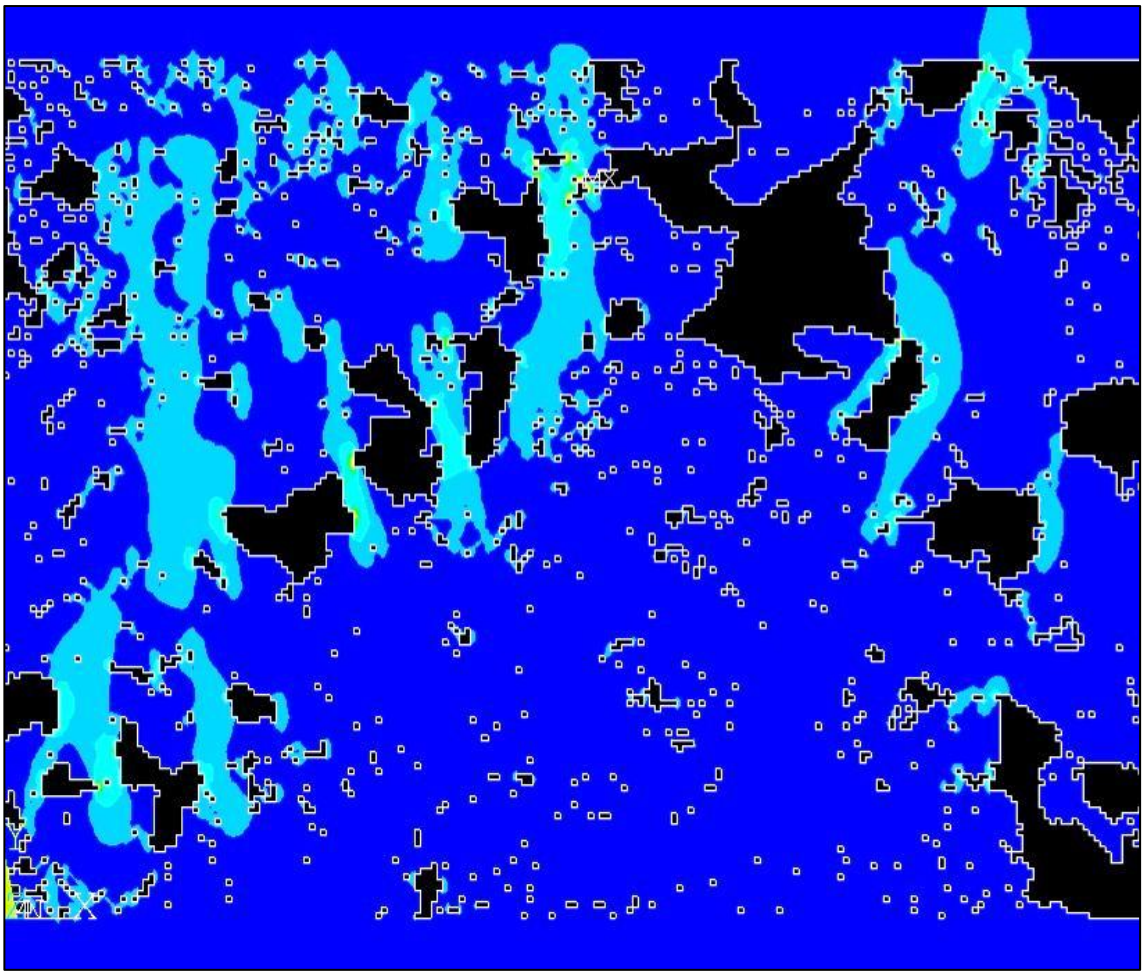

Figure 7.4: Schematic first principal stress distribution for an example microstructure model with displacements applied in the y-direction. Note the continuum bands at the top and bottom for load application.

7.3. Model Parameters

Clearly defining the model parameters, such as material inputs, geometric factors and post processing results is vital to ensure that the response of the model can be fully characterised. In addition, the various parameters associated with the model are optimised before the simulations take place, thus ensuring that they are utilised in an efficient manner. These factors are discussed in the following sections.

7.3.1. Geometric Considerations

The original micrographs contained approximately 221 mega pixels. Since the methodology relies on an equal number of elements being used to mesh the model, the

image resolution must by substantially reduced. Bitmaps from this reduced resolution image are then applied to the appropriate methodology to generate a representative microstructure model. The ANSYS version utilised in this work has a limit of 256000 nodes in a model. Alternative versions enable the use of a greater number of nodes; however, it was found that this limit enables models with a suitable level of detail to be created. In addition, a modest increase in model detail results in a prohibitively large increase in the processing time for the model.

Construction of the microstructural model is in a pseudo 2D configuration and therefore requires the use of 3D 'hex' elements in order to give the model depth. The type used to mesh these models is SOLID65 which have a total of eight nodes, one in each of the element corners to create a cube. Since the elements are cubic in geometry, the 'edge length' (*i.e.* the linear dimensions between each node) will be the same in all three dimensions. The geometry of the bulk model is fixed (10 x 10 mm) and as such the element edge length is dependent on the number of elements used in its construction and thus the resolution of the image bitmap. For example, if the model is generated form a bitmap comprised of 10000 pixels (*i.e.* 100 x 100), each element in the model will have an edge length of 0.1 mm in the x, y and z directions. Elements share common nodes when the model is meshed and thus determining the number of nodes, *N*, in a square model containing eight node elements, can be calculated using the expression:

$$N_{Nodes} = 8 + 8(N_{Elem} - 1) + 2(N_{Elem} - 1)^2 \qquad \text{Equation [7.1]}$$

where N_{Elem} is the number of elements along the x and y dimensions. Thus, the total number of elements in the meshed model is ${N_{Elem}}^2$. Note that this expression is only applicable to a square model utilising eight node elements. Modification of this expression would be required to consider alternative geometries or element types. The plot shown in Figure 7.5 demonstrates the relationship between nodes and element divisions along the x and y linear axes. Using this relationship it can be determined that the maximum number of elements along the linear axes that corresponds to the node limit is 356, meaning a total of 126736 eight node elements may be used in the construction of a representative microstructure model.

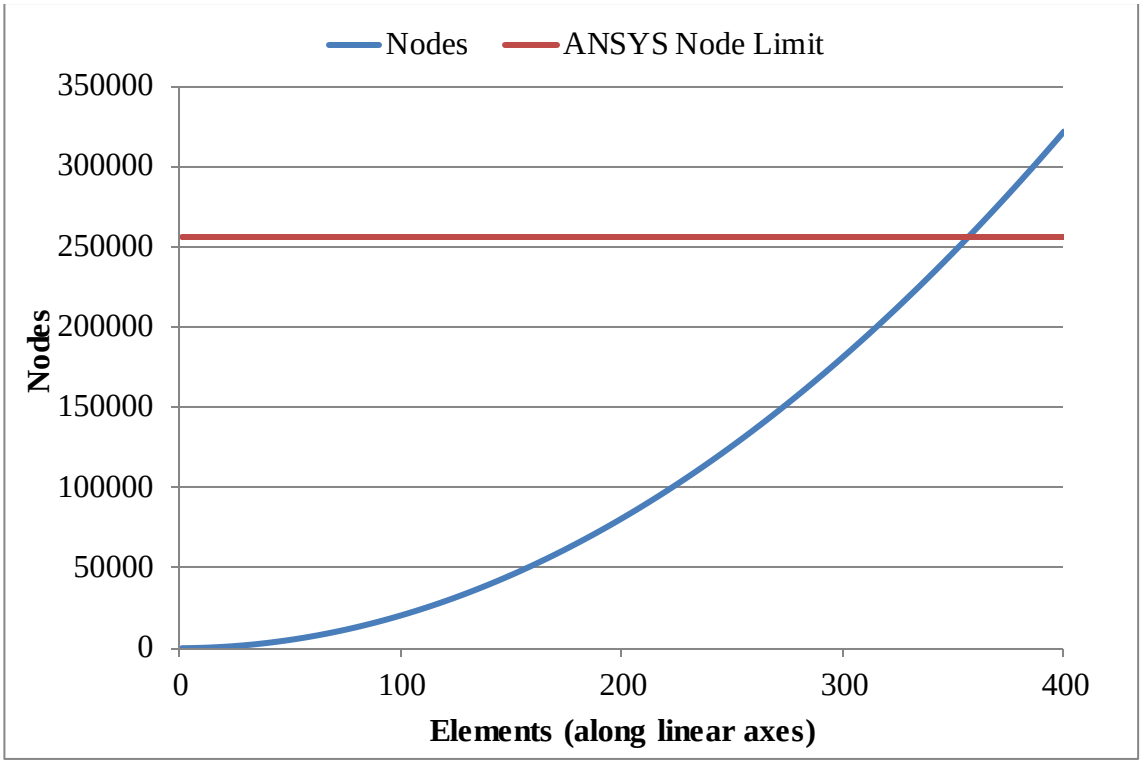

Figure 7.5: Plot to determine the maximum number of element in an ANSYS model due to the imposed node limit.

In order to create models with the highest possible level of detail, the maximum number of elements was used. Although this level of detail requires longer solution times, it is within an acceptable range. Taking this into consideration, the resolution of the resized images must be equal to the maximum number of elements (*i.e.* 356 x 356 pixels). The edge length of elements in a model with this resolution is calculated as being approximately 0.0281 mm. Therefore the dimensions of the three-dimensional model volume are 10 x 10 x 0.0281 mm. Figure 7.6 shows the conversion of the resized image for Sample one into an ANSYS FEA model prior to the application of loads and constraints. The threshold methodology was applied to a micrograph of Sample one using the appropriate segmentation value. A minimum pore area of 100 μm^2 was used to 'filter' out the smaller pores and allow for a more representative comparison between samples. This image was then converted into a 1-bit format and a bitmap generated. The data from this bitmap was used to create the microstructure model (Figure 7.6(b)).

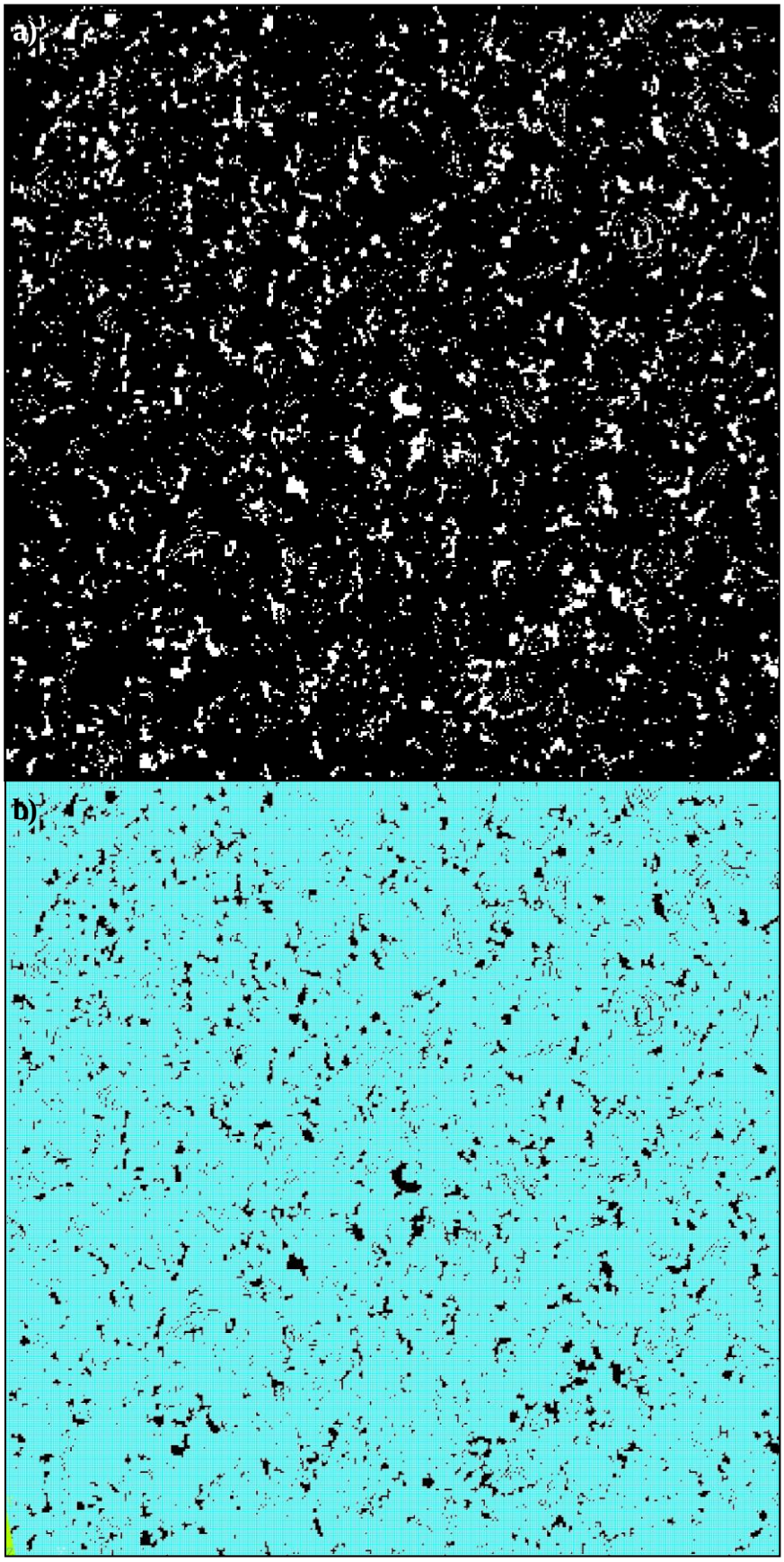

Figure 7.6: Model construction for Sample one showing a) resized 1-bit image, threshold 100 μm^2 (356 x 356 pixels) and b) simulated microstructure ANSYS FEA model.

Reducing the resolution in any image will inevitably lead to some distortion of feature size and shape. Due to the magnitude of these resolution changes, it is expected that a large amount of the detail and intricacies of the features will be lost. One example of this is shown in Figure 7.7 which demonstrates a large feature extracted from Sample one in both original resolution and after it is resized. Although still recognisable as the original feature, the details and overall shape of the pore in the resized image are altered significantly. For the purposes of modelling fracture it is expected to have a limited effect

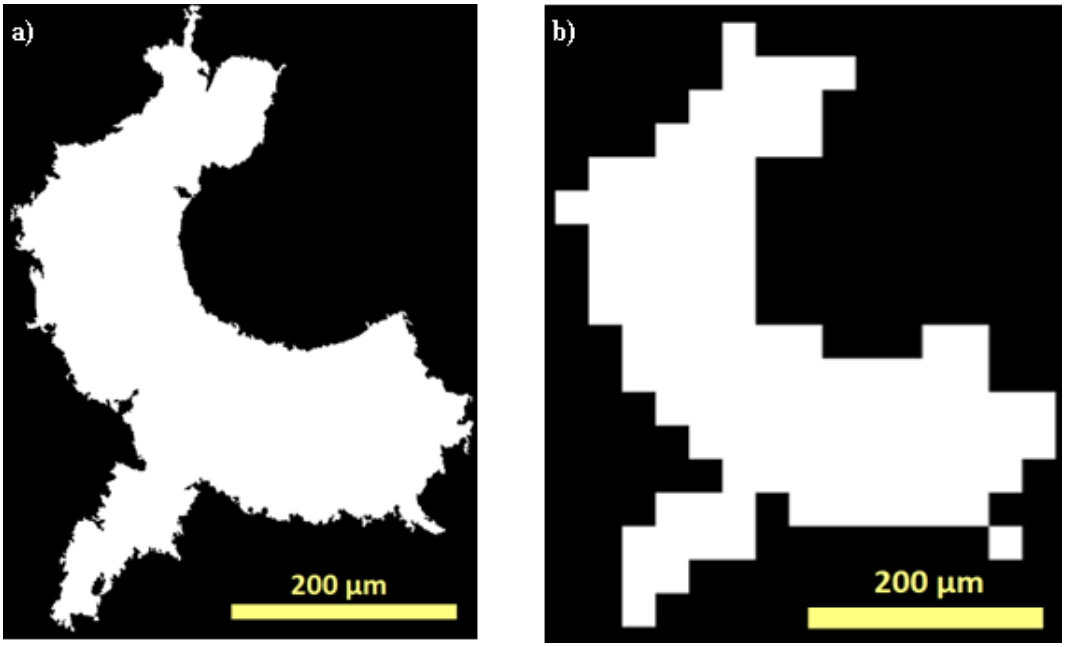

Figure 7.7: Large pore extracted from a) Sample one original image and b) Sample one resized image (356 x 356).

Table 7.1 shows pixel resolution data from the two images and the characterised pore area. Deviation of characterisation values is expected, however, the scale of these deviations will determine whether this method of resizing is adequate.

Table 7.1: Resolution and pore area data for the original and resized images.

	Original Image	**Resized Image**
Resolution	837 x 624	20 x 18
Pixels	522288	360
Pore Area (μm^2)	85352	84472

Although the total number of pixels in the resized image is less than 0.07% of the original, the pore area decreases by approximately 1%. This simple comparison demonstrates that despite a vast reduction in resolution and the loss of detail, the overall shape and size of the microstructural features remains largely intact. Total porosity values for the original and resized images with a minimum area threshold of 100 μm^2 are show in Table 7.2.

Table 7.2: Total porosity from original and resized images with a minimum area threshold of 100 μm^2.

Sample	Porosity (%)		Porosity Decrease (%)
	Original Image	Resized Image	
1	9.94	9.57	3.73
2	9.86	9.48	3.89
3	10.25	10.08	1.70
4	10.60	10.10	4.65
5	10.13	9.76	3.70
6	9.96	9.54	4.22

As with the comparison of the single pore, the resized images show a decrease in observed porosity in the sample. The scale of this decrease is between 1.70 and 4.65%, which is greater than the previously observed deviation in the single pore. This is likely a consequence of smaller pores in the sample being eliminated when the image is resized. Although the decrease in porosity will have an effect on the determination of mechanical properties and fracture parameters, the microstructure models remain representative in terms of both the distribution of pore size and shape.

7.3.2. Material Parameter Inputs

Accurate representation of graphite in the microstructure model is dependent on the utilisation of the correct input parameters. Elastic modulus and Poisson's ratio are required before the model can be solved. These inputs are solely applied to the 'solid' material and not to the simulated porosity. As such, approximations for the elemental properties will differ from that of bulk material. Properties will remain the same between models to ensure that any variations are due to the effect of porosity.

Elastic modulus of the material is of critical importance when modelling in an FEA environment. Successful output of data from the model is dependent on the determination of a representative approximation for this value. In a similar manner to that described by Holt (2008), the Knudsen equation can be used to calculate the elastic modulus, E_0, of a 'solid' model (*i.e.* without porosity):

$$E_0 = \frac{E}{e^{-b\eta}} \qquad \text{Equation [7.2]}$$

where, E is the elastic modulus of the bulk material (*i.e.* inclusive of porosity), b is a constant derived from experimental values and η is the porosity ratio. The mean elastic modulus values from literature (shown in Table 3.1) may be used to define a bulk material modulus of 11.14 GPa. Rice's (1996) approximation of 3.6 is used to define the constant b. It is important to use a pore fraction that is representative of the bulk material and therefore the average value for fractional porosity, 0.1935, is applied when calculating the modulus (Table 6.2). Calculation of a representative elastic modulus using the determined variable yields a value of 22.36 GPa. Since this value is only applied to the solid areas of the model and not the porosity, it should be representative of the bulk graphite modulus when porosity is taken into account.

Poisson's ratio for bulk IM1-24 is commonly stated as being 0.17 (Hartley *et al.* (1996), Tucker *et al.* (1993)). Maruyama *et al.* (1995), whilst investigating physical properties of graphites as a function of irradiation, determined that the dependence of Poisson's ratio on porosity is small. Nevertheless, the study defined a linear relationship between porosity and Poisson's ratio, ν, when the materials were irradiated:

$$\nu = 0.24(1 - 0.58P) \qquad \text{Equation [7.3]}$$

where, P is porosity. The linear relationship was extrapolated to give a 'graphite matrix' value of 0.24. This value is the theoretical value for Poisson's ratio at zero porosity. The Poisson's ratio of the microstructure model will only apply to the solid material and not account for the porosity thereby making this analogous to the aforementioned graphite matrix. Therefore, a representative Poisson's ratio for the model can be approximated to 0.24.

7.4. Crack Propagation

Quantitative data outputs such as stresses and strains can begin to characterise the material and demonstrate how porosity influences the mechanical performance. This can be expanded through the simulation of crack propagation. These data can then be used to determine load-displacement curves and other fracture parameters associated with experimental testing of graphite. Simulated crack propagation would also establish how the porosity influences growth as it extends through the material. Simulated growth can be achieved through removal of elements that exceed set criteria. Critical stress criterion would, for example, remove elements when they exceed a set threshold. This method is shown schematically in Figure 7.8.

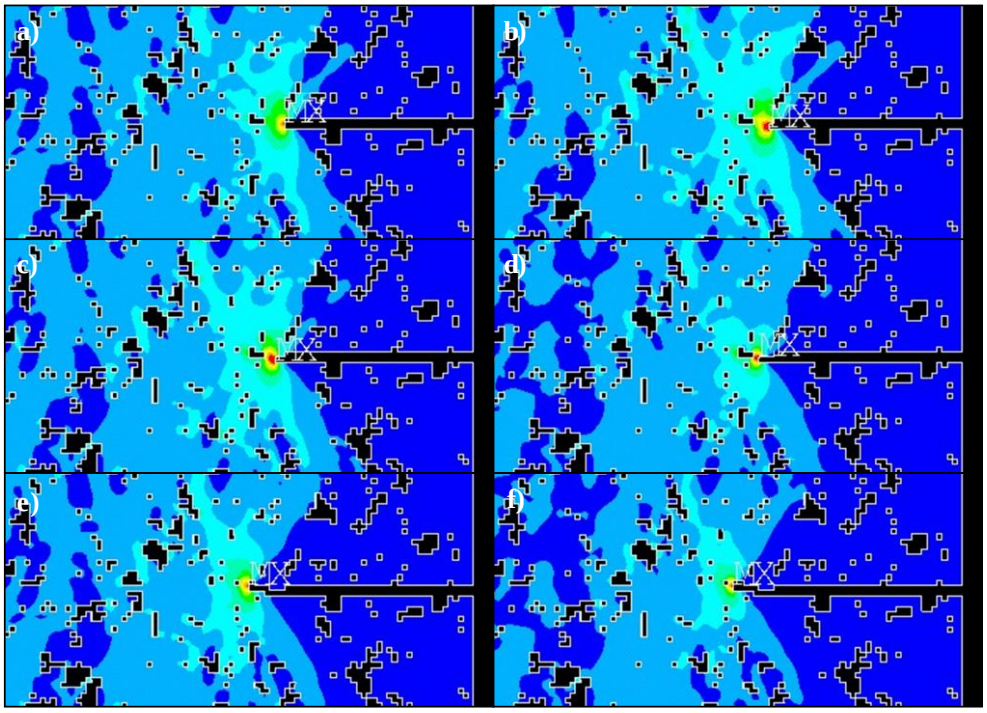

Figure 7.8: Simulated crack propagation based on removal of elements above a critical stress criterion. Note that this is example is purely schematic.

After the model has been solved the area of crack initiation is identified based on the appropriate criteria (*e.g.* critical stress threshold). Elements that meet or exceed the criteria are considered to have 'failed' and are therefore removed from the model, thus creating a crack. Elemental data is output at this stage to allow determination of material properties at each increase in crack length. After all the required elements have been removed, the load/displacement is increased so as to promote further crack growth.

The model is then resolved and the process of removing elements that meet the criterion is repeated. It may be the case that in applying this methodology some elements will be above the failure threshold without increasing loads/displacements. In such instances, the loads/displacements applied to the model will remain the same and the process continued.

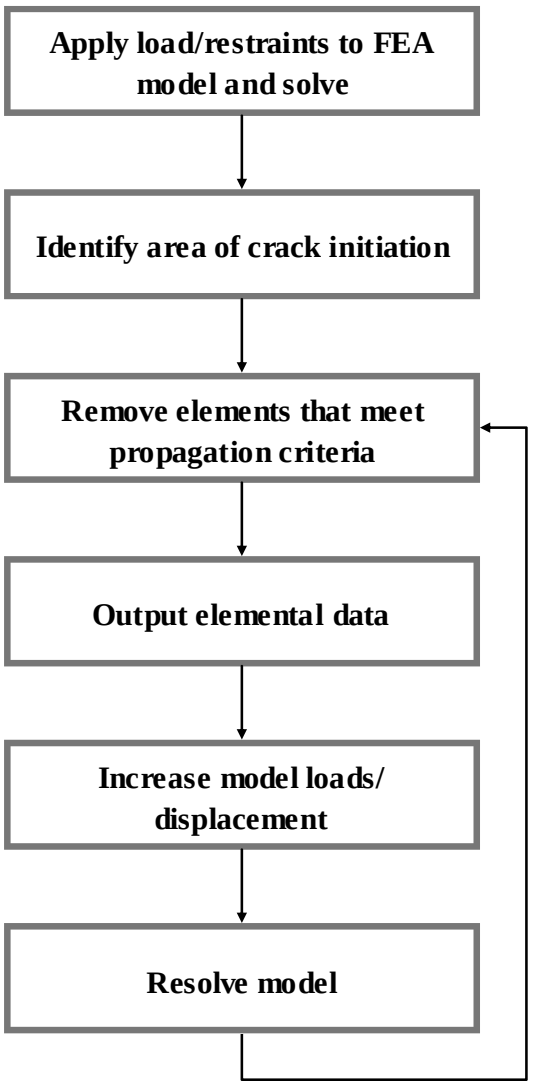

Figure 7.9: Methodology to simulate crack propagation though removal of elements that exceed a predetermined threshold.

Determination of an appropriate threshold is potentially problematic due to a lack of mechanical data on a micro scale. For example, if graphite is assumed to have a tensile strength of 20 MPa, it is unlikely that the application of an equivalent strength as an element removal criterion would result in a representative bulk properties. It is likely that to determine representative model properties, the element removal stress will be far higher than the expected bulk strength of the material. A representative element

threshold can be applied when considering the removal criteria to simulate typical mechanical characteristics of the graphite being investigated. The methodology to determine a representative element failure stress is outlined in Figure 7.10.

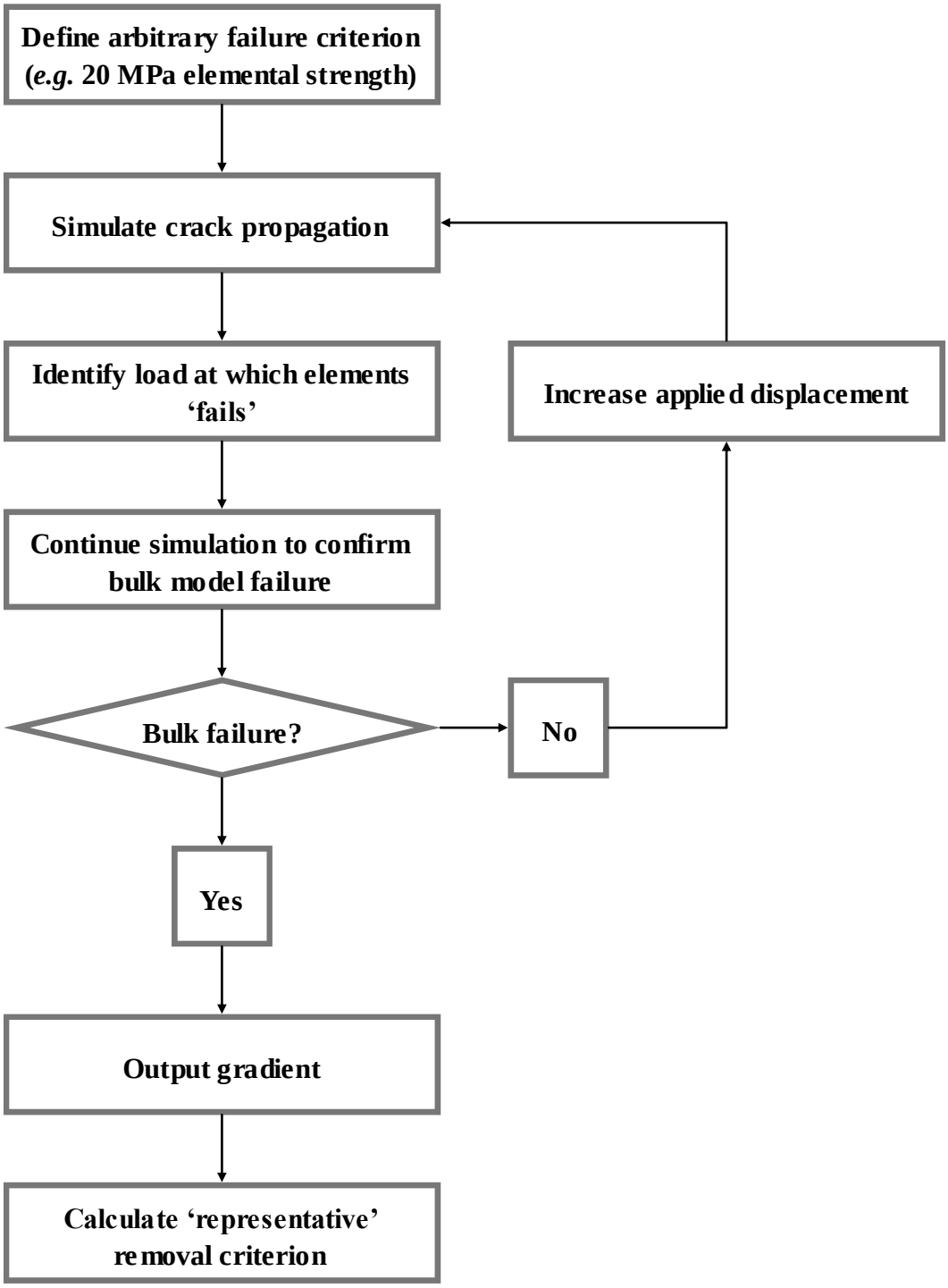

Figure 7.10: Methodology to determine an element removal criterion that allows for a representative bulk model strength.

Before simulating the crack propagation through the model a value close to the expected tensile strength for graphite (20 MPa) is used for this example. Thus, the first element will fail when the loads/displacements are sufficient to cause the first principle stress to reach or exceed 20 MPa. The load at which this first element fails is output and the simulation continued. The crack extension is continued after the first element is removed to determine if the failure was sub critical or indeed the onset of a macro-crack. If the model does exhibit initial micro-cracking, the model is resolved with an increased load/displacement and the process repeated until the model reaches a critical load and can thus be considered to have failed. This load may be used to determine the bulk model strength since the cross sectional area can be calculated form the previously define width and depth dimensions (10 mm and 0.0281 mm respectively). The bulk model strength (σ_M) is plotted against the element removal stress (σ_E) to determine the gradient of the line (G_L) from the expression:

$$G_L = \sigma_E / \sigma_M \qquad \text{Equation [7.4]}$$

A representative element removal stress (σ_{RC}) is calculated using the equation:

$$\sigma_{RC} = \mathrm{G}_L \sigma_T \qquad \text{Equation [7.5]}$$

where, σ_T is representative of graphite's tensile strength. A schematic plot used in the determination of a representative failure criterion is shown as Figure 7.11. Through application of the appropriate methodology, the initial element removal stress (*e.g.* point 1, σ_E) relates to the corresponding bulk model strength (*e.g.* point 1, σ_M). This relationship is linear and thus the gradient of the line can be used to calculate a model strength that corresponds to the expected tensile strength of graphite (*e.g.* at point 2 $\sigma_M = \sigma_T$).

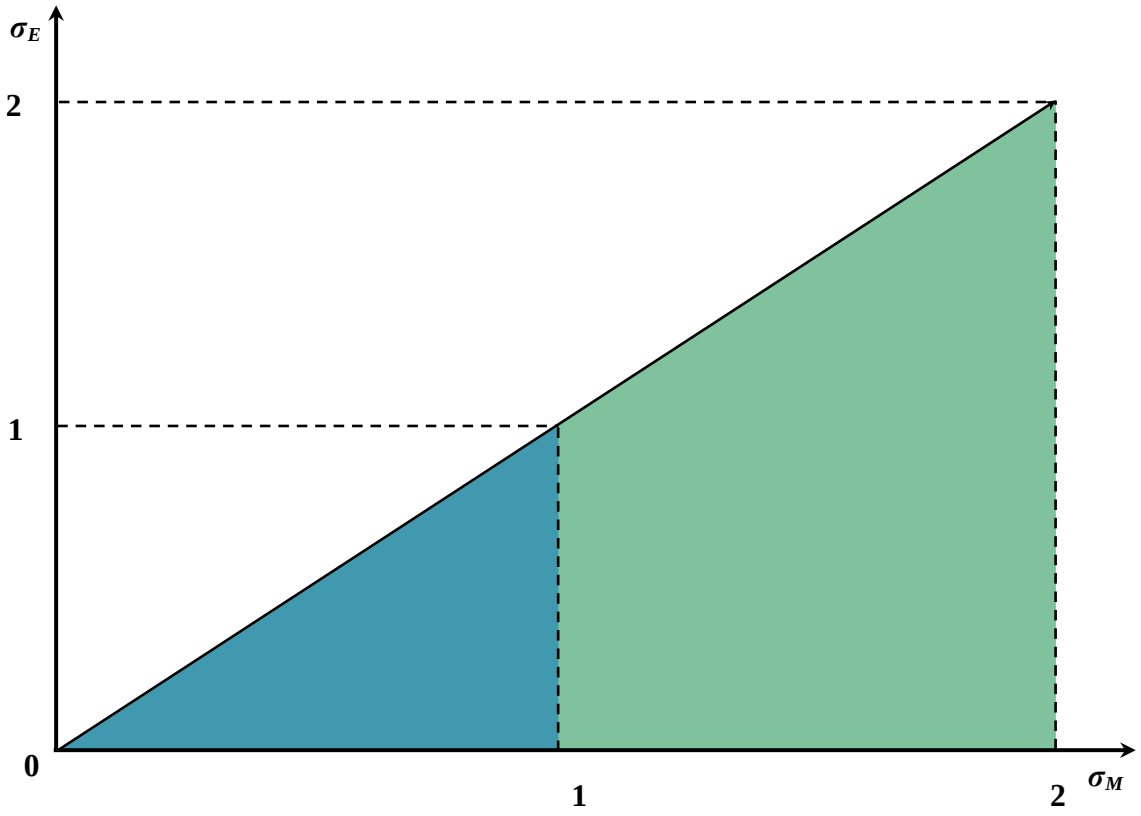

Figure 7.11: Schematic plot of bulk model strength (σ_M) against element removal stress (σ_E). Points 1 and 2 correspond to two example points used to determine a representative failure criterion.

These simulations are physically very small compared to typical experimental tests from which mechanical data is ascertained. As such, it is important to consider issues relating to scale and appreciate that any values from this modelling work may not be representative when applied to a larger volume of material.

Experimental data cannot be applied directly since the elements do not include any porosity. However, experimentally determined values for bulk material can be used to compare with computationally derived 'strength' values. This procedure would require a number of 'element strengths' to be modelled. Altering the strength of individual elements would in turn have an effect on the crack propagation and thus the output load-displacement curves. Determining which element strength corresponds to an appropriate 'bulk strength' for the material should predict a representative material response when the simulation is complete. The bulk strength of the model is defined as the peak of the load-displacement curve. Successful application of the described

methodology will result in a representative load-displacement curve and thus a value for the model bulk strength.

7.5. Loading Scenarios

The volumetric shape of the microstructure models is a cuboid with a total of six surfaces. The 'front' and 'back' surface of the model are reserved for the removal of porosity and subsequent simulation of results and are therefore not suitable for the application of boundary conditions. The four areas the make up the top, bottom, left and right sides of the model may be used to create a loading scenario. When considering how best to represent the appropriate scenarios, boundary conditions can be applied to nodes, lines or areas. Additionally, the type of load or restraint can have an effect on the model simulations. Restraining the model is analogous to the conditions imposed when undertaking a mechanical test. This may mean that nodes, lines or areas are fixed in all directions or a degree of freedom (DOF) in a particular axis may be permitted. Loading can be achieved by applying a displacement or a force to the appropriate region of the model. The location and magnitude of the load is varied to ensure the scenario is representative.

7.5.1. Displacement Loading

Applying a displacement can be to either restrain or load the model. For example, applying a zero displacements to an area will fix in its current position. Positive or negative displacement values will simulate an external movement on the model when it is solved. The direction of the movement (*i.e.* positive or negative) allows for tensile and compressive scenarios to be simulated. In the interests of maintaining a symmetrical model, two surfaces can be displaced in opposite directions. Figure 7.12 shows a tensile loading scenario for a model with displacements applied to the top and bottom surfaces. The displacements are uniform over the applied surface and all the model is free to move in the X-axis. Changing the location of these displacements to the left and right surfaces allows for the analysis of an alternative loading direction. Further, changing the polarity of the displacements (*e.g.* positive to negative) examines the mechanical response to a compressive loading scenario.

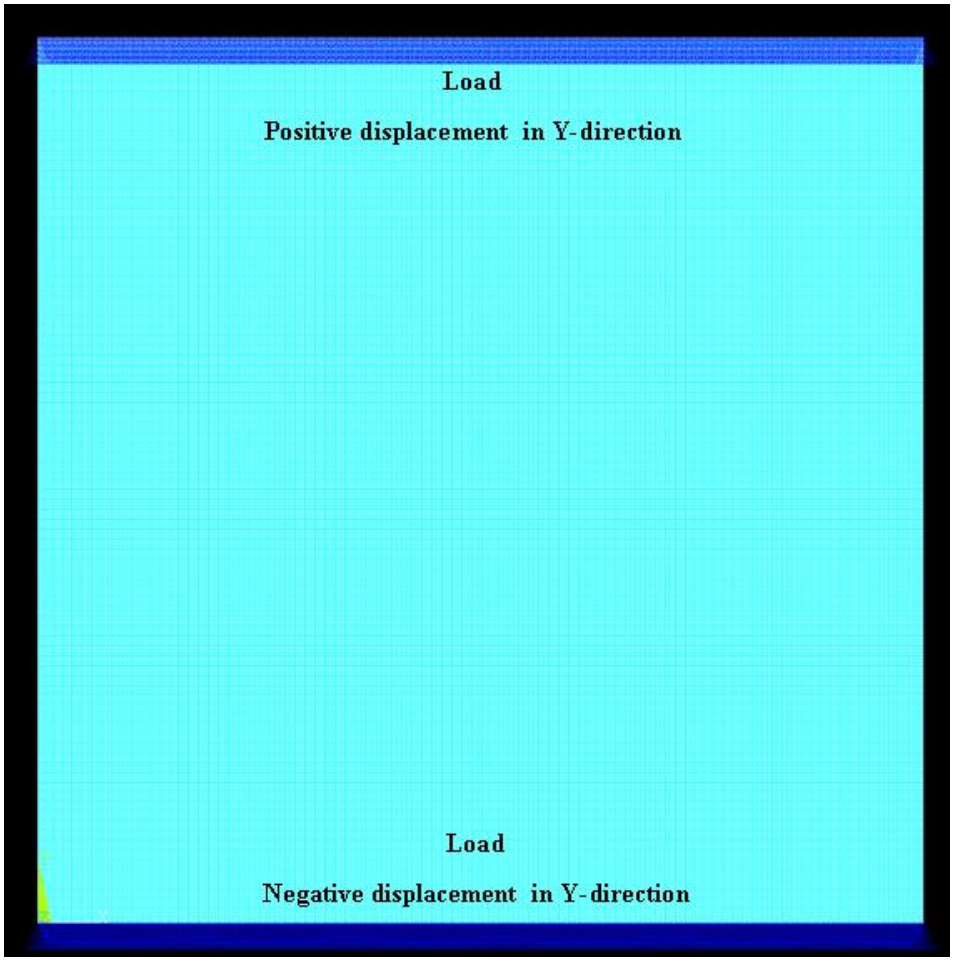

Figure 7.12: Example of a tensile displacement loading scenario in the Y-direction. Compression of the sample may be achieved by changing the polarity of both displacements.

Applying displacement to the model surfaces ensures that boundary condition load is evenly distributed. As such, it is analogous to modelling an experimental test. For example, applying a tensile displacement effectively simulates a tensile test, albeit, simplifying the mechanical performance to focus on two dimensions. Additionally, this model can approximated to the high stress region on the tensile surface of a flexural (*i.e.* three and four point bend) sample where fracture is typically initiated. Figure 7.13 illustrates this approximation with a 10 x 10 x 0.0281 mm volume within the tensile region of a 15 x 15 x 100 mm three-point bend specimen.

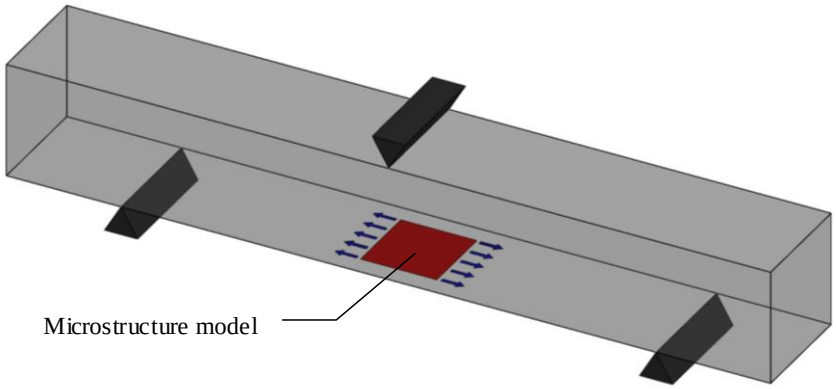

Figure 7.13: Schematic to illustrate how a displacement loaded microstructure model may approximate to the tensile region in a three-point flexural test.

Displacement loading of a sample is sufficient to solve a model and characterise the mechanical properties. Progressive removal of elements may result in the redistribution of stresses, however, upon reloading; elements may remain above the failure threshold, thereby increasing the crack length without altering the external displacement applied to the sample. The macro-crack could potentially be arrested and require an increase in displacement to propagate further. Micro-cracking in the sample may occur prior to or in conjunction with the macro-crack, as is often observed in experimental testing of graphite (Allard *et al.*, 1991).

7.5.2. Notched Sample

In order to model progressive crack growth (*i.e.* experimental testing of CT or SENB samples) the applied loads and constraints are altered to better represent this scenario. Experimental geometries designed to promote controlled crack growth commonly feature a notch to concentrate stresses into a small volume of the sample. It is from this region of high stress that the crack is generally initiated. Crack initiation in these tests will typically occur at relatively small loads, thus ensuring that the residual energy in the test machine does not contribute to catastrophic failure of the sample. Although this consideration may be ignored when modelling a sample computationally, a simulated notch would still have the advantage of controlling the point at which a crack is initiated. Figure 7.14 show the loads and constraints applied to a notched model to enable progressive crack growth to be simulated. The bottom surface is restrained in the Y-direction but is free to move in the X-axis. Forces are evenly applied to the top

surface to exert a stress on the notch tip, from where the crack propagates when the defined criteria is reached or exceeded. The displacement of elements at or near the loaded surfaces will be non-uniform and dependent on their relative vicinity to the notch as well as porosity. For example, the maximum displacements in the Y-direction will typically occur at the corners located above and below the notch. After the crack initiates, it will effectively increase the notch in the sample and thus affect the displacement of the model.

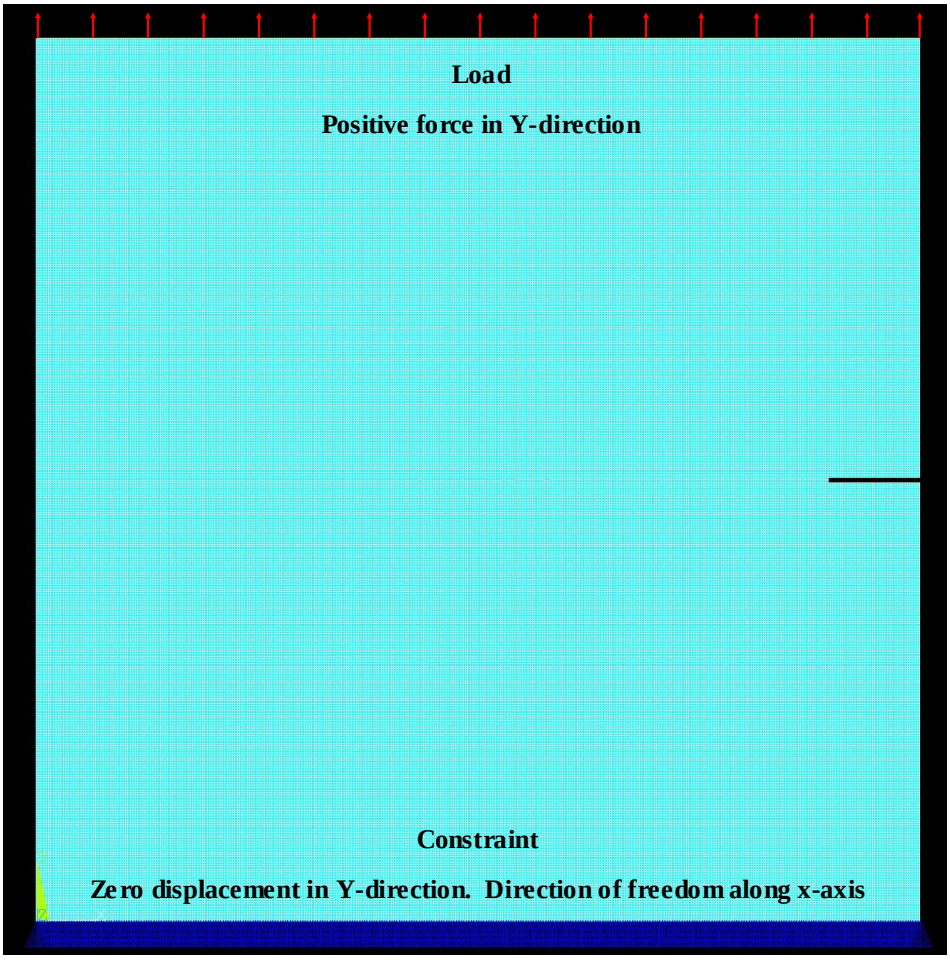

Figure 7.14: Example of a tensile force loading scenario on a notched sample.

Notched models are created through removal of appropriate elements. The model is constructed from a 10 x 10 mm square and consists of a 356 x 356 grid of elements. In order to maintain the symmetry of the model, the notch is two elements 'wide'. Using this information and knowledge of how elements are sequentially numbered, an expression can be derived to determine which elements should be removed to create notches of varying depths. Since the notch is required to be two elements wide, two

expressions (U_1 and U_2) are needed to define the 'upper limits' for which elements should be removed:

$$E_{U1} = \frac{W_E H}{2} \qquad \text{Equation [7.6]}$$

$$E_{U2} = \frac{W_E (H+1)}{2} \qquad \text{Equation [7.7]}$$

where, W_E and h are the number of elements divisions across the width and height of the model respectively (*i.e.* both 356 for this particular model). The 'lower limit' of the element removal range is determined using the expression:

$$E_{L1}, E_{L2} = U - \frac{W_E}{W_L} D \qquad \text{Equation [7.8]}$$

where, U is the upper limit (*i.e.* substitution of E_{U1} or E_{U2}), W_L is the width of the model in mm and D is the required depth of the notch in mm. The two ranges for removal are therefore determined as being element numbers L_1 to U_1 and L_2 to U_2.

Plotting the force input against the maximum displacements calculated by the model is geometrically representative of a compact tension test and should enable controlled crack growth through the model. Compact tension experiments typically apply a cyclic loading scenario, which helps ensure the crack propagation through the sample is progressive. Although some of the fracture mechanisms associated with this experimental set up cannot be simulated (*e.g.*, crack bridging, friction *etc.*), a revised methodology is implemented to maintain an energy balance as the crack propagates through the model. This energy balance approach requires a modification of the existing element removal algorithm.

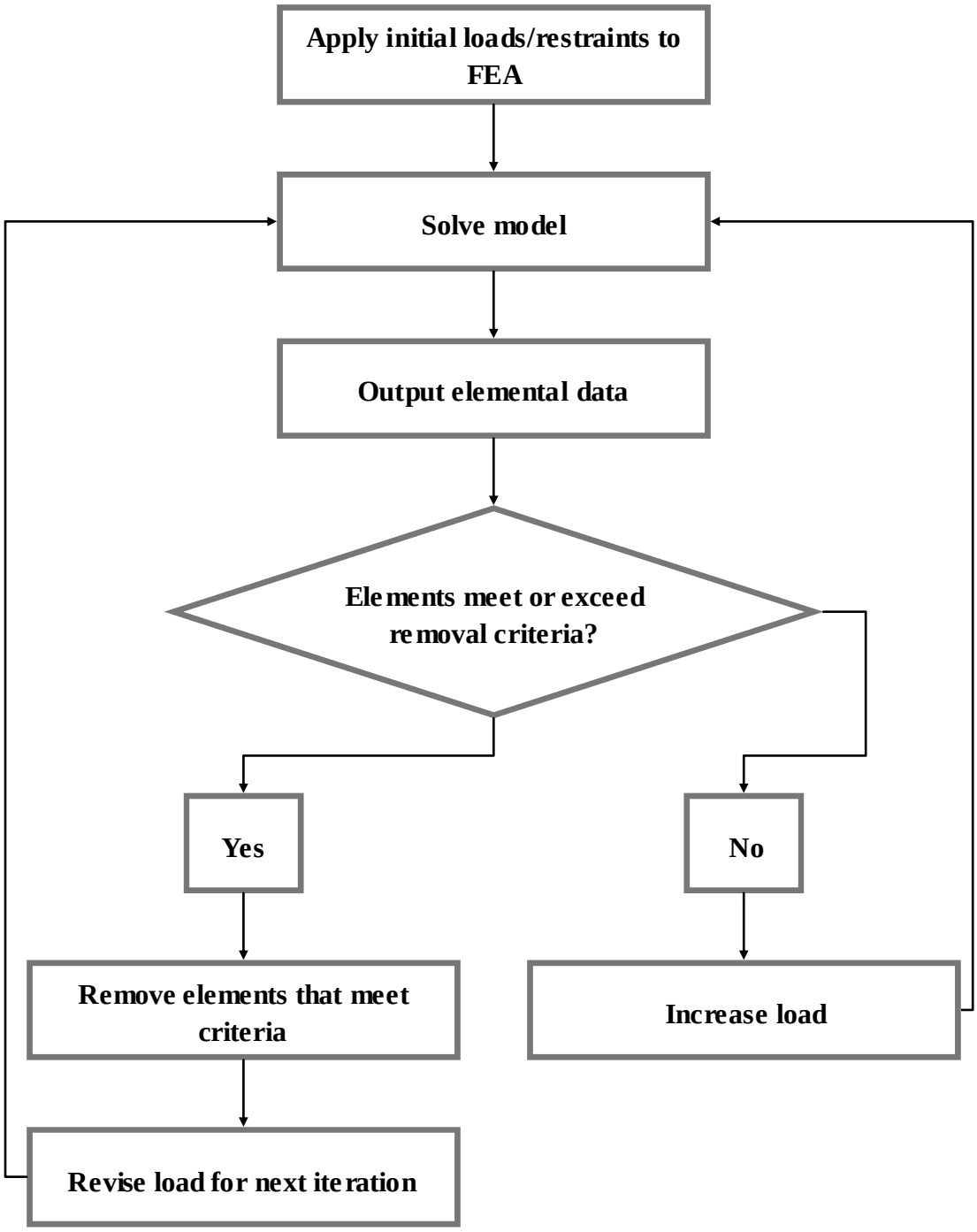

Figure 7.15: Modified methodology to simulate a cyclic loading scenario for crack propagation.

The general methodology for the removal of elements and thus propagate a crack through the model remains largely the same. The primary modification is with regards to the revision of loads before the model is resolved. The initial applied force is calculated using the stiffness gradient of the model to ensure the loads just exceed the failure criteria and initiate fracture in the model (*i.e.* only one element fails). At this point, elements above a failure threshold are removed, thus propagating the crack.

Resolving the model with the same applied force after the removal of elements would result in an increase in the displacement and thus an increase in the total strain energy as shown schematically in Figure 7.16 (a). This increase in energy is unrepresentative of an experimental process and as such, the applied load must be revised to ensure that the energy remains the same between iterations. Further, it is important to account for the energy removed from the model as a consequence of element removal. Therefore the energy balance is derived as:

$$U_2 = U_1 - U_{Element} \qquad \text{Equation [7.9]}$$

where, U_2 is the model energy after element removal, U_1 is the initial energy and $U_{Element}$ is the energy removed from the system due to element removal. Figure 7.16 (b) schematically demonstrates this energy balance approach. Upon removing the elements the model is reloaded with a force that satisfies Equation 7.9.

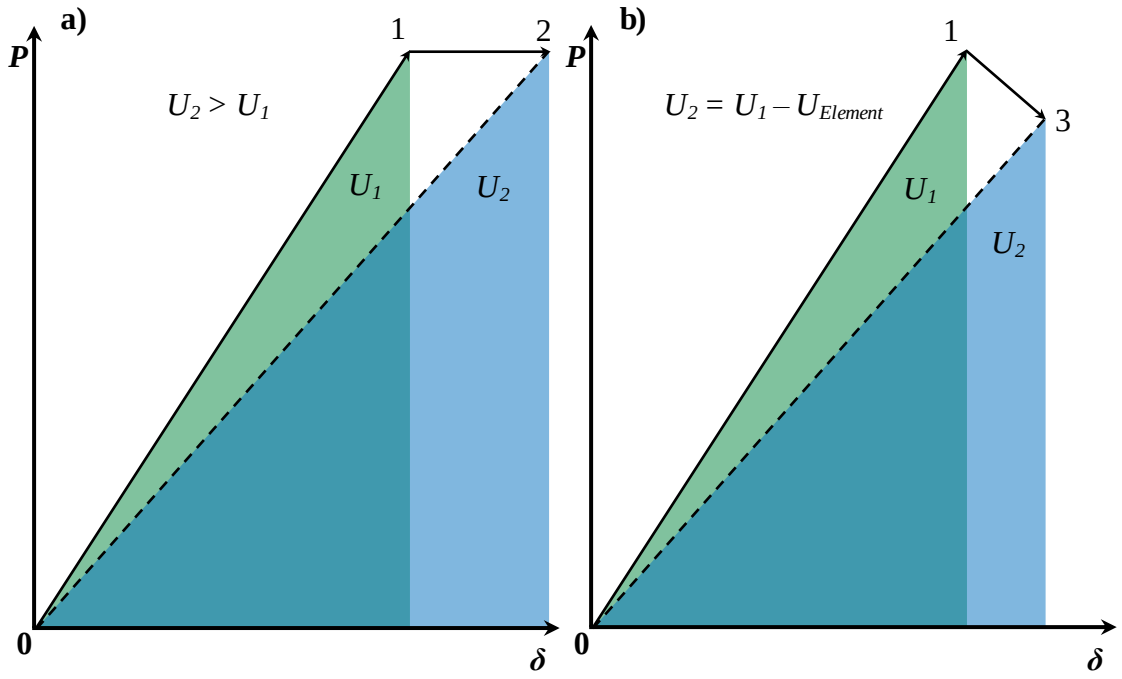

Figure 7.16: Schematic representation of a typical load-deflection response for a) removing elements whilst maintaining the same applied force and b) taking into consideration the energy balance of the system.

The gradients for the lines 0 to 2 and 0 to 3 shown in Figure 7.16 (a and b respectively) are identical. It is therefore possible to use the data from point 2 to accurately

determine a suitable force at point 3 (P_2) that corresponds to the required energy (U_2) using the expressions:

$$U_2 = P_2\delta_2 \qquad \text{Equation [7.10]}$$

$$\delta_2 = P_2\frac{\delta_1}{P_1} \qquad \text{Equation [7.11]}$$

where, δ_2 is the model displacement when loaded with the force P_2, P_1 is the initial force applied to the model and δ_1 the initial displacement. Suitable values for P_2 are determined through an iterative process and must satisfy the following expression:

$$\frac{U_2}{U_1 - U_{Element}} = 1 \qquad \text{Equation [7.12]}$$

7.5.3. Outputs

Displacing the model by a set increment is analogous to moving the cross head on a mechanical test machine. The displacement 'input' should therefore be plotted against a load which corresponds to the reading from a load cell during a mechanical test. The applied load (F) at any displacement can be calculated though use of the equation:

$$F = 2\frac{U}{\delta} \qquad \text{Equation [7.13]}$$

where, U is the total strain energy for the model, determined by summing the elemental strain energy data and δ is the input displacement. Application of a force to the model, to simulate progressive crack growth allows for the output of element displacement data to be used to plot load-deflection curves.

Load-deflection data from the application of forces to a notched model simulates a controlled crack growth experiment. The force input is plotted against the output value for maximum displacement in the Y-direction. Since the model is loaded symmetrically, the maximum and minimum values for displacement are summed to give an overall displacement. Data for each element is processed and the maximum values are determined to characterise the material response. In additional the following elemental data will be output from the model:

- First principal stress and strain.
- Von Mises stress and strain.
- Elemental displacements in x and y directions.

Energy values from the model are acquired from the area under load-deflection plots. The method used to determine these values is similar in principal to the traditional graph paper calibrating, cutting, and weighing procedure. The energy contained within a plot (U_T) is defined as the load multiplied by the deflection ($P \times \delta$). Energy input into the model may be characterised as the area under the load-deflection curve (U_C). Figure 7.17 shows how these energies may be represented on a schematic load-deflection curve.

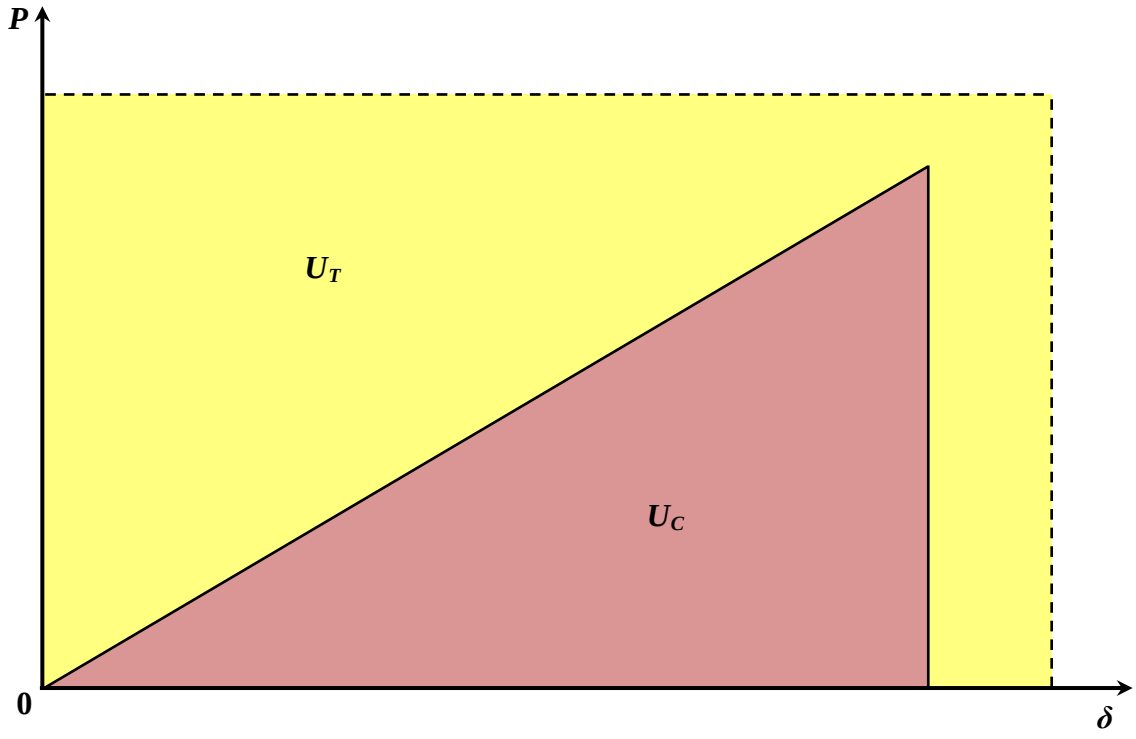

Figure 7.17: Schematic representation of the methodology to segment area under load-deflection plots.

The energy under the curve can be calculated as a proportion of the total plot area using the expression

$$U_C = \frac{U_T}{A_T} A_C \qquad \text{Equation [7.14]}$$

where, A_T and A_C are the total area and area under the curve respectively. Load-deflection plots are output as image files and analysed using the software 'Image Pro Plus' to determine values for A_T and A_C. The number of pixels contained within the total area is measured using simple characterisation tools. This data can then be used to calculate the effective energy per pixel. Areas under curves are measured by thresholding the image to segment the specific area of interest, thus determining the number of pixels that are contained within it. This method is far more accurate, consistent and time efficient than the graph paper calibrating, cutting, and weighing procedure.

7.6. Chapter Summary

This chapter has detailed the development of a simulated microstructure model. Determination of suitable input parameters has been explained with consideration for theoretical relationships between material properties and porosity. Algorithms that are utilised for the construction, solution and data output of the models are discussed.

Chapter Eight will utilise the methods outlined in this chapter to generate computational data from the FEA models. Additionally, the output data will be discussed in relation to experimentally derived results.

Chapter 8 – Simulation Results

The previous chapter explained the considerations associated with the development of a representative microstructure model. The subsequent application of the developed methods focused on the following aspects:

- Elastic response of models and the variation between models due to pore distributions.
- Crack propagation through a model subject to tensile displacement and the load-deflection response.
- Crack propagation through a notched sample with an applied tensile force and the load-deflection response.

This chapter presents and explains the simulation result as well as discussing their validity when compared to experimental testing.

8.1. Tensile Simulations

Initial results are based on the elastic response of the model when a displacement is applied. Data from these tests can be used to determine the elastic portion of a load-deflection curve. Tensile displacement in x and y axes are applied to the microstructure model separately to produce two data sets per sample. Comparing the two separate data sets for each model along with consideration for the pore distribution shows how the directionality of porosity affects the mechanical response of the model. Additionally, consideration of the relative responses between samples will determine how the porosity in the sample influences the material properties when loads are applied.

Figure 8.1 and Figure 8.2 show examples of the first principal stress distribution when the model is displaced in the y and x axes respectively. These models are displaced by 0.01 mm. At this stage, the value is arbitrary and is used purely to demonstrate the relative variations between samples and loading orientations. Additional examples showing the von Mises stresses and y-displacement are shown in Figure 8.3 to Figure 8.6. All of the plots are element solutions which are averaged at common nodes.

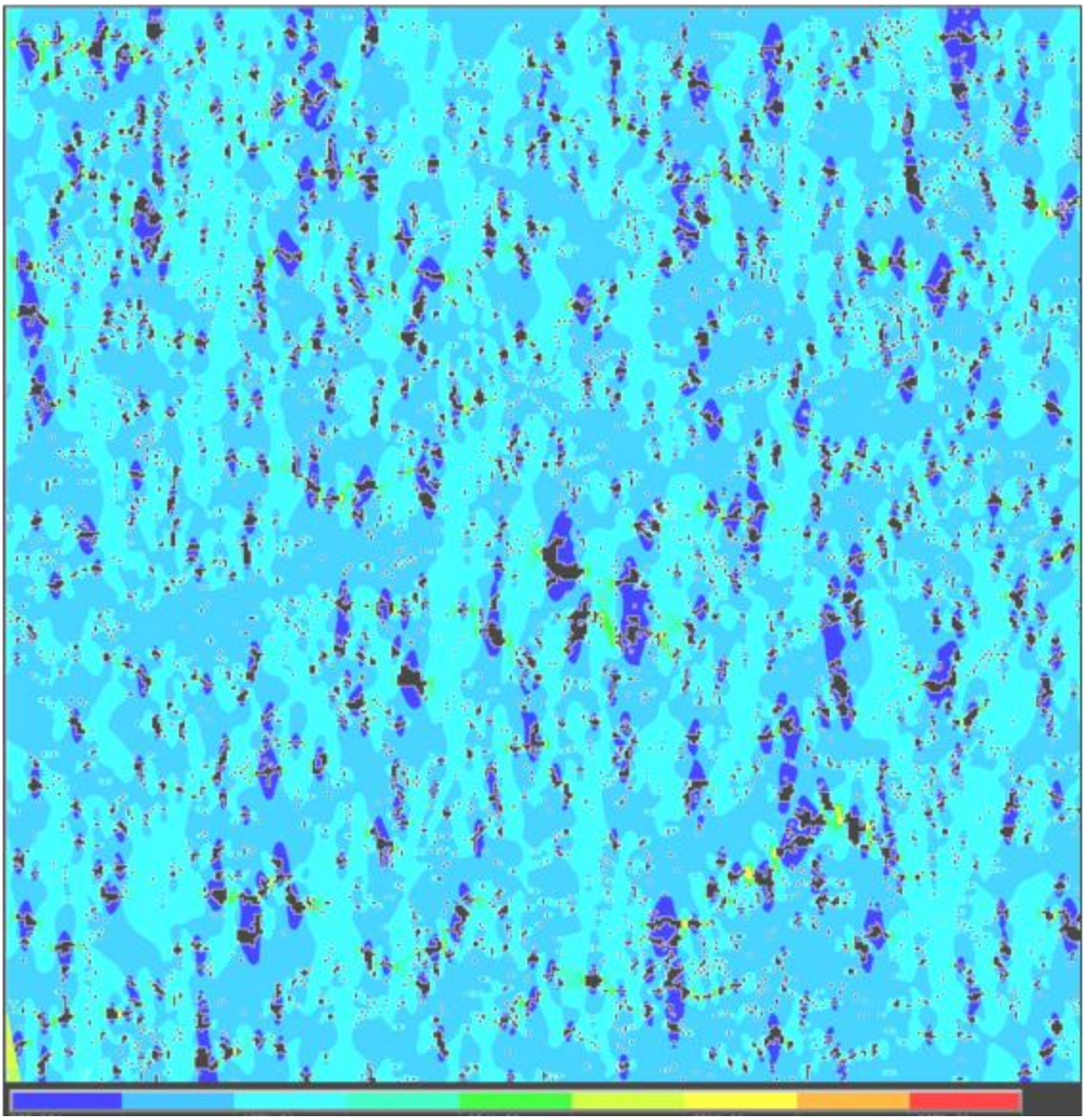

Figure 8.1: Sample one schematic tensile displacement in Y-direction. First principal stress distribution (blue indicates low stress, red indicates high stress)

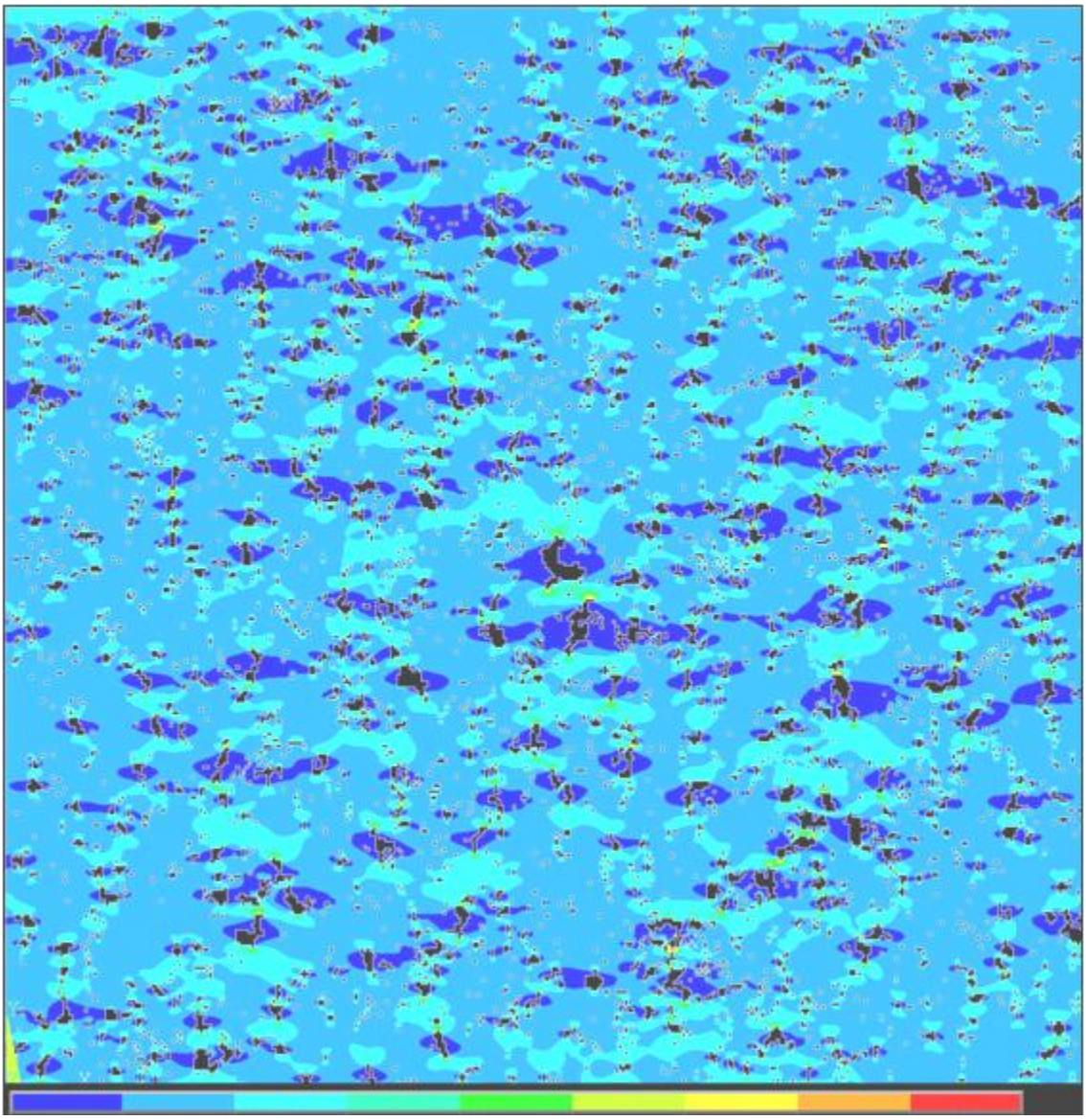

Figure 8.2: Sample one schematic tensile displacement in X-direction. First principal stress distribution (blue indicates low stress, red indicates high stress).

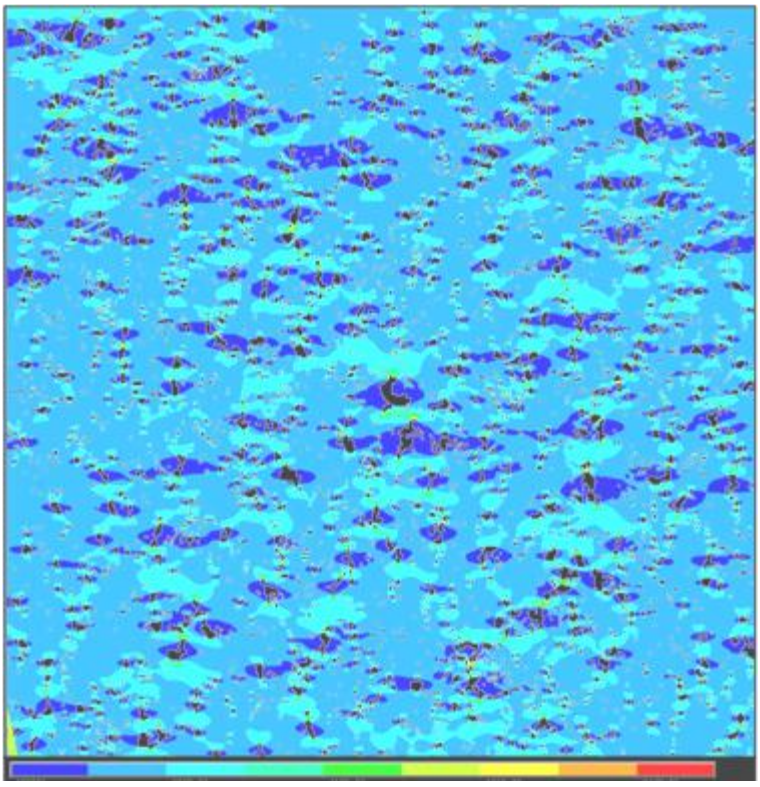

Figure 8.3: Sample one schematic tensile displacement in Y-direction. von Mises stress distribution (blue indicates low stress, red indicates high stress).

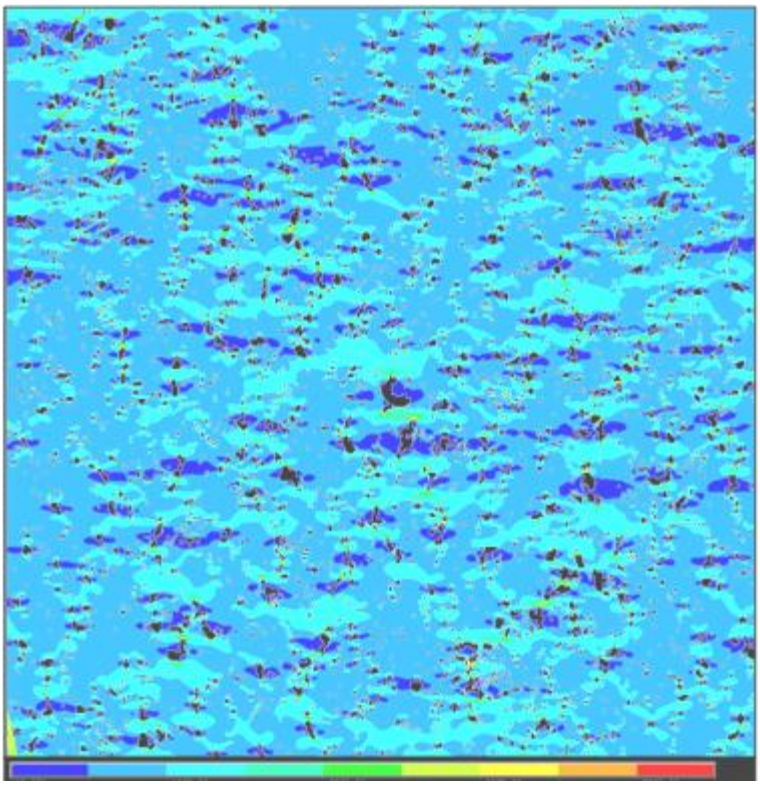

Figure 8.4: Sample one schematic tensile displacement in X-direction. von Mises stress distribution (blue indicates low stress, red indicates high stress).

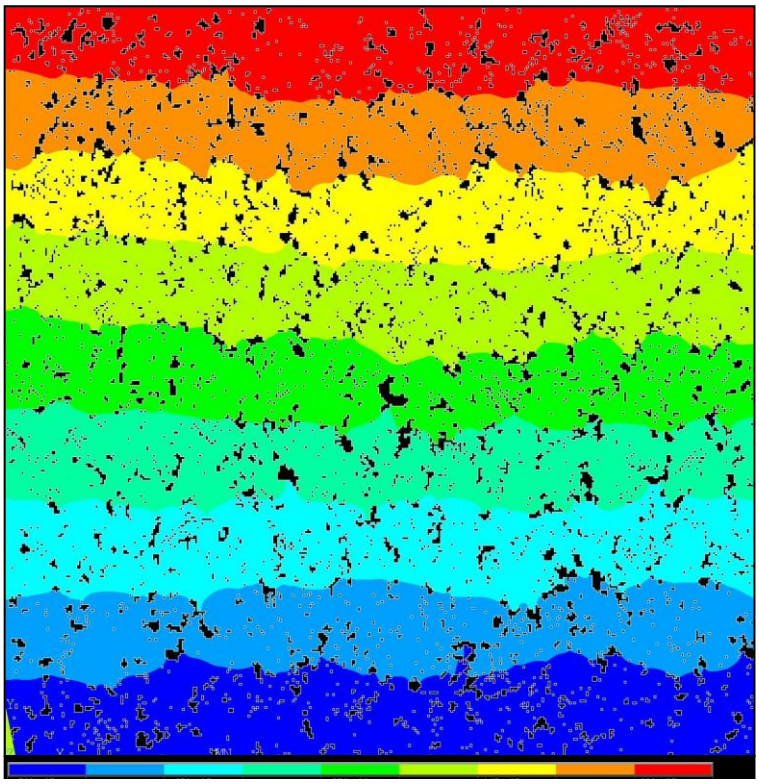

Figure 8.5: Sample one schematic tensile displacement in Y-direction. Displacement in Y-direction (blue indicates low displacement, red indicates high displacement).

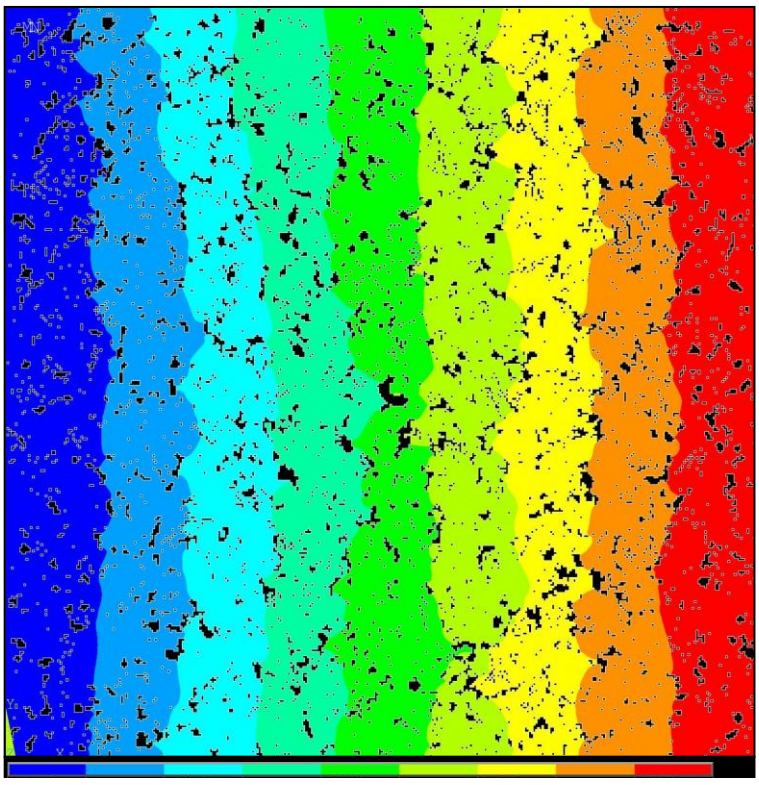

Figure 8.6: Sample one schematic tensile displacement in X-direction. Displacement in X-direction (blue indicates low displacement, red indicates high displacement).

It is clear that the orientation in which the model is displaced will affect the property distribution as is demonstrated by the previous set of images. Regions of high stress (both von Mises and first principal) tend to be located at the boundary of pores orientated perpendicular to the applied displacement as shown in Figure 8.7 (a). Further, high stress regions are observed in the narrow 'bridges' between adjacent pores as shown in Figure 8.7 (b).

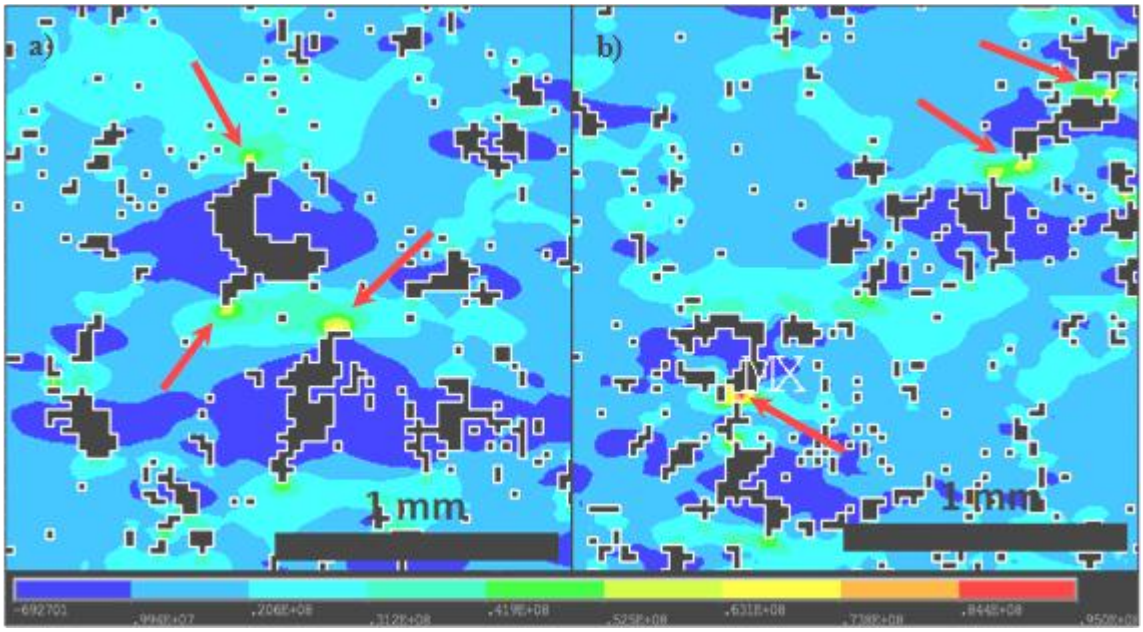

Figure 8.7: Magnified examples of first principal stress distributions around pores from Sample one loaded with a displacement in the X-direction showing a) stress concentrations at the pore boundaries and b) high stress regions between adjacent pores.

As would be expected, the maximum and minimum displacements in the models are at the loaded region and are approximately equal to the applied displacement. However, the model's displacement distribution is influenced by the porosity as shown by the non-uniformity of the magnitude banding in Figure 8.5 and Figure 8.6.

The initial elastic response of the models (*i.e.* prior to removal of elements) is shown in as a normalised chart in Figure 8.8. Although there is a similar response from each of the models, they do some variation in the gradient of this initial curve (*i.e.* the bulk stiffness of the model). Since the material inputs, model geometry and the applied boundary conditions are nominally the same; the observed variations are solely due to the porosity.

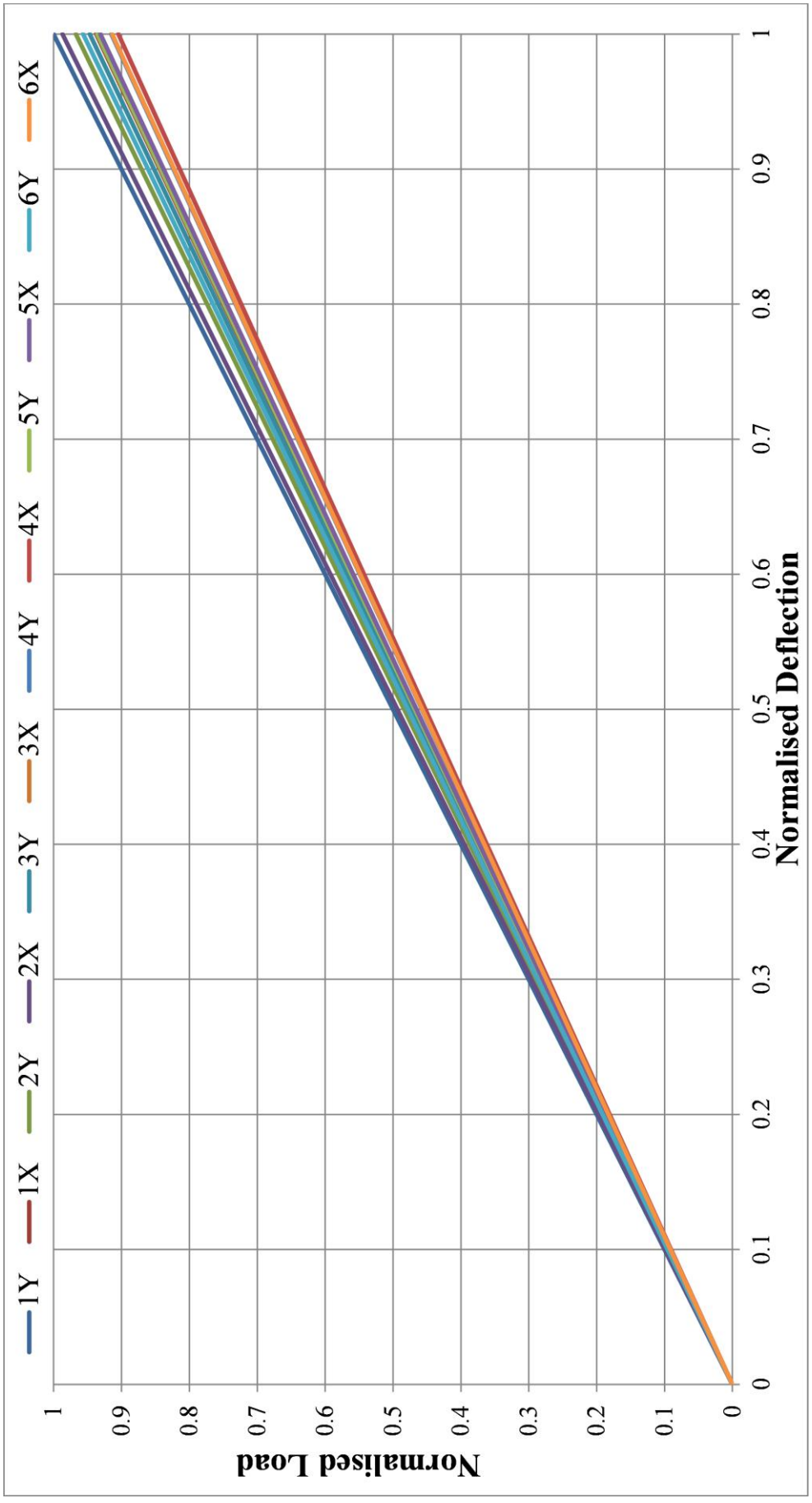

Figure 8.8: Normalised load-deflection curves showing the initial elastic response of the six samples loaded in x and y directions.

Analysis of the elastic gradients shown in Figure 8.8 indicates that the amount of porosity is not the only factor in determining the bulk stiffness of the model. Mechanical performance of the model is dependent on the loading direction. This effect is evidenced by the gradient variation between models loaded in x and y directions. Table 8.1 shows the normalised stiffness gradients for the twelve models along with the normalised porosity values.

Table 8.1: Normalised porosity and gradient of load-deflection curve for the twelve models.

Sample	Load Direction	Normalised Gradient	Normalised Porosity
1	Y	1.000	0.948
	X	0.937	
2	Y	0.967	0.939
	X	0.987	
3	Y	0.947	0.998
	X	0.934	
4	Y	0.915	1
	X	0.905	
5	Y	0.936	0.966
	X	0.931	
6	Y	0.957	0.945
	X	0.914	

Loading the model in either the x or y direction is shown to alter the stiffness gradient. For example, consider models 1Y and 1X which are both constructed from the same microstructural data. The stiffness gradient for model 1x is approximately 6% less than 1Y. This observation is apparent in all the data sets, albeit with varying degrees of severity, thus supporting the view that this graphite is near isotropic. It should be noted that this effect is likely to be exaggerated due the small scale of the models and does not necessarily represent the material on a practical scale (*e.g.* quantities used in manufacture of reactor components). Generally, models with higher percentage porosities demonstrated a lower stiffness gradient, as shown in Figure 8.9, which is consistent with experimental observations. This relationship has been well documented, in particular with regards to changes in the elastic moduli as a result of graphite oxidation (*e.g.* Videl *et al.*, 1999). However, some models are shown to deviate significantly from this trend. For example, models 4X and 6X both exhibit a similar

gradient, however, Sample four is characterised as being approximately 5.5% more porous than Sample six. This is likely a result of the pore directionally, for example, pores oriented perpendicular to the applied load will demonstrate a lower stiffness since they will effectively be 'opened' when the model is simulated. This observation serves to further demonstrate the considerable effect pore distributions can have on the material.

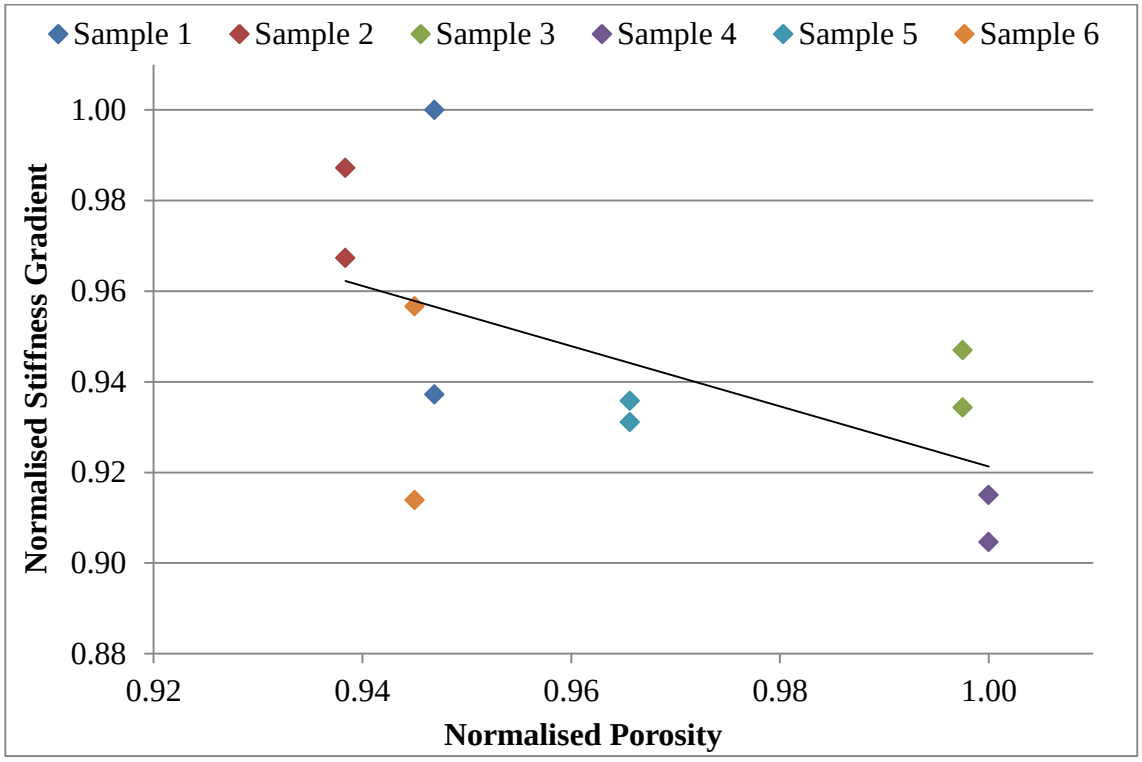

Figure 8.9: Plot to show the relationship between porosity and stiffness for the six models when loaded in both x and y orientations.

8.2. Simulated Tensile Crack Propagation

Previously, the influence of porosity on the material properties has been discussed. Among other properties, this has shown how stress distribution plots give an indication as to how the porosity affects the location of high and low stress regions in the model. Application of the element removal methodology to a model with an applied tensile displacement demonstrates the crack propagation path(s) through the material microstructure. In addition, the collation of elemental data at each propagation cycle enable the determination of bulk material properties (*e.g.* strength, deflection to failure, energy *etc.*) through consideration of load-deflection plots.

8.2.1. Defining a Representative Element Removal Criterion

As discussed in Section 7.4, consideration of the element removal criterion is required to attain representative properties for the bulk model. The methodology explained in this section is applied to the tensile models. Figure 8.10 shows the load-deflection plots for five models simulated with an applied element removal stress of 30 MPa. Each model was simulated in both the x and y directions to determine the load value at the point of bulk failure. The model was considered to have failed when a minimum of 5% decrease was observed from the peak load. Sample three is not included in this plot since it required re-polished (explained in Chapter 6). At the time of simulation the model was not yet constructed and was therefore unable to be included in the work to determine a representative failure stress.

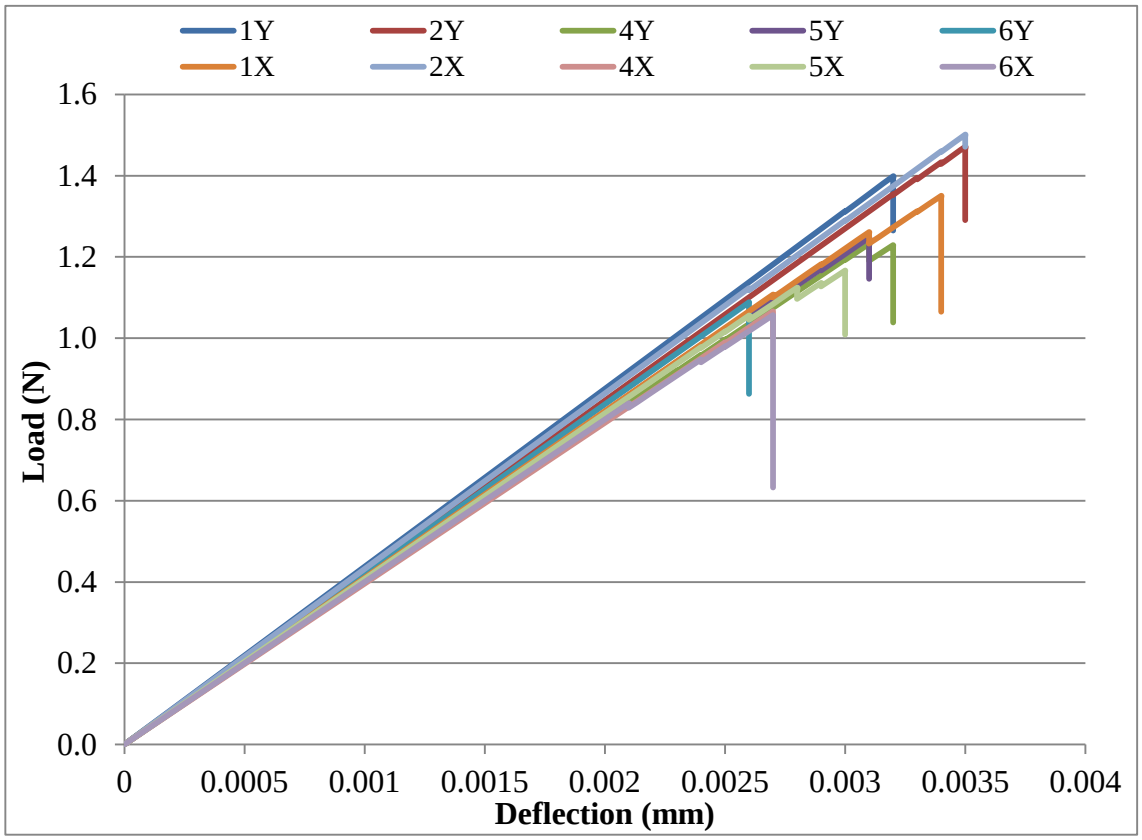

Figure 8.10: Load-deflection plots for five models with a simulated displacement applied in the x and y directions. Element removal stress for all models was 30 MPa.

The element failure stress is dependent on the determination of a characteristic tensile strength for graphite. Table 8.2 shows the tensile strength from a number of

experimental studies. The average tensile strength from these investigations is 17.91 MPa which corresponds to an applied model failure load of 5.03 N. Bulk failure of the models at this load will give a simulation tensile strength value that is representative of graphite.

Table 8.2: Experimental determination of tensile strength of graphite.

Study	Tensile Strength (MPa)
Brocklehurst (1977)	22
Neighbour (1993)	14.22
Kelly (2000)	17.5
Mean	**17.91**

Data from the computation simulations with an element failure stress of 30 MPa is shown in Table 8.3.

Table 8.3: Model data to determine a representative element failure stress. Load and strength columns show the bulk model properties with an applied element failure stress of 30 MPa. Representative element failure stress is calculated using the average tensile strength, 17.91 MPa.

Displacement Direction	Sample	Load at Failure (N)	Bulk Strength (MPa)	Gradient	Representative Element Failure Stress (MPa)
Y	1	1.40	4.98	6.03	107.89
	2	1.47	5.24	5.73	102.57
	4	1.23	4.39	6.84	122.45
	5	1.25	4.44	6.76	120.98
	6	1.09	3.88	7.74	138.63
X	1	1.35	4.81	6.24	111.73
	2	1.50	5.34	5.61	100.52
	4	1.07	3.80	7.90	141.52
	5	1.17	4.15	7.22	129.35
	6	1.06	3.76	7.97	142.78
Mean		1.26	4.48	6.80	**121.84**
Standard Deviation		0.16	0.56	0.84	**15.13**

The load at failure for each of the models is recorded and the bulk strength calculated. Average model strength for the ten simulations is calculated as being 4.48 MPa with a standard deviation of 0.56 MPa, which is far lower than the experimental value of 17.91 MPa. As previously discussed, this may be attributed to the element removal stress. This data suggests that the 'strength' of individual elements in this model should be

greater than the initially applied failure stress to output representative mechanical parameters. Using the gradient from each simulation a representative element stress can be calculated. This calculated value indicates the required element failure stress for each model to output bulk strengths of 17.91 MPa. The average for the ten simulations is approximately 122 MPa with a standard deviation of 15.13 MPa. This removal criterion does appear to be very high when considering the relatively low tensile strength of graphite; however, it is important to distinguish between bulk strength of experimental materials and the individual elemental strength in a model. Whilst the experimentally derived bulk strength of graphite takes account of the porosity, the elemental strength applies solely to the solid material. Additionally, as previously discussed, there is potential for significant scaling issues when comparing experiment data with that of the computational simulations. However, utilising a representative element failure stress will enable the output mechanical data that is more characteristic and allow for more direct comparisons between experimental and simulated data. Further, the relative effect of porosity on the mechanical performance will be easily determined through the use of a consistent removal criterion between models and loading scenarios. The element removal criterion for the crack propagation will therefore be approximated to 120 MPa.

8.2.2. Simulation Results

Due to the number of iterations required to simulate crack propagation through the models, it is not feasible to include images for all the models. Illustrative examples, Figure 8.11 and Figure 8.12, show the first principal and Y-displacement distributions at a number of crack iterations. Table 8.4 details which element removal iteration corresponds to each picture. Videos for each model may be found on the accompanying DVD (see Appendix A for details). Simulations were stopped and thus the models are considered to have failed when the force drops to below 5% of the peak recorded load.

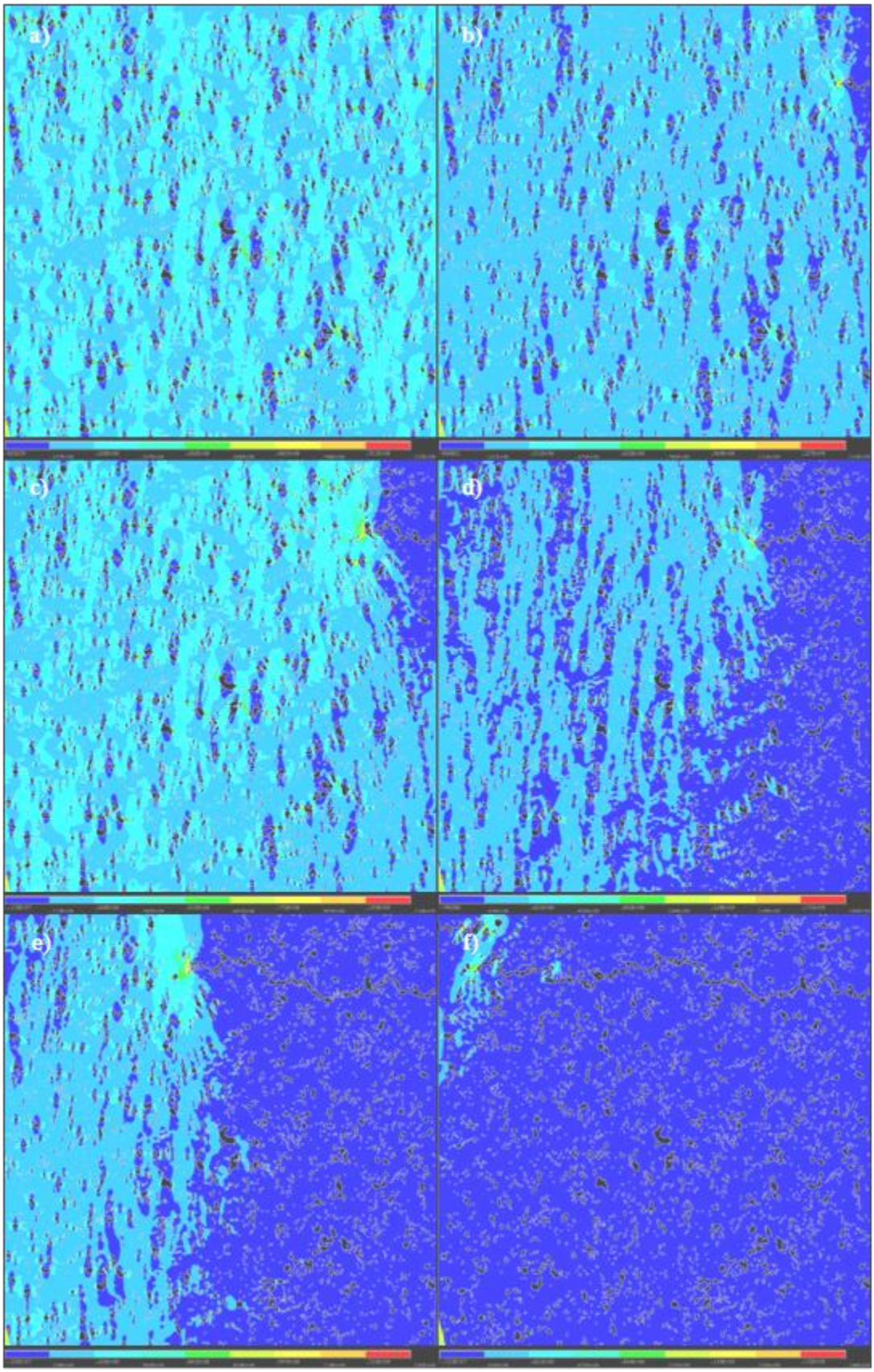

Figure 8.11: Schematic first principal stress distributions (blue indicates low stress, red indicates high stress) in Sample one at a number of crack extensions. Details for these example plots are shown in Table 8.4.

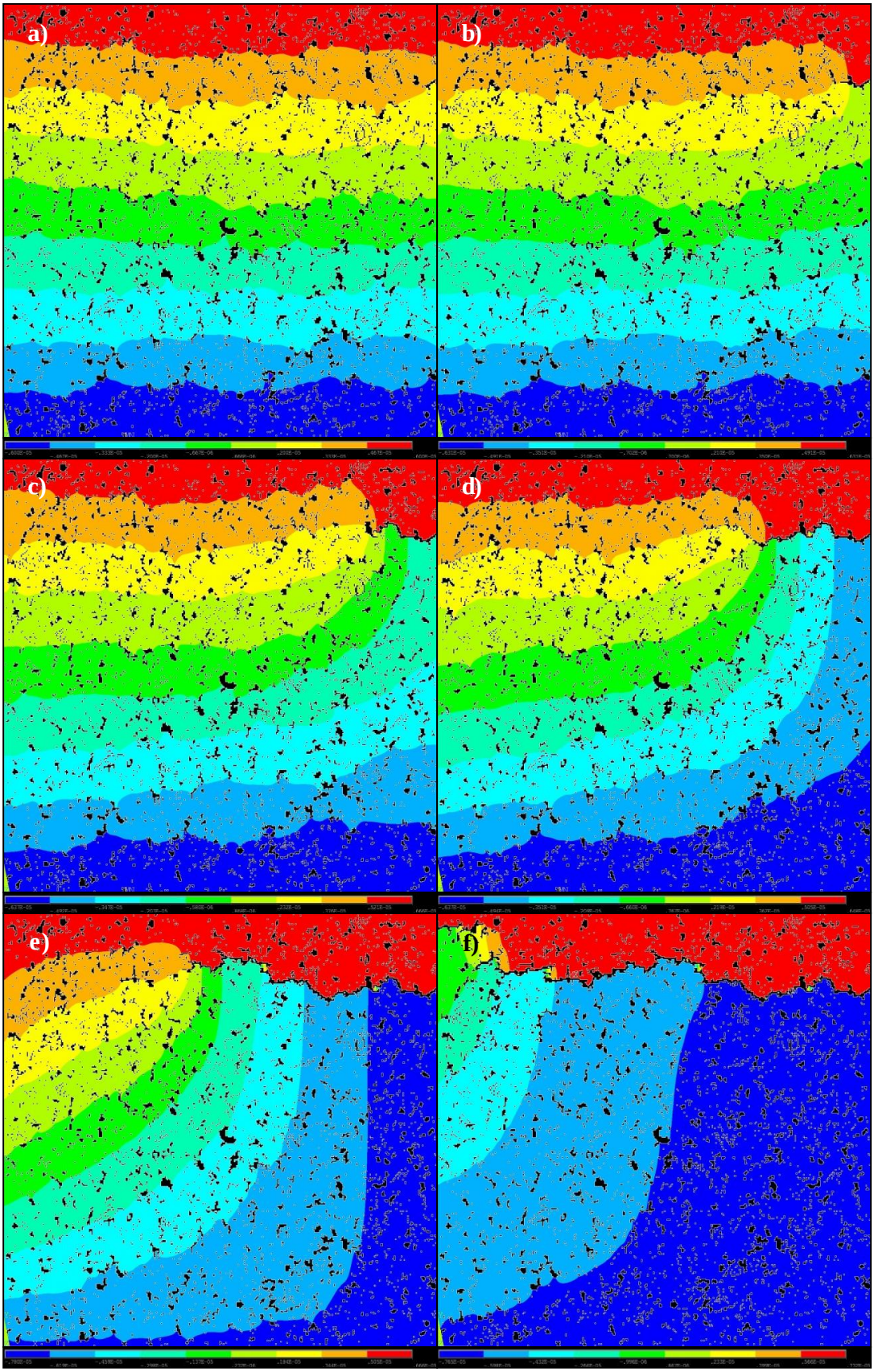

Figure 8.12: Schematic Y-displacement distributions (blue indicates low displacement, red indicates high displacement) in Sample one at a number of crack extensions. Details for these example plots are shown in Table 8.4.

Table 8.4: Details as to which element removal iteration corresponds to each image in Figure 8.11 and Figure 8.12.

Image	Element removal Iteration
a)	15
b)	30
c)	45
d)	60
e)	75
f)	95

The removal of elements after each simulation and thus the extension of the crack is effectively demonstrated in the previous images (Figure 8.11 and Figure 8.12) by the redistribution of stresses and displacements between iterations. The first principal stress distributions show that as the crack propagates through the model, the high stress region is repeatedly relocated to the area surrounding the crack tip. Although this high stress region is primarily shown to advance ahead of the crack tip this is not exclusive and additional areas are observed throughout the microstructure. The majority of these localised high stresses are below the element removal criterion and therefore do not contribute to the fracture of the model. However, some element removals are located a significant distance from the failure path, thus simulating micro-cracking in the model. Micro-cracking may occur prior to the onset of the macro-crack or in conjunction with the bulk failure of the model. This is consistent with experimental observations that define 'stable' micro-cracks prior to failure and the coalescence of micro-cracks to form a 'branched' macro-crack (*e.g.* Heard *et al.*, 2010). Figure 8.13 shows two examples of micro-cracking from Sample five. Initial loading of this model results in a high stress between two pores (d). The resulting micro-crack (e) is the first element removed from this model and does not directly contribute to the failure path of the macro-crack. The largest pore in the model (b) also experiences some micro-cracking (c) as a result of the seventh and eighth element removal iterations. This example of micro-cracking occurs in conjunction with additional element removals; however, this specific pore does not directly interact with the failure path.

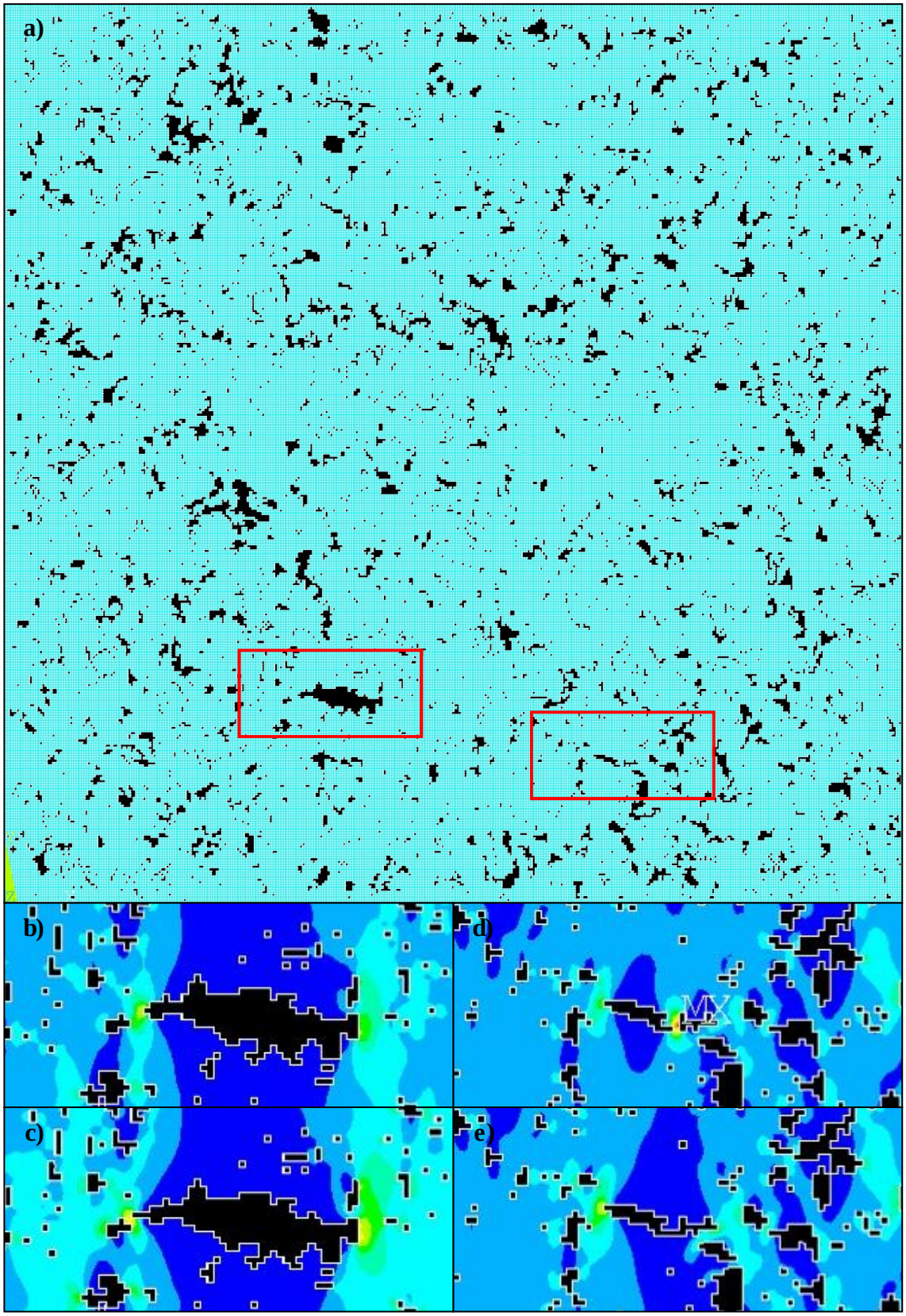

Figure 8.13: Example of two micro-cracks in Sample five. a) meshed model before crack initiation. b) and d) show the areas of interest before cracking. c) and e) show the areas after cracking.

Load-deflection plots and fracture paths for all six models are shown in Figure 8.14 to Figure 8.25. Load-deflection plots for each model show data points at which elements are removed. Micro-cracking is observed in some models and appears on the load-deflection plots as small decreases in calculated load prior to the onset of the macro crack. It should be noted that some pre peak decreases in load are due to porosity arresting macro-crack propagation. Such instances require an increase in displacement to encourage continued crack growth. Additional micro-cracks may occur after the peak load; however, these are generally indistinguishable on the load-deflection curve. Large drops in calculated load between iterations are primarily due to the crack advancing through a pore.

Y-displacement plots for each model are used to better illustrate the fracture path. Since displacements are applied to both the top and bottom surfaces of the models, the displacement distributions will effectively be either positive or negative upon bulk fracture (*i.e.* there is no connecting material between fractured halves). As such the positive displacement is represented by the red region and the negative displacement by blue.

Figure 8.26 shows all the load-deflection plots for all six tensile models. This figure demonstrates the variations in the mechanical properties between models. Relative variations in model stiffness are demonstrated by the different gradients exhibited upon loading, prior to crack initiation. The bulk strength of each model is calculated using the peak load values from the simulation results. Displacement to failure in a tensile model is usually related to the bulk strength; however, processes such as micro-cracking can have an effect on this mechanical characteristic. The required Energy input to cause a model to fail is calculated by determining the area under the load-deflection plot. The method used to determine this value is explained in Section 7.5.3.

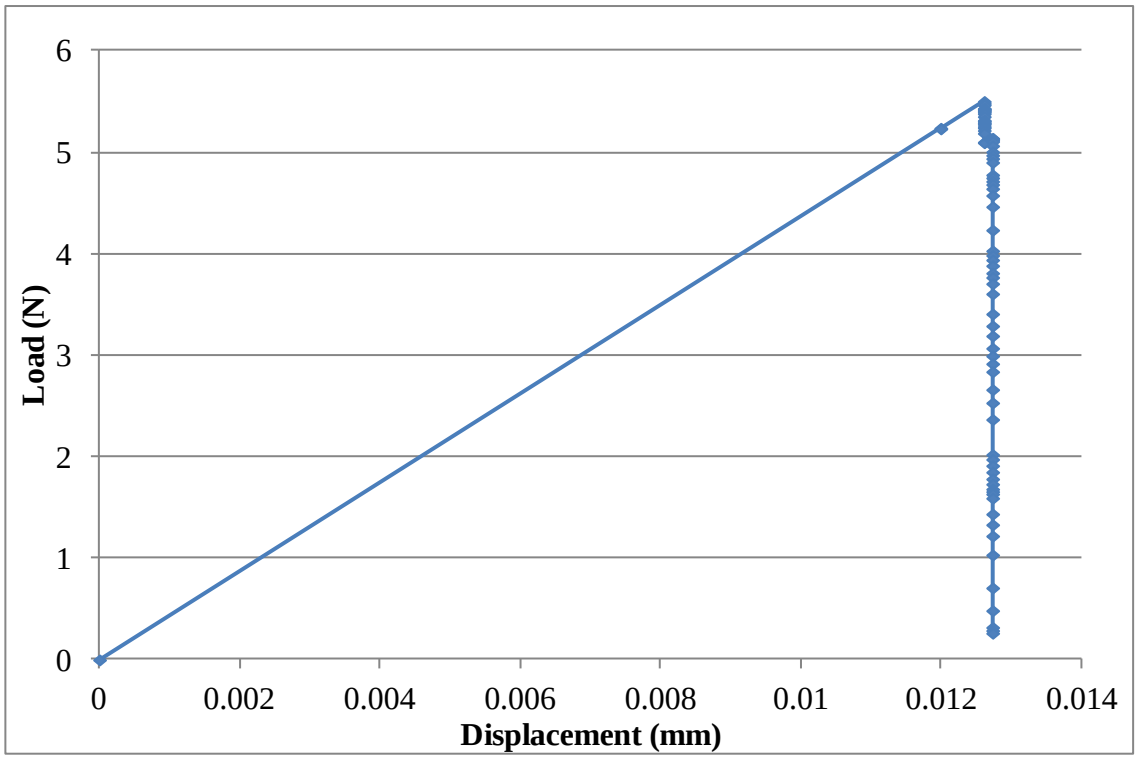

Figure 8.14: Load-deflection plot for tensile displacement model of Sample one.

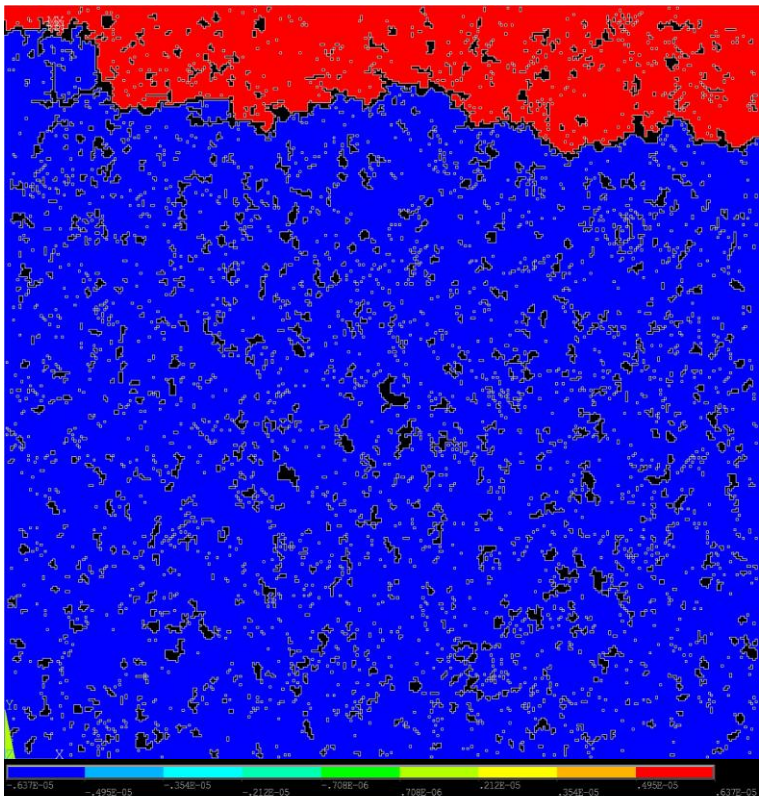

Figure 8.15 Simulated failure path through Sample one.

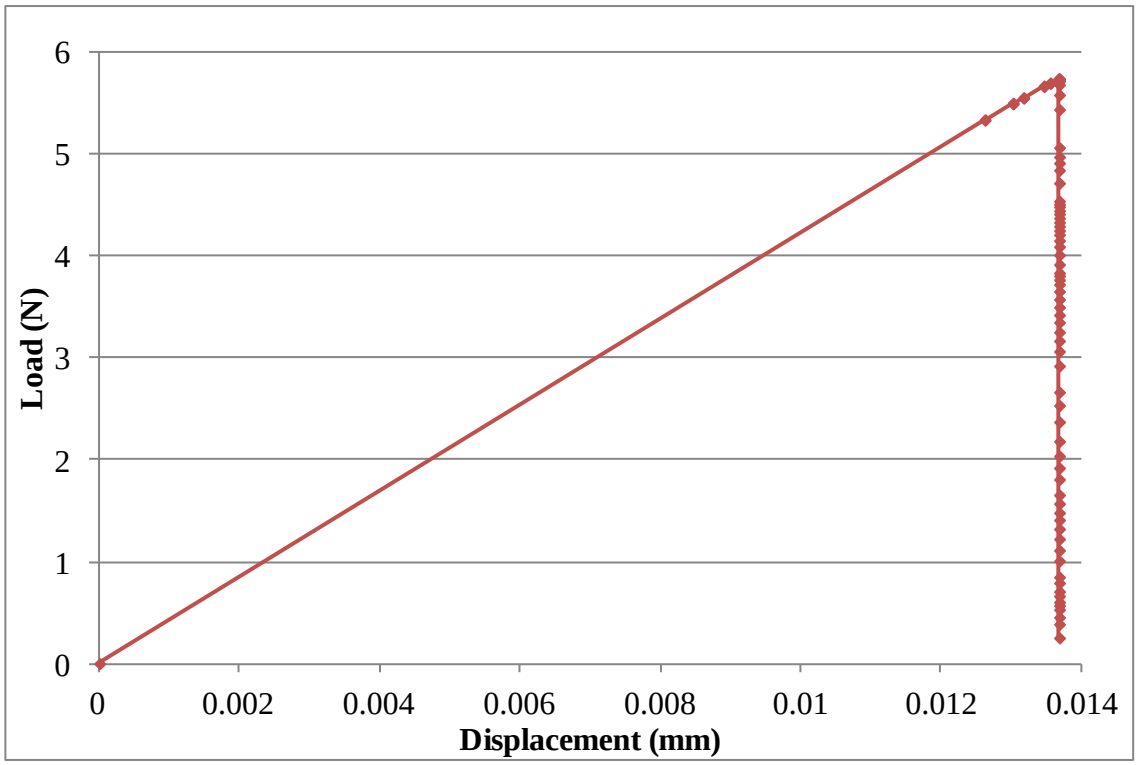

Figure 8.16: Load-deflection plot for tensile displacement model of Sample two.

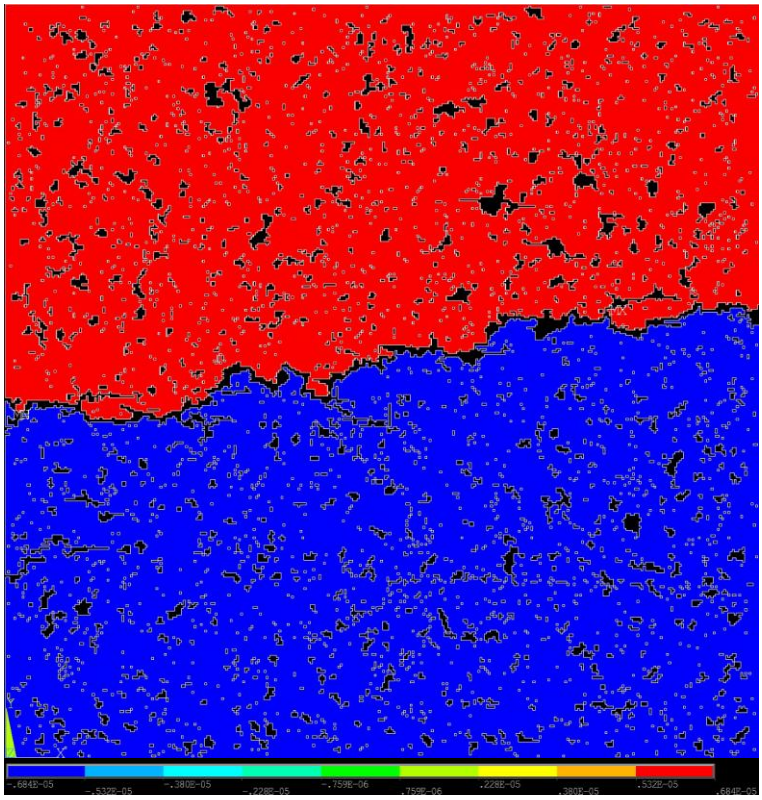

Figure 8.17: Simulated failure path through Sample two.

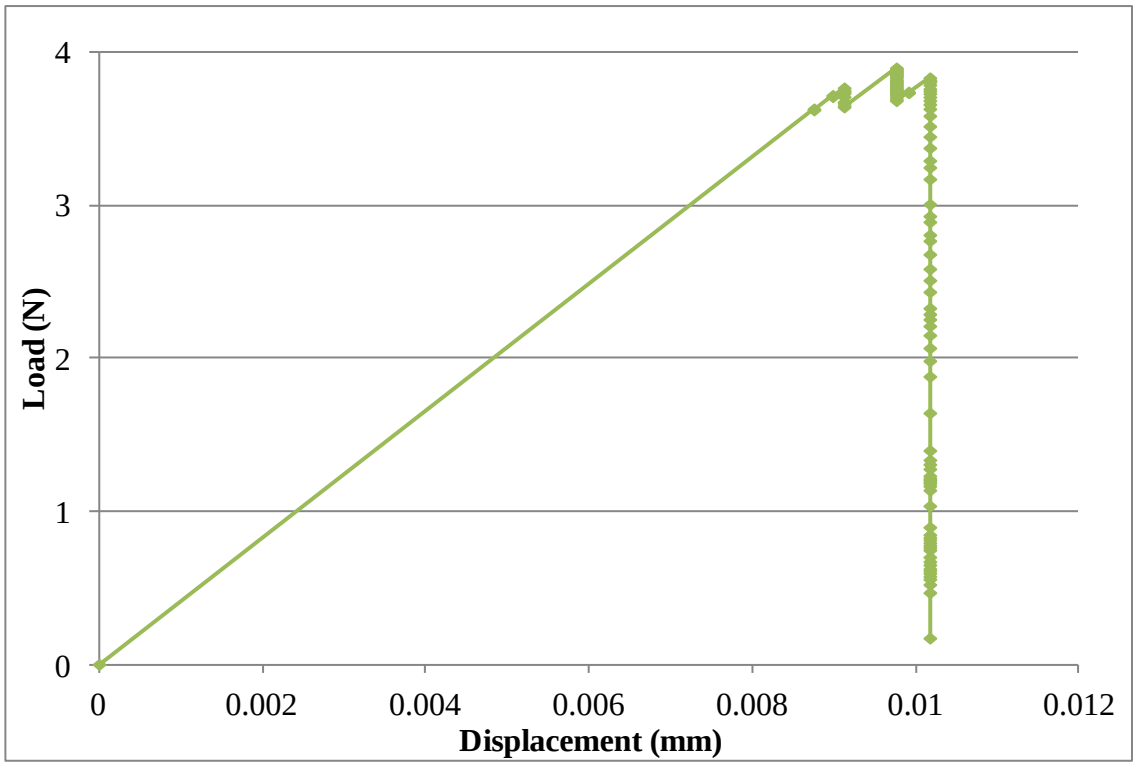

Figure 8.18: Load-deflection plot for tensile displacement model of Sample three.

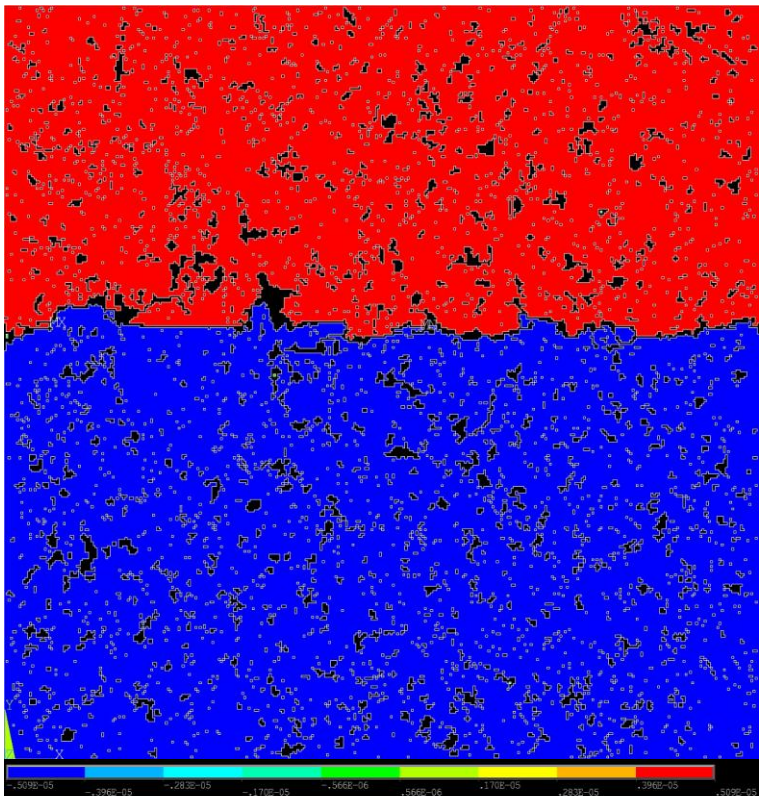

Figure 8.19: Simulated failure path through Sample three.

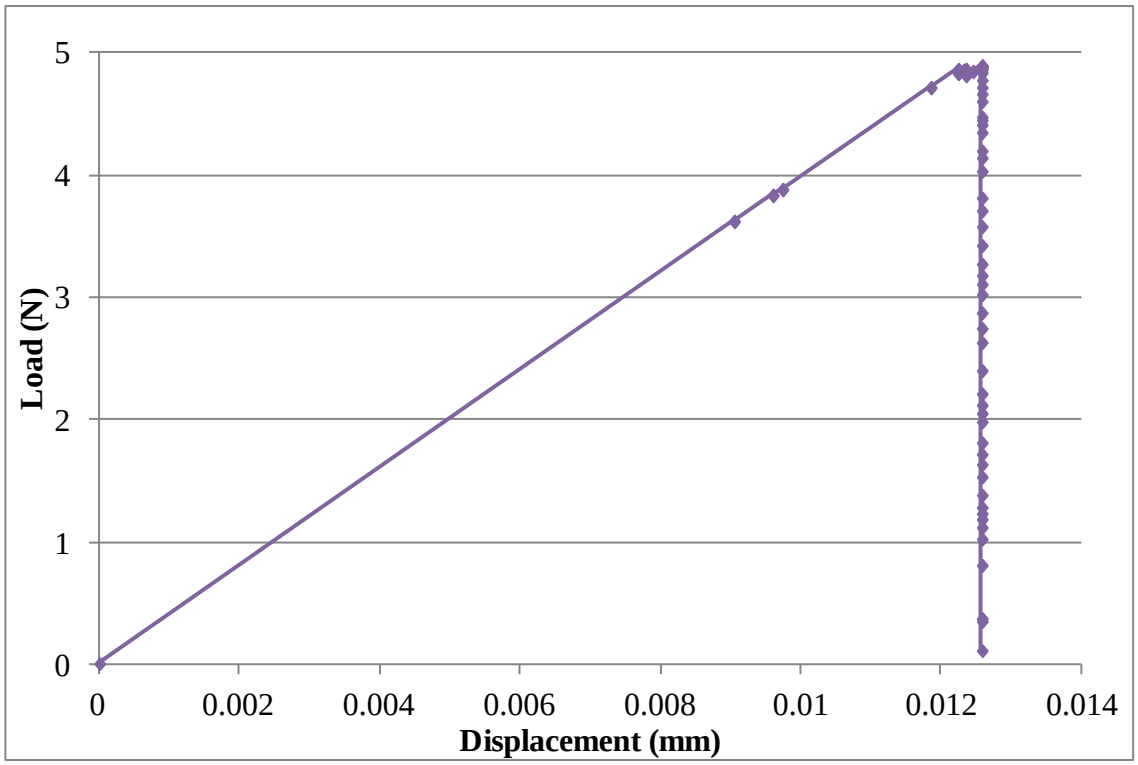

Figure 8.20: Load-deflection plot for tensile displacement model of Sample four.

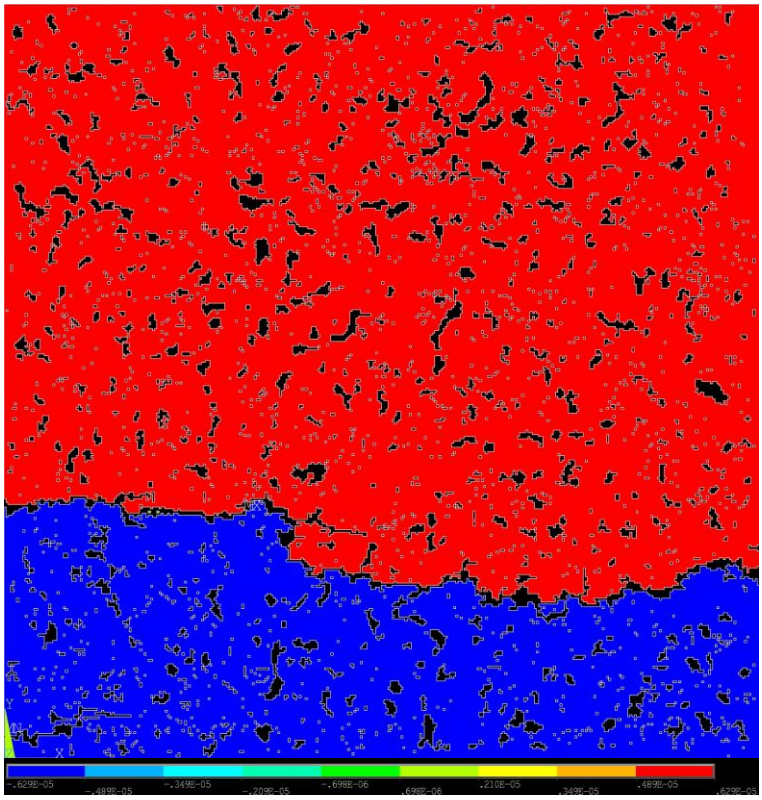

Figure 8.21: Simulated failure path through Sample four.

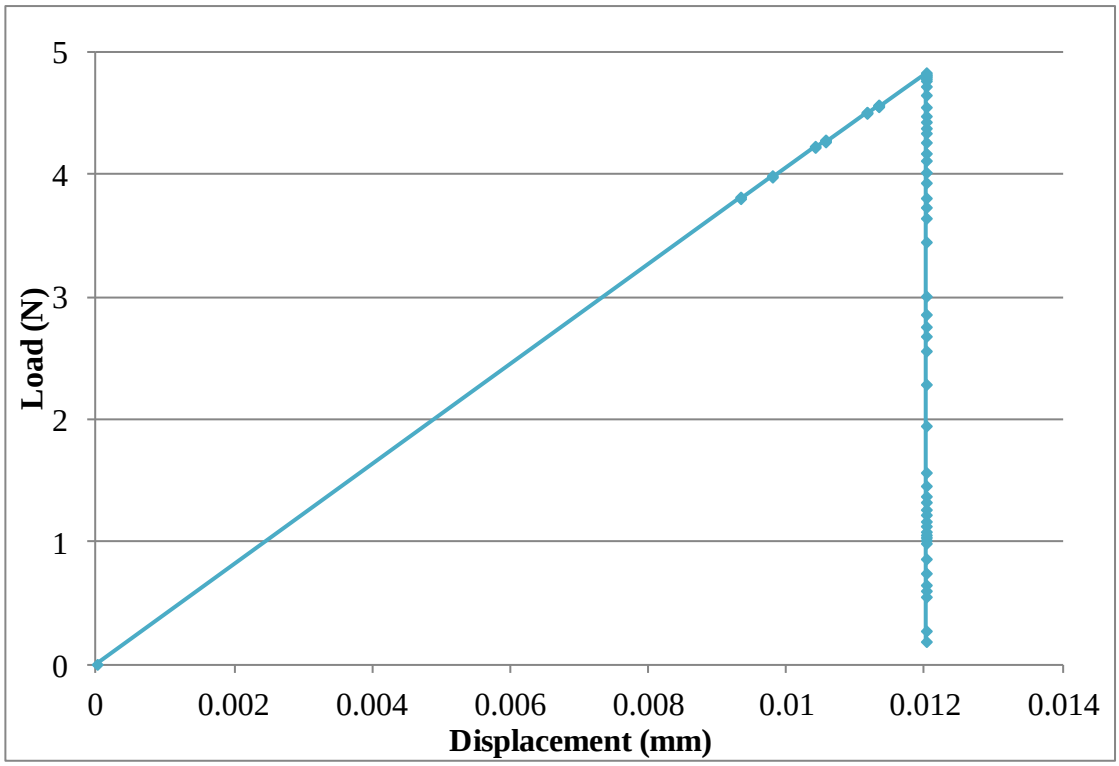

Figure 8.22: Load-deflection plot for tensile displacement model of Sample five.

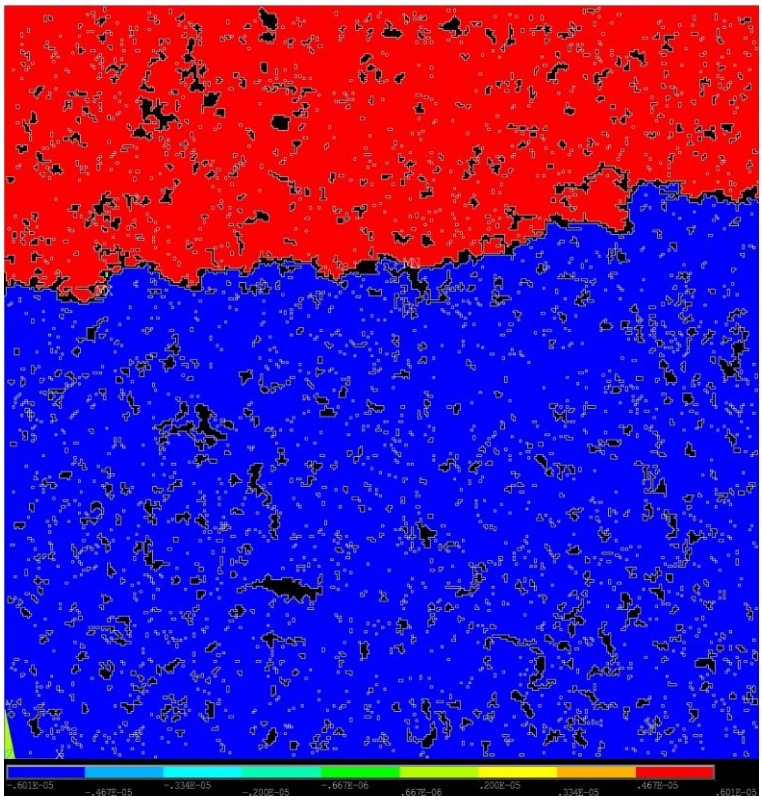

Figure 8.23: Simulated failure path through Sample five.

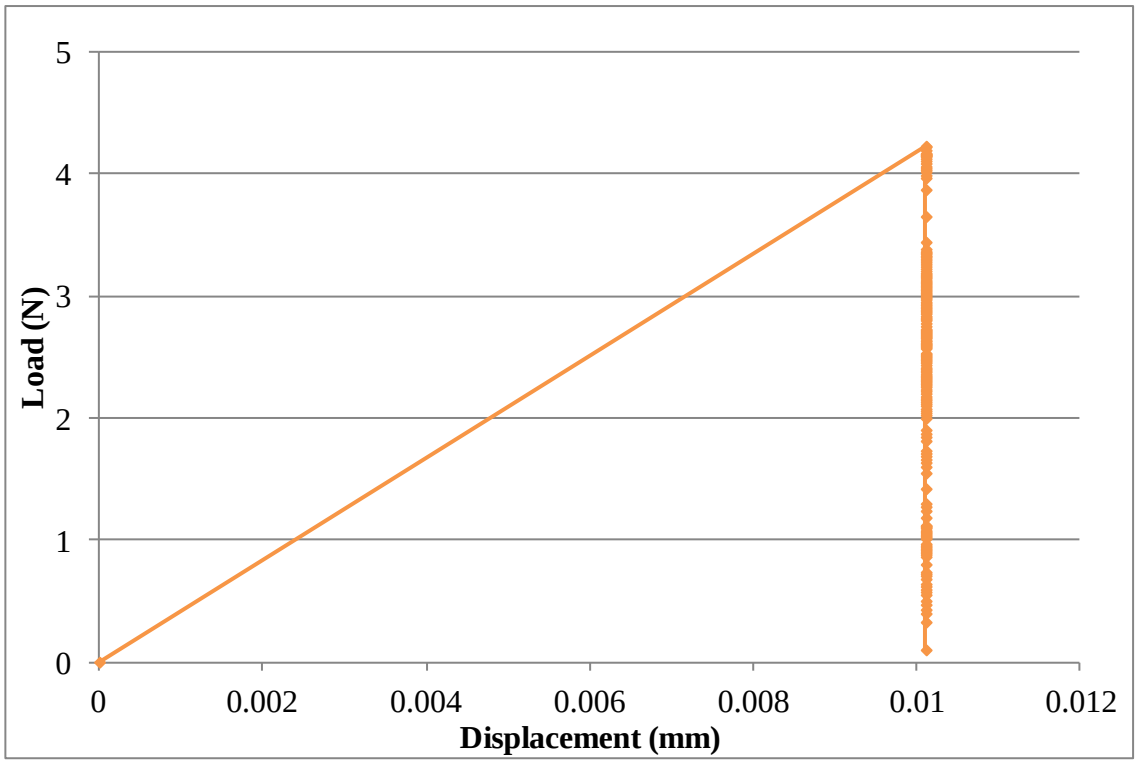

Figure 8.24: Load-deflection plot for tensile displacement model of Sample six.

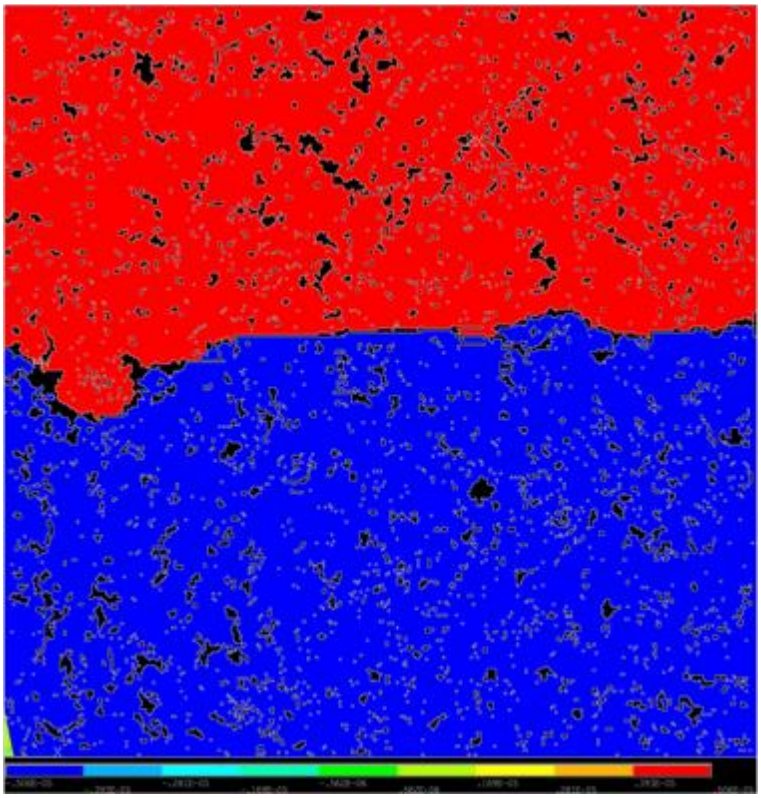

Figure 8.25: Simulated failure path through Sample six.

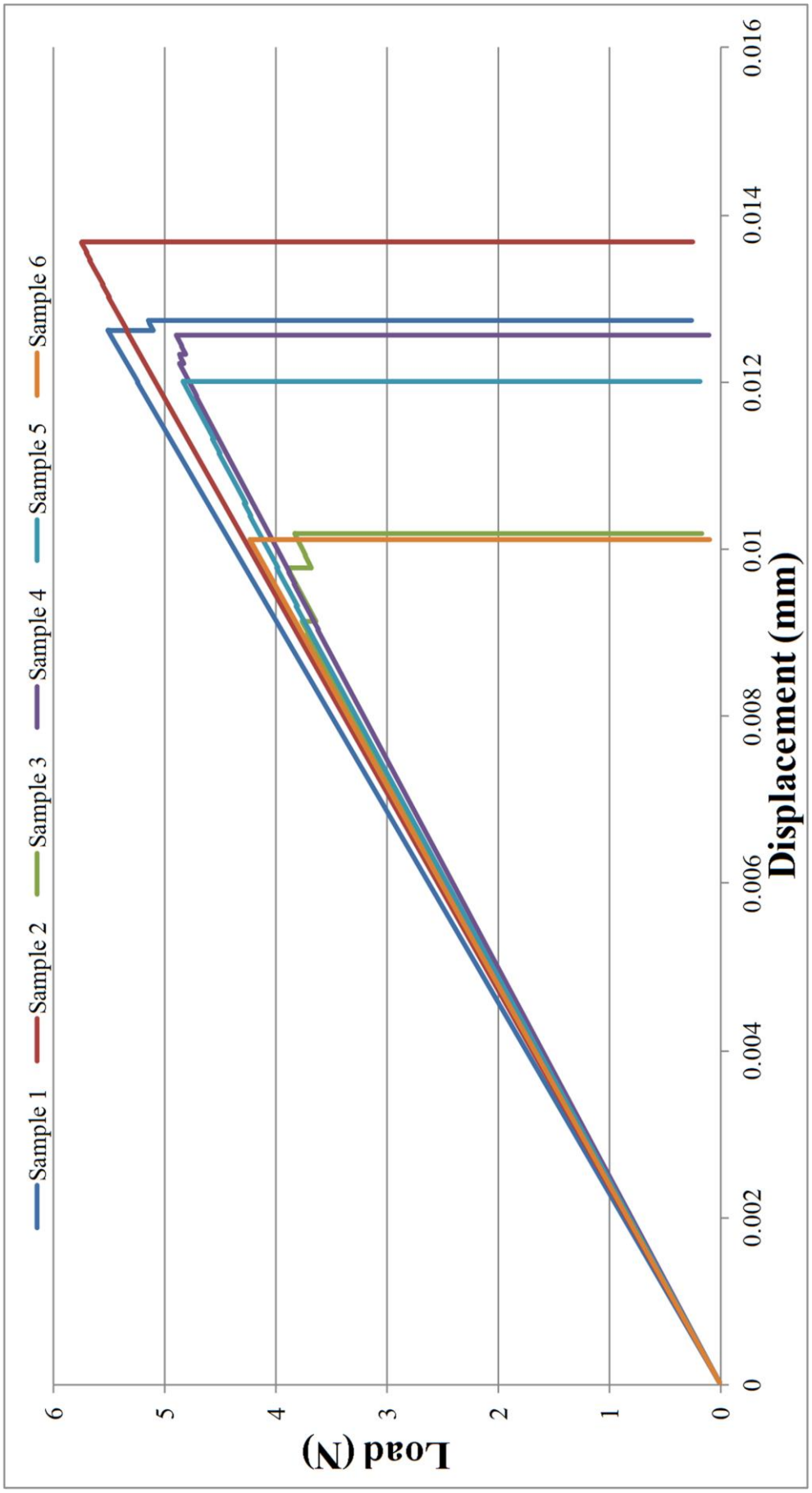

Figure 8.26: Load-displacement plots for all six tensile displacement models.

A summary of the mechanical data ascertained from these models is shown in Table 8.5. Data in this table is primarily determined from interpretation of the load-deflection response as well as knowledge of the physical model characteristics and loading scenario.

Table 8.5: Summary of data from tensile displacement model.

Sample	Element Removal Iterations	Peak Load (N)	Bulk Strength (MPa)	Young's Modulus (GPa)	Displacement to Failure (mm)	Work to Failure (μJ)
1	78	5.51	19.62	15.56	0.0127	35.39
2	72	5.74	20.44	15.07	0.0137	39.59
3	109	3.90	13.87	14.75	0.0102	21.25
4	71	4.89	17.41	14.26	0.0126	31.43
5	69	4.83	17.20	14.58	0.0120	29.52
6	177	4.23	15.05	14.89	0.0101	21.41
Mean	96	4.85	17.27	14.85	0.0119	29.77
Standard Deviation	42.39	0.71	2.53	0.45	0.0015	6.75

The element removal iterations refer to the number of times the removal methodology is repeated in order to cause failure of the model. The number of iterations has little bearing on the overall mechanical response and thus the determined properties. The deviation in the number of iterations between models is largely due to the amount of porosity across the crack path (*i.e* more pores in the failure region require fewer iterations). This is demonstrated by Sample six which has a large region with little porosity in the centre of the failure path and as such requires a greater number of removal iterations to cause bulk fracture. As is generally expected with graphite, the calculated bulk strength shows significant variations between models. Sample three has the lowest strength at 13.87 MPa and Sample two the highest with a strength value of 20.44 MPa. The mean bulk strength of 17.27 MPa is consistent with the experimental values of 17.91 MPa. This is to be expected since the element removal criterion was defined to ensure a representative mechanical output form the model. Note that since the cross sectional area is consistent throughout the six models, the peak load is proportional to the bulk strength. Young's modulus values for each model are higher than the estimated experimental value of 11.14 GPa. This may be attributed to the calculation of representative stiffness of graphite containing zero porosity (*i.e.* model elements). Calculations using the Knudsen equation were based on a material

containing 19.35% porosity; however, each model contained a significantly lower pore area due to the exclusion of small features as a result of resolution limitations. Although it has been demonstrated that the location of pores and the overall distribution can have a significant effect on the stiffness, the overriding factor is the pore fraction. Thus, since the models have a smaller pore fraction they subsequently demonstrate a higher Young's modulus than experimental data. Displacement to failure values are generally expected to correlate to the peak load. The models conform to this relationship which the exception of Samples three and six. Although Sample six has a higher peak load value the displacement to failure is less than Sample three. This is due to significant non-critical failures in this sample prior to bulk fracture. These non-critical failures are primarily due to the crack being arrested though interaction with porosity. Subsequent iterations require an increase in the applied displacement to further propagate the crack. The variation exhibited by this batch of models serves to demonstrate the significant effect porosity distributions have on the mechanical response of graphite.

Figure 8.27 shows a detailed view of the failure paths for each of the six models. As with previous examples of failure paths, a Y-displacement plot is used to better demonstrate the crack paths. The tortuosity of this path is due to crack deflection along the random pore distributions in graphite (and thus the simulated microstructure in the model). As discussed in literature (*e.g.* Becker *et al.* (2011)), Ouagne *et al.* (2002) *etc.*), crack paths in graphite are generally expected to be heavily influenced by porosity as they follow a path of least resistance through the microstructure.

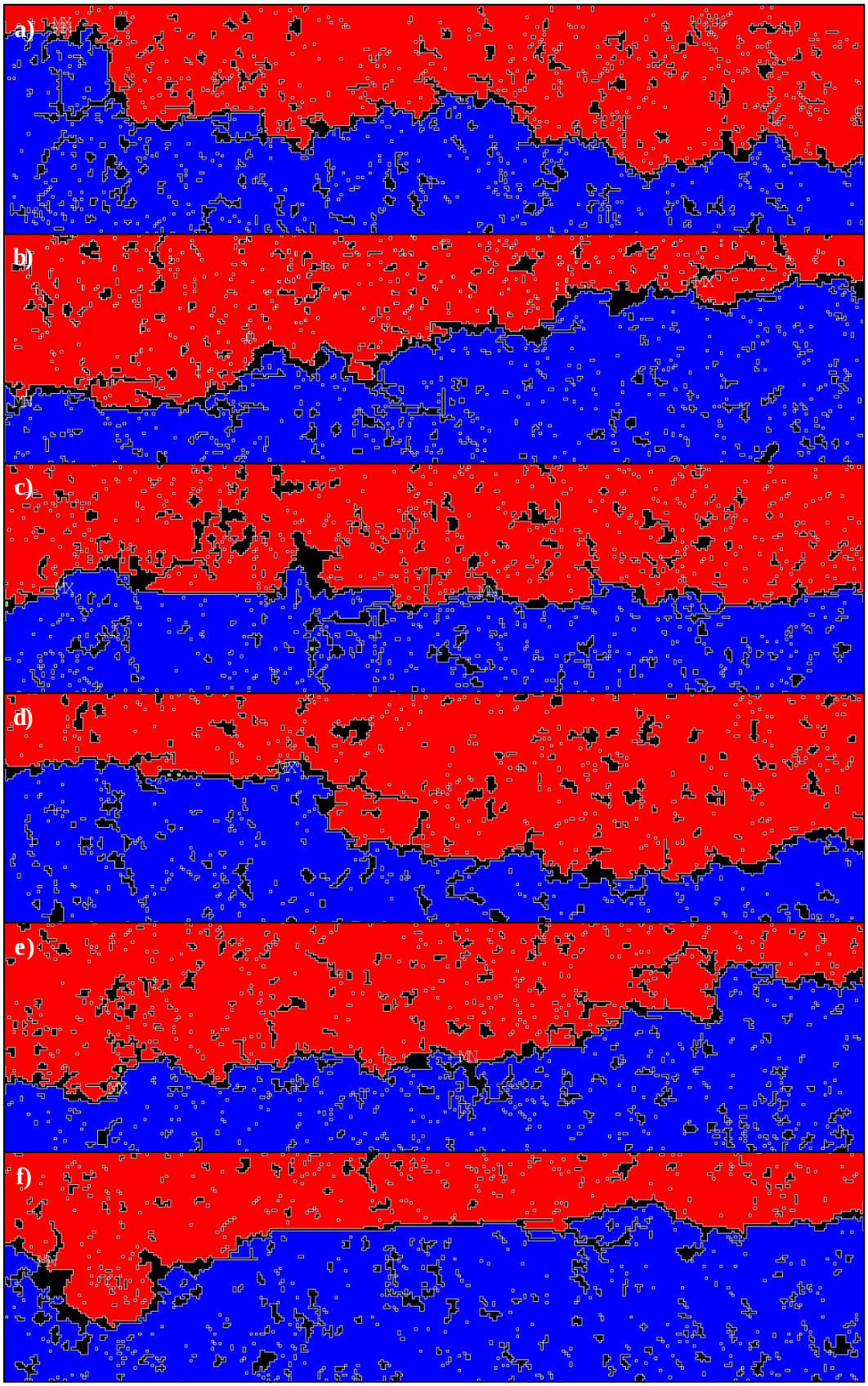

Figure 8.27: Tortuosity of cracks through tensile models for a) Sample one, b) Sample two, c) Sample three, d) Sample four, e) Sample five, f) Sample six.

8.2.3. Experimental Comparisons

The two dimensional nature of these models combined with the fact that they are constructed on a very small scale compared to typical experimental test specimens makes comparisons with experimental data difficult. However, this section will attempt to analyse the computationally derived properties alongside corresponding experimental data to determine their relative similarities. In addition, this analysis should give an indication as to how representative the simulations are of experimental testing of graphite.

The six simulated models were constructed from micrographs of six samples of material. Additionally, these samples were tested in three-point bend configuration. Figure 8.28 shows the load-deflection plots for each of these six samples. Additionally, normalised experimental and simulated load-deflection plots are shown in Figure 8.29 to enable easier comparison of the data. It should be noted that the initial portion of the experimental load-deflection curves are inclusive of elastic energy being stored in the test machine resulting in a gradual increase in plot gradient. Since the models are simulated in a 'perfectly elastic' environment, they do not experience this effect.

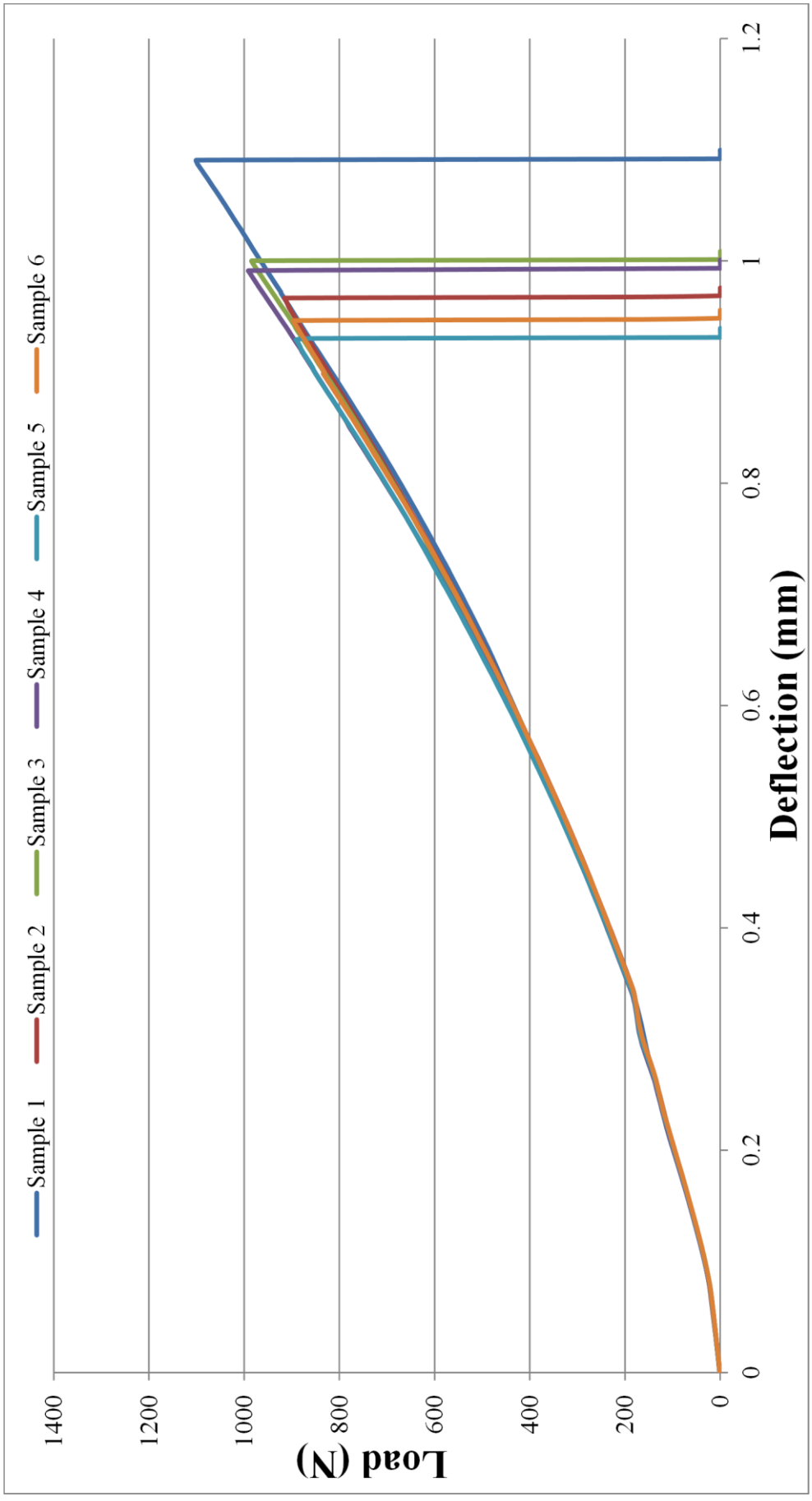

Figure 8.28: Load-displacement plots for six experimental three-point bend samples.

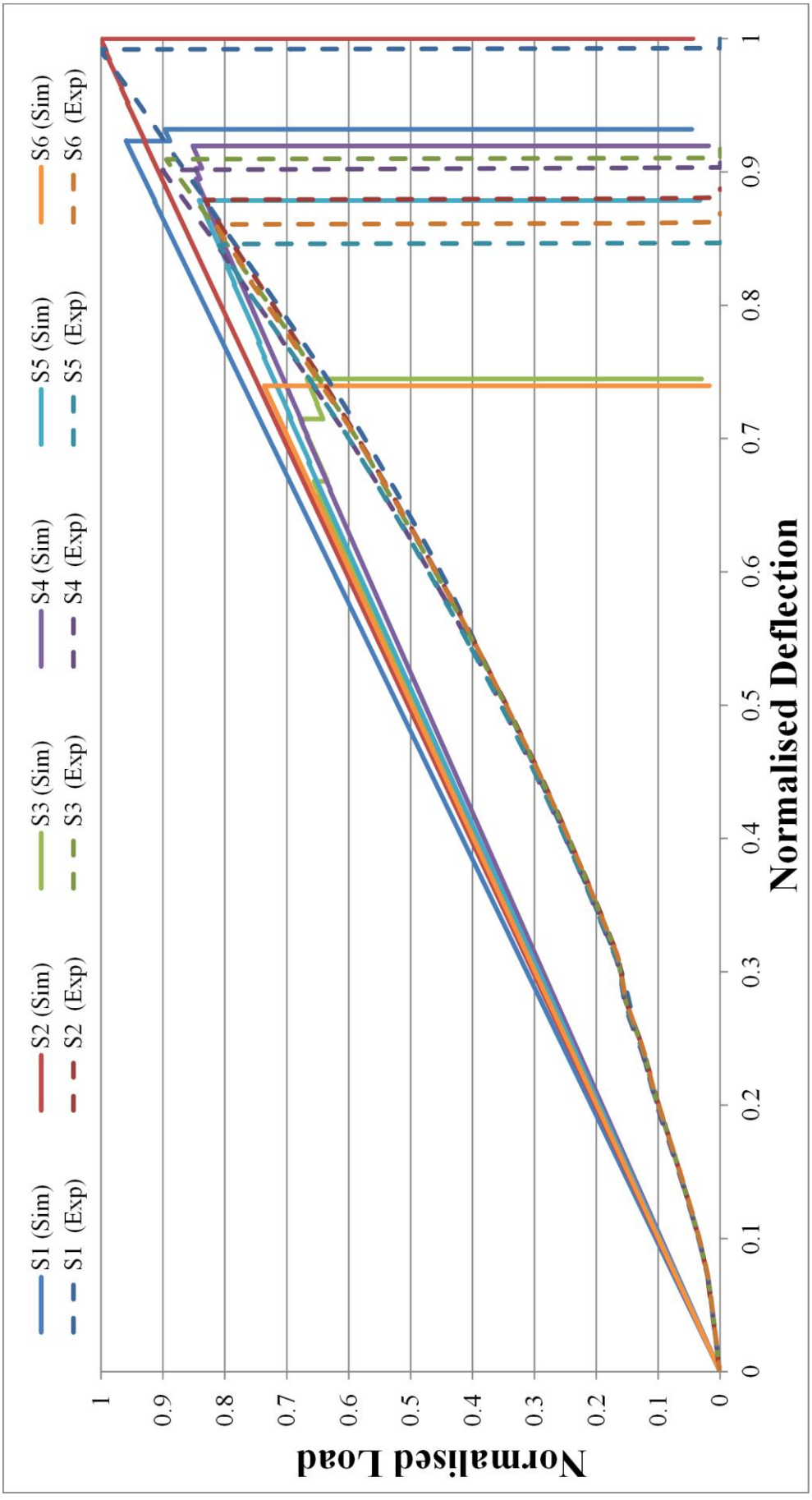

Figure 8.29: Normalised load-displacement plots for all six tensile displacement models and six experimental three-point bend samples.

Although the three-point bend test is a different configuration and the samples were much larger (15 x 15 x 100 mm) than the simulated models the load-deflection and failure response of the material is largely consistent with the computational results. Additionally, the peak load and deflection to failure values show significant variations between samples in a similar manner to the models. Table 8.6 shows the data for these six experimental samples. Note that the Young's modulus is not included since flexural and tensile tests yield very different moduli and thus the simulated and experimental stiffness values cannot be directly compared.

Table 8.6: Experimental data for six samples tested in three-point bend configuration.

Sample	Peak Load (N)	Bulk Strength (MPa)	Displacement to Failure (mm)	Work to Failure (J)
1	1101.40	34.45	1.092	0.4741
2	916.29	28.58	0.968	0.3510
3	984.43	30.86	1.001	0.3853
4	991.29	31.09	0.993	0.3851
5	891.77	27.97	0.931	0.3263
6	896.95	28.14	0.947	0.3343
Mean	963.69	30.18	0.988	0.3760
Standard Deviation	80.04	2.50	0.057	0.0541

The average bulk strength for the six experimental samples was 30.18 MPa, approximately 75% higher than the simulated strength. This can be accounted for, partially at least, through consideration of the relative test configurations. Flexural strength is commonly stated to be 1.3 times greater than tensile strength (Brocklehurst 1977). Applying this factor to the simulated tensile data gives an approximated flexural strength for the computational models. After application of this 'correction' factor, the experimental strength is still approximately 35% higher than the computational predictions. Possible reasons for this discrepancy may be due to the relative difference between experimental and computational scenarios such as issues of scale or the differences between a two dimensional model and a volumetric sample.

Table 8.7: Simulated and experimental strength values including equivalent flexural strength for simulated models.

Sample	Strength (MPa)		
	Simulated (Tensile)	Experimental (Flexural)	Simulated (Equivalent Flexural)
1	19.62	34.45	25.50
2	20.44	28.58	26.57
3	13.87	30.86	18.04
4	17.41	31.09	22.64
5	17.20	27.97	22.36
6	15.05	28.14	19.57
Mean	17.27	30.18	22.45
Standard Deviation	2.53	2.50	3.00

Normalised data for simulated and experimental results is shown in Table 8.8. This enables a comparison of the experimental and simulated data for each sample as well as averages and standard deviations.

Table 8.8: Normalised mechanical data for simulated models and experimental tests.

Sample	Simulated/ Experimental	Peak Load	Bulk Strength	Displacement to Failure	Work to Failure
1	Simulated	0.960	0.960	0.932	0.894
	Experimental	1.000	1.000	1.000	1.000
2	Simulated	1.000	1.000	1.000	1.000
	Experimental	0.832	0.830	0.886	0.740
3	Simulated	0.679	0.679	0.745	0.537
	Experimental	0.894	0.896	0.917	0.813
4	Simulated	0.852	0.852	0.920	0.794
	Experimental	0.900	0.902	0.909	0.812
5	Simulated	0.842	0.842	0.879	0.746
	Experimental	0.810	0.812	0.853	0.688
6	Simulated	0.736	0.736	0.740	0.541
	Experimental	0.814	0.817	0.868	0.705
Mean	Simulated	0.845	0.845	0.869	0.752
	Experimental	0.875	0.876	0.905	0.793
Standard Deviation	Simulated	0.124	0.124	0.106	0.187
	Experimental	0.073	0.072	0.052	0.114

Due to the probabilistic nature of pore distributions and the relatively small sample area, it is unrealistic to expect a relative comparison between experimental samples and computational models. Indeed, application of Pearson's correlation coefficient to the normalised strength and displacement to failure data sets both result in a factor of less than 0.24, suggesting a very small positive correlation (Rodgers *et al.*, 1988). Taking into account this small coefficient, it is not possible to identify any meaningful comparisons between experimental and simulated results from this limited data set. However, the normalised data statistics from simulated models are comparative to the experimental results. Standard deviations for the simulated models are generally larger than that of experimental samples. For example, bulk strength standard deviations are 0.124 and 0.072 for simulated and experimental results respectively. Although these differences could potentially be due to the probabilistic nature of the pore distributions, the primary reason is likely to be the relative test geometries. The effect of large pores and relative pore locations can be dramatic with regards to the crack initiation load. This is particularly evident in the model for Sample three which demonstrates a low peak load (and thus strength) due to the presence of a large critically oriented pore. Experimental test samples are likely to contain a greater number of large pores since they are larger volumes. However, the effect of large, critically orientated pores may be mitigated by the presence of material in the z-direction. Another cause of fracture initiation in the simulations was stress concentrations across 'bridges' between pores. These features occurred when two critically oriented pores were located in close proximity. Sufficient quantities of such features contribute to the failure path since they 'link' with one another thus defining a path of least resistance through the model. Although the same effect may be observed through experimental testing, it is likely to be less dramatic in larger three dimensional samples.

8.3. Notched Model Simulation Results

The primary purpose of the notch in these models is to control the point of crack initiation. As such, it is vital to construct a model with a sufficiently deep notch to create a region of high stress from which the crack will be initiated. Constructing models with a notch depth of 1 mm (*i.e.* one tenth of the model width) allows for significant crack growth whilst ensuring the stress concentration is sufficient to initiate failure at the notch tip. This is shown using Sample one as an example in Figure 8.30.

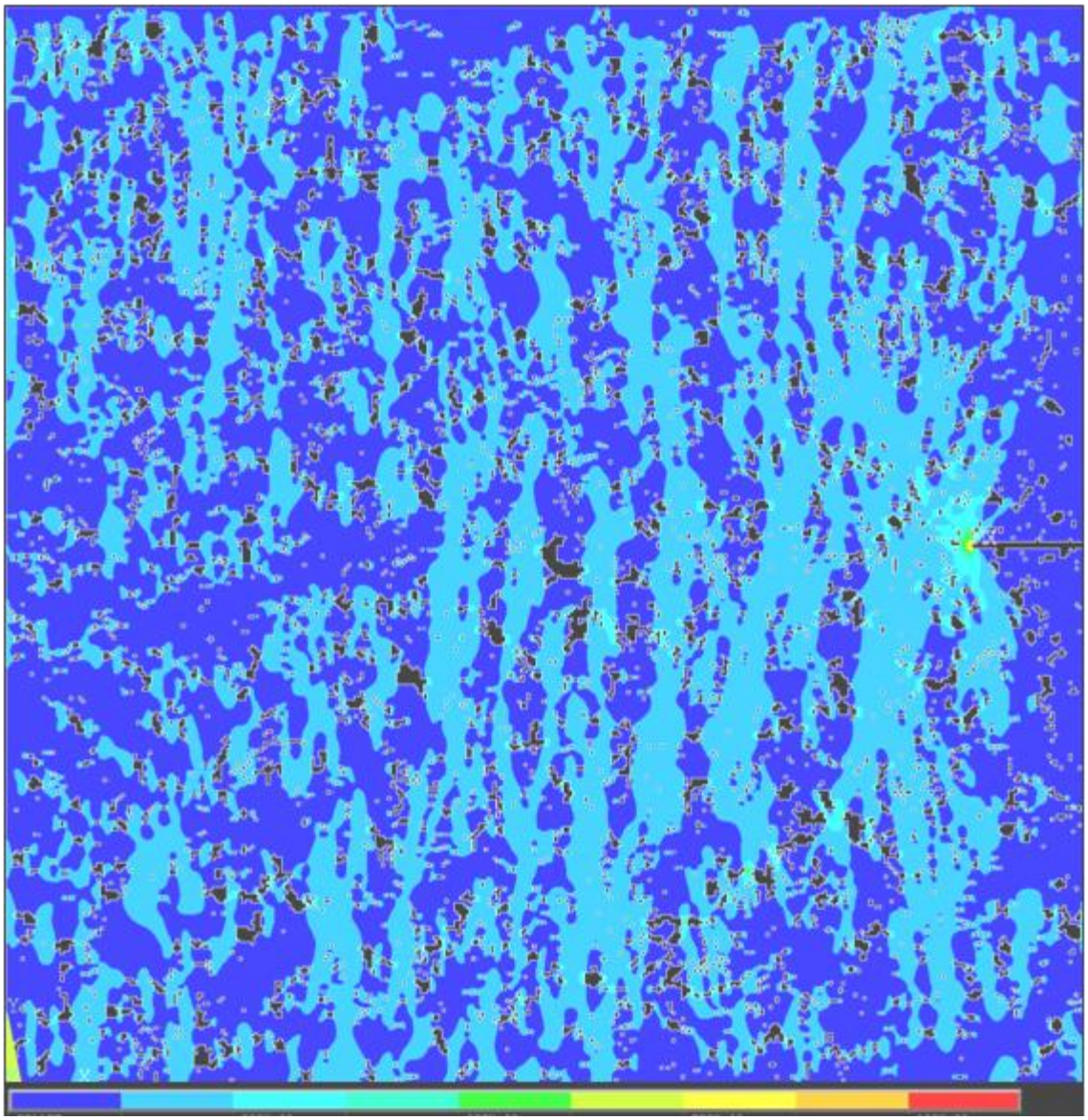

Figure 8.30: Schematic first principal stress distribution of Sample one with a notch depth of 1 mm (blue indicates low stress, red indicates high stress).

Illustrative examples showing the crack propagation through notched models are shown in Figures Figure 8.31 and Figure 8.32. Details for these models such as the crack length at the illustrated iterations are shown in Table 8.9.

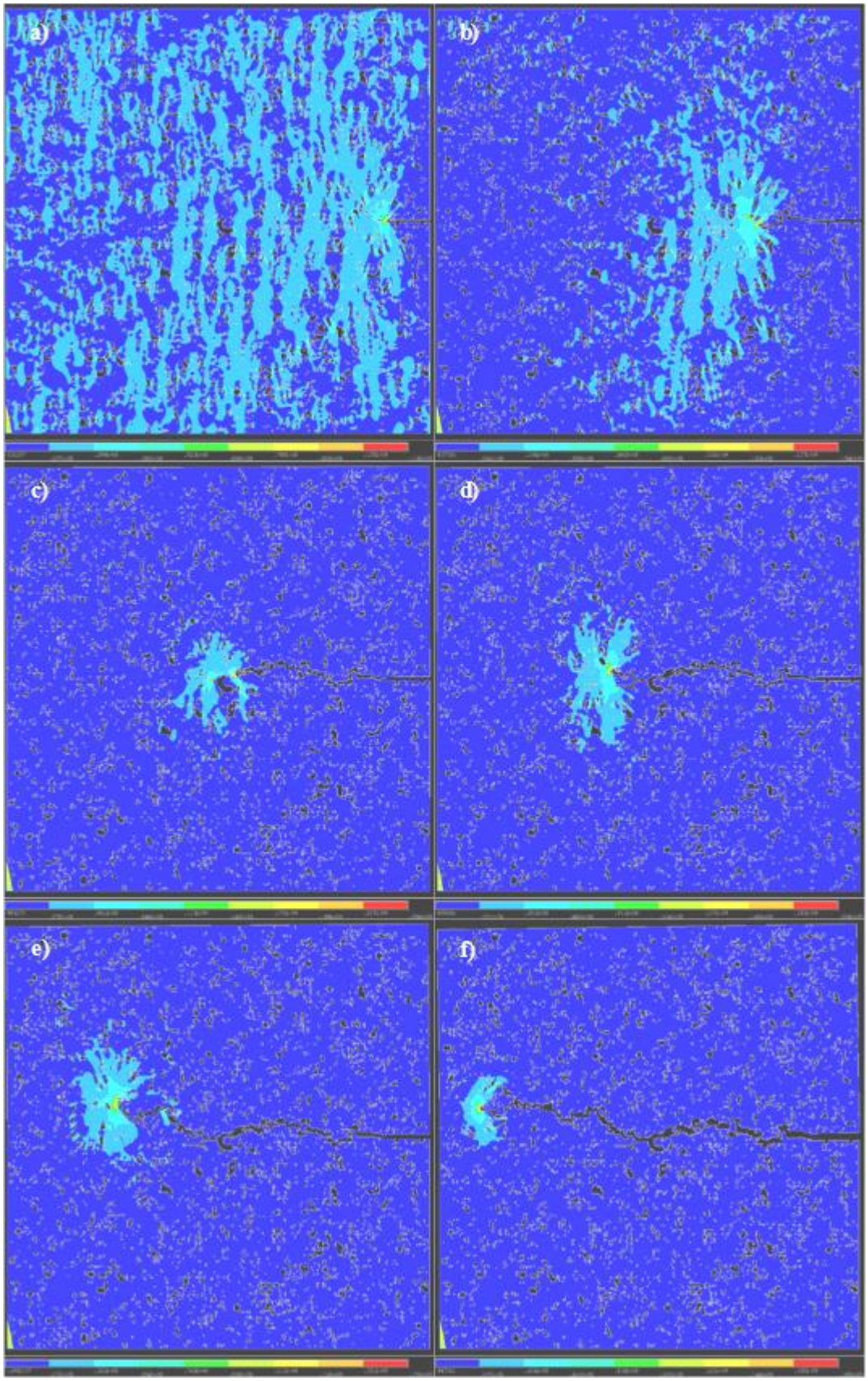

Figure 8.31: Schematic first principal stress distributions (blue indicates low stress, red indicates high stress) in Sample one notched model at a number of crack extensions. Details for these example plots are shown in Table 8.9.

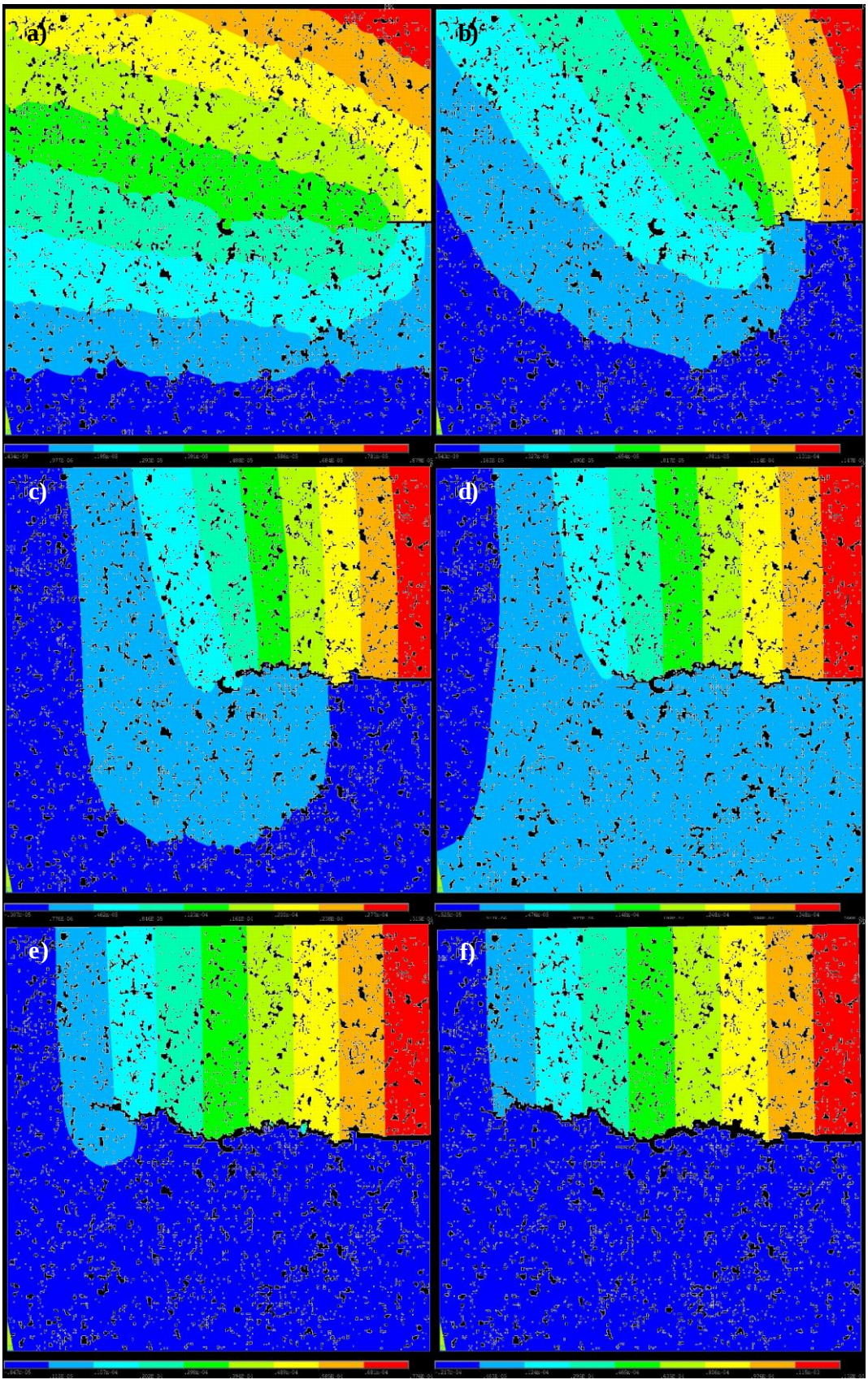

Figure 8.32: Schematic Y-displacement distributions (blue indicates low displacement, red indicates high displacement) in Sample one notched model at a number of crack extensions. Details for these example plots are shown in Table 8.9.

Table 8.9: Crack length and crack opening displacement details for the illustrative Figures Figure 8.31 and Figure 8.32.

Image	Element removal Iteration	Crack Length (mm)	Crack Opening Displacement (mm)
a)	1	0	0
b)	30	1.43	0.0133
c)	46	3.61	0.0288
d)	57	4.89	0.0373
e)	70	6.96	0.0703
f)	85	8.00	0.1166

Similarly to the tensile simulations, the notched models show that crack extension is deflected along porosity resulting in crack path tortuosity. Another mechanism in these models that contributes to a tortuous fracture path is crack branching. Figure 8.33 shows an example of this process. The crack branching mechanism shown in these figures illustrates how the initial macro-crack (a) branches into two simultaneously propagating fracture paths (b) before the original crack path is arrested (c). This mechanism is observed in all of the simulations, however, some model only exhibit a small amount of crack branching (*e.g.* less than five elements).

Load-deflection plots and fracture paths for all six notched models are shown in Figure 8.34 to Figure 8.45. Load-deflection plots for each model show data points which correspond to the element removal iterations. Generally, displacement values used in notched experimental samples are defined as either crack opening displacement (COD) or load-point displacement. Crack opening displacement is defined at the distance the notch opening is extended as a result of external inputs. Experimentally determined COD's are typically measured using a specially designed strain gauge applied to the notch opening (ASTM E399). Determination of this value in the simulations is achieved through analysis of the elemental displacement data, specifically, the two elements at the notch opening (element numbers 63012 and 64080). Each model is considered to have failed when the force input decreases below 5%. Additionally, Figure 8.46 shows the load-deflection plots for each of the six notched models. Comparisons of these plots demonstrate the relative effects of porosity on the crack propagation. Fracture path of each model is demonstrated by a Y-displacement plot. The model is constrained at the bottom surface and as such the area below the advancing crack experiences minimal displacement (dark blue region). Maximum

displacements in these models are located in the area above the advancing crack and as such are roughly similar to the calculated COD. Figure 8.47 shows the crack propagation through all six models. Similarly to the tensile models, the crack path shows significant tortuosity due to deflection towards areas of porosity.

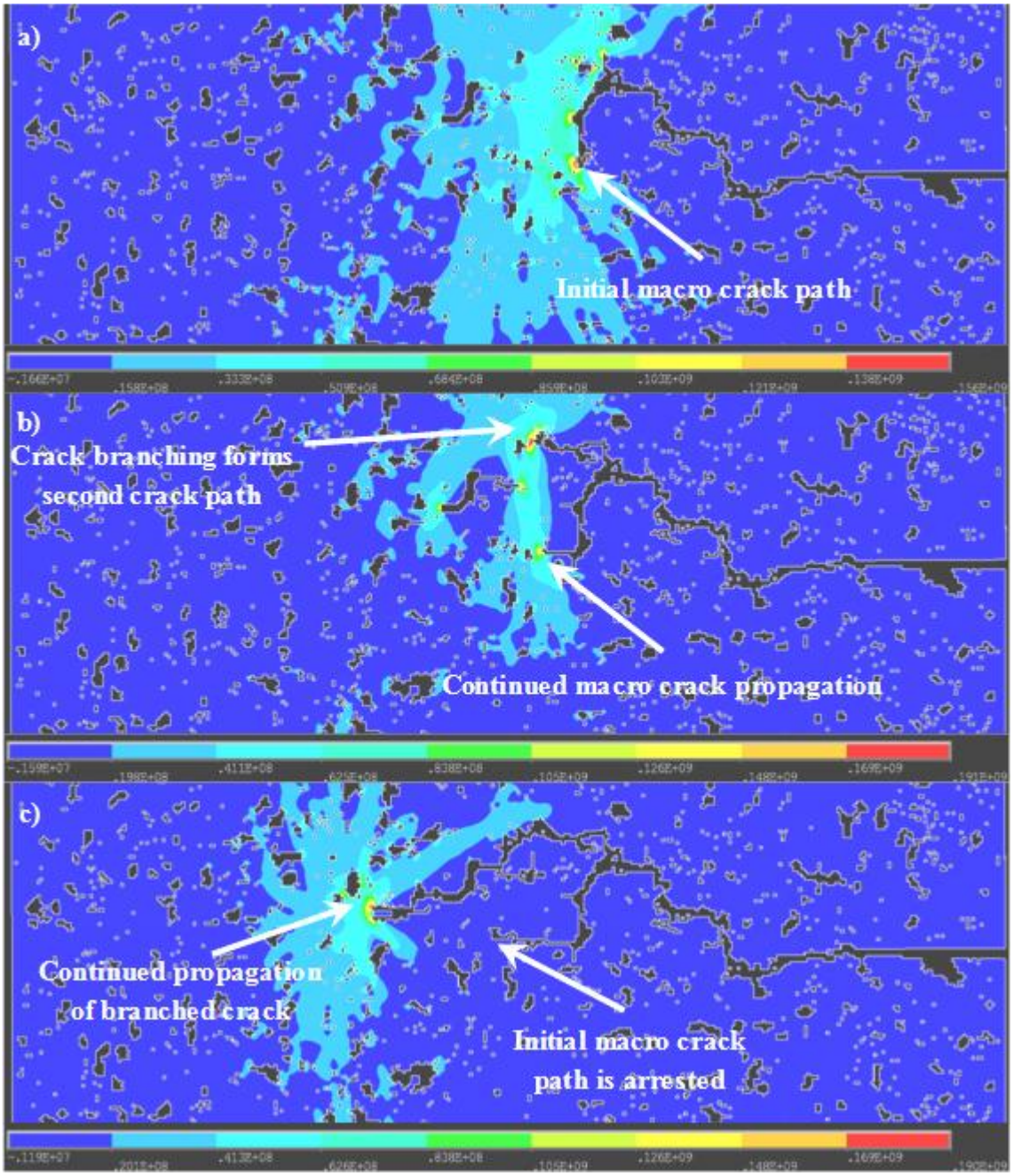

Figure 8.33: Example of crack branching in Sample four. a) Initial failure path of macro-crack. b) Simultaneous propagation of macro-crack and crack branching. c) Initial crack path is arrest and the branched crack continues propagation as a macro-crack.

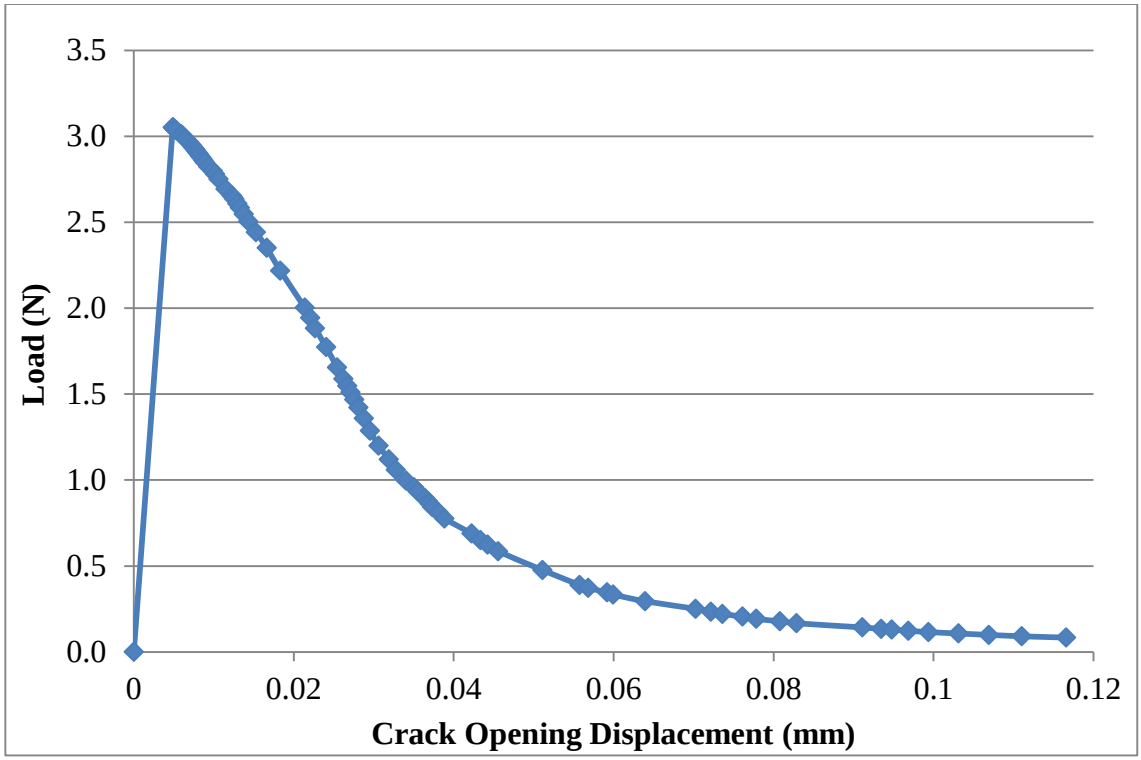

Figure 8.34: Load-deflection plot for Sample one notched model.

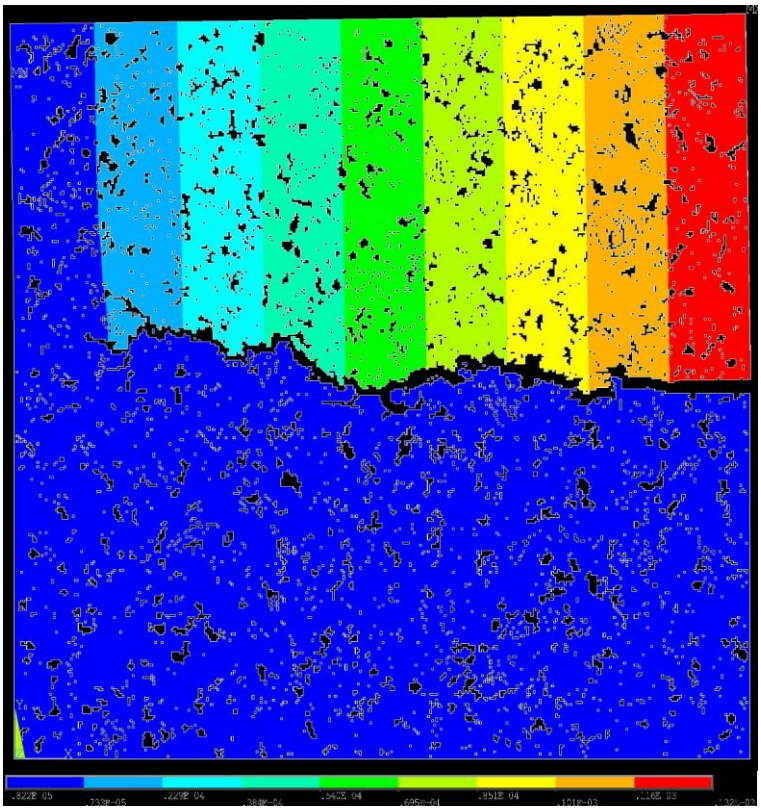

Figure 8.35: Simulation failure path through Sample one notched model.

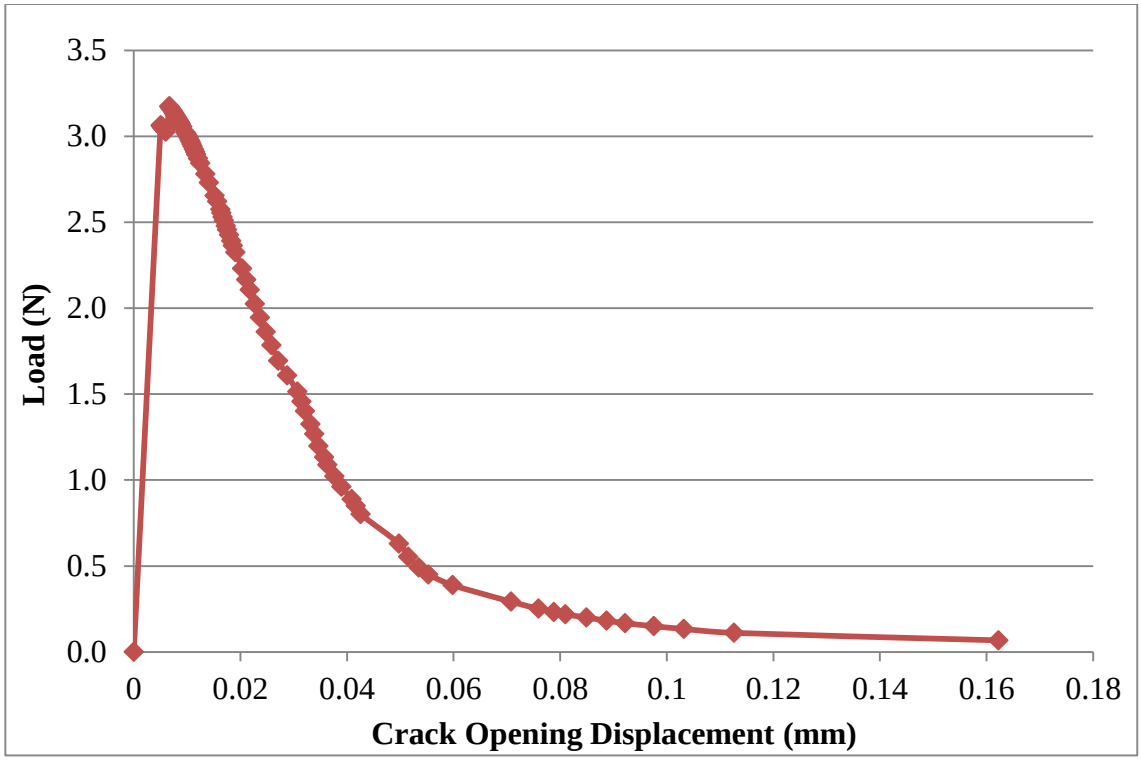

Figure 8.36: Load-deflection plot for Sample two notched model.

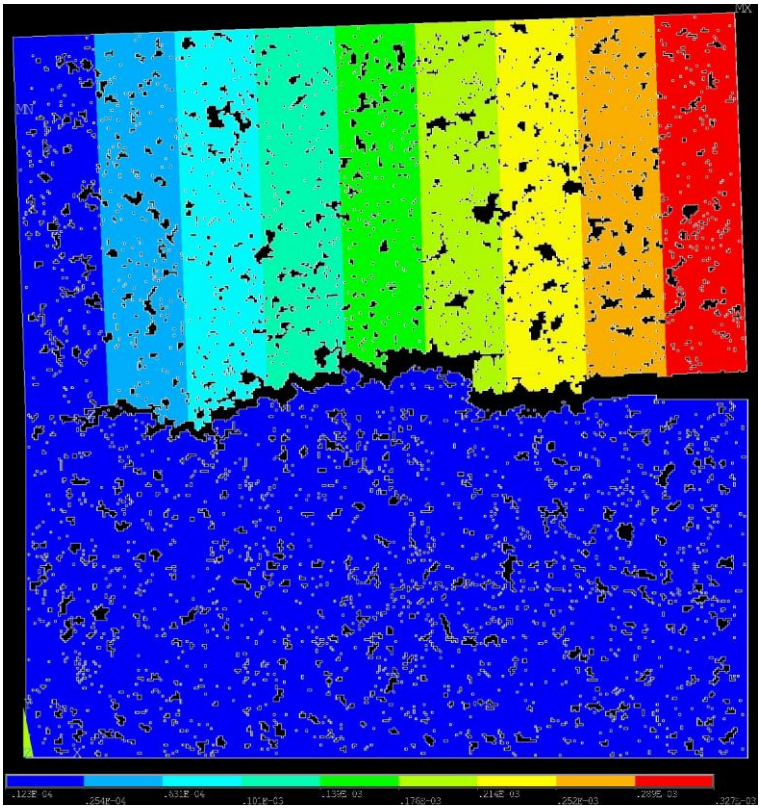

Figure 8.37: Simulation failure path through Sample two notched model.

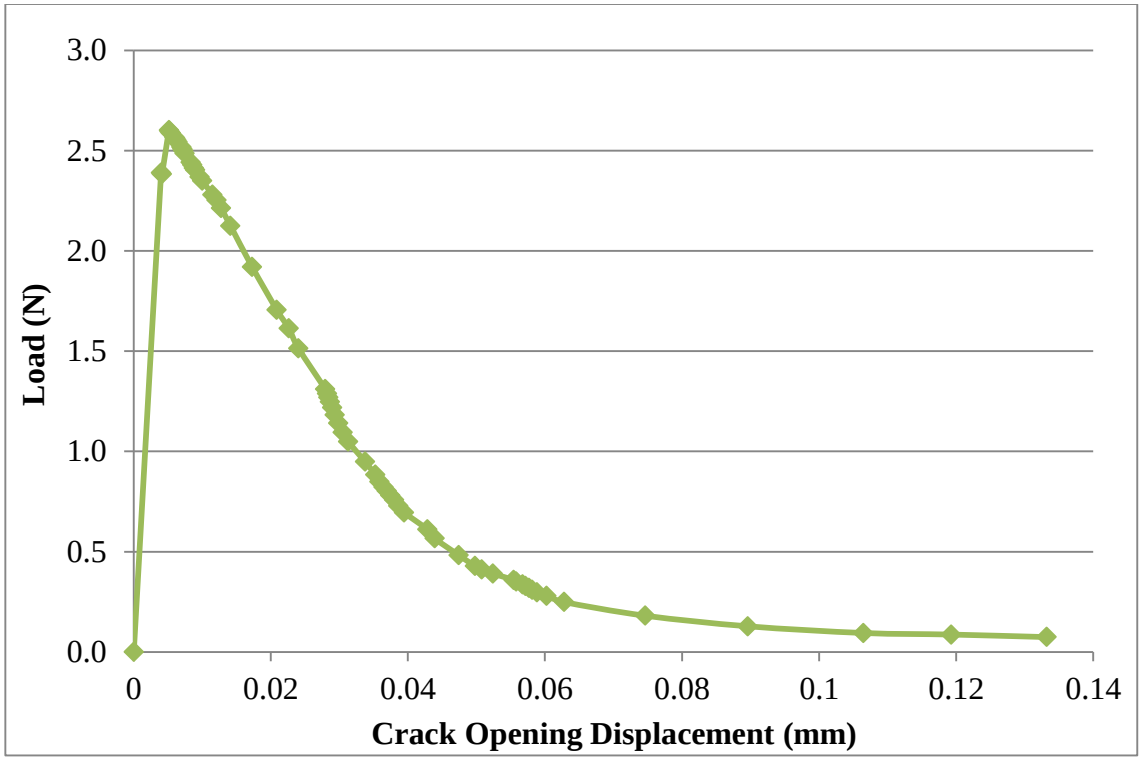

Figure 8.38: Load-deflection plot for Sample three notched model.

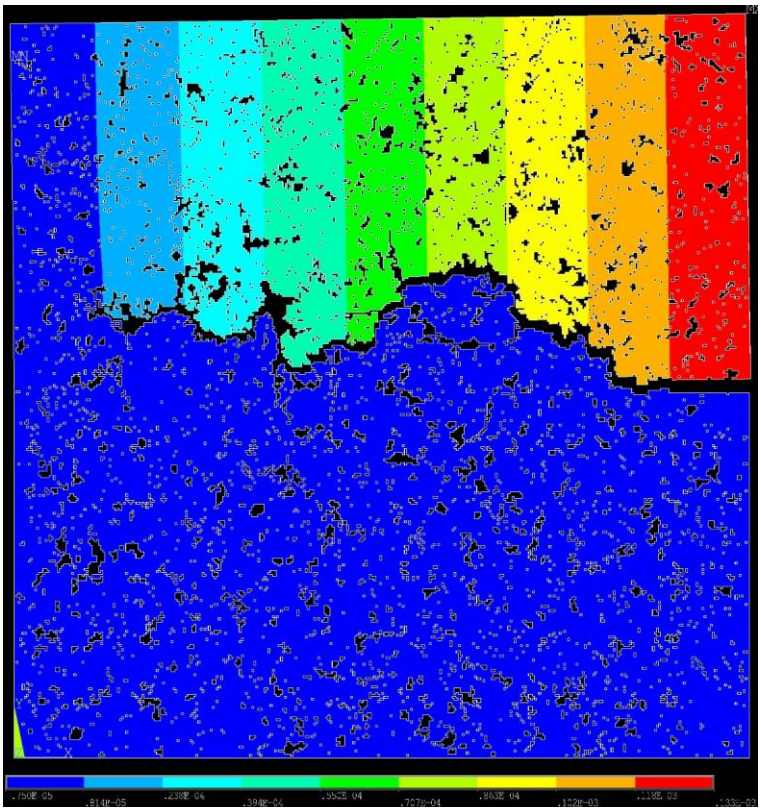

Figure 8.39: Simulation failure path through Sample three notched model.

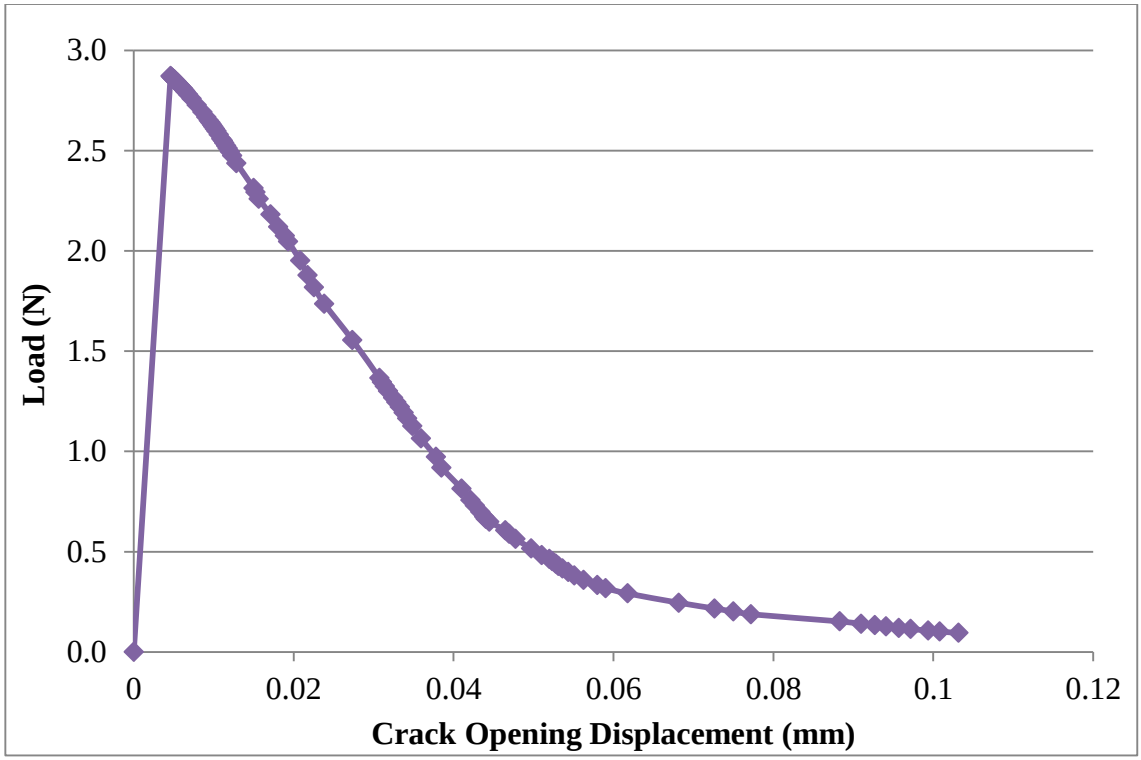

Figure 8.40: Load-deflection plot for Sample four notched model.

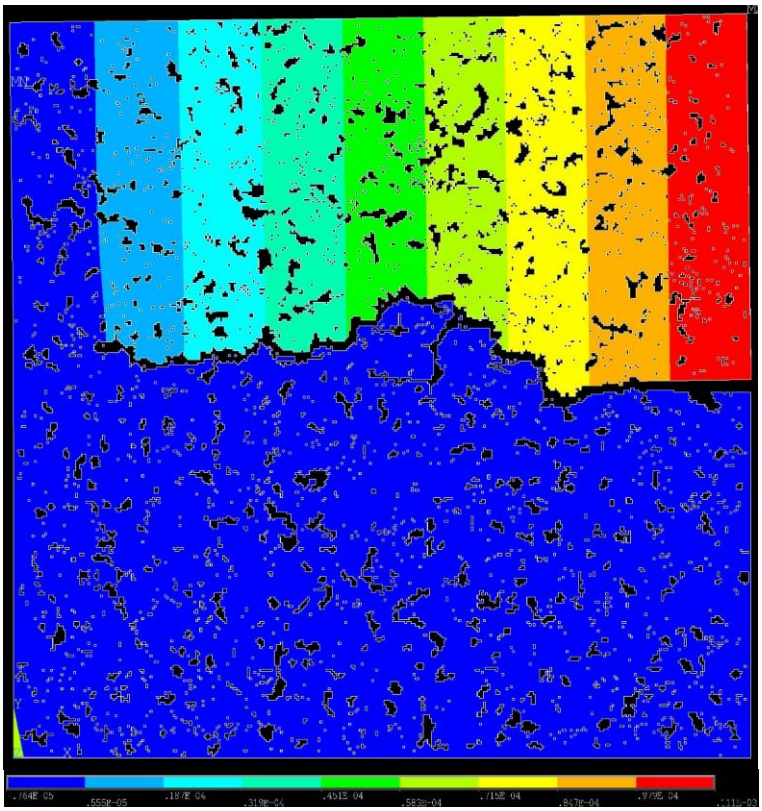

Figure 8.41: Simulation failure path through Sample four notched model.

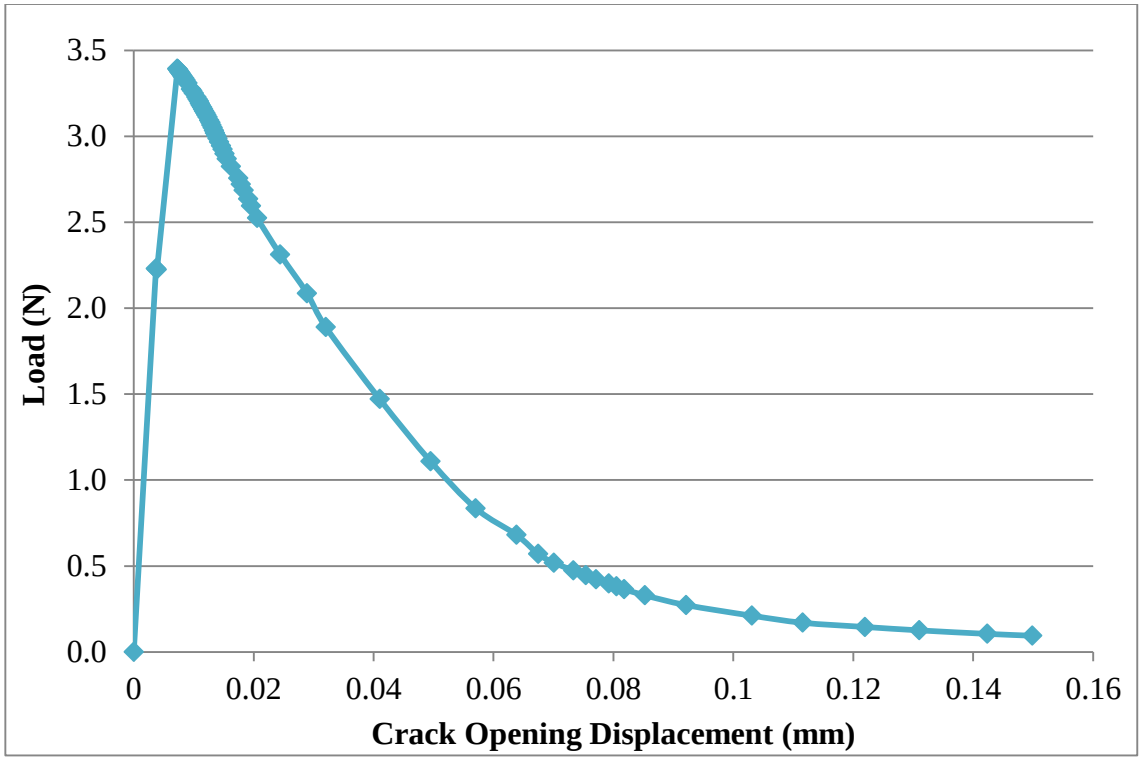

Figure 8.42: Load-deflection plot for Sample five notched model.

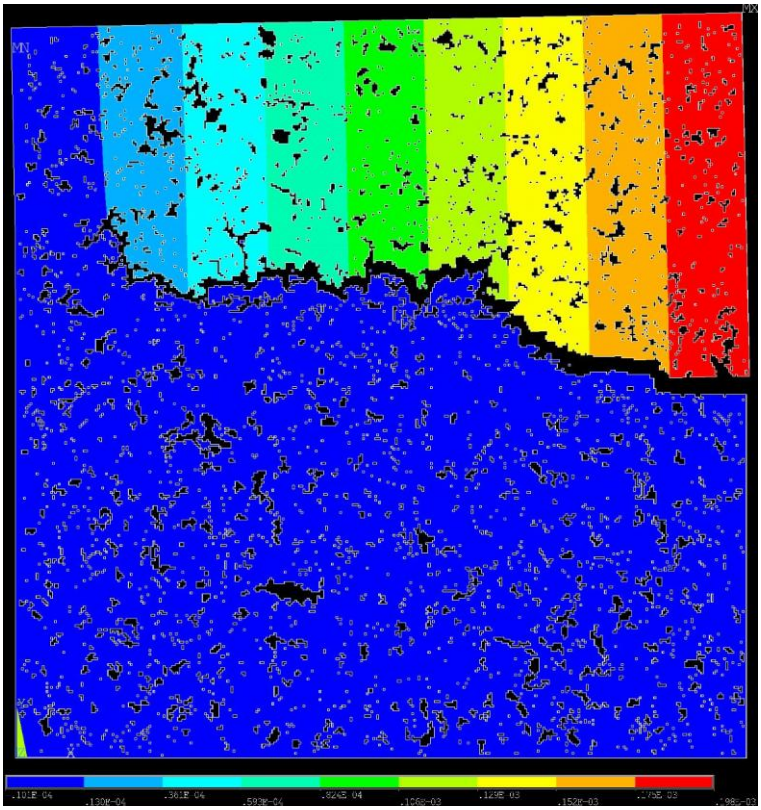

Figure 8.43: Simulation failure path through Sample five notched model.

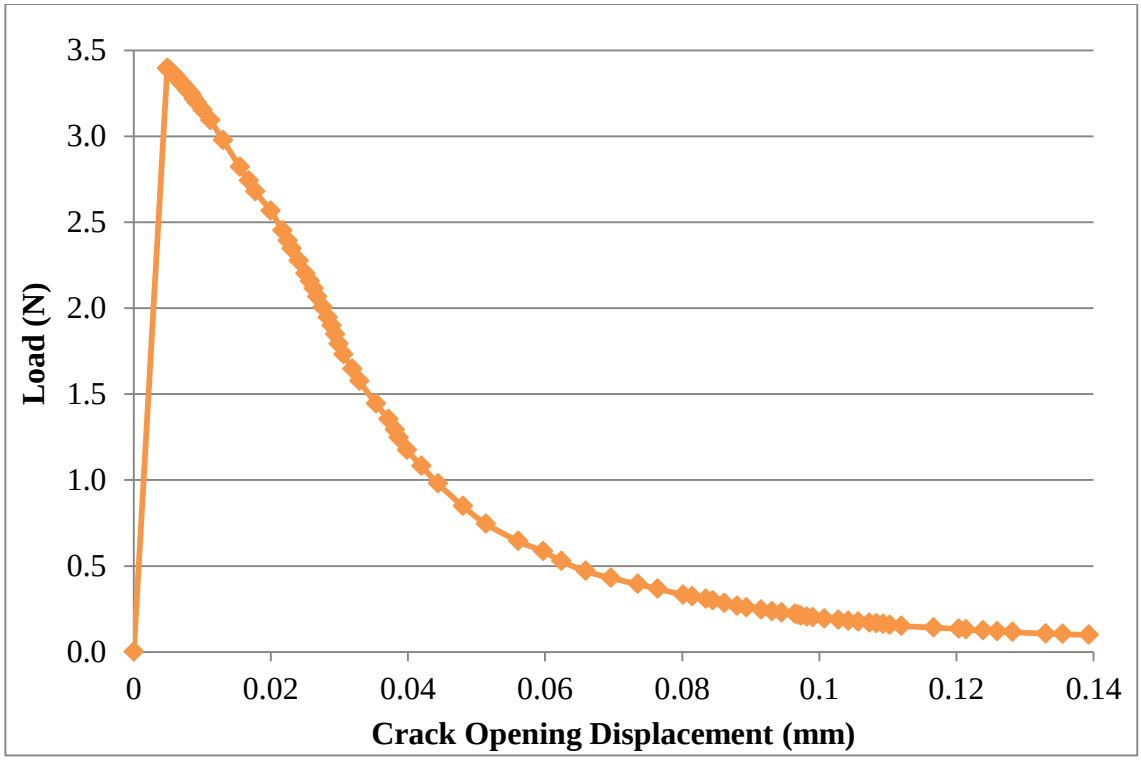

Figure 8.44: Load-deflection plot for Sample six notched model.

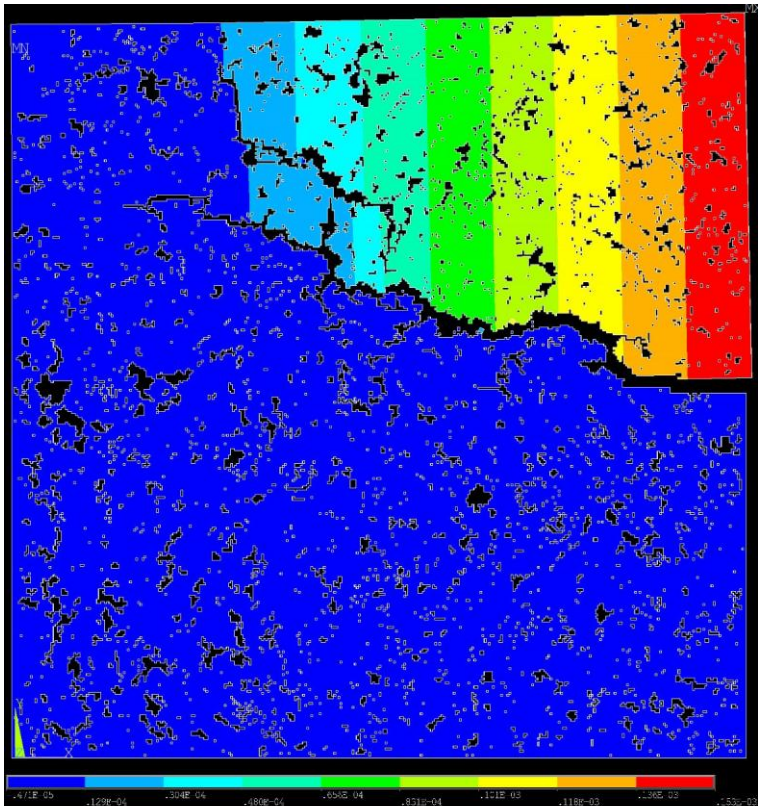

Figure 8.45: Simulation failure path through Sample six notched model.

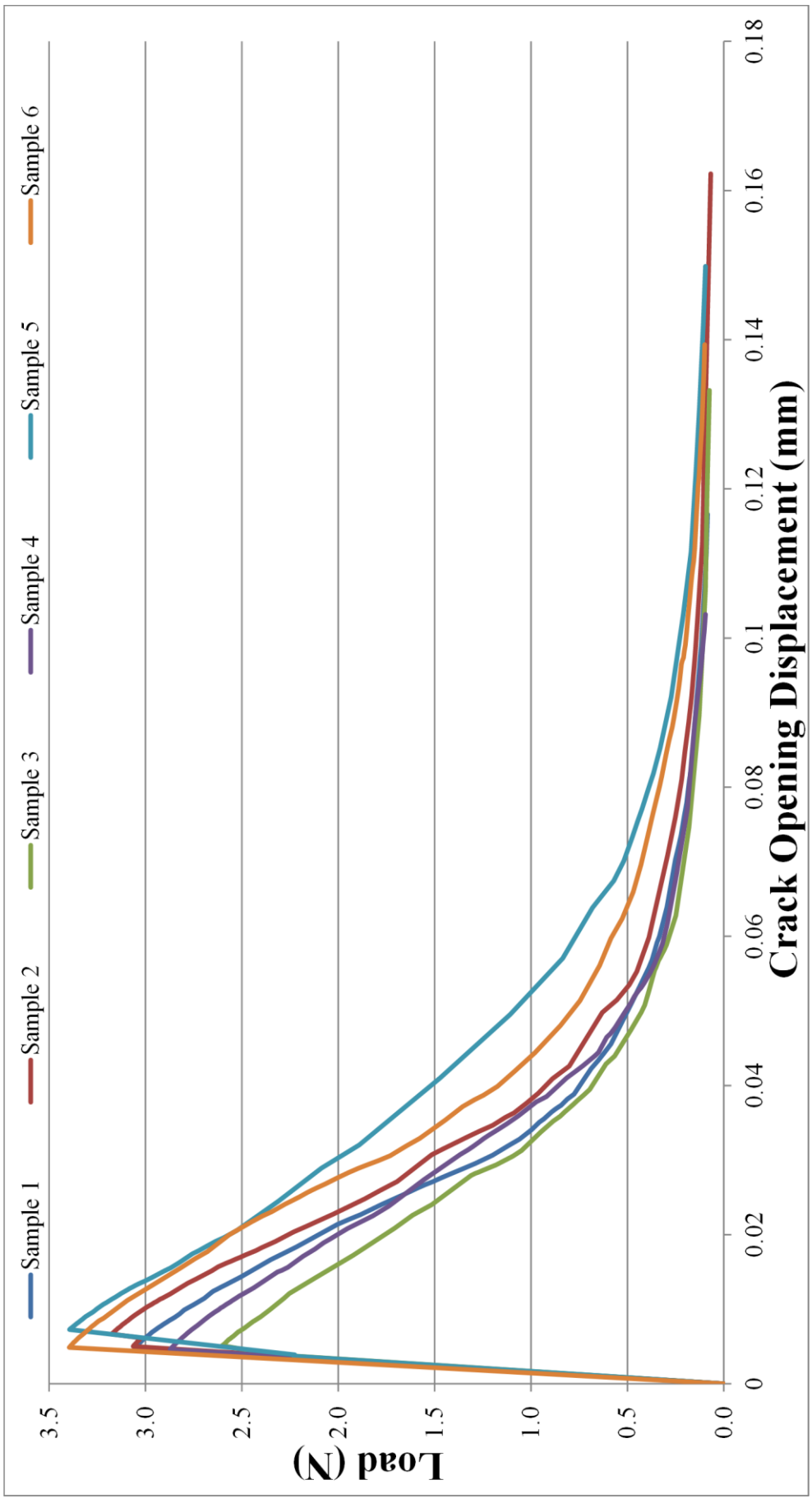

Figure 8.46: Load-displacement curves for all six notched models.

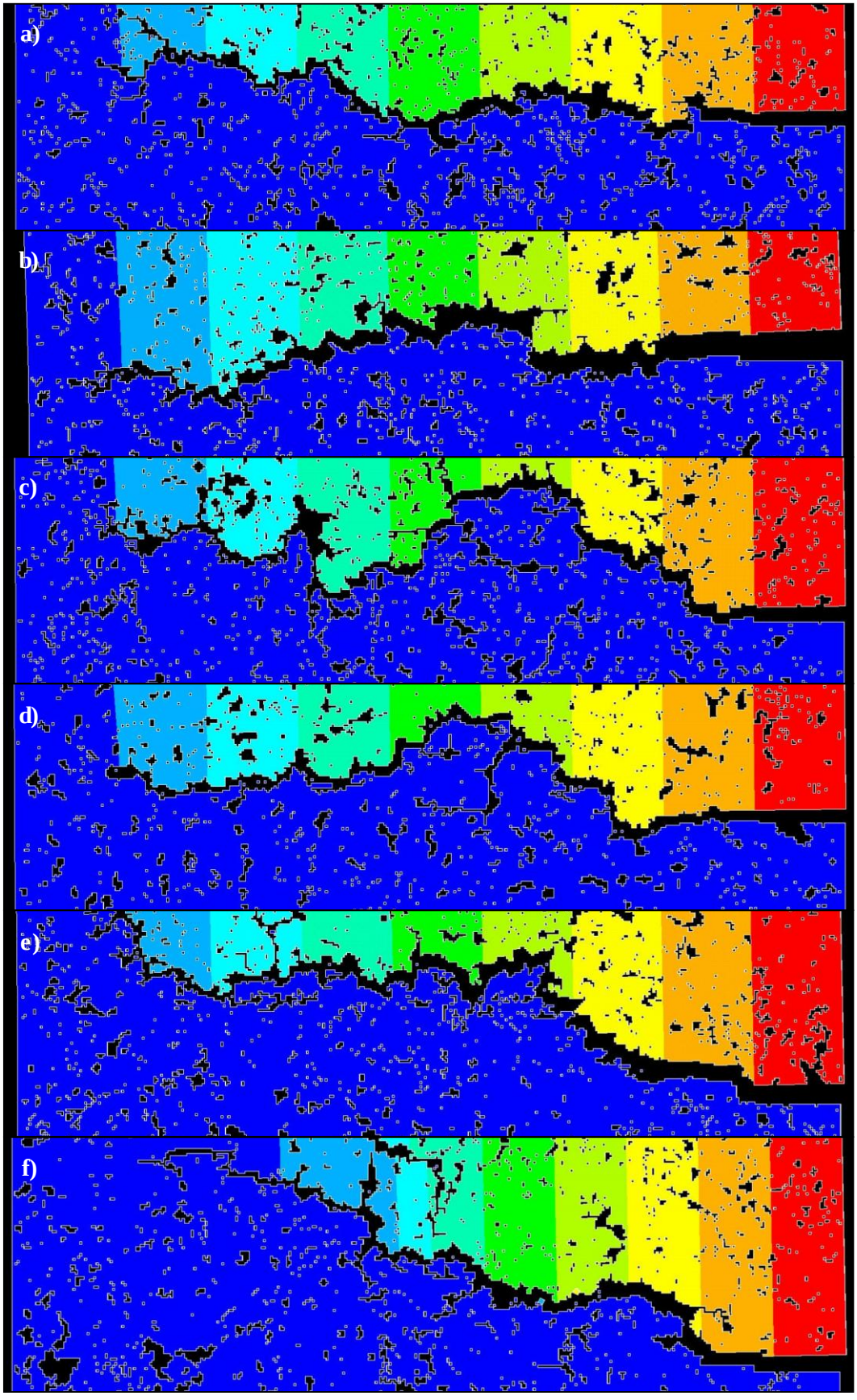

Figure 8.47: Crack path tortuosity through notched models for a) Sample one, b) Sample two, c) Sample three, d) Sample four, e) Sample five, f) Sample six.

The first noticeable discrepancy between the simulated and experimental load-deflection plots is the absence of pre-peak micro-cracking in the computational models. Micro-cracking in experimental samples occurs due to localised stress concentrations within the fracture process zone ahead of the crack tip. Although some samples did demonstrate some pre peak microcracking (Samples two, three and five), the peak load was sharp in all models and did not show the softening response commonly associated with graphite. The most likely reason for this observation is that in a two-dimensional model the maximum stress was entirely focused at the notch tip and did not allow for any significant localised stress concentration. In contrast, volumetric samples are far more likely to contain features that could potentially lead to such concentrations. Additionally, a three-dimensional stress distribution is likely to be asymmetric due to the probabilistic nature of the pore distribution, thus leading to a greater likelihood of pre-peak micro-cracking.

Table 8.10 provides a summary of the mechanical data for the notched models. Linear elastic fracture parameters, critical stress intensity factor, K_{IC}, critical strain energy release rate, G_{IC}, and work of fracture (*wof*), γ_{wof}, are included in addition to data regarding element removal iteration, peak load, applied stress and total energy.

Table 8.10: Summary of data for six notched models.

Sample	Element Removal Iterations	Peak Load (N)	Applied Stress (MPa)	Total Energy (μJ)	K_{IC} (MPa·m$^{0.5}$)	G_{IC} (Jm^{-2})	γ_{wof} (Jm^{-2})
1	84	3.05	10.87	96.09	1.04	31.42	189.98
2	89	3.18	11.30	108.95	1.04	50.26	215.40
3	65	2.60	9.26	84.37	0.89	31.70	166.81
4	93	2.87	10.22	92.69	0.98	26.77	183.25
5	70	3.39	12.08	140.38	1.16	56.12	277.54
6	94	3.40	12.08	128.13	1.16	31.90	253.32
Mean	82.5	3.08	10.97	108.43	1.04	38.03	214.38
Standard Deviation	11.18	0.28	1.01	19.95	0.10	10.99	39.44

Peak loads (and thus the applied stresses) are, as expected, lower than those output from the tensile models due to the stress concentration at the notch tip. Additionally, the standard deviation of the notched models is proportionally less than the tensile simulations (see Table 8.11). This suggests that peak load and thus failure initiation of

notched simulations are less variable, which is likely due to the notch providing a consistent defect between models. Conversely, failure initiation in tensile models results from the probabilistic pore distribution, thereby accounting for the increased variability.

Table 8.11: Comparison of peak load for tensile and notched models in addition to consideration for the effect of porosity.

Sample	Model Porosity (%)	Peak Load (N)	
		Tensile	Notched
1	9.57	5.51	3.05
2	9.48	5.74	3.06
3	10.08	3.90	2.60
4	10.10	4.89	2.87
5	9.76	4.83	3.39
6	9.54	4.23	3.40
Mean		4.85	3.06
Standard Deviation		0.65	0.28
Std. Dev. / Mean (%)		13.38	9.12

Table 8.11 also shows the porosity for each model (note that this value does not include the initial notch). Initial consideration for the relationship between porosity and peak load suggests that models with higher porosities will show a decrease in peak load and thus bulk strength. Indeed, applying Pearson's correlation coefficient to these data yields values of -0.540 and -0.672 for the tensile and notched models respectively, suggesting a moderate to strong negative correlation (Rodgers *et al.*, 1988). This relationship is further demonstrated by plotting the peak load against porosity (see Figure 8.48). The available data does suggest that model strength decreases with porosity, as has been demonstrated through experimental testing (*e.g.* Brocklehurst, 1977). Due to the small amount of available data, it is not possible to definitively state that more porous models are weaker; however, the similarities between experimental results and the computational simulations are encouraging.

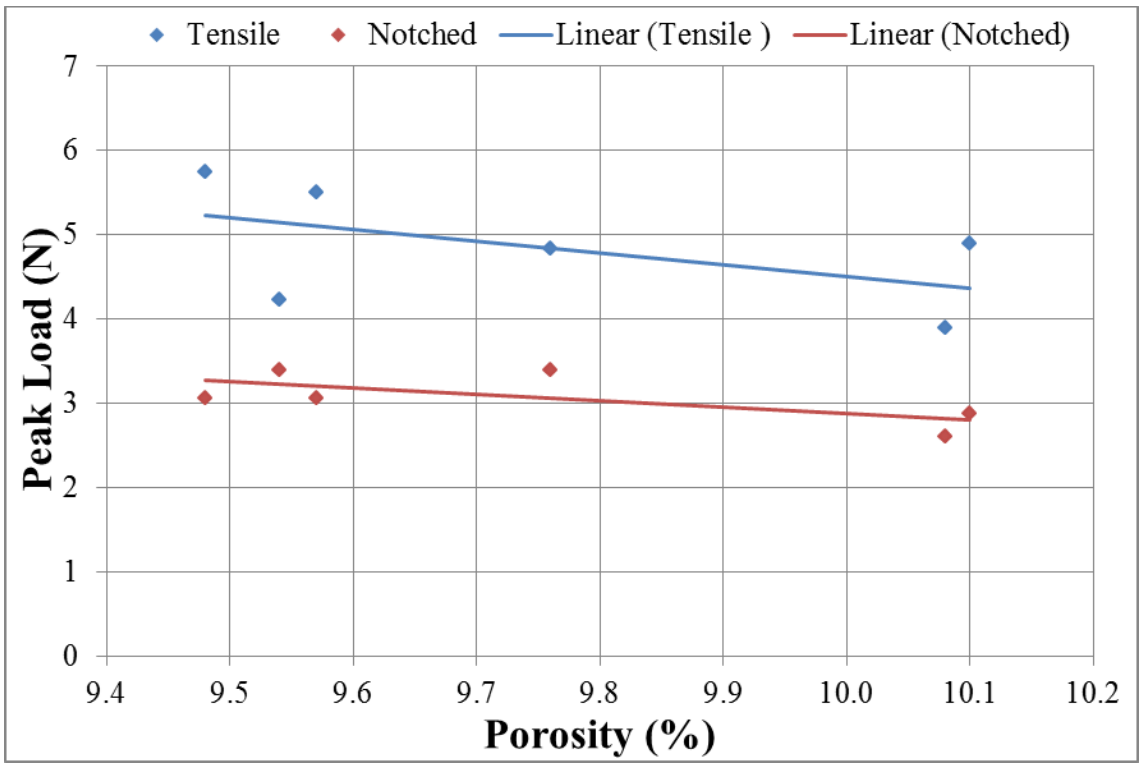

Figure 8.48: Plot to demonstrate the relationship between porosity and peak load for both tensile and notched models.

Critical stress intensity factor, K_{IC}, for each model was calculated using expressions in ASTM 399.

$$K_{IC} = \sigma^{\text{init}} {a_0}^{0.5} \text{Y}\left(\frac{a_0}{W}\right) \qquad \text{Equation [8.1]}$$

where, σ^{init} is the stress at fracture initiation (peak load applied stress in Table 8.10), a_0 is the notch depth, 1 mm, W is the model width, 10 mm, and $Y(a_0/w)$ is a geometric factor calculated as being 3.028 using Equation 3.25. The average value for critical stress intensity was calculated as 1.04 MPa·m$^{0.5}$ with a standard deviation of 0.1 MPa·m$^{0.5}$. These simulated values compare favourable to experimentally derived critical stress intensities which typically range between 0.8 and 1.5 MPa·m$^{0.5}$ (*e.g.* Ouagne *et al.* (2002), Brocklehurst, (1977) (see Table 3.3)). These values for K_{IC} were calculated using a CT sample geometric factor ($Y(a_0/w)$). Considering that they are representative of experimental values it suggests that the model geometry is analogous to a CT sample.

Critical strain energy release rate, G_{IC}, is obtained using the equation:

$$G_{IC} = \frac{U_1}{b(W - a_0)} \qquad \text{Equation [8.2]}$$

where, U_1 is the area under the load-displacement curve up to the point of fracture initiation and b is the model thickness, 0.0281 mm. The average critical strain energy release rate for the models was calculated as 38.03 Jm^{-2} with a standard deviation of 10.99 Jm^{-2}. These values are significantly lower than the experimentally determined 138 ± 10 Jm^{-2} observed by Ouagne (2002). The same paper gave values of 79 ± 10 Jm^{-2} for PGA graphite. The discrepancy between the two critical strain energy release rates was suggested to be due to a greater amount of elastic energy being stored in the IM1-24 before the peak load is reached. This explanation is consistent with the simulated results since the absence of pre peak micro-cracking means that the relative displacement to peak load is lower (thus resulting in lower energy to peak load values) than experimental CT samples. Indeed, comparisons of Samples five and six demonstrate this effect. Despite near identical peak loads, Samples five and six have calculated G_{IC} values of 56.12 and 31.90 Jm^{-2} respectively. Sample five is one of the samples to demonstrate pre-peak microcracking and as a result has a G_{IC} value that is approximately 75% greater than Sample six.

The work of fracture γ_{wof} is determined using the equation:

$$\gamma_{wof} = \frac{U_T}{2b(W - a_0)} \qquad \text{Equation [8.3]}$$

where, U_T is the total area under the load-displacement curve (Total energy in Table 8.10). Average work of fracture for the six models was 214.38 Jm^{-2} with a standard deviation of 39.44 Jm^{-2}. This is higher than the value of 136 ± 9 Jm^{-2} determined though experimental testing by Ouagne (2002). Interestingly, PGA graphite tested in the same configuration gave a *wof* value of 170 ± 31 Jm^{-2}, which is more representative to the simulated values in terms of average and standard deviation. The relatively high *wof* in PGA is suggested to be an indication of a greater amount of subcritical cracking compared with the IM1-24. This could potentially be a factor when analysing simulated results since crack branching is observed in most of the models.

In addition to LEFM values, non-linear fracture toughness parameters may also be derived for the computational data. K_R curves plot the stress intensity factor K_I, against increasing crack length and are determined using the equation:

$$K_R(n) = \sigma(n)a(n)^{0.5}\mathrm{Y}\left(\frac{a(n)}{W}\right) \qquad \text{Equation [8.4]}$$

where, $\sigma(n)$ and $a(n)$ are the stress and crack length at the n^{th} iteration respectively and $Y(a(n)/w)$ is a geometric factor.

The energy based parameter; J_R is also plotted as function of increasing crack length at iteration, n, using the equation suggested by Rice *et al.* (1973):

$$J_R(n) = \frac{2U(n)}{b(W - a(n))} \qquad \text{Equation [8.5]}$$

where, $U(n)$ and $a(n)$ are the energy and crack length at the n^{th} iteration respectively. Energy values are determined by calculating the area under the load-deflection curve for each cycle (see Figure 3.7). After each iteration, it is considered that there is a new the sample (or in this case model) with a crack of length a.

Figure 8.49 to Figure 8.60 show the K_R and J_R curve for each of the six models. These parameters are plotted against the crack length ($a - a_0$). As expected the K_R values at a crack length of zero are close to the K_{IC} values shown in Table 8.10, since this is the critical stress intensity required to initiate fracture of the model. There is a significant amount of scatter in all of the plots which may be attributed to the determination of crack length and the fracture mechanisms occurring within the simulated microstructure. Utilising image analysis software to measure the crack length is accurate; however, determining the location of the crack tip can be problematic due micro-cracks and crack branching. There is an inherent variability when calculating non-linear fracture parameters due to their dependence on energy and stress values which are affected by microstructural variations (*e.g.* Ouagne *et al.* (2002) Allard *et al.* (1991) *etc.*). Each of the plots shows an initial rise followed by a 'plateau' region which corresponds to steady state crack propagation. The plateau is then be followed by either an increase or decrease in K_R or J_R values. Some examples of J_R curves (Samples one and three) do not contain enough data to conclude a post-plateau trend.

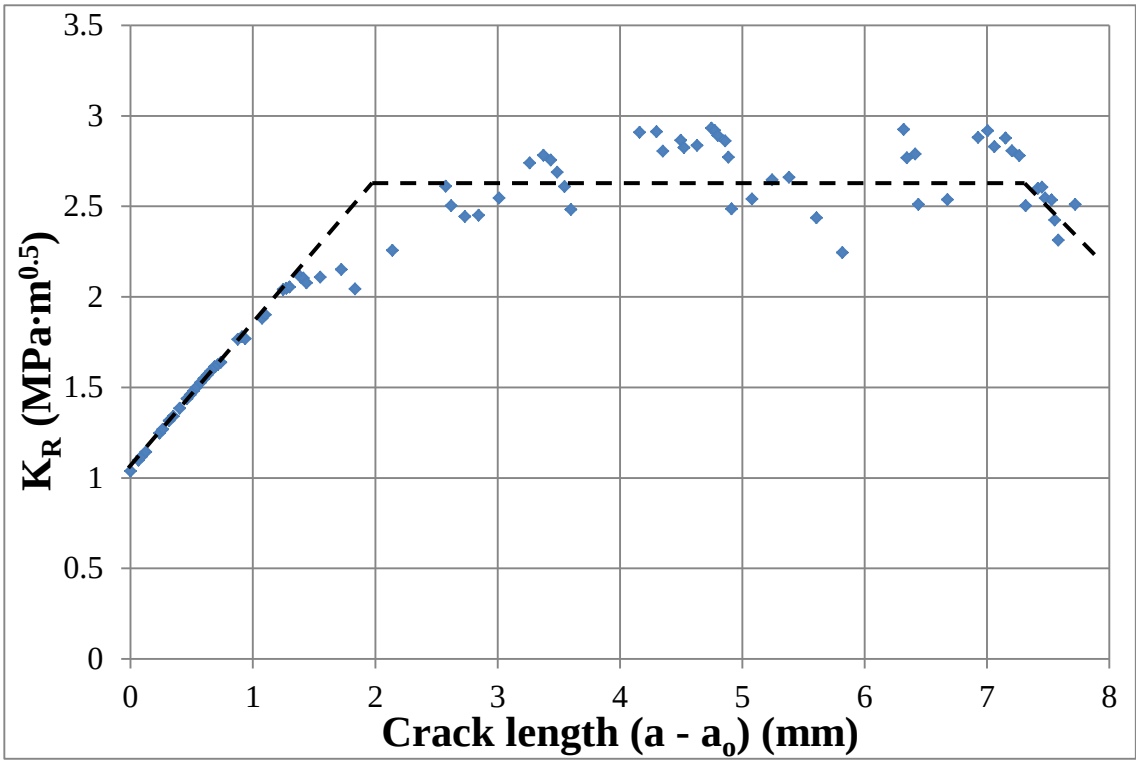

Figure 8.49: Simulated K_R curve for Sample one.

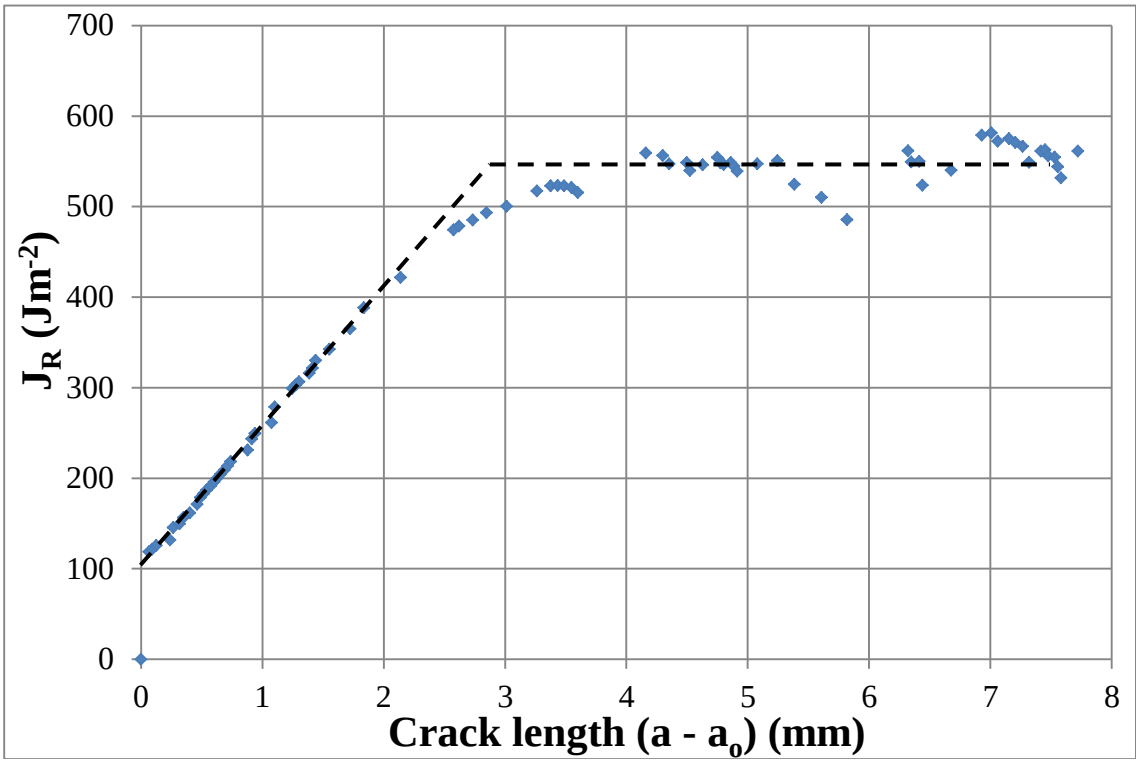

Figure 8.50: Simulated J_R curve for Sample one.

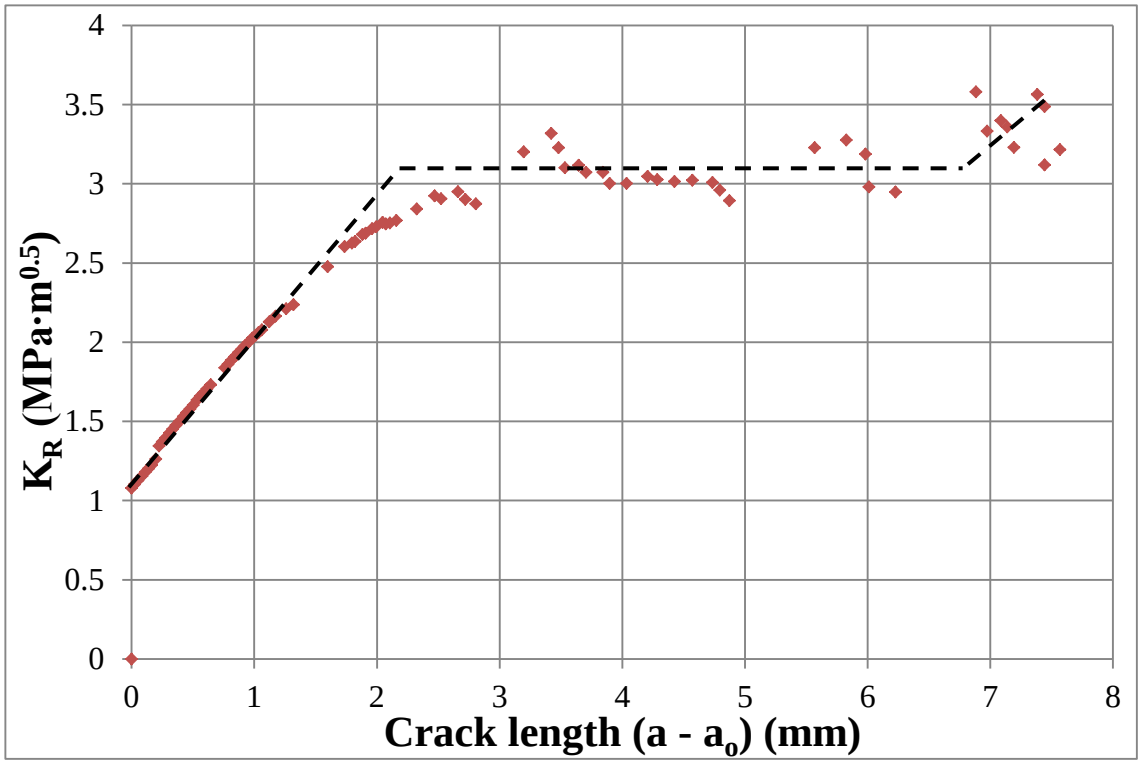

Figure 8.51: Simulated K_R curve for Sample two.

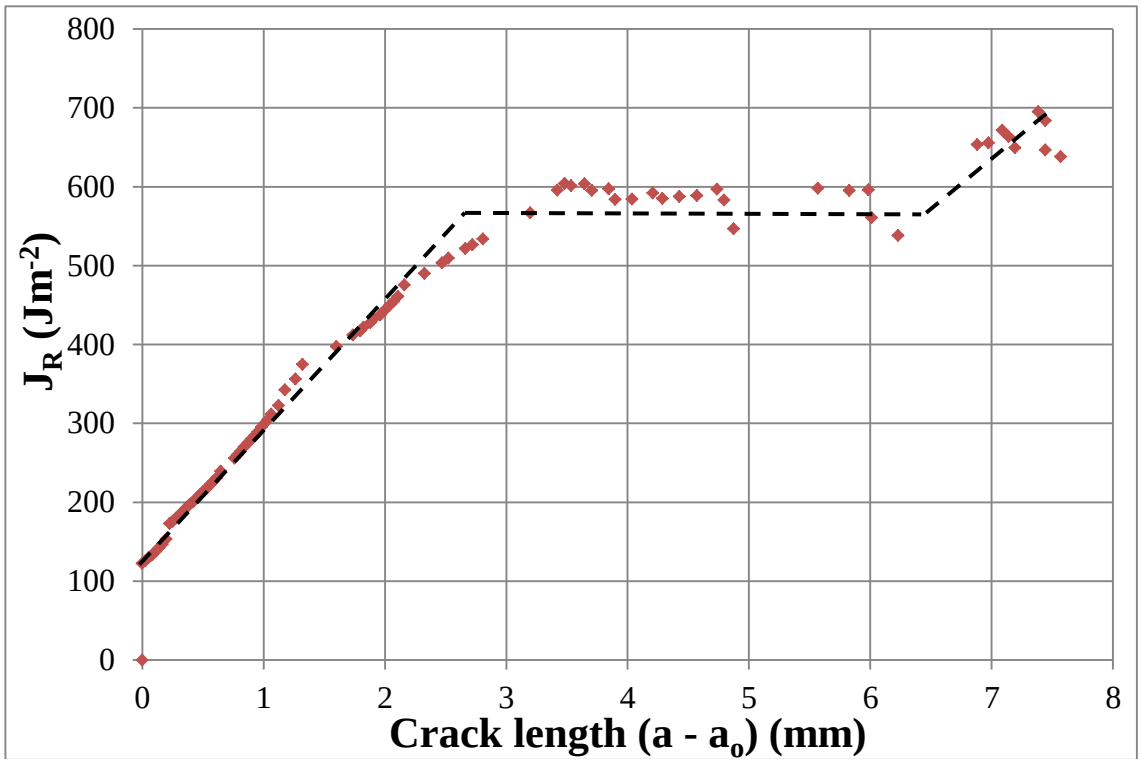

Figure 8.52: Simulated J_R curve for Sample two.

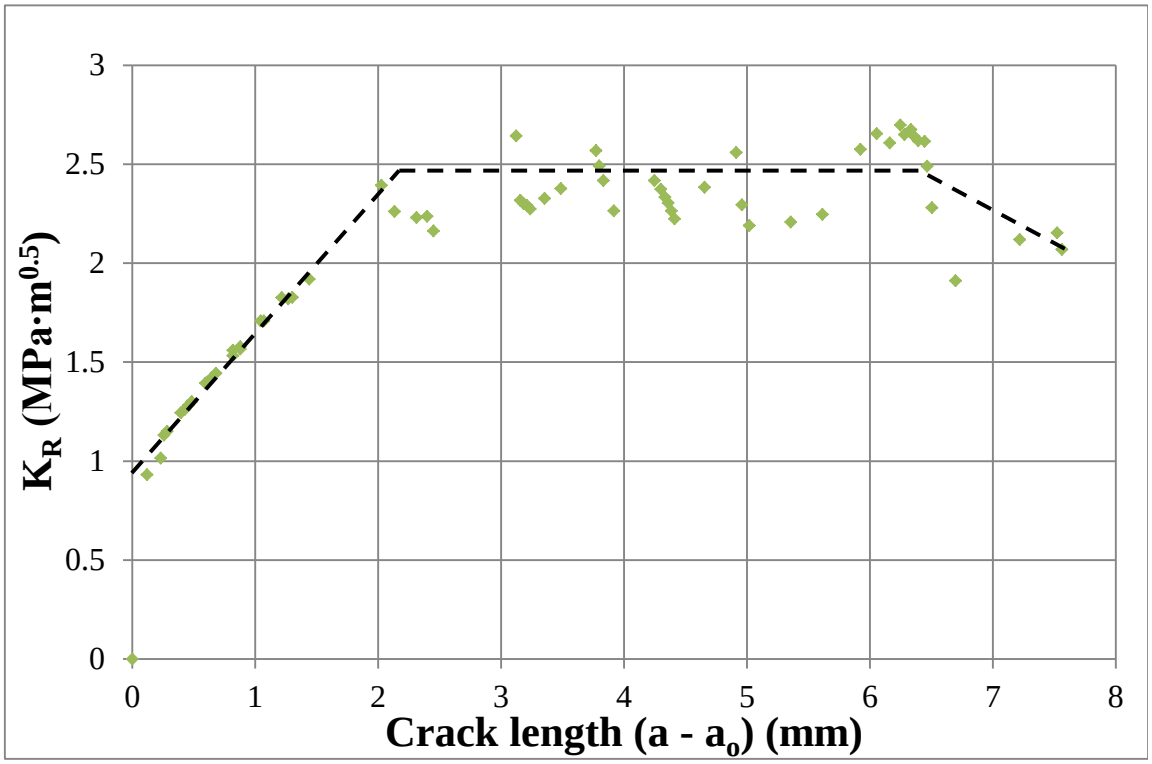

Figure 8.53: Simulated K_R curve for Sample three.

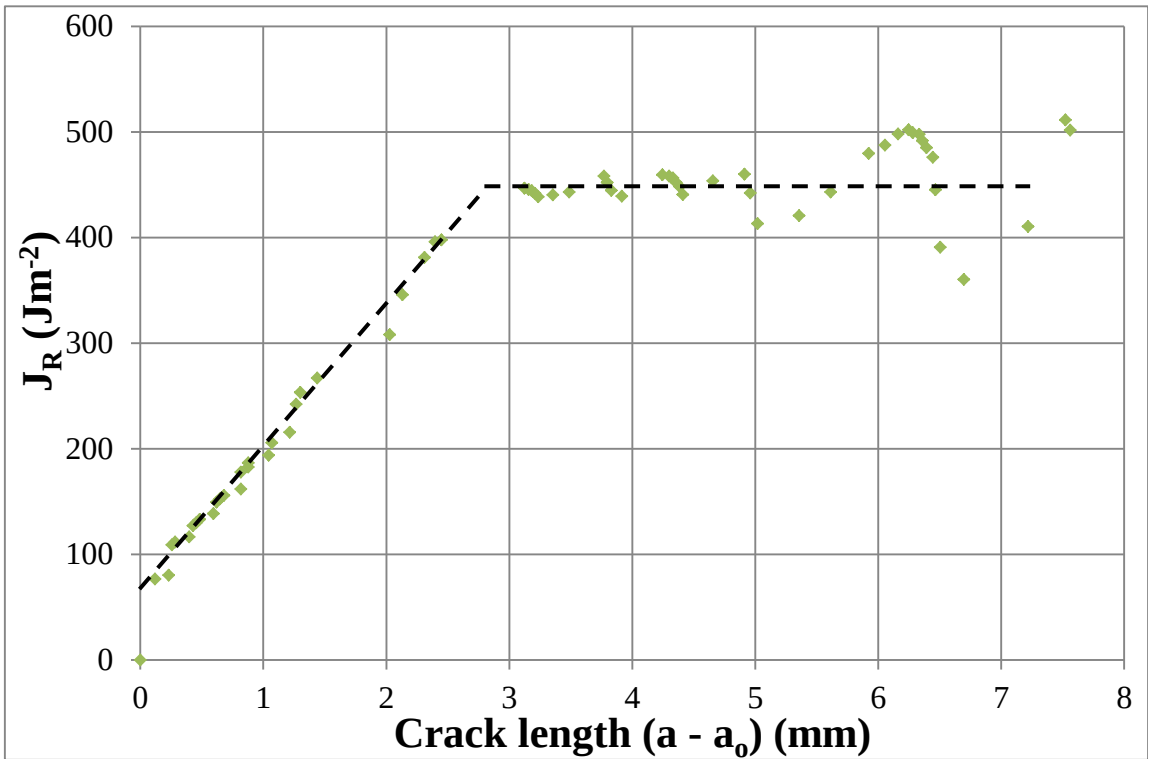

Figure 8.54: Simulated J_R curve for Sample three.

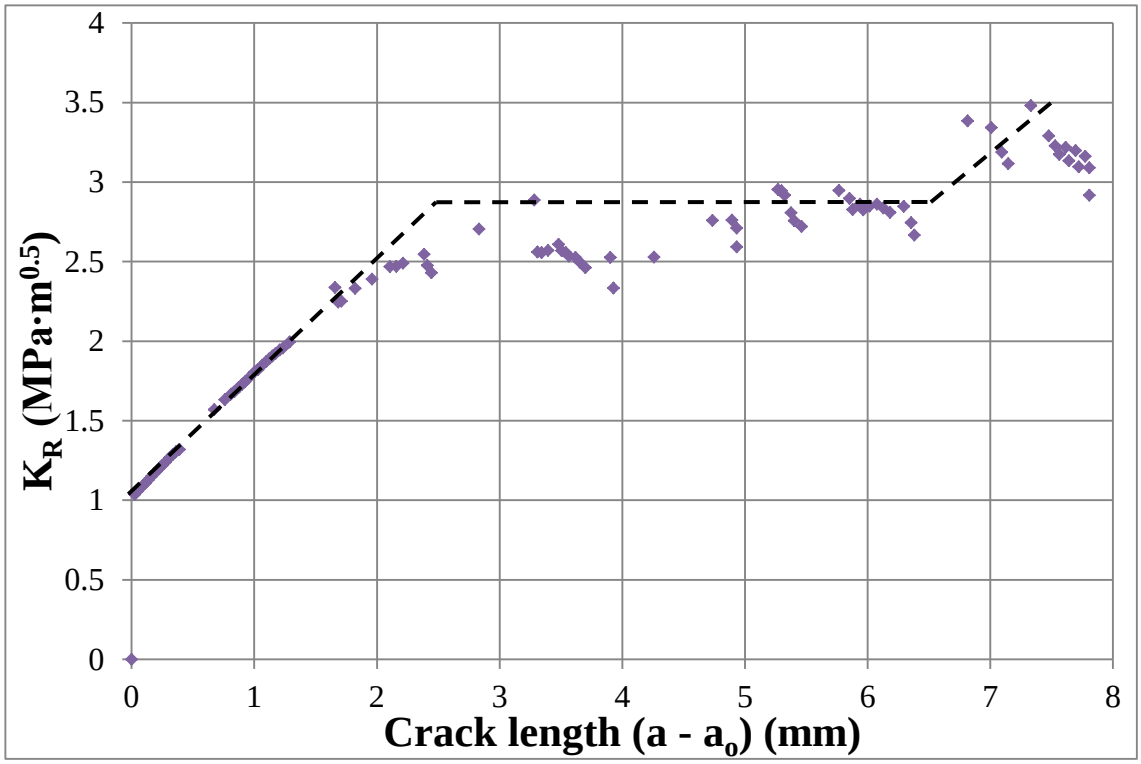

Figure 8.55: Simulated K_R curve for Sample four.

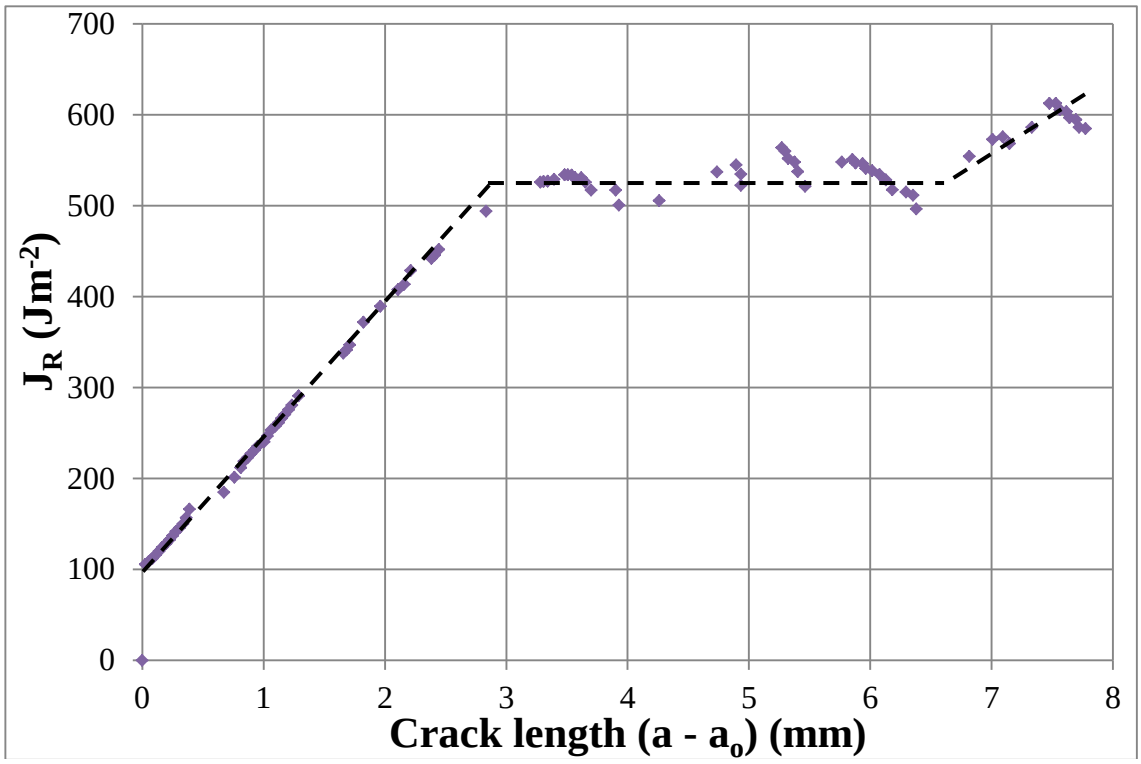

Figure 8.56: Simulated J_R curve for Sample four.

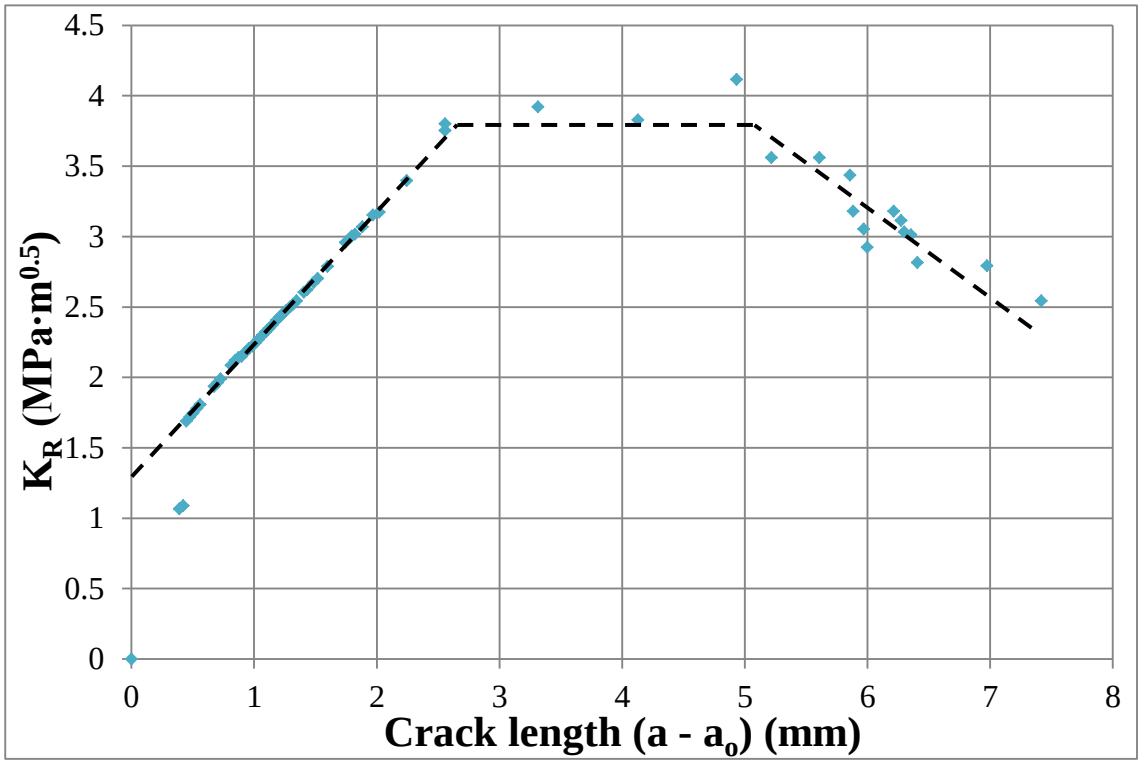

Figure 8.57: Simulated K_R curve for Sample five.

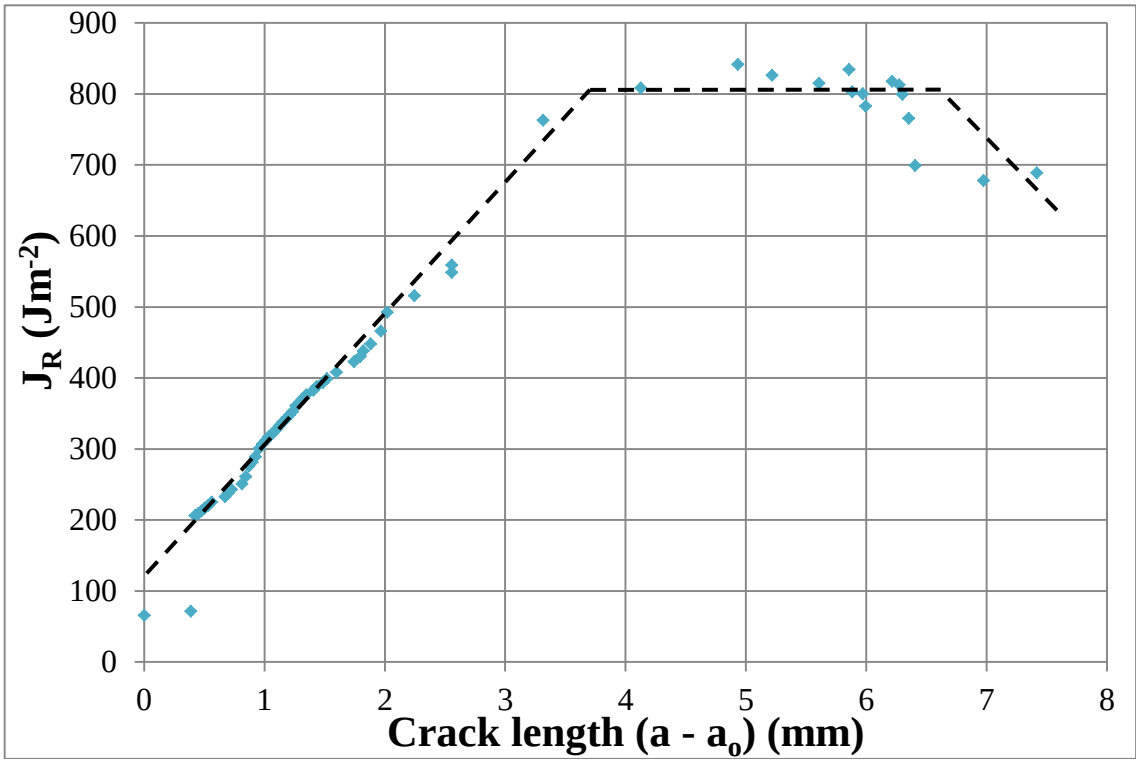

Figure 8.58: Simulated J_R curve for Sample five.

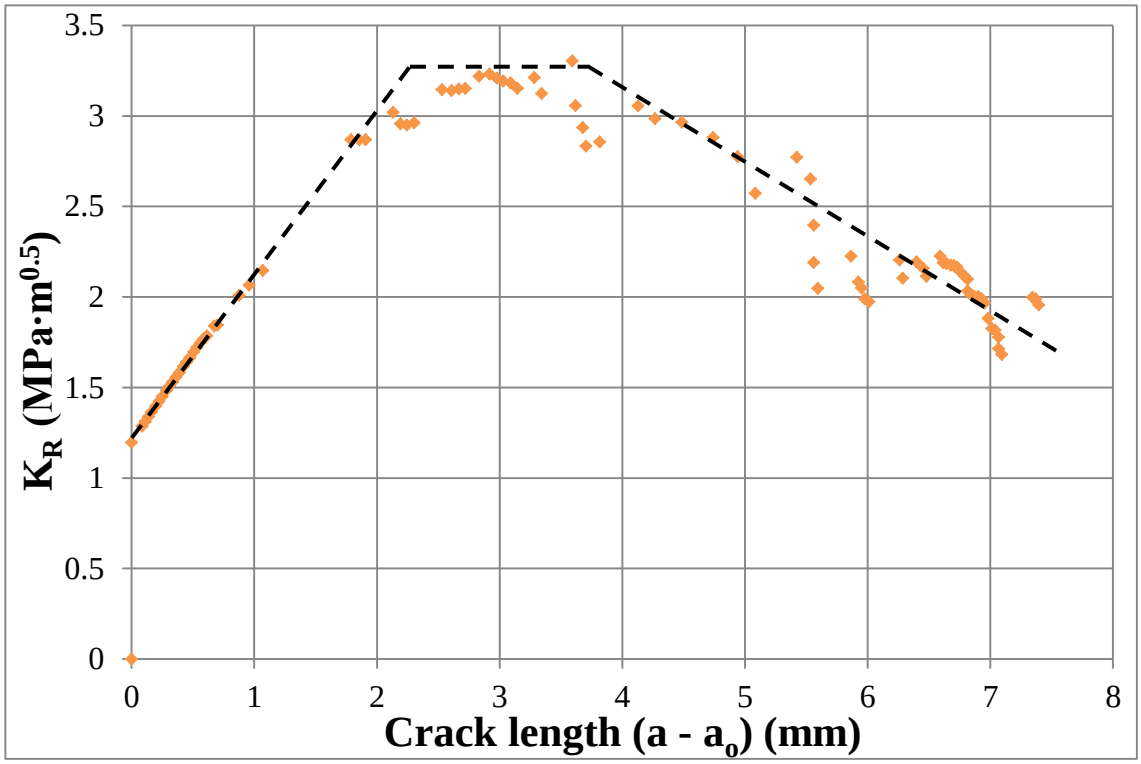

Figure 8.59: Simulated K_R curve for Sample six.

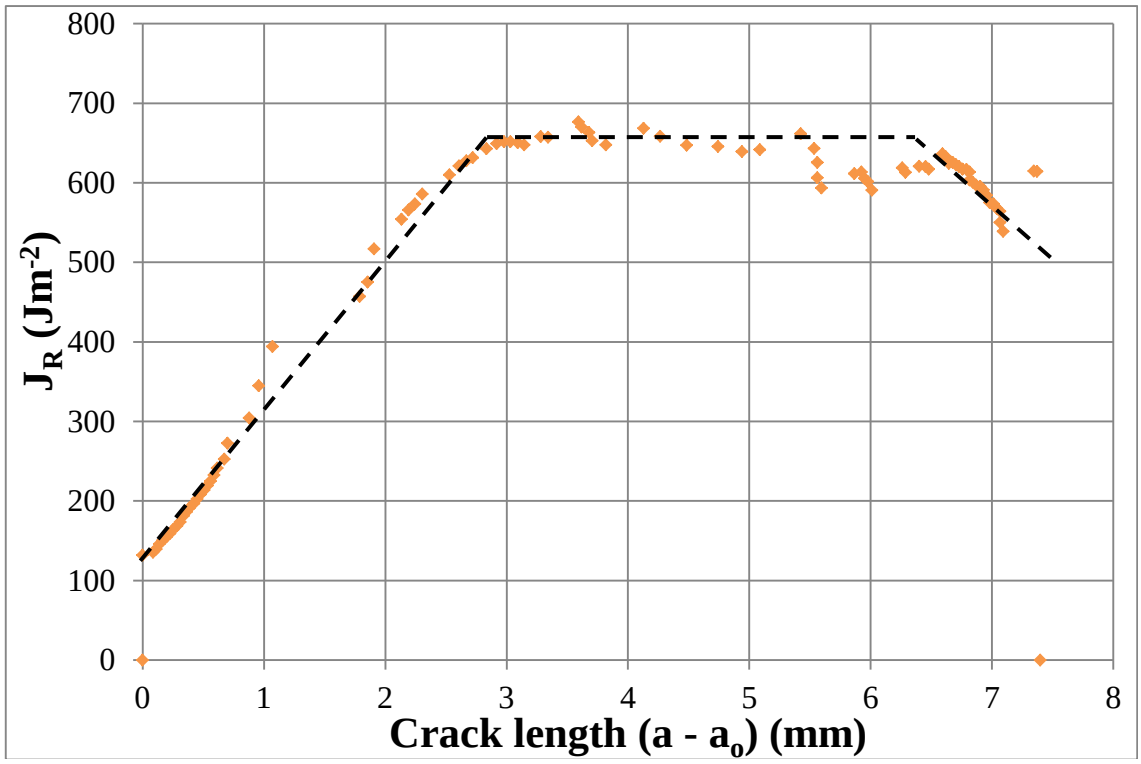

Figure 8.60: Simulated J_R curve for Sample six.

Initial rises in the energy increases in K_R curves can be due to crack bridging by grains which toughens the material as a result of compressive stresses on crack surfaces (Sakai *et al.* (1988), Allard *et al.* (1991)). This mechanism is not present in the computational models, however, additional processes, such as microcracking, may also contribute to the shape of crack growth resistance curves (Evans *et al.* (1984)). Initial K_R values correspond to K_{IC} values, which as previously discussed, are representative of graphite. The average initial value for J_R is approximately 114 Jm^{-2} with a standard deviation of 39 Jm^{-2}. This is representative of the initial J_R value of approximately 100 Jm^{-2} determined through experimental testing by Ouagne *et al.* (2002). The large standard deviation of this is due to the variability in porosity close to the notch tip.

Each of the models demonstrated a plateau region after the initial rise. This region corresponds to steady state propagation of the macro-crack and process zone. Although the initial values for these parameters showed close agreement with experimentally derived results, the rise to the plateau region was far greater than experimental results, which showed an increase to approximately 1.6 $Mpa \cdot m^{0.5}$ and 200 Jm^{-2} for K_R and J_R respectively. Determining the exact crack length at which steady state crack propagation begins is problematic due to the scatter of the data, however, the best estimate for these values is shown in Table 8.12. The discrepancy is likely due to the relative difference in geometry between experimental samples and computational models.

Table 8.12: Best estimates for the parameters associated with the onset of the plateau region.

Sample	**K_R Curve**		**J_R Curve**	
	Crack length (mm)	K_R ($Mpa \cdot m^{0.5}$)	Crack length (mm)	J_R (Jm^{-2})
1	2.0	2.6	2.8	550
2	2.2	3.1	2.7	570
3	2.2	2.5	2.8	450
4	2.4	2.8	2.8	520
5	2.5	3.8	3.7	800
6	2.2	3.3	2.8	660
Mean	2.3	3.0	2.9	592
Standard Deviation	0.2	0.4	0.3	112

Analysing the shape of the six K_R curves reveals that K_R increases in two (Samples two and four) and decreases in four samples after the plateau region. Responses that show a decrease were described by Allard *et al.* (1991) as being typical of carbon materials. This observation is explained in by a decrease in stress intensity factor as the crack approaches the edge of the sample. Experimental determination of K_R curves by Sakai *et al.* (1988) and Ouagne *et al.* (2002) showed an increase in stress intensity after the plateau region (similar to Samples two and four). This is determined to be a result of a rapid increase in the function $Y(a(n)/w)$ at longer crack lengths. Indeed, this function does show a marked increase as the crack approaches the rear face of the sample. Therefore, at this stage in the failure process, slight changes in the applied load can have a significant effect on the calculated stress intensity. With the exception of Samples one and three, which could not be definitely identified as showing a rise or fall, the response of the J_R curves for each model closely matched that of the K_R curves. Similarly to the response of the K_R curves, Sakai *et al.* (1988) and Ouagne *et al.* (2002) observed a decrease in J_R as the crack continues to extend. These responses are attributed to the interaction of the process zone with the rear face of the model. Increases in J_R are likely due to toughening mechanisms such as microcracking or the presence of large pores that impede the fracture path. The deviation in K_R and J_R curves between models is accounted for by their respective load-deflection responses which vary as result of the inherent probabilistic microstructure of this material.

In addition to the previously described parameters, *R*-curves are also commonly used to define non-linear fracture of graphite. However, determining representative *R*-curves from these models is not viable due to the limitations of the method. The total energy required per unit surface increase, *R*, is comprised of elastic energy, *J*, and pseudo plastic energy ϕ_p. Discrimination between these two components is achieved by attributing areas of the load-deflection curve to elastic and pseudoplastic energies (*i.e.* the observed residual displacement upon unloading of an experimental specimen). Although the elastic energy, *J*, can be represented through the modelling approach (as previously demonstrated), the pseudoplastic component cannot, since it is not represented and as such does not have a measurable energy.

8.4. Chapter Summary

This chapter presented and discussed the results from computational simulations. Initial results from tensile configuration demonstrated the effect of porosity on the bulk stiffness of models. It was shown that the directionality of the porosity as well as the overall quantity can have an influence on the determined stiffness. Crack propagation through both the tensile and notched models showed significant crack tortuosity due to the deflection towards pores.

Mechanical properties for the tensile models were relatively representative of results determined through experimental testing. The relative standard deviation was slightly higher; however, this could be explained through consideration of geometric factors and the probabilistic nature of the graphite microstructure. Load-deflection plots for tensile models were consistent with the expected response from similar experimental tests. Notched models were also typical with the exception of the pre-peak softening response. Simulated notched models did not show this response due to a lack of micro-cracking prior to the onset of the macro-crack. Computational derived K_{IC} values compared favourably with experimental results, however, energy based fracture parameters, G_{IC} and *wof* were less representative.

Chapter Nine will discuss and conclude the work presented in this thesis as well as suggesting potential future expansions and applications for the devised methodology.

Chapter 9 – Discussion and Conclusions

Throughout this thesis, a significant amount of experimental, microstructural and computational data has been generated. This chapter will discuss the findings of these results and consider the success of the experimental programme, microstructure characterisation and FEA simulations. Critical evaluation of the developed simulation methodology will discuss the limitations of this technique and suggest potential modifications that would enable more representative outputs and enhanced versatility of the model.

9.1. Experimental Programme

The experimental programme, outlined in Chapter 5, was undertaken to investigate the presence of disparate flaws. Observation of such flaws would allow for a detailed characterisation of the material through determination of the failure distribution (*i.e.* bimodal). Experimental and material selection was carefully considered to ensure that any disparate flaws observed during testing were due to the microstructural variations and not a result of manufacturing defects. Further, a biaxial test configuration was utilised to increase the probability of observing disparate flaws (*i.e.* there is a greater chance that flaws will be critically oriented to the applied stress (Brocklehurst, 1977)). Despite these considerations and a substantial number of graphite samples being tested (~600 in total) the cumulative failure curves for both sample geometries were shown to be close to a normal distribution. Some samples did demonstrate relatively low strengths; however, as would be expected from a normal distribution, a similar number of samples had relatively high strengths. Although this experimental programme did not provide enough evidence to definitively confirm the presences of a disparate flaw population in EY9 grade graphite, it did provide a large data set of mechanical strengths. Data from this experimental programme suggested that the disparate flaw population in graphite is a function of the specific material grade (*i.e.* coarse grained graphites may contain a greater variety of flaws) or mechanical test (*i.e.* not observable when subjecting a small volume of material to a high stress is in a B3B method). Additionally, it could be hypothesised that the disparate flaw population may be

function of the manufacturing method and as such the simple geometry and careful preparation inhibited the observation of such distributions.

In addition to graphite, glass and a ligament material were tested to determine the relative strength distributions of two different microstructures. Glass slides were tested in three-point bend configuration due to their regular geometry and their availably, thereby allowing for 523 strength values to be determined. The cumulative failure plot for the glass strength data was consistent with a normal distribution. However, the spread of this distribution was very large with the weakest sample demonstrating a strength value that was approximately 31% of the strongest. This large variation in determined strength was likely due the relative significance of surface flaws in the thin samples.

Ligament material was tested in three-point flexural configuration. The purpose of this experimental programme was to determine the strength distribution of a material that has potential for 'extreme' structural variations (*i.e.* analogous to highly oxidised graphite). In order to fully characterise the material, 626 samples were manufactured and tested. This highly probabilistic structure did demonstrate a large variation in bulk strength values. This variation is likely due, at least in part, to the inconsistent bulk density of the samples since there was a moderate positive correlation between bulk strength and bulk density of the sample. Cumulative strength data for this material demonstrated a normal distribution. This observation indicates that despite the extreme variations in the structure there is no evidence of a disparate mode failure.

Further experimental tests were undertaken to aid in the determination of representative mechanical properties for computational simulations. Twelve three-point flexural and eighteen compression tests were performed on IM1-24 graphite. In addition to these tests, six samples were sectioned and prepared for microstructural characterisation. This data and its application to the simulation work is discussed further in Section 9.3.

9.2. Microstructural Characterisation

Determination of pore distributions in this thesis was focused on larger pores since these are the more likely to contribute to variations in mechanical properties on an

experimental scale. As such, it was determined that optical microscopy would provide sufficient detail to characterise the material, despite the resolution limitations. Additionally, the process of incorporating this data into microstructural models is limited by the FEA program which would exclude the small pore distribution.

Microstructural characterisation of graphite is vital due to the intrinsic relationship between mechanical performance (*e.g.* stiffness, strength *etc.*) and porosity. Complete characterisation of graphite is difficult due to the probabilistic nature of the pore networks. As such, sampling a large area of the material is advantageous since it enables a large amount of pore data to be ascertained. The characterisation programme outlined in this thesis involved the generation of composite micrographs. A total of 99 micrographs were 'tiled' to create a single large image (10 x 10 mm) which formed the basis for microstructural characterisation and subsequence modelling work. Six micrographs were created using this technique and an appropriate segmentation methodology was applied to output pore data. Development of a suitable threshold methodology was required to ensure pores were sampled correctly. It was found that applying a representative pore fraction (*e.g.* between 19 and 20% for IM1-24 graphite) to the image was not suitable for this investigation. Surrounding material was included in the threshold at these fractions indicating that a lower threshold value was required to output a correct segmentation (*i.e.* porosity). Upon application of an appropriate methodology, the observed porosity was far lower than the expected value determined through density measurements. This discrepancy is account for by the significant percentage of pores that are not observed through optical microscopy due to their small size.

Microstructural characterisation of the images was complicated by the relative image brightness which varied as a result of differences in surface reflectivity of the samples. Although this did not affect the segmentation methodology, the suitable greyscale level was not consistent between samples. This observation did however, have an influence on the observation of small pores in the images. Observations of very small pores (less than 10 μm^2) were somewhat obscured in the brighter images. This is demonstrated by the relatively dark image of Sample one which shows a porosity percentage of 14.05%, which is at least 0.96% higher than the other samples. However, when the minimum area threshold is increased to 10 μm^2, this value decreases to 0.28%. Further increases

in minimum area threshold are effective at demonstrating the large variations in the number of observed pores and their contribution to sample porosity. Samples with the largest number of observed pores do not necessarily contain the highest porosity percentage. For example, Sample four contains the fewest number of pores above 1000 μm^2, yet has the highest percentage contribution, thus suggesting that the porosity observed in this image contains a greater proportion of large pores. This is shown further by the skewed pore size distribution (Figure 6.20) compared with the other samples.

9.3. Representative Microstructure Simulations

Overall, the modelling programme was successful in replicating the graphite microstructure in an FEA environment. Reductions in the image resolution were required to satisfy computational limitations. However, despite this reduction, each model showed only a small decrease in porosity from the original image and maintained a representative distribution of features. The effect of porosity was visually represented in stress distributions and showed concentrations around pores of critical orientation. Addition concentrations were observed in regions containing numerous pores separated by small 'bridges' of material.

Initial computational experiments determined that the porosity has an effect on the model stiffness. Generally, models containing a smaller porosity percentage demonstrate a higher stiffness. This observation is consistent with experimentally and theoretically derived data. Interestingly, the distribution of porosity also influenced the determined stiffness of the model. This was confirmed by comparing the stiffness of the same sample in two different orientations. Results from all samples showed deviations in recorded stiffness when the loading orientation was changed. These observations support the statement that IM1-24 is a 'near isotropic' graphite.

Crack propagation through simulated tensile samples showed a typical fast fracture response. Although the experimental results were determined using three-point flexural tests, the general failure response was largely consistent with the computational data. The effect of micro-cracking was larger in the simulated load-deflection curves, which is likely due to the small scale of the models. Numerous micro-cracks were observed

throughout the computational programme and were typically a result of stress concentrations in small regions of material (*e.g.* the aforementioned material 'bridges'). Experimentally determined strength of graphite was higher than the computational predictions as was the relative standard deviation. One possible reason for these observations is due to the relative geometries of experimental samples and computational models. It could be hypothesised that stress concentration in 3D volumetric samples are more dispersed due to interactions in the z-direction.

Load-deflection curves from notched model results do not show the typical pre-peak softening response expected of graphite due to micro-cracking in the material. Since the computational results are based on a two dimensional model, stresses are effectively concentrated at a single point. However, in a volumetric sample there is a greater likelihood of additional stress concentrations that could lead to microcracking. Experimental notched samples (*e.g.* compact tension) may also experience asymmetric loading which could cause pre-peak stress concentrations, thus leading to a greater degree of micro-cracking. The lack of micro-cracking in the simulations leads to a critical strain energy release rate, G_{IC}, value that is lower than should be expected from graphite. The magnitude of this value is dependent on the energy at peak load. Micro-cracking is a toughening mechanism and as such the relative energy at peak load is lower in the simulated models. This is demonstrated further by relative increase in G_{IC} for the two Samples (two and five) that do show pre-peak micro-cracking. Conversely, work of fracture values, which take into consideration the total energy require to cause fracture of the model, were higher than typically expected parameters for IM1-24. This could be due to extensive microcracking in the process zone as the crack propagates through the model. This explanation is consistent with the large range of *wof* values output from simulated results. The degree of micro-cracking and thus toughening mechanisms varied significantly between models which consequently affected the determined *wof* parameters. Critical stress intensity, K_{IC}, values determined using the simulated results showed good agreement with typical experimentally determined parameters.

Non-linear fracture parameters, K_R and J_R, were calculated as a function of increasing crack growth. The response demonstrated by these curves was typical of carbon materials. Initial rises in K_R and J_R values were attributed to toughening mechanisms

(*i.e.* micro-cracking and the effect of porosity) and were followed by a plateau region which corresponds to steady state propagation of the macro-crack and process zone. Following this plateau region, the curves demonstrated either a rise or fall. Although both responses have been observed in experimentally derived fracture parameters, this is largely due to the difference in material composition (*e.g.* grain size, porosity content *etc.*). Since these models are constructed from the same material, the observed discrepancies are likely due to regions of porosity in the material affecting the crack propagation. The small scale of the model may also contribute to these observations, since large pores have a greater (relative) influence on the crack propagation. Numerical values for the initiation point for K_R and J_R curves were shown to be consistent with experimental results; however, the increase to the plateau region was higher than expected for both parameters. This indicates higher fracture toughness relative to experimental results which could also an effect of micro-cracking and porosity in the model.

R-curves could not be calculated from the simulated results since they rely on the determination of the pseudoplastic energy component, which cannot be measured using the applied methodology.

Crack paths in both tensile and notched models show significant tortuosity due to deflection towards porosity. This observation is consistent with experimental results which suggest that cracks tend to follow a path of least resistance through the microstructure. In addition to the effect of porosity, experimental considerations of failure path also take into account the location and geometry of filler particles. However, this factor is not simulated since filler and binder material are not distinguished in the model.

9.4. Conclusions

This thesis has presented a novel methodology for creating and simulating a representative microstructure in an FEA environment. The primary conclusions determined from this work are as follows:

1) The method used to generate representative microstructure models was shown to accurately transpose pore data from optical microscopy into ANSYS. Pore size, shape and overall distribution are simulated in the models and were shown to be representative despite reductions in resolution. Analysis of the computational solutions enabled a better understanding of how porosity influences microstructural processes. Determined bulk properties of the simulated models were successful in replicating expected results from experimental tests. Although material properties (*e.g.* strength) did vary from experimental results, this can be accounted for through consideration of the respective test configurations and the probabilistic nature of the material. The range of computational results was greater than that of experimental tests; however, this is likely due to geometric considerations. Increases in model porosity predicted lower bulk strengths which is consistent with experimentally determined results.

2) The percentage porosity has an influence on the predicted stiffness of the model. As the pore volume increased the bulk stiffness of the model decreased. Although this trend was observed, it was also apparent that the distribution of porosity also influences the bulk stiffness.

3) Crack propagation through the microstructural models demonstrated the effect of porosity on the fracture path. Data output from each crack extension increment enabled the analysis of properties as a function of crack propagation. Simulated values for K_{IC} were representative of IM1-24, however, energy based values G_{IC} and *wof* were less consistent. Non-linear fracture parameters showed a typical response associated with carbon materials, however, the plateau values were far higher than those typically expected from experimental testing. Inconsistencies between the sample response after the plateau region (*i.e.* some showed a decrease whilst others showed an increase) were due to the relative effect of toughening mechanisms within the individual models. Since the model geometry is small, the relative scale of toughening through micro-cracking and porosity can vary dramatically between models as a result of the probabilistic microstructure.

4) Complexities and inaccuracies relating to the output of quantifiable data were generally a result of the vast geometric differences between the computational models

and experimental samples. Despite these difficulties, all computationally derived values were within an order of magnitude of the expected experimental results.

5) A suitable method for the microstructural characterisation of graphite was developed. This method was shown to be suitable for analysing the pore distribution in the graphite. Cumulative size distribution charts demonstrated the relative contribution of pores of a given size as well as the inherent variability of the graphite structure. Inconsistencies with regards to the relative sample reflectivity resulted in difficulties characterising small pores (> 1 μm^2) in some samples. As such, a minimum size threshold of 10 μm^2 was applied to all the data to ensure that the analysis was constant across all samples.

6) Extensive mechanical characterisation of EY9 graphite, glass slides and ligament material showed a normal failure distribution. The absence of a bimodal distribution suggests that disparate flaws are a function of the material of experimental arrangement. Additionally, it could be hypothesised that manufacturing defects contribute to the presence of critically oriented flaws in experimental samples.

9.5. Further Work

The versatility of the developed computational method means that it has potential for widespread applications. Some examples of possible further work are:

1) Application to different grades of graphite or other materials. This methodology could be used with any microstructure and would require little modification to the basic procedure. The method used to segment constituents from optical micrographs and the conversion macro can be readily applied to alternative materials, however, geometric factors and elemental input parameters (*e.g.* Young's modulus and Poisson's ratio) would require separate consideration.

2) Consideration of different material constituents (*e.g.* binder and filler materials) could be included in the model through the use of different material properties for the components. This modification would enable a more accurate representation of the microstructure and could potentially provide a more realistic fracture response. This

proposed extension could be limited due to difficulties in accurately determining input parameters for the different constituents.

3) The work could be expanded into three-dimensions through application of the methodology to computational tomography (CT). CT scans of graphite show 2D 'slices' of the microstructure at regular intervals (see Figure 9.1). 3D models would have the added advantage of demonstrating pore interactions in the Z-direction which would enable a more realistic loading scenario. Additionally, this modification may result in a more representative failure response (*e.g.* greater degree of micro-cracking *etc.*)

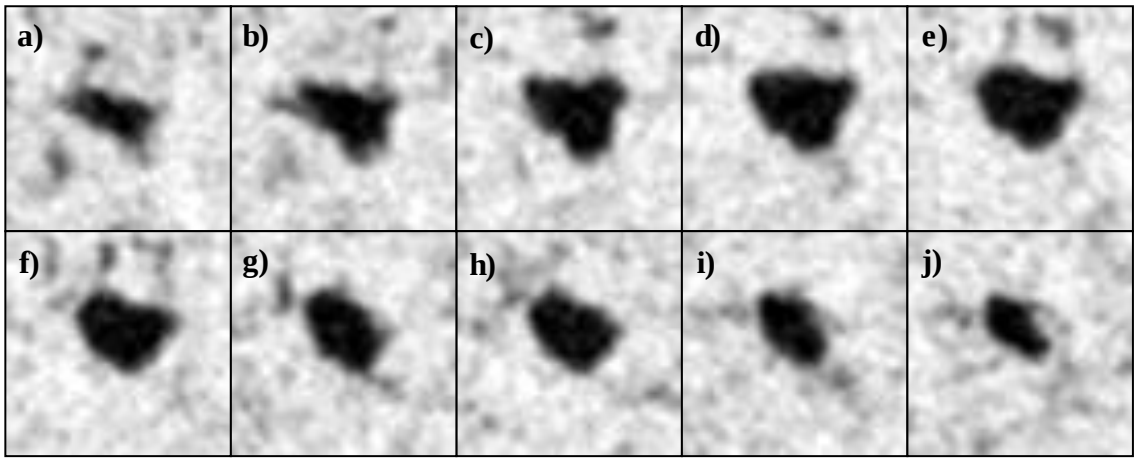

Figure 9.1: CT scan of IM1-24 graphite. Each image (a to j) has dimension 2 x 2 mm and are taken at 0.037 mm increments in the z-direction.

In order to create a 3D model, pore data from each image is segmented separately. This data must then be converted into a suitable *.lgw format that is input into ANSYS to remove elements from corresponding layers. Once the model has been created in the FEA environment, loads and constraints may be applied and computational solutions derived. This process with an applied X-direction displacement is schematically demonstrated in Figure 9.2.

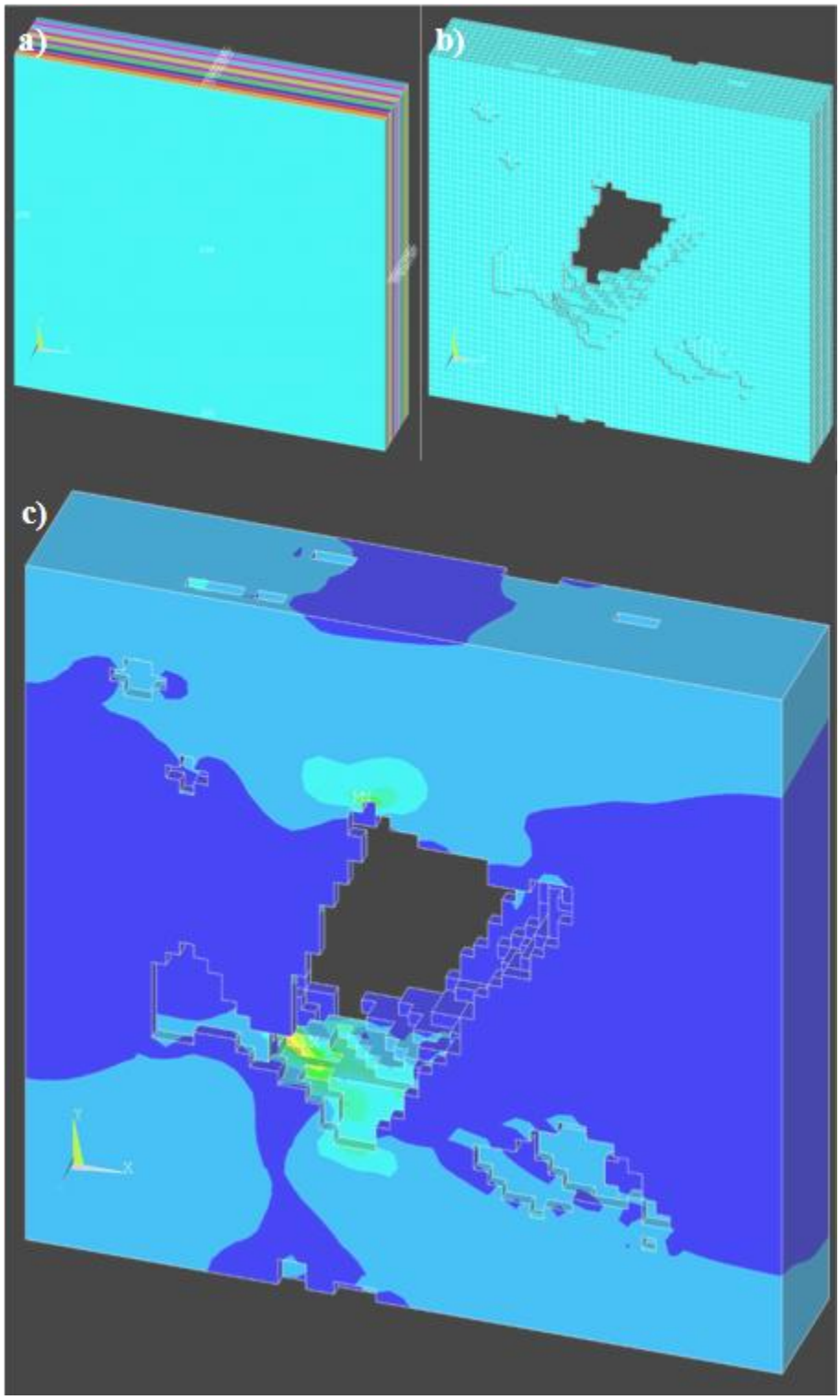

Figure 9.2: Example of the methodology used to construct a 3D representative microstructure model showing a) constructed layer volumes from which elements are removed, b) representative microstructure and c) first principal stress distribution for displacement in the X-direction.

4) Application of simulated methodology to microstructures generated using simulated microstructure methods. One such example is the computational program developed by Lynch *et al.* (2007). The simulated microstructure and a schematic solution are shown in Figure 9.3.

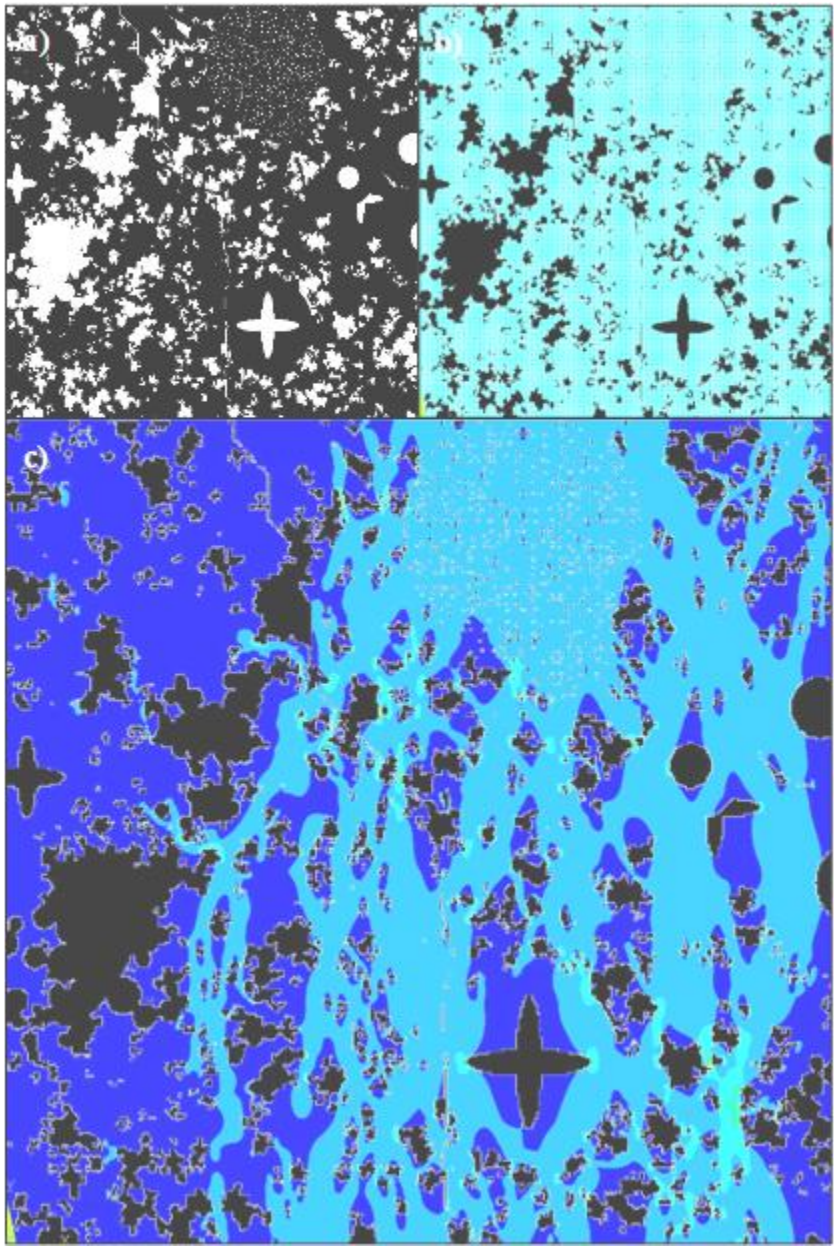

Figure 9.3: Example of the methodology used to simulate a probabilistic microstructure showing a) microstructure generated using probabilistic code, b) conversion into an FEA model and c) first principal stress distribution for a Y-displacement.

References

Abe, H., Naito, M., Hotta, T., Shinohara, N., Uematsu, K. (2003). Flaw Size Distribution in High-Quality Alumina. *Journal of the American Ceramic Society*, 86, [6]. 1019-1021.

Acheson, E. G. (1985). United States Patent Office, No. 579,523. Manufacture of Graphite. Patented: September, 29, 1896.

Ahmed, K.M. (1987). The Dynamic Response of Mulii-Layer AGR Core Brick Arrays. *Nuclear Engineering and Design*, 104, 1-66.

Akhmetov, M. M., Goryunov, V. S., Ezhov, B. M., Zaltseva, S. A., Galeeva, Z. G., Karpinskaya, N. N., Abrosimov, A. A. (1980). Calcination of Petroleum Coke in Rotary-Hearth Furnace. Translated from *Khimiya i Tekhaologiya Topliv i Masel*, 3, 32-35.

Allard, B., Rouby, D., Fantozzi, G., Dumas, D. and Lacroix, P. (1991). Fracture Behaviour of Carbon Materials. *Carbon*, 29, 457-468.

Amelinckx, S., van Dyck, D., van Landuyt, J., van Tendeloo, G. (Ed.) (1997). Handbook of Microscopy: Applications in Materials Science, Solid-State Physics and Chemistry, Methods I. Weinheim, VCH.

Arnold, L. (1979). Atomic Energy in Britain 1939 – 1975. United Kingdom atomic energy authority. Authority Historians office, AERE Harwell.

ASTM C565-83. (1987) Standard Test Method for Tension Testing of Carbon and Graphite Mechanical Materials. American Society for Testing and Materials.

ASTM C651-70 (Reapproved 1977). (1977). Standard Test Method for Flexural Strength of Manufactured Carbon and Graphite Articles Using Four-point Loading at Room Temperature. American Society for Testing and Materials.

ASTM C695-81. (1987). Standard Test Method for Compressive Strength of Carbon and Graphite. American Society for Testing and Materials.

ASTM C749-73. (Reapproved 1979). (1979). Standard Test Method for Tensile Stress-strain of Carbon and Graphite. American Society for Testing and Materials.

ASTM E399-90. (1981). Standard Test Method for Plane-strain Toughness of Metallic Materials. American Society for Testing and Materials.

ASTM E561-81. (1981). Standard Test Method for R-curve Determination. American Society for Testing and Materials.

Babout, L., Mummery, P. M., Marrow, T. J., Tzelepi, A., Withers, P. J. (2005). The Effect of Thermal Oxidation on Polycrystalline Graphite Studied by X-ray Tomography. *Carbon*, 43, 765-774.

Barrett, E. P., Joyner, L. G., Halenda, P. P. (1952). The Determination of Pore Volume and Area Distributions in Porous Substances. I. Computations from Nitrogen Isotherms. *Journal of American Chemical Society*. 73, [1], 373-380.

Becker, T. H., Marrow, T. J., Tait, R. B. (2011). Damage, Crack Growth and Fracture Characteristics of Nuclear Grade Graphite Using the Double Torsion Technique. *Journal of Nuclear Materials*, 414, 32-43.

Bernal, B. A. (1924). The Structure of Graphite. *Proceedings of the Royal Society A*, 106, 749-773.

Berre, C., Fok, S. L., Marsden, B. J., Babout, L., Hodgkins, A., Marrow, T. J., Mummery, P. M. (2006). Numerical Modelling of the Effects of Porosity Changes on the Mechanical Properties of Nuclear Graphite. *Journal of Nuclear Materials*, 352, 1-5.

Berre, C., Fok, S. L., Mummery, P. M., Ali, J., Marsden, B. J., Marrow, T. J., Neighbour, G. B. (2008). Failure Analysis of the Effects of Porosity in Thermally Oxidised Nuclear Graphite Using Finite Element Modelling. *Journal of Nuclear Materials*, 381, 1-8.

Best, J. V., Stephen, W. J., Wickham, A. J. (1985). Radiolytic Graphite Oxidation. *Progress in Nuclear Energy*, 16, [2]. 127-178.

Bjerregaard, L., Geels, K., Ottesen, B., Rückert, M. (2000). Struers: Metalog Guide. Bøhm Offset, Denmark.

Bousfield, B. (1992). Surface Preparation and Microscopy of Materials. Chichester, Wiley.

Börger, A., Supancic, P., Danzer, R. (2002). The Ball on Three Balls Test for Strength Testing of Brittle Siscs: stress distribution in the disc. *Journal of the European Ceramic Society*, 22 [9-10], 1425-1436.

Buch, J. D. (1976). Mechanical Behaviour Model for Graphites, Properties Related to Fracture Toughness, ASTM STP 605, 124.

Burchell. T. D. (1986). Studies of Fracture in Nuclear Graphites. PhD Thesis. University of Bath, U.K.

Burchell, T. D. (1996). A Microstructurally Based Fracture Model for Polygranular Graphites. *Carbon*, 34, [3], 297-316.

Burchell, T. D. (2002). Neutron Irradiation Damage in Graphite and its Effects on Properties, in *Proceedings Carbon 2002*, Beijing, China, September 15–19, 2002.

Brocklehurst, J.E., Darby, M. I. (1974). Concerning the Fracture of Graphite Under Different Test Conditions, *Materials Science and Engineering*, 16, 91-106.

Brocklehurst, J. E. (1977). Fracture in Polycrystalline Graphite. *Chemistry and Physics of Carbon*, 13, 146-258.

Brocklehurst, J. E., Adam, R. W. (1983). Mechanical Tests on Graphite with Simulated Radiolytic Oxidation Gradients. UKAEA Report ND-R-853(S).

Carpenter, E. W., Norfolk, D. J. (1984). Lattice of Power: Graphite Core Life. Nuclear Energy, *Journal of the British Nuclear Engineering Society*, 23, 83-96.

Chung, D. D. L, (2002). Review Graphite. *Journal of Material Science*, 37, 1475-1489.

Corum, J. M. (1966). Determination of the Fracture Toughness of ECCR-type AGOT Graphite. United States Atomic Energy Commission Report. ORNL-4030.

Cowlard, F. C., Lewis, J. C. (1967). Vitreous Carbon – A New Form of Carbon. *Journal of Material Science*, 2, 507-512.

Darby, M. I. (1976). A Fracture Mechanics Approach to the Failure of Graphite in Laboratory Tests. *International Journal of Fracture Mechanics*, 12, [5], 745-757.

Davidge, R. W., Tappin, G. (1968). The Effective Surface Energy of Brittle Materials. *Journal of Materials Science*, 3, 163-173.

Devon, M. (2008). Private communication.

Diamond, S. (1970). Pore Size Distribution in Clays. *Clay and Clay Minerals*, 18, 7-23.

Easton, A. (2007). Determination of the Effect of Sample Geometry Upon the Biaxial Strength of Engineering Materials. BEng thesis, University of Hull.

Eatherly, W. P., Janes, M., Mansfield, R. L., Bourdeau, R. G., Meyer, R. A. (1958). Physical Properties of Graphite Materials for Special Nuclear Applications. *Second United Nations International Conference on the Peaceful Uses of Atomic Energy*, June 1958.

Ellis, A. T., Staple, K. M. (2007). The Management of Magnox Graphite Reactor Cores to Underwrite Continued Safe Operation. Management of Ageing Processes in Graphite Reactor Cores. Royal Society of Chemistry, Special Publication No. 309, 2-9.

Evans, M. (1978). Porosity in Graphites. PhD Thesis. University of Newcastle upon Tyne.

Evans, A. G., Faber, K. T. (1984). Crack-Growth Resistance of Microcracking Brittle Materials. *Journal of the American Ceramic Society*, 67, 255-260.

Feates, F. S. (1969). Radiolytic Oxidation of Single Crystal Graphite. *Transactions of the Faraday Society*, 65, 211-218.

Fok, S. L., Mitchell, B. C., Smart, J., Marsden, B. J. (2001). A Numerical Study on the Application of the Weibull Theory to Brittle Materials. *Engineering Fracture Mechanics*, 68, 1171-1179.

Franklin, R. E. (1950). The Structure of Graphitic Carbons. *Acta Crystallographica*, 4, 253-261.

Giesche, H. (2006). Mercury Porosimetry: a General (Practical) Overview. *Particle & Particle Systems Characterization*, 23, 1-11.

Gillin, L. M. (1967). Deformation Characteristics of Nuclear Grade Graphites. *Journal of Nuclear Materials*, 23, [3], 280-288.

Godfrey D. J. (1985). Fabrication, Formulation, Mechanical Properties, and Oxidation of Sintered Si_3N_4 Ceramics Using Disk Specimens. *Materials Science and Technology*, 1, 510-515.

Gopalaratnam, V. S., Shah, S. P. (1985). Softening Response of Plain Concrete in Direct Tension. *American Concrete Institute Journal*. Technical Paper. May-June 1985, 310-323.

Greenstreet,W. L., Smith, J. E., Yahr, G. T. (1969). Mechanical Properties of ECCR-type AGOT Graphite. *Carbon*, 7, [1], 15-45.

Greenwood, N. N., Earnshaw, A. (1984). Chemistry of the Elements. Pergamon Press, Oxford.

Griffith, A. A. (1920). The Phenomena of Rupture and Flow in Solids. *Philosophy Transaction of the Royal Society of London*, 221, 163-198.

Haag, G. (2005). Properties of ATR-2E Graphite and Property Changes due to Fast Neutron Irradiation. Forschungszentrum, Jülich Report.

Hacker, P. J., Neighbour, G. B., McEnaney, G. B. (2000), The Coefficient of Thermal Expansion of Nuclear Graphite with Increasing Thermal Oxidation. *Journal of Physics D: Applied Physics*, 33, 991-998.

Hagos, B., Jones, A. N., Marrow, T. J., Marsden, B. J. (2010). Microstructural Analysis of Irradiated Nuclear Graphite Waste. *DIAMOND Conference*. Manchester, United Kingdom.

Hartley, M., McEnaney, B. (1996), Blunt Indentation of Core Graphite. Graphite Moderator Lifecycle Behaviour, International Atomic Energy Agency, Vienna, IAEA-TECDOC-901, 263-274.

Heard, P. J., Wootton, M. R., Moskovic, R., Flewitt, P. E. J. (2010), Crack Initiation and Propagation in Pile Grade A (PGA) Reactor Core Graphite Under a Range of Loading Conditions. *Journal of Nuclear Materials*, 401, 71-77.

Hindley, M. P., Mitchell, M. N., Blaine, D. C., Groenwold, A. A. (2012). Observations in the Statistical Analysis of NBG-18 Nuclear Graphite Strength Tests. *Journal of Nuclear Materials*, 420, 110-115.

Hoek, E., Bieniawski, Z. T. (1965). Brittle Rock Fracture Propagation in Rock Under Compression. *International Journal of Fracture Mechanics*, 1, 137-155.

Holt, M. (2008). Issues of Scale in Nuclear Graphite Components. PhD Thesis, University of Hull.

Holloway, D. G. (1968). The Fracture of Glass. *Physics Education*, 3, 317-322.

IAEA. (2006). Characterization, Treatment and Conditioning of Radioactive Graphite from Decommissioning of Nuclear Reactors. IAEA-TECDOC-1521, September 2006.

Inagaki, M., Suwa, T. (2000). Pore Structure Analysis of Exfoliated Graphite Using Image Processing of Scanning Electron Micrographs. *Carbon*, 39, 915-920.

Inagaki, M. (2009). Pores in Carbon Materials-importance of Their Control. *New Carbon Materials*, 24 [3], 193-232.

Irwin, G. R. (1958). Fracture, *Handbuch der Physik*, Springer-Verlag, Berlin, 6, 551.

Jäger, H., Frohs, W., Banek, M., Christ, M., Daimer, J., Fendt, F., Friedrich, C., Gojny, F., Hiltmann, F., Meyer zu Reckendorf, R., Montminy, J., Ostermann, H., Müller, N., Wimmer, K., von Sturm, F., Wege, E., Roussel, K. and Handl, W. (2010). Carbon, 4. Industrial Carbons. Ullmann's Encyclopedia of Industrial Chemistry.

Jeong, S. M., Park, S. E., Lee, H. L. (2002). Fracture Behaviour of Alumina Ceramics by Biaxial Ball-on-3-ball Test. *Journal of the European Ceramic Society*, 22, 1129-1135.

Jones, A. N., Hall, G. N., Joyce, M., Hodgkins, A., Wen, K., Marrow, T. J., Marsden, B. J. (2008). Microstructural Characterisation of Nuclear Grade Graphite. *Journal of Nuclear Materials*, 381, 152-157.

Kane, J., Karthik, C., Butt, D. P., Windes, W. E., Ubic, R. (2011). Microstructural Characterization and Pore Structure Analysis of Nuclear Graphite. *Journal of Nuclear Materials*, 415, 189-197.

Kelly, B. T. (1981). Physics of Graphite. Applied Science, Essex, England.

Kelly, B. T. (2000). The Structure and Manufacture of Nuclear Grade Graphite, Irradiation Damage in Graphite Due to Fast Neutrons in Fission and Fusion Systems, IAEA-TECDOC-1154, IAEA.

Kennedy C. R., Eatherly, W. P. (1986). The Statistical Characterization of Tensile Strengths for a Nuclear-type Core Graphite. Technical Report. CONF-8609133-1.

Kennedy, C. R., Montgomery, S. C. (1990). Statistics of Fracture in Two Grades of Isotropic Graphite. *Journal of Nuclear Materials*, 171, 49-53.

Kennedy, C. R. (1993). The Brittle Ring Test for Graphite. *Carbon*, 31 [3], 519-528.

Kipling, G. D. (2008). Determination of the Effect of Sample Geometry upon the Biaxial Strength of Engineering Materials. BEng thesis, University of Hull.

Kipling, G. D., Easton, A., Neighbour, G. B. (2010). Biaxial Testing: Appropiate for Mechanical Characterisation? Securing the Safe Performance of Graphite Reactor Cores. Royal Society of Chemistry, Special Publication No. 328, 152-160.

Klutke, G., Kiessler, P. C., Wortman, M. A. (2003). A Critical Loot at the Bathtub Curve. *IEEE Transaction on Reliability*, 52 [1], 125-129.

Knibbs, R. H. (1967). Fracture in Polycrystalline Graphite. *Journal of Nuclear Materials*, 24, 174-187.

Kralj, B., Humphreys, S. J., Duncan, B. G. J. (2007). Seismic Modelling of an AGR Nuclear Reactor Core. Management of Ageing Processes in Graphite Reactor Cores. Royal Society of Chemistry, Special Publication No. 309, 193-200.

Lipson, H., Stokes, A. R. (1943). The Structure of Graphite. *Proceedings of the Royal Society A.* 181, 101-105

Lynch, C., Neighbour, G. B. (2007). Development of a Code to Predict Fundamental Material and Fracture Properties of Nuclear Graphite. Management of Ageing Processes in Graphite Reactor Cores. Royal Society of Chemistry, Special Publication No. 309, 91-99.

Maier-Komor, P. (2009). Uranium Isotope Separation from 1941 to the Present. *Nuclear Instruments and Methods in Physics Research A*, 613, 465-472.

Marlowe, M. O. (1970). Elastic Properties of Three Grades of Fine Grained Graphite to 2000^{o}C. NASA Contract, NAS1-9852, June 25, 1970.

Marsden, B. J., Hall, G. N., Wouters, O., Vreeling, J. A., van der Laan, J. (2008). Dimensional and Material Property Changes to Irradiated Gilsocarbon Graphite Irradiated Between 650 and 750^{o}C. *Journal of Nuclear Materials*, 381, 62-67.

Maruyama, T., Kaito, T., Onose, S., Shibahara, I. Change in Physical Properties of High Density Isotropic Graphites Irradiated in the "JOYO" Fast Reactor. *Journal of Nuclear Materials*, 225, 257-272.

Maul, P. R., Robinson, P. R., Steer, A. G. (2010). Understanding AGR Graphite Brick Cracking Using Physical Understanding and Statistical Modelling. Securing the Safe Performance of Graphite Reactor Cores. Royal Society of Chemistry, Special Publication No. 328, 103-110.

McLachlan, N. (1992). The Modelling of Polycrystalline Graphite Fracture and Deformation Properties. PhD Thesis. University of Exeter.

Media Cybernetics. (2012). Application Note, Stitching and tiling images. Accessed 29th October 2012, http://www.mediacy.com/pdfs/.

Minshall, P. C., Sadler, I. A., Wickham, A. J. (1995). Radiolytic Graphite Oxidation Revisited. Specialists meeting on graphite moderator lifecycle behaviour. Bath (United Kingdom). 24-27 Sep 1995. International Atomic Energy Agency, Vienna (Austria). IAEA-TECDOC--901, 181-191.

Moore, A. W., Ubbelohde, A. R., Young, D. A. (1962). An Induction Furnace for Operations up to 3400°C Using Well Oriented Graphite. *British Journal of Applied Physics*, 13, 393-398.

Mostafavi, M., Marrow, T. J. (2011). In Situ Observation of Crack Nuclei in Poly-granular Graphite Under Ring-on-ring Equi-biaxial and Flexural Loading. *Engineering Fracture Mechanics*, 78, 1756-1770.

Mrozowski, S. (1954). Mechanical Strength, Thermal Expansion and Structure of Cokes and Carbons, Proceedings of the 1st and 2nd Conference on Carbon, Waverley Press, USA.

Murdie, N., Edwards, I. A. S., Marshi, H. (1986). Changes in Porosity of Graphite Caused by Radiolytic Gasification by Carbon Dioxide. *Carbon*, 24, [3], 267-275.

Nakayama, J. (1965). Direct Measurement of Fracture Energies of Brittle Heterogeneous Materials. *Journal of American Ceramic Society*, 48, [11], 583-587.

Neighbour, G. B. (1993). Microstructural Processes Leading to Fracture in Nuclear Graphites. PhD Thesis, University of Bath.

Neighbour, G. B. (2000). Modelling of Dimensional Changes in Irradiated Nuclear Graphites. *Journal of Physics D: Applied Physics*, 33, 2966-2972.

Neighbour, G.B., Hacker, P.J. (2001). The Variation of Compressive Strength of AGR Moderator Graphite With Increasing Thermal Weight Loss. *Materials Letters*, 51, 307-314.

Neighbour, G. B. (2008). Private communication.

Nemeth, N. N., Bratton, R. L. (2010). Overview of Statistical Models of Fracture for Nonirradiated Nuclear-graphite Components. *Nuclear Engineering and Design*, 240, [1], 1-29.

Nightingale, R. E. (1962). Nuclear Graphite. Academic Press. London, England.

Orowan, E. (1949). Fracture Strength of Solids. *Reports on Progress in Physics*, 12, 185-232.

Orowan, E. (1955). Energy Criteria of Fracture, *Welding Research. Supplement*, 34, 157-160.

Ouagne. P., Neighbour, G. B., McEnaney, B. (2002). Crack Growth Resistance in Nuclear Graphites. *Journal of Physics D: Applied Physics*, 35, 927-934.

Ouagne, P., Neighbour, G. B., McEnaney, B. (2005). Influences of Oxidation on the Toughness Parameters for Two Nuclear Grade Graphites. *Journal of Physics D: Applied Physics*, 38, 1259-1264.

Ovri J. E. O. (2000). A Parametric Study of the Biaxial Strength Test for Brittle Materials. *Materials Chemistry and Physics*, 66, 1-5.

Pagniano R. P., Seghi R. R., Rosential S. F., Wang R., Katsube N. (2005). The Effect of a Layer of Resin Luting Agent on the Biaxial Flexure Strength of Two All-ceramic Systems. *The Journal of Prosthetic Dentistry*, 93 [5] 459-466.

Patrick, J. W. (1995). Porosity in Carbons. Edward Arnold, London.

Picard, M. D. (1985). Geology and Energy Resources. Uinta basin of Utah: Salt Lake City, Utah Geological Association, Publication 12, p. 257-262.

Price, R. J. (1976). Statistical Study of the Strength of Near-Isotropic Graphite. Technical Report GA-A-13955. OSTI-7145652. Accessed 26th October 2012, http://www.osti.gov/bridge/servlets/purl/7145652-9IwYD8/.

Price, R. J. (1979). Strength of irradiated graphite: A review. International working group on High Temperature Reactors Specialists' Meeting on Mechanical Behavior of Graphite for High Temperature Reactors. June 11-13, 1979, Gif-sur-Yvette, France.

Prince, N. (1979). Technology of Graphite Moderator Structures. *British Nuclear Engineering Society*. 18, 267-275.

Ragan, S., Marsh, H. (1983). Review: Science and Technology of Graphite Manufacture. *Journal of Materials Science*, 18, 3161-3176.

Reddy, J. N. (2004). An Introduction to Nonlinear Finite Element Analysis. Oxford University Press, Oxford, United Kingdom.

Reed, J. (2008). Private communication.

Rice, J.R., Paris, P.C., Merkle, J.G. (1973). Progress in Flaw Growth and Fracture Toughness Testing, *ASTM STP*. 536, 231-245.

Rice, R. (1998). Porosity of Ceramics. Marcel Dekker, New York.

Rice, R. W. (1996). Comparison of Physical Property-porosity Behaviour with Minimum Solid Area Models. *Journal of Material Science*, 31, 1509-1528.

Ritter H. L., Drake, L. C. (1945). Pore-Size Distributions in Porous Materials, Pressure Porosimeter and Determination of Complete Macropore-Size Distributions. *Industrial and Engineering Chemistry Analytical Edition*, 17 [12], 782-786.

Robinson, G. (2011). Private communication.

Robinson, G. (2012). Private communication.

Rodgers, J. L., Nicewander, W. A. (1988). Thirteen Ways to Look at the Correlation Coefficient. *The American Statistician*, 42, 59-66.

Romanoski, G. R., Burchell, T. D. (1991). The Effect of Specimen Geometry and Size on the Fracture Toughness of Nuclear Graphites. Twentieth Biennial Conference on Carbon, University of California, Santa Barbara, California, USA. June 23-28, 1991.

Rose, A. P. G., Tucker, M. O. (1982). A Fracture Criterion for Nuclear Graphite. *Journal of nuclear materials*, 110, 186-195.

Rose, A. P. G. (1985). Calculation of Critical Stress Intensity Factors of Nuclear Graphite From Small Specimen Tests. *Carbon*, 23, [4], 387-393.

Rouquerol, J., Fairbridge, C. W., Everett, D. H., Haynes, J. H., Pernicone, N., Ramsay, J. D. F., Sing, K. S. W., Unger, K. K. (1994). Recommendation for the Characterisation of Porous Solids (Technical Report). *Pure and Applied Chemistry*, 66, [8], 1739-1758.

Russ, J.C. (1990). Computer-Assisted Microscopy. The Measurement and Analysis of Images. New York, Plenum Press.

Sakai, M., Yamasaki, K. (1983a). Numerical Fracture Analysis of Chevron-Notched Specimens: I, Shear Correction Factor, *k*. *Journal of the American Ceramic Society*, 66, 371-375.

Sakai, M., Urashima, K., and Inagaki, M. (1983b). Energy Principle of Elastic-plastic Fracture and its Application to the Fracture Mechanics of Polycrystalline Graphite. *Journal of the American Ceramic Society*, 66, 868-874.

Sakai, M., Yoshimura, J., Goto, Y., Inagaki, M. (1988). *R*-Curve Behaviour of a Polycrystalline Graphite: Microcracking and Grain Bridging in the Wake Region. *Journal of the American Ceramic Society*, 71, 609-616.

Schlangen, E., Flewitt, P. E. J., Smith, G., Crocker, A., Hodgkins, A. (2011). Computer Modelling of Crack Propagation in Porous Reactor Core Graphite. *Key Engineering Materials*, 452-453, 729-732.

Shibata, T., Ishihara, M. (2001). Grain/Pore Microstructure-based Evaluation Method for Variation of Mechanical Property of Graphite Components in the HTGR. *Transactions, SMiRT 16*, Washington DC, August 2001.

Simmons, J. H. W. (1965). Radiation Damage in Graphite. Pergamon Press, Oxford, United Kingdom.

Sing, K. S. W., Everett, D. H., Haul, R. A. W., Moscou, L., Pierotti, R. A., Rouquerol, J., Siemieniewska, T. (1985). Reporting Physisorption Data for Gas/Solid Systems with Special Reference to the Determination of Surface Area and Porosity. *Pure and Applied Chemistry*, 57, [4], 603-619.

Slonczewski, J. C., Weiss, P. R. (1958). Band Structure of Graphite. *Physical Review*, 109, 272-279.

Smart, J., Mitchell, B. C., Fok, S. L., Marsden, B. J. (2003). The Effect of the Threshold Stress on the Determination of the Weibull Parameters in Probabilistic Failure Analysis. *Engineering Fracture Mechanics*, 70, 2559-2567.

Splaris, C. N. (1956). The Micropore Structure of Artificial Graphite. *The Journal of Physical Chemistry*, 60 [11], 1480-1483.

Spence, J. C. H. (2008). High-Resolution Electron Microscopy. Oxford University Press, Oxford.

Steer, A. G. (2007). AGR Core Design, Operation and Safety Functions. Management of Ageing Processes in Graphite Reactor Cores. Royal Society of Chemistry, Special Publication No. 309, 10-17.

Struers Ltd. Generic methods for the preparation of carbon products / graphite. January 2012. http://www.struers.com/modules/emetalog/generic_view.asp?method=1219. Accessed 6th January 2012. Information regarding the grinding and polishing of optical microscopy samples.

Sun, L., Hodgkins, A., Marrow, J., Fok, A. S. L., Marsden, B. J. (2004). An Experimental Study on the Porosity Networks in Nuclear Graphite. *2nd International Topical Meeting on High Temperature Reactor Technology*, Beijing, China, September 22-24, 2004.

Tattersall, H. G., Tappin, G. (1966). The Work of Fracture and its Measurement in Metals, Ceramics and other Materials. *Journal of Materials Science*, 1, 296-301.

Taylor, R., Brown, R. G., Gilchrist, K., Hall, E., Hodds, A. T., Kelly, B. T., Morris, F. (1967). The Mechanical Properties of Reactor Graphite. *Carbon*, 5, [5], 519-531.

Taylor, W. R., Clift, S. E., Warner, M. D., Neighbour, G. B. (1997). Kinematic Study of Radially Keyed Graphite Moderator Cores. Report for Health and Safety Executive: NUC 56/382, University of Bath.

Tsang, D. K. L., Marsden, B. J. (2006). The Development of a Stress Analysis Code for Nuclear Graphite Components in Gas-cooled Reactors. *Journal of Nuclear Materials*, 350, 208-220.

Tucker, M. O., Rose, A. P. G., Burchell, T. D. (1986). The Fracture of Polycrystalline Graphites. *Carbon*, 24 [5], 581-602.

Tucker, M. O., McLachlan, N. (1993). Fracture and Microstructure of Graphites. *Journal of Physics D: Applied Physics*, 26, 893-907.

Vidal, J. M., Mays, T. J. (1999). Mechanical Properties and Oxidation of Nuclear Graphites. *British Ceramic Proceedings*, 60, 123-124.

Virgil'ev, Y. S. (1997). The Radiation Change in the Coefficient of Linear Thermal Expansion of Carbon Materials. *Atomic Energy*, 82 [6], 414-421.

Warner, M. D., Taylor, W. R., Clift, S. E., Neighbour, G. B. (1998). Kinematic Study of Radially Keyed Graphite Moderator Cores. Report for Health and Safety Executive: NUC 56/382-Ext 1, University of Bath.

Warren, B. E., Chipman, D. R. (1954). Small Angle X-ray Scattering Study of Radiation Damage in Graphite. USAEC Report KAPL-1204, Massachusetts Institute of Technology.

Washburn, E. W. (1921). The Dynamics of Capillary Flow. *Physical Review*, 17 [3], 273-283.

Weibull, W. (1939). A Statistical Theory of the Strength of Materials. *Proceedings of the Royal Swedish Institute for Engineering Research*, 151, 1-45.

Weibull, W. (1951). A Statistical Distribution Function of Wide Applicability. *Journal of Applied Mechanics*, 18, 293-297.

Wen, K., Marrow, J., Marsden, B. (2008). Microcracks in Nuclear Graphite and Highly Oriented Pyrolytic Graphite (HOPG). *Journal of Nuclear Materials*, 381, 199-203.

Wen, K., Marrow, J., Marsden, B. (2008). The Microstructure of Nuclear Graphite Binders. *Carbon*, 46, 62-71.

Wigner, E. P. (1946). Theoretical Physics in the Metallurgical Laboratory of Chicago. *Journal of Applied Physics*, 17, 857-863.

Wong, H. S., Head, M. K., Buenfeld, N. R. (2006). Pore Segmentation of Cement-based Materials from Backscattered Electron Images. *Cement and Concrete Research*, 36, 1083-1090

Yarema, S. Y. (1995). On the Contribution of G. R. Irwin to Fracture Mechanics. *Material Science*, 31 [5], 617-623.

Appendix A – Image and Videos

This section details the images and videos included on the accompanying DVD. The location of the files is included along with a brief description of what they demonstrate (see Table A.1). Note that the included images are in *.jpg format due to file size limitations. Microscopy images are captured in *.tif format which is much higher quality and thus ensures accurate characterisation of the material.

Additionally, a *.pdf file showing the minimum pore area classifications for samples two to six demonstrating minimum area thresholds of 1000 and 10000 μm^2 are included on the DVD.

File registry: Images and Videos > Pore area classifications.

Bright field micrographs for the six microscopy samples are also included in this appendix (see Figures A.1 to A.6).

Table A.1: Image and video registry for files included on accompanying DVD.

Folder	Subfolder		File Name	Description
Images and Videos	Sample 1	Images	S1-1	Bright field Light Micrograph
			S1-2	8-bit Greyscale
		Videos	S1-V1	Tensile configuration - first Principal Stress
			S1-V2	Tensile configuration - y-displacement
			S1-V3	Notched configuration - first Principal Stress
			S1-V4	Notched configuration - y-displacement
	Sample 2	Images	S2-1	Bright field Light Micrograph
			S2-2	8-bit Greyscale
		Videos	S2-V1	Tensile configuration - first Principal Stress
			S2-V2	Tensile configuration - y-displacement
			S2-V3	Notched configuration - first Principal Stress
			S2-V4	Notched configuration - y-displacement
	Sample 3	Images	S3-1	Bright field Light Micrograph
			S3-2	8-bit Greyscale
		Videos	S3-V1	Tensile configuration - first Principal Stress
			S3-V2	Tensile configuration - y-displacement
			S3-V3	Notched configuration - first Principal Stress
			S3-V4	Notched configuration - y-displacement
	Sample 4	Images	S4-1	Bright field Light Micrograph
			S4-2	8-bit Greyscale
		Videos	S4-V1	Tensile configuration - first Principal Stress
			S4-V2	Tensile configuration - y-displacement
			S4-V3	Notched configuration - first Principal Stress
			S4-V4	Notched configuration - y-displacement
	Sample 5	Images	S5-1	Bright field Light Micrograph
			S5-2	8-bit Greyscale
		Videos	S5-V1	Tensile configuration - first Principal Stress
			S5-V2	Tensile configuration - y-displacement
			S5-V3	Notched configuration - first Principal Stress
			S5-V4	Notched configuration - y-displacement
	Sample 6	Images	S6-1	Bright field Light Micrograph
			S6-2	8-bit Greyscale
		Videos	S6-V1	Tensile configuration - first Principal Stress
			S6-V2	Tensile configuration - y-displacement
			S6-V3	Notched configuration - first Principal Stress
			S6-V4	Notched configuration - y-displacement

Figure A.1: Bright field micrograph of Sample one.

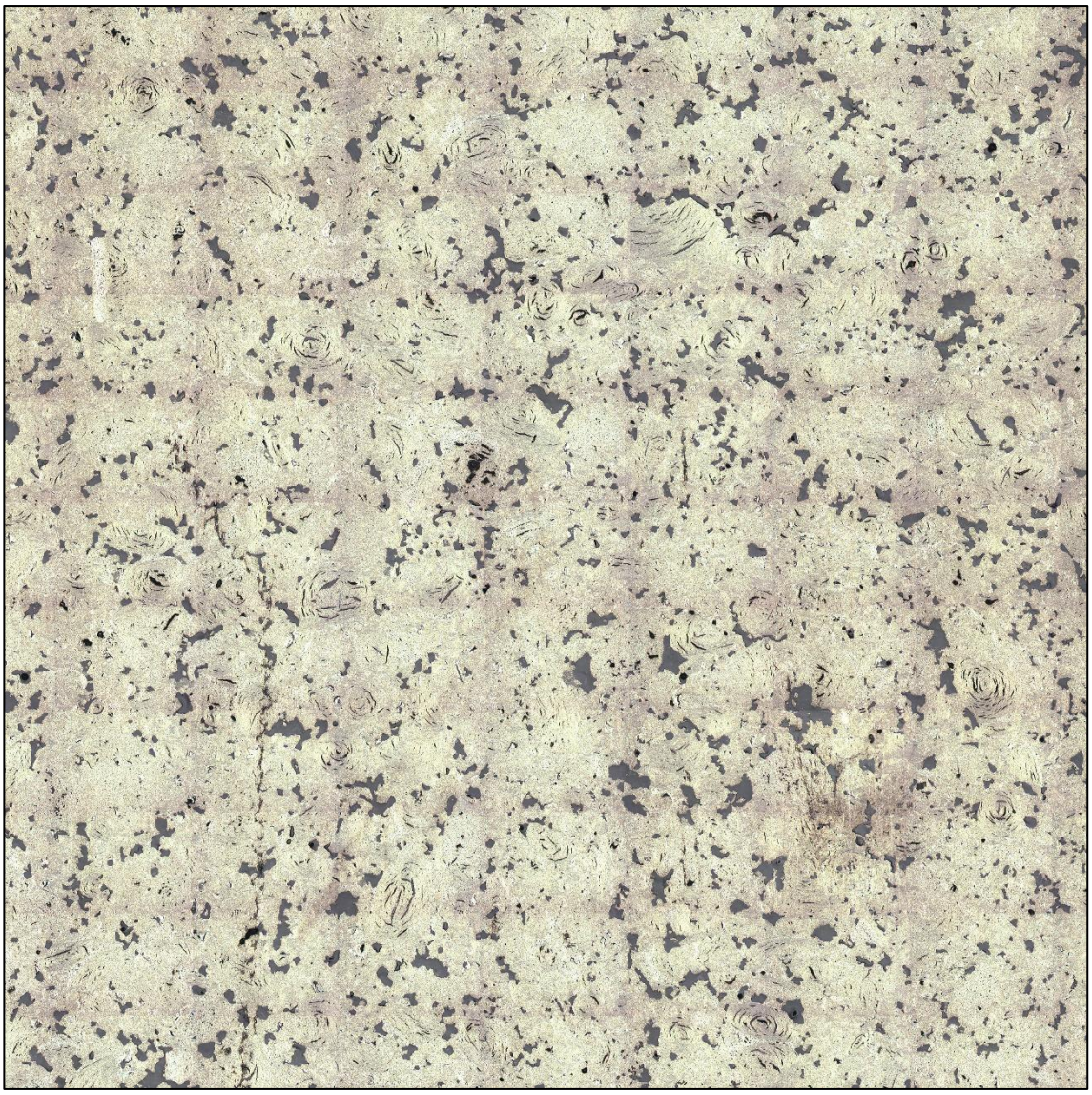

Figure A.2: Bright field micrograph of Sample two.

Figure A.3: Bright field micrograph of Sample three.

Figure A.4: Bright field micrograph of Sample four.

Figure A.5: Bright field micrograph of Sample five.

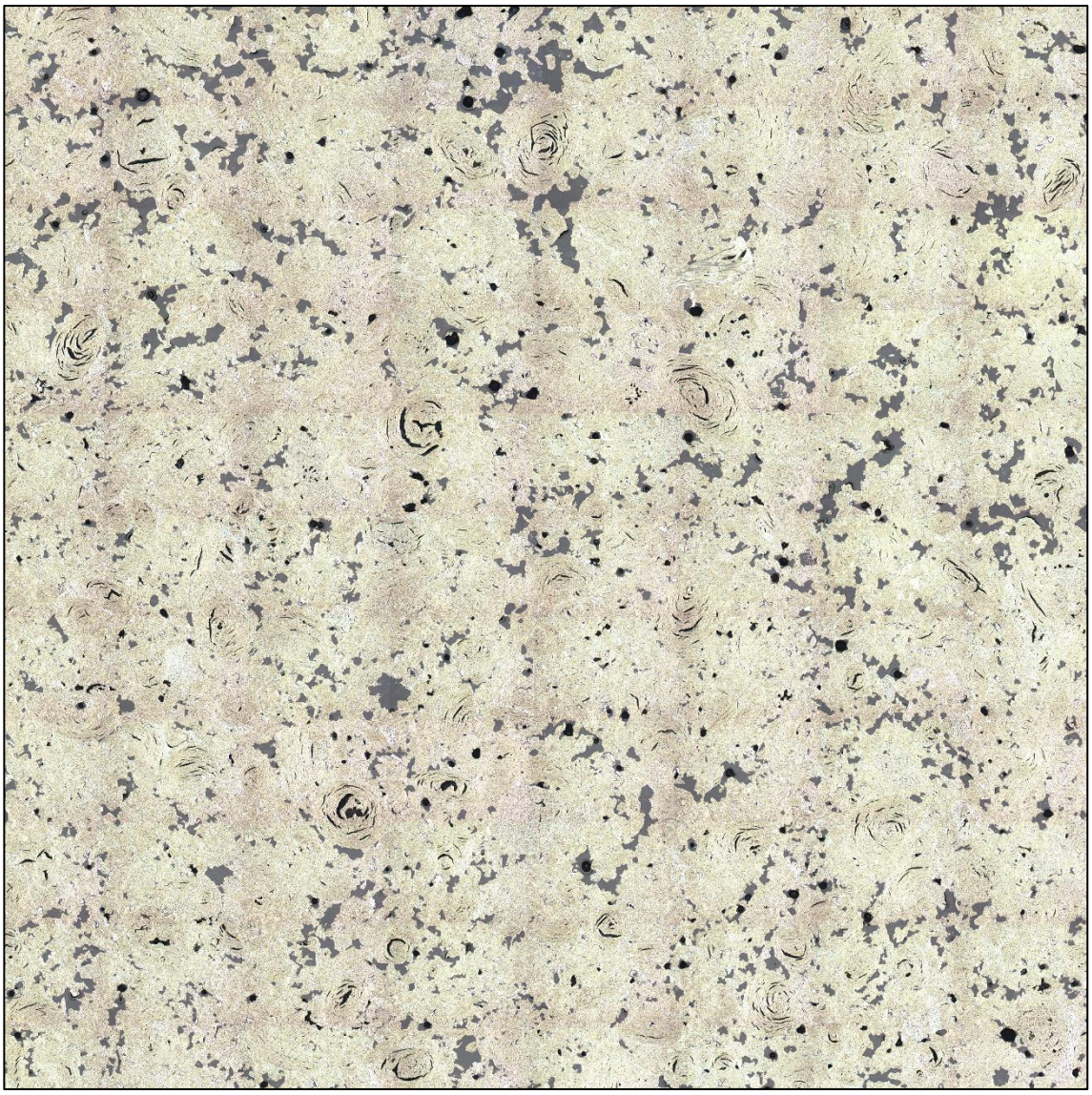

Figure A.6: Bright field micrograph of Sample six.

Appendix B – Method to Generate Representative Microstructure

This section will detail the procedure used to create a representative microstructure model in ANSYS. Although microstructural data in this thesis was ascertained through use of Image Pro Plus, alternative programs may be used providing they allow segmentation of objects and will output data as a bitmap. Note that the details of this procedure are relatively broad and may be applied to alternative materials providing they meet the necessary prerequisites.

B.1. Segmentation and Output of Features

1. Determine a suitable image threshold and apply the segmentation, cleaning borders if necessary.
2. Create 1-bit image from segmentation.
3. Resize image to suit the requirements of the investigation and any software limitations.
4. Output pixel data as a bitmap.
5. Copy bitmap data to clipboard.

B.2. Macro Conversion

1. Open file on DVD (Model Construction > Macro conversion).
2. Paste bitmap matrix in cell F6.
3. Select cell B2 and run macro (CTRL + M).
4. Select range to copy (*i.e.* the entire bitmap matrix).
5. Select destination cell D6 and click 'OK'.
6. Once the macro is complete the *.lgw file may be saved in a *.txt file ready to be imported into ANSYS.

B.3. ANSYS Conversion

1. Crete an area within ANSYS that corresponds to the dimensions of the micrograph.

2. Define mesh edge length as being the linear dimension divided by the number of pixels.
3. Extrude the area by a value equal to the element edge length.
4. Mesh the model.
5. Import element removal data.
6. Apply appropriate loads and constraints to model areas.
7. Solve mode